Technische Universität München
TUM School of Life Sciences

3D printing and texture modulation of cereal-based matrices

Ahmed Raouf Fahmy

Vollständiger Abdruck der von der TUM School of Life Sciences der Technischen Universität München zur Erlangug des akademischen Grades eines

Doktors der Ingenieurwissenschaften (Dr. -Ing.)

genehmigten Dissertation.

Vorsitz:	apl. Prof. Dr.-Ing. habil. Petra Först
Prüfer*innen der Dissertation:	1. Prof. Dr.-Ing. Thomas Becker
	2. Prof. Dr. Bernd Hitzmann
	3. Prof. Dr. Kathrin Castiglione

Die Dissertation wurde am 02.11.2022 bei der Technischen Universität München eingereicht und durch die TUM School of Life Sciences am 21.03.2023 angenommen.

Do not let your difficulties fill you with anxiety, after all it is only in the darkest nights that stars shine more brightly.

Ali Ibn Abi Talib AS

Acknowledgements

To all who supported me during this exciting and enlightening journey I have to say, thank you. First, I would like to express my sincere gratitude to Prof. Dr. Thomas Becker for his supervision at every stage of my PhD. I highly appreciate his insightful comments and suggestions about methodologies and results which greatly improved my scientific skills and made me a better researcher.

Moreover, a huge appreciation to Prof. Dr. Mario Jekle for his guidance, encouragement and positive support. His creative scientific ideas were one of the most imperative pillars in the creation of this dissertation. And most importantly, he played an important role in my personal development and in the development of my professional career. Furthermore, a special thanks to the group of cereals and process engineering for their help, support and of course for all of the fun and enjoyable time we spent at work or outside of work.

I would like to thank Prof. Dr. Bernd Hitzmann and Prof. Dr. Kathrin Castiglione for agreeing to evaluate my dissertation and I am thankful to Prof. Dr. Petra Först for accepting the assignment of chairperson of the examination committee.

I owe everything to my parents and my brother who always supported me, believed in me and believed in what I could achieve. Thank you so much for always being there for me and for believing in me since I was a child.

From the bottom of my heart, I am grateful to my beautiful wife and the love of my life Nada for her endless love, patience, support and for our little sunshine Farida. I will always love you both.

To all of my friends, in Egypt and in Germany, thank you for all of your support and all of the good time we had and we will have together. Although there was a great distance and I was often busy, you continued supporting me to achieve my lifelong dream.

This one is for you, my amazing grandpa Hassan El-Beik. I hope you can see me and I know that you are proud of me.

Preface

The results and publications presented in this thesis were developed from 2018 to 2021 at the Technical University of Munich, TUM School of Life Sciences, Institute of Brewing and Beverage Technology, Research Group Cereal Technology and Process Engineering.

Peer-reviewed articles

The following four peer reviewed articles (shown in chronological order) were generated in the mentioned period of this research work:

1. **Fahmy, A. R.**, Becker, T., & Jekle, M. (2020). 3D printing and additive manufacturing of cereal-based materials: Quality analysis of starch-based systems using a camera-based morphological approach. Innovative Food Science & Emerging Technologies, 63 (April), 102384. https://doi.org/10.1016/j.ifset.2020.102384
2. **Fahmy, A. R.**, Amann, L. S., Dunkel, A., Frank, O., Dawid, C., Hofmann, T., Becker, T., & Jekle, M. (2021). Sensory design in food 3D printing – Structuring, texture modulation, taste localization, and thermal stabilization. Innovative Food Science & Emerging Technologies, 72 (August), 102743. https://doi.org/10.1016/j.ifset.2021.102743
3. **Fahmy, A. R.**, Vogt, U. T., Jekle, M., & Becker, T. (2022). Hardness targeted design and modulation of food textures in the elastic-regime using 3D printing of closed-cell foams in point lattice systems. Journal of Food Engineering, 320 (May), 110942. https://doi.org/10.1016/j.jfoodeng.2022.110942
4. **Fahmy, A. R.**, Jekle, M., & Becker, T. (2022). Texture modulation of starch-based closed-cell foams using 3D printing: Deformation behavior beyond the elastic regime. Journal of Texture Studies, 1-17. https://doi.org/10.1111/jtxs.12729

Contents

Abbreviations

3D	Three dimensional
AM	Additive Manufacturing
RP	Rapid Prototyping
STL	Standard Tessellation Language
FLM	Food Layered Manufacturing
FDM	Fused Deposition Modelling
SLS	Selective Laser Sintering
BJ	Binder Jetting
NIR	Near Infrared
FEM	Finite Element Modelling
°C	Degree Celsius
TPA	Texture Profile Analyzer
DSC	Differential Scanning Calorimetry
CLSM	Confocal Laser Scanning Microscopy
PFM	Phenomenological Foam Model
HT-PFM	Hardness Targeted Phenomenological Foam Model
SC	Simple Cubic
BCC	Body-centered Cubic
FCC	Face-centered Cubic
NaCl	Sodium Chloride
2-AFC	Two-Alternative Forced Choice
P	Porosity
Pa	Pascal
N	Newton
E	Young's modulus
σ	Normal stress
σ_y	Yield stress
τ	Shear stress
ϵ	Strain
η	Damping coefficient
E_p	Plateau stiffness
γ	Densification coefficient
H	Hardness
G`	Storage modulus
G``	Loss modulus
CO_2	Carbon dioxide
MC	Methylcellulose
min	Minute
s	Second
µ	Micron
XG	Xanthan Gum

Abstract

The introduction of 3D printing in the structuring of starch-based foams is based on its accuracy, precision, reproducibility, and control over layer-based properties. From an application perspective and due to its principle of operation, 3D printing of starch-based materials is implemented for processing of novel textures, for designing of sensory perception and for personalizing nutrition. Regarding research purposes, 3D printing can be implemented to enhance processing reproducibility and to eliminate textural variability and inherited defects associated with traditional texturing processes. Typical structural imperfections are associated with the traditional structuring processes of starch-based foams such as non-periodic ordering of gas cells, defects, and non-uniformity of gas cell walls. Such inherited structural heterogeneity obstructs the elucidation of structure, texture, and sensory perception due to the lack of reproducibility. As most studies found in literature focus either on printability of materials or texture variation through arbitrary methods, there is a gap in knowledge and comprehensive methodologies in the texture design/modelling and the elucidation of texture-taste interactions using 3D printing. The objective of this thesis was to develop 3D printing methodologies for material printability characterization, taste localization, and targeted texture creation for starch-based foams. Through this method-driven approach, printing quality dependencies and structure-deformation relations were determined.

A camera-based morphological method was developed to assess the printing quality and accuracy of starch-based materials through in-line image acquisition and processing. Furthermore, this method elucidates the behavior of the printed materials in terms of their rheological response and therefore, establishing key quality and defect parameters for material selection. The developed method was used to characterize the relation between the rheological properties of two starch-based materials with varying hydration levels and their behavior during and after printing. The printing quality assessment was performed where the geometric features of the printed structures were measured and compared to the design parameters and the materials' rheological behavior. Serving as a key methodology, the developed method facilitates material selection based on the fundamental viscoelastic behavior.

Development and validation of an innovative 3D structuring and localization method was achieved. This method was designed to accommodate texturing, in-line thermal treatment, and flavor/aroma localization for enabling the elucidation of mechanistic texture-taste interactions. The approach used focused thermal stabilization technique and dynamic attenuation of printing settings to achieve constant textural properties independent of the localized taste concentration or configuration. Furthermore, the 3D structuring and localization method serves as a new framework for obtaining complete behavioral understanding to create custom flavor profiles.

A 3D printing method was developed for the design of textural properties in the elastic regime instead of only texture modulation. The main aim was to enable the design of 3D printed structures based on specific values of textural properties. A hardness targeted phenomenological foam model HT-PFM was derived, which is a model describing the empirical relationship between the foam properties and the resultant hardness which is based on observations of the system behavior and not directly derived from theory. The derived phenomenological model enables the design of 3D printed structures depending on the selected or required textural properties. The model was developed and validated using a complete 3D printing method allowing for targeted heat induced material transitions to actively modulate the material's mechanical properties. At the same time, fundamental textural relations in the elastic regime were elucidated for 3D printed closed-cell foams using analytical methods and transient mechanical FEM simulations. After achieving a textural design model in the elastic regime, further nonlinear large-strain behavior was elucidated. The overall deformation behavior, strain rate-dependent and viscoelastic responses of 3D printed closed-cell foams were characterized. At different strain conditions, the deformation, structural stresses, densification behavior, and failure criteria were investigated and characterized depending on the foam design characteristics. This method and characterization enable the complete mapping of deformation and textural behavior of 3D printed closed-cell foams which facilitates, for the first time, the production of cellular food structures with specifically targeted textural behavior.

Finally, this thesis focuses on establishing the foundation for 3D printing of starch-based textures by the development of generalized methodologies in 3D texturing, in-line monitoring and thermal stabilization as well as techniques for the design of textural properties and spatial localization of flavors. Additionally, characterization of

fundamental material-process interactions and textural relations of 3D printed starch-based cellular foams is performed.

Zusammenfassung

Die Methodik des 3D Druckes eignet sich durch die im hohen Maße gegebene Genauigkeit, Präzision und Reproduzierbarkeit, sowie der Kontrollierbarkeit der schichtbasierten Eigenschaften für die Herstellung von stärkebasierten Schäumen. Werden solche Produkte mittels traditioneller Methoden hergestellt, sind undefinierte texutrelle Eigenschaften unumgänglich. Die Etablierung der hochpräzisen 3D-Druck-Methodik im Bereich stärkebasierter Schäume würde eine Möglichkeit zur definierten Strukturierung und Texturierung schaffen. Im herkömmlichen Strukturierungsprozess ist die Entstehung von undefinierten Texturen auf eine aperiodische Anordnung der Gasblasen, Defekte und unregelmäßige Zellwände zurückzuführen. Die Unkontrollierbarkeit und damit schlechte Reproduzierbarkeit dieser strukturellen Heterogenität erschwert die Aufklärung der Zusammenhänge zwischen Struktur, Textur und sensorischer Wahrnehmung. In bisherigen Veröffentlichungen im Bereich des 3D Drucks lag der Fokus entweder auf der Druckbarkeit (Printablity*)* von Materialien oder der Variation von Texturen durch die Anwendung verschiedenster Druckmethoden, wohingegen ein Mangel an Wissen und Methodik zur gezielten Aufklärung von Textur-Geschmacksinteraktionen durch die Anwendung von Texturierungs- und Modellierungsansätze im 3D Druck besteht. Das Ziel dieser Arbeit war daher die Entwicklung von Methoden für den 3D Druck zur Charakterisierung der Printability, gezielten Texturierung von stärkebasierten Schäumen sowie zur Geschmackslokalisierung. Durch die Nutzung dieses methodisch getriebenen Ansatzes sollen Abhängigkeiten der Druckqualität und des Texturverhaltens zellulärer Strukturen unter Deformation aufgeklärt werden.

In einem ersten Schritt wurde eine kamerabasierte, morphologische Methodik entwickelt, um die *Printability* von stärkebasierten Materialien durch eine *in-line* Bildaufnahme und –auswertung zu ermöglichen. Durch die Anwendung der Methodik konnte darüber hinaus das Verhalten der gedruckten Materialien bezüglich ihrer rheologischen Antwort aufgeklärt werden. Die darauf definierten Schlüsselparameter zur Qualitätsbeurteilung, erlauben eine Auswahl geeigneter Druckmaterialien. Durch die Anwendung dieser Methodik wurde der Zusammenhang zwischen dem rheologischen Verhalten von verschiedenen stärkebasierten Materialien unterschiedlichen Wassergehalts und deren Verhalten während und nach dem

Druckprozess ermittelt. Weiterhin wurde die Druckqualität durch den Vergleich der geometrischen Formen der gedruckten Strukturen und den zugrundeliegenden Designvorgaben evaluiert und diese mit dem rheologischen Verhalten in Zusammenhang gesetzt. Die somit entwickelte Methodik dient als Grundlage für die Auswahl von Druckmaterialien basierend auf ihrem viskoelastischen Verhalten.

Weiterhin wurde eine innovative 3D Strukturierungs- und Lokalisierungsmethode entwickelt und validiert. Hintergrund dieser Entwicklung war die Zusammenführung von Texturierungsvorgängen, einer *in-line* thermischen Behandlung und einer modulierenden Geschmacks- und Aromalokalisierung für die Aufklärung der mechanistischen Zusammenhänge zwischen Textur- und Geschmackswahrnehmung. Durch die Nutzung fokussierter thermischer Stabilisierungstechniken und einer dynamischen Anpassung der Druckeinstellungen, wurden konstante Textureigenschaften erreicht, welche unabhängig von der Lokalisation von Geschmacksstoffen waren. Darüber hinaus kann basierend auf dieser entwickelten 3D Strukturierungs- und Lokalisierungsmethode ein umfassendes Verständnis über den sensorischen Eindruck in Abhängigkeit der Lokalisierung und Konzentration von Geschmacksstoffen erreicht werden.

Im Weiteren wurde eine 3D-Druck Methode für das gezielte Design von Textureigenschaften im elastischen Regime entwickelt, welche sich vom bisher gängigen Ansatz der reinen texturellen Modulation abhebt. Hauptziel dieser Methodik war die Gestaltung von 3D-gedruckten Strukturen zur Erzielung definierter textureller Eigenschaften. Das hierbei entwickelte Hardness Targeted Phenomenological Foam Model (HT-PFM) erlaubt die Gestaltung von 3D-gedruckten Strukturen ausgehend von definierten texturellen Eingabegrößen. Das HT-PF Modell wurde hierbei entwickelt und validiert, um durch gezielte hitzeinduzierte Übergänge die mechanischen Eigenschaften von Materialien zu modulieren. Gleichzeitig wurden durch die gemeinsame Anwendung von analytischen Methoden und transient mechanischen FEM Simulationen fundamentale texturelle Zusammenhänge für 3D-gedruckte Schäume mit geschlossener Zellstruktur aufgeklärt. Auf Grundlage dieses Texturdesignmodelles, welches im elastischen Bereich Gültigkeit besitzt, wurden auch im nichtlinearen Bereich das belastungsabhängige Verhalten dieser Strukturen aufgeklärt. Hierzu wurde das Deformationsverhalten, die Abhängigkeit von der Deformationsrate und das viskoelastische Verhalten von 3D-gedruckten Schäumen

mit geschlossener Zellstruktur quantifiziert. Für unterschiedliche Belastungsarten wurden hierbei das Deformations-, strukturelle Spannungs- und Verdichtungsverhalten, sowie die Grenzbedingungen für Materialzuverlässigkeit untersucht und in Abhängigkeit des Schaumdesigns betrachtet. Die entwickelte Methodik und Charakterisierung ermöglicht somit eine vollständige Aufklärung des Deformationsverhaltens und der Textur von 3D-gedruckten Schäumen mit geschlossener Zellstruktur, wodurch erstmalig die gezielte Herstellung von zellulär geschäumten Lebensmitteln mit maßgeschneidertem texturellen Verhalten ermöglicht wird.

Die vorliegende Arbeit konzentriet sich diese Arbeit auf die Schaffung der Grundlage für den 3D-Druck von stärkebasierten Texturen durch die Entwicklung allgemeiner Methoden in der 3D-Texturierung, in-line monitoring und thermischen Stabilisierung sowie Methoden für das Design von Textureigenschaften und die räumliche Lokalisierung von Geschmacksstoffen. Darüber hinaus wird die Charakterisierung grundlegender Material-Prozess-Wechselwirkungen und Texturbeziehungen von 3D-gedruckten stärkebasierten Texturen durchgeführt.

1 Introduction

As the use of additive manufacturing AM or 3D printing technologies in the texturing of foods and starch-based material systems is relatively newly adopted, several advantages as well as challenges exist. Complex food structures can be produced incorporating customized textures, functional ingredients, and personalized nutrition which is enabled by the geometrical accuracy and precision of 3D printing (Nachal et al., 2019; J. Sun et al., 2018; J. Sun, Peng, et al., 2015; Wegrzyn et al., 2012). From a scientific perspective, 3D printing can also be used for obtaining and elucidating complex material, textural, and sensorial relationships (Fahmy et al., 2021). This is performed by the manipulation of material's constituents and structural properties as well as by the targeted incorporation of aroma and flavor active compounds.

In this chapter, 3D texturing approaches are highlighted as well as key technological adaptation challenges and requirements for the texturing of food and starch-based material systems. In section 1.1, state of the art 3D food printing techniques is presented. This section also gives an overview on the printing behavior of food materials. Section 1.2 presents the theory and application of texture modulation using 3D printing as well as the knowledge gap in the applied research. Moreover, section 1.3 introduces the post-processing techniques used after 3D texturing. At the end of this chapter, the objectives and the framework of the thesis are presented in section 1.4.

Following the outline of section 1.4, chapter 0 presents the developed methods, conducted research and obtained results for 3D printing and texturing of starch-based materials. Subsequently, a critical discussion of the applied methods, approaches and results is highlighted in chapter 3.

1.1 3D printing of food material systems

Originally, AM was invented for the fabrication of complex structures in a single step to eliminate processing on multiple stages. The development of 3D printing technologies was first introduced in the fabrication of engineering materials such as polymers, metals, and ceramics (Hull & Arcadia, 1984; Kodama, 1981). For the same operation concept, 3D printing has evolved over the years to transform logistics and manufacturing processes to include multiple methods, materials, and technological equipment (Jordahl et al., 2018; Otcu et al., 2019). Due to its continuous development, 3D printing technologies are being integrated in various industrial and research sectors like construction, biomedical and most recently the food sector. The adoption of the technology in different industries is attributed to the approach's associated advantages including personal customization, material saving, high precision and design flexibility (Mitchell et al., 2018).

3D printing is an automated electro-mechanical manufacturing approach. It is a rapid prototyping RP technique where 3D geometries are planarly structured from point to point and built in a layer-by-layer approach from 3D CAD models (Godoi et al., 2016). The operation of 3D printing technologies is applied on multiple stages (Pereira et al., 2021). The first stage is the design and modeling of the constructs using a CAD software. After the design is completed, STL file of the model is generated. The second stage is uploading of the design on the printing or slicing software where the material-dependent printing settings are defined. Such settings include the layer thickness, printing temperature, and speed. In this stage, the model is converted into individual layers and the printing settings are applied. The slicing of the bulk models into layers is essential to perform the layer-based fabrication through 3D printing. Finally, through the printing software, a G-code (machine instruction programming language) is generated and communicated to the printer's hardware to perform the manufacturing process.

Food production and processing using 3D printing is called food layered manufacturing FLM where structures are built layer-by-layer (ASTM-International, 2012). In the food sector, structuring of viscous food materials was first introduced through a modified open source 3D printer design (Malone & Lipson, 2007). In general, the purpose of applying 3D printing in food structuring is associated with the personalization, new textures, and enhanced nutritional aspects (Keunings et al., 2016; Lipton et al., 2010;

Periard et al., 2007; Vesco & Lipson, 2009). Finally, the adoption of 3D printing technologies in the structuring of food materials is challenging due to the wide variation of physiochemical properties of food materials.

1.1.1 3D food printing techniques

Different types of 3D printing technologies are applied and studied for food fabrication. The adopted process are categorized depending on the state or type of used material as 2 main categories exist (Godoi et al., 2016; J. Sun, Peng, et al., 2015). The first category is extrusion and deposition technologies, shown in Figure 1-1. This approach relies on extrusion and deposition of viscous and liquid-based food materials. Moreover, this category includes FDM or material extrusion and Ink-jet printing. The second category is powder-based technologies. As shown in Figure 1-2, these AM technologies are applied on powder-based materials where structures are bound together using a binding mechanism such as liquid binders, hot air, and lasers. Powder based technologies include Binder Jetting BJ, Hot air sintering, and Selective Laser Sintering SLS (Fan Yang et al., 2017). All 3D printing techniques either modified or not, rely on the mentioned techniques for the design and processing of food structures.

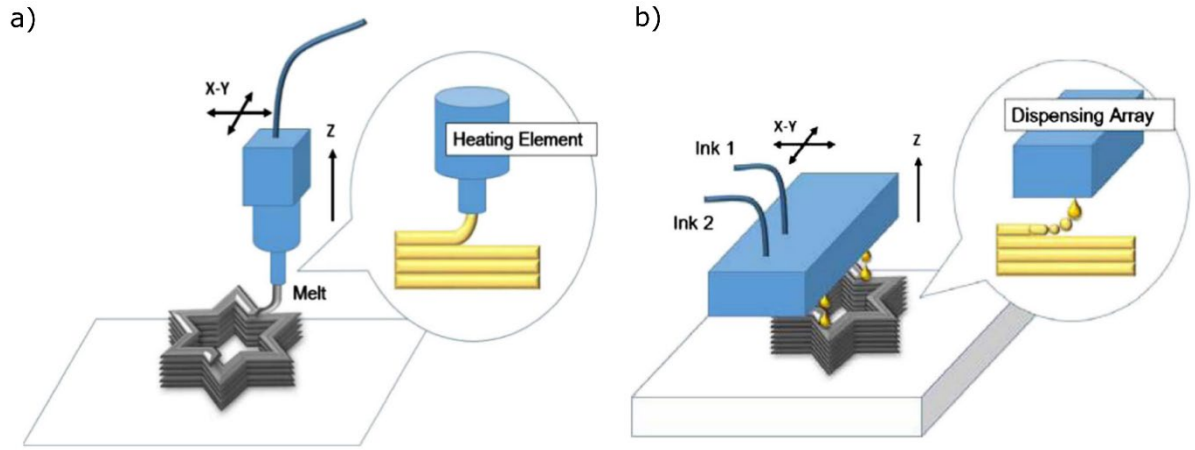

Figure 1-1: Extrusion and deposition 3D printing technologies (J. Sun, Zhou, et al., 2015): a) FDM 3D printing; b) Ink-Jet 3D printing.

FDM or material extrusion 3D printing is the main technique used in texturing of foods and starch-based material systems. It is used due to its ability to handle high viscosity and viscoelastic systems like dough (Fahmy et al., 2020). FDM 3D printing uses an extrusion system to deposit the material through a fine nozzle (M. Zhang et al., 2017). There are three extrusion principals applied for food materials which are screw-based extrusion, syringe-based extrusion, and air pressure extrusion (Guo et al., 2019;

Makino et al., 2017). In screw-based extrusion, the materials are transported to the nozzle through a moving screw. Direct force through a motor or a piston is used to transport the materials through the nozzle in syringe-based extrusion. For FDM 3D printing, the applied extrusion principle influences the printing behavior and geometrical quality depending on the viscoelastic behavior of the printed food material.

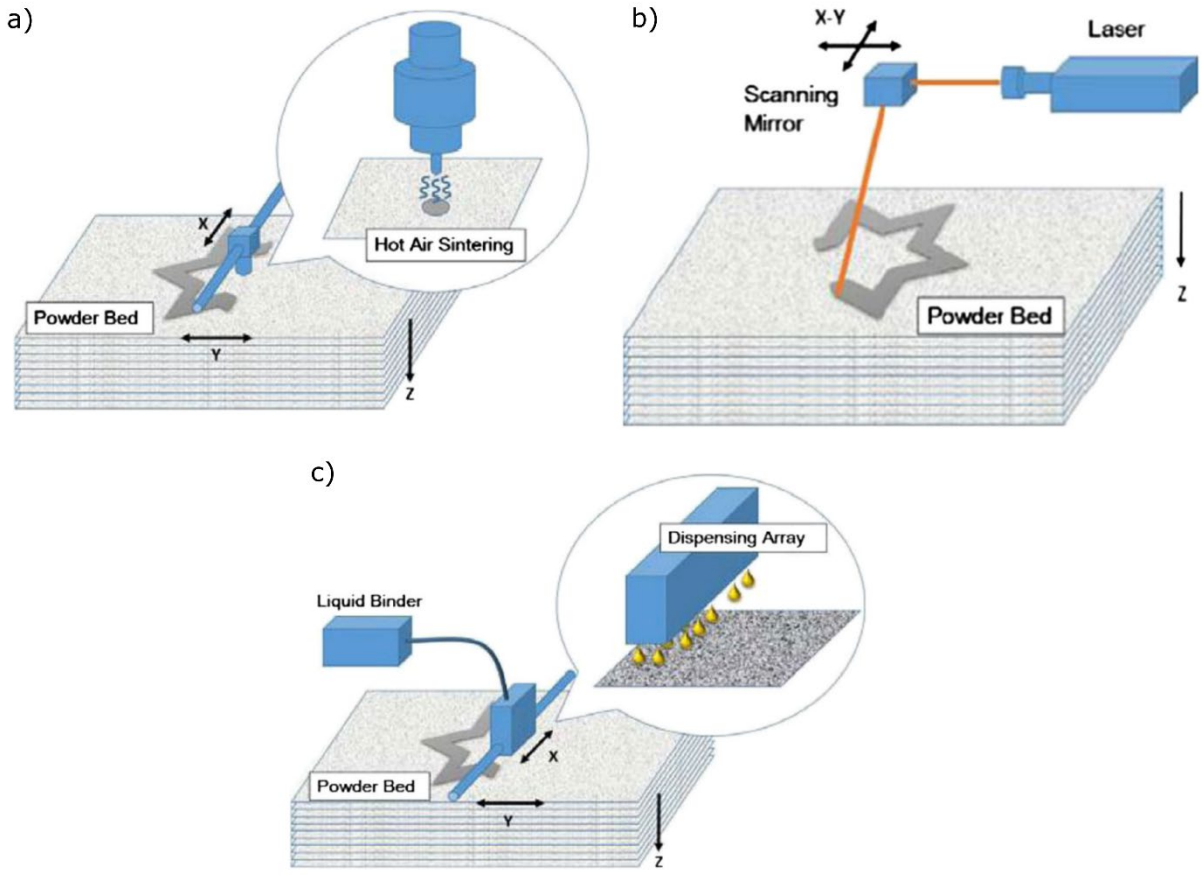

Figure 1-2: Powder-based 3D printing technologies (J. Sun, Zhou, et al., 2015): a) Hot air sintering; b) Selective laser sintering SLS; c) Binder jetting BJ.

1.1.2 Printing behavior and printing quality assessment

Material-process interactions define the geometrical quality of the printed structures. The printing quality of food and starch-based materials is assessed for optimizing the printing process and material selection (Lanaro et al., 2017). Different studies were conducted concerning the applicability of using different food formulations with material extrusion 3D printing. Concerning the assessment of printing quality, studies used a range of food and starch-based materials to correlate geometrical attributes with the rheological behavior and viscoelastic response of the materials. The studied formulations included hydrocolloid and starchy gels, cereal-based matrices, potato and wheat starch-based formulations, cheese, chocolates, and a combination of fruits and

vegetables (Álvarez-Castillo et al., 2021; Feng et al., 2020; Keerthana et al., 2020; Y. Liu et al., 2019; Z. Liu et al., 2019; Paolillo et al., 2021; Phuhongsung et al., 2020; E. T. Pulatsu et al., 2020; Sager et al., 2021; Y. Sun et al., 2020; Theagarajan et al., 2020; Varghese et al., 2020). This section of the thesis focuses on the printing quality assessment parameters and factors affecting the printing accuracy of FDM or material extrusion printing.

Several factors were identified that influence the printing precision and accuracy of food and starch-based systems (M. Zhang et al., 2017): a) extrusion principle, b) processing parameters or printing settings, c) rheological response of the materials. Considering the rheological properties of the printed materials, the viscosity should satisfy 2 conditions. The viscosity of the material should be low enough to allow the successful extrusion of the material. Also, it should be high enough in combination with the elastic component of the material to hold subsequent deposited layers and to eliminate structural collapse or slumping (Kim et al., 2017; Godoi et al., 2016; M. Zhang et al., 2017). Also, shear-thinning behavior and post-printing structural regeneration is required for the reason mentioned previously.

As an example of a printability study focusing on the material's rheological response, Lui et al. investigated the influence of rheological properties on 3D printing quality of mashed potato formulation with different concentrations of potato starch (Z. Liu et al., 2017). The authors concluded that, concerning rheological-based material selection, the starch-based material should possess a suitable elastic modulus G` and yield stress σ_y for maintaining printed shapes. Also, a relative low consistency index k and flow behavior index n is required for successful extrusion. For the study's process dependent approach, the authors showed that through the increase of starch concentration (at 2% on weight bases) to obtain specific rheological levels, sufficient extrudability and printability can be obtained. The study concluded that a k of 118.44 [Pa.s^n] and a mechanical strength through a σ_y of 312.2 [Pa] leads to stable structures while printing at a feature resolution of 2 mm (Z. Liu et al., 2017). Also, the lack of addition of starch to the formulation induced a decrease in the G` frequency response and in the yield stress with a σ_y of 195.9 [Pa] which led to structural collapse and slumping behavior. On the other hand, increasing the starch concentration above a certain level (at 4% on weight bases) led to poor extrudability. This occurred at a high k of 214.3 [Pa.s^n] and at a high σ_y of 370.3 [Pa]. Although the authors investigate the

influence of the material's rheological response on 3D printing, the analysis of the printed structures were not done quantitatively using precise analytical methods. Also, the printability evaluation was done on complex structures where structural simplification could be useful in obtaining direct correlations between the rheological response and geometrical parameters as well as viscoelastic induced defects.

The processing parameters are also crucial in the resultant quality of the printed food structures. Such processing parameters include the nozzle diameter, height, extrusion rate, and printing speed. Hao et al. obtained a model defining the critical nozzle height for food deposition using chocolate as a reference material (Hao et al., 2010):

$$h_c = \frac{V_d}{v_n D_n} \quad (1.1)$$

Where, h_c is the critical or optimal nozzle height [mm], V_d is the extruded volume per unit time [mm^3/s], v_n is the printing speed [mm/s], and D_n is the nozzle diameter [mm]. The authors showed that at a height lower that the calculated h_c protrusion occurs in the direction perpendicular to the deposition directions. This occurs as the extruded volume at the selected printing speed is higher than the available space under the nozzle. Conversely, at heights higher than the calculated critical height, the printing accuracy decreases as the material does not reach the printing platform in the required time. Another example of processing setting is the nozzle diameter. The study by Wang et al. showed that the use of nozzle diameter (0.8 mm and 1.5 mm) not compatible with the material-dependent flow rate led to printing inconsistencies and affected the printing precision and surface quality of fish-based gels (L. Wang et al., 2018). Furthermore, the printing speed and extrusion rate are also a main determinant in the resultant quality. A study by Khalil and Sun proposed an equation for determining the printing speed (Khalil & Sun, 2007). The nozzle movement rate can be determined using the selected nozzle diameter as well as the material-dependent flow rate (Khalil & Sun, 2007):

$$v_n = \frac{4Q}{\pi D_n^2} \quad (1.2)$$

Where v_n is the critical or optimal movement speed [mm/s], Q is the material flow rate [mm^3/s] and D_n is the nozzle diameter [mm]. Results showed that a velocity greater than the calculated critical value led to an overall lower extruded volume while a lower

velocity led to an overall higher extruded volume which resulted in geometrical inaccuracies in the printed structures (Khalil & Sun, 2007).

1.2 Textural modulation using 3D printing

The texture of foods is scientifically explained as the interaction of the resultant structural, mechanical and surface properties (A. S. Szczesniak, 2002). Highly dependent on the type of food, texture plays an important role in the food process engineering field (Bourne, 2002; Monaco et al., 2008). Concerning starch-based food products such as bread, the texture is a fundamental component in influencing the sensory perception and consumer's acceptance (S. Wang et al., 2013). Having a significant impact on consumer perception, the texture of starch-based products is dictated by its pore structure, overall porosity and pore distribution (Scanlon & Zghal, 2001; Zghal et al., 2002). Most importantly, the structure of starch-based foams defines the products' handling as well as it affects the product's mastication performance (Gao et al., 2018; S. Wang et al., 2011). Furthermore, the mastication process which is dictated by the textural behavior can be related to the nutritional characteristics (Takahashi et al., 2009). This is highly dependent on the formation process of cellular starch-based foams.

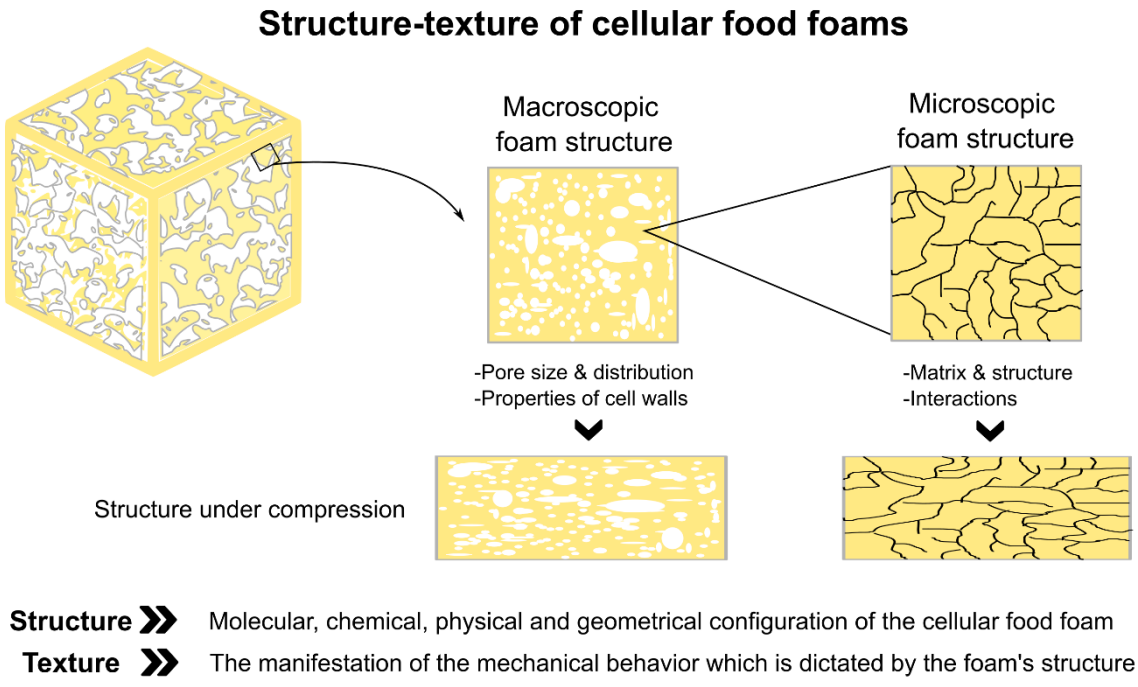

Figure 1-3: Relation between structure and texture of cellular food foams.

The processing and formation of cereal- and starch-based foams such as the bread crumb involves a superposition of physical and chemical processes. The processing is

performed on 3 stages which are mixing and development of the dough, formation of the foam structure, and stabilization of the porous structure (Kent & Evers, 1994). During the mixing and development of the dough, 3 processes occur which are hydration, development of a protein network, and occlusion of air. At the time of hydration, a large amount of water is absorbed by the biopolymers in particular by the hydrophilic groups on the protein molecules (Farrand, 1969). The extent of water uptake by starch is altered by the amount of crystallite shearing the occurs during the milling process (Evers et al., 1984; Scanlon et al., 1988). For the development of the gluten network, the mechanical kneading input converts the flour and water mixture into a cohesive dough mass through the insoluble flour proteins (Bloksma & Bushuk, 1988; Weegels et al., 1996). The proteins form complexes with lipids and some carbohydrate components like the starch granules and other filler materials to form a coherent viscoelastic structure encapsulating the air cells (Bloksma, 1990b, 1990a). This is apparent when the dough is optimally developed. Acting as the cell wall material in the transitioned crumb, optimal development of the protein network is essential for the structuring of the crumb (Zghal et al., 1999).

Occluded air is one significant component of the developed dough. The occlusion of air occurs during the mixing process and also from the air trapped in the bulk volume of the flour mass (Campbell et al., 1991; Chamberlain & Collins, 1979; Shimiya & Yano, 1987, 1988). In subsequent operations and processes, no generation of new cells occur despite the action of leavening agents (Baker & Mize, 1941). Considering the formation of the foam structure inside the dough, CO_2 gas is generated within the liquid phase through the action of the used leavening agent. Due to a concentration gradient, the gas diffuses in solution to the air nuclei. Then, the density of the dough decreases as the nuclei expand into gas cells (Chamberlain & Collins, 1979; Shah et al., 1998). The final proofing stage is the determinant of the bread crumb regardless form the mixing action or the subdivision of cells in the sheeting and molding processes (Shah et al., 1998).

For the stabilization of the cellular structure, the crumb structure is set by the conversion of the liquid phase to a solid phase during thermal stabilization or baking. A dominant class of polymers in the cellular cell walls is transitioned by the moisture-heat regime during the baking process. Partial melting of the hydrated starch granules occurs as well as the aggregation of a polymer class with the gluten proteins

(Blanshard, 1986; Donovan, 1979; Weegels et al., 1994). The cell wall material of the stabilized crumb structure is a proven complex composite as also molecules manifested form the starch granules contribute to the molecular associations (Biliaderis, 1991; Martin et al., 1991). During baking, further expansion of the gas cells occur which is controlled by the viscosity and mechanical properties of the cell walls (Fan et al., 1999).

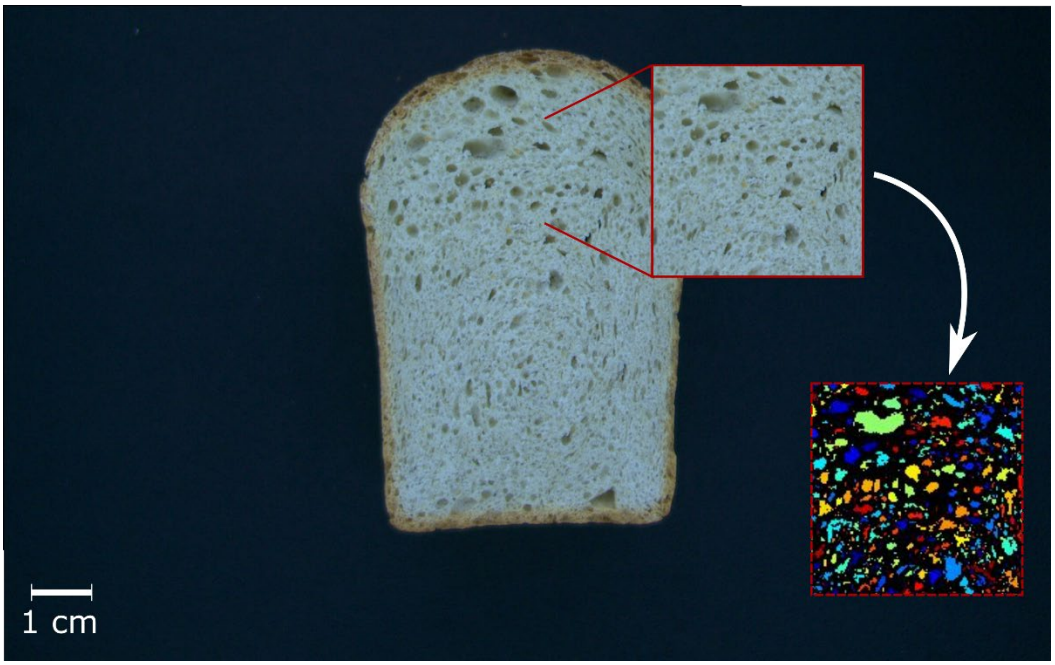

Figure 1-4: 2D image analysis of the crumb structure and pore labelling for wheat bread.

The deviations in air occlusion during the mixing of different doughs give rise to cellular solids with different structures. Also, the expansion and distribution of gas cells are highly dependent on the non-independent nature of gas cell growth and the subsequent processing operations such as punching, sheeting, and molding. Moreover, the macroscopic physical properties of the crumb is affected by the concentration of starch in the cell walls and by the degree of melting (Evans & Lips, 1992; Luyten & van Vliet, 1995; Soulaka & Morrison, 1985). Therefore, this in turn induces deviations in the resultant mechanical properties of the developed foams (Benning, 1969; Brezny & Green, 1990; Chaffanjon & Verhelst, 1992).

1.2.1 Mechanical behavior of starch-based foams

During handling and mastication, the physical texture of cereal- and starch-based foams such as bread is characterized by the mechanical behavior. Referring to the loading response of the whole foam structure, the mechanical behavior is in defined

by a combination of the solid matrix properties, relative density, and pore distribution (Cauvain & Young, 2006; S. Wang et al., 2013). The material constituents which controls the solid matrix properties explains the loading response of structural elements of the cellular structure on a material level (Ashby, 2001; Avalle et al., 2007; Roylance, 2008; Sharma, 2010).

Starch-based foams are two-phase cellular composite solids with high porosity (Scanlon & Zghal, 2001; Zghal et al., 2002). A starch-based cellular solid is a structure composed of an interconnected network of struts or plates with a dispersed fluid or gas phase. There are two main types of cellular solids, open- and closed-cell foams (L. J. Gibson, 1989; Lorna J. Gibson & Ashby, 1999). Cellular materials of open-cell nature are characterized by an interconnected internal structure and gas cells. On the other hand, cellular materials of closed-cell nature are defined by a solid membrane covering and isolating individual gas cells. The structure of cereal- and starch-based foams are considered to be of open-cell nature where the cells are mainly of polyhedral design which can be contributed to the forming process (Gao et al., 2018; Jang et al., 2008; Landers et al., 2008).

Starch-based cellular materials are categorized as elastomeric open-cell foams based on their quasi-static compressive behavior (Gao et al., 2018; L. J. Gibson, 1989). The large deformation stress-strain behavior follows 3 distinct regimes: a) an elastic regime, b) a yielding and stress plateau regime, and c) a strain locking or densification regime. Each deformation phase or regime defines a particular mechanism of deformation. First, the elastic regime is defined by the bending of cell walls or by the elastic compression of the cell struts. Second, the stress plateau deformation can be described depending on the constitutive material of the cell walls as plastic yielding, elastic buckling or brittle fracture. Third, strain locking or densification occurs when the cells have completely collapsed due to the meeting of opposing cell walls. As shown in Figure 1-5, this region is distinguished by the non-linear increase behavior of stress. However, the tensile behavior of elastomeric open-cell foams is slightly different (L. J. Gibson, 1989). The stress plateau does not occur where it is truncated by tensional cell alignment. Furthermore, the textural properties of starch-based foams are directly related to the described deformation behavior and the response of the structure to mechanical loading.

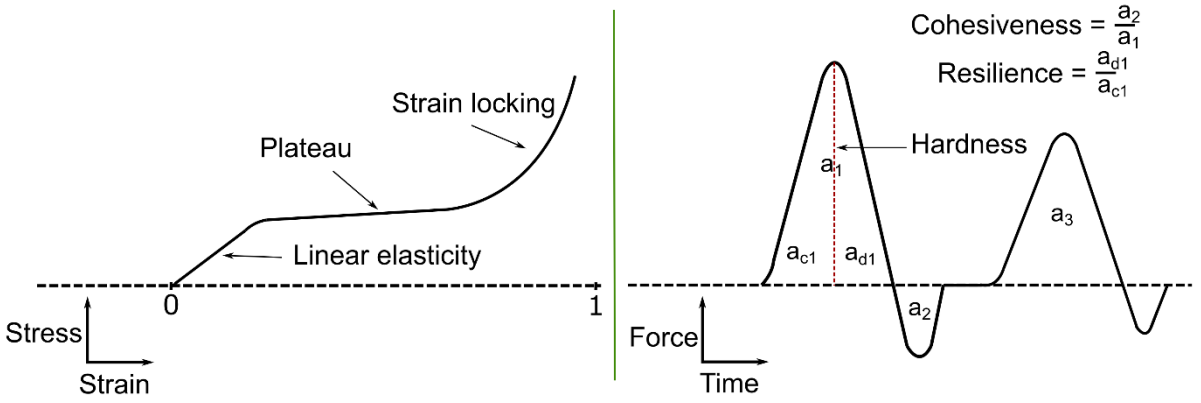

Figure 1-5: (Left) stress-strain behavior of elastomeric foams under quasi-static compression; (Right) TPA force-time characterization through a double compression test.

The textural properties are described scientifically as the manifestation of the interactions between material, structural, and surface properties (Corp & Plains, 1973; A. S. Szczesniak, 1963; Trinh & Glasgow, 2012). The textural behavior of starch-based foams is elucidated using a double compression test through texture profile analysis TPA. Also, other analytical and sensorial methods exist in literature. For simplification, the textural properties are categorized in 2 groups. The first group (called initial) which are obtained from the first compression cycle include the hardness and fracturability of the tested structure. The hardness is the obtained peak force for a pre-defined level of deformation while the fracturability is the force where structural collapse or failure first occurs (Micha Peleg, 2019). The second group of textural properties are described as masticatory as the tend to approximate the chewing behavior of structures. This group includes the structural cohesiveness, the adhesiveness, the gumminess, the springiness, and the chewiness. The cohesiveness is correlated to the strength of the material's internal bonds; the adhesiveness denotes the work required to overcome adhesion while the gumminess is the energy required to disintegrate the cellular structure. Moreover, the springiness or elasticity is defined as the rate at which a deformed structure returns to its original state while the chewiness is described as the mechanical energy required to chew a solid food structure. The mechanical behavior and textural properties of starch-based foams influences the functional, mastication and sensory characteristics (A. S. Szczesniak, 2002). Therefore, the introduction of 3D printing approaches is promising for the control and customization of starch-based textures.

1.2.2 3D printing and fabrication of starch-based textures

The modulation and variation of textures using 3D printing is performed through the selection of ingredients and through the manipulation of the microstructural interactions, material properties, and morphology of the cellular structure (Pereira et al., 2021). Recently, several studies found in literature showed successful modulation of textural properties of printed structures using different starch-based materials (A. Derossi, Caporizzi, Oral, et al., 2020; A. Derossi, Caporizzi, Paolillo, et al., 2020; Jonkers et al., 2020; Z. Liu, Bhandari, et al., 2018; Z. Liu & Zhang, 2021; Noort, Vancauwenberghe, et al., 2017; Piovesan et al., 2020; E. Pulatsu et al., 2020; Severini et al., 2016; Varghese et al., 2020; Fan Yang et al., 2019; L. Zhang et al., 2018). Moreover, most studies concentrate on elucidating the influence of the printed internal cellular structure on the textural properties. On the other hand, only few studies focus on the targeted design of textural properties using 3D printing.

One of the earlier studies to demonstrate variable starch-based textures through morphological manipulation using 3D printing, Noort et al. showed a texture modulation approach using different cellular configurations and material micro-porosity (Noort, Van Bommel, et al., 2017; Noort, Vancauwenberghe, et al., 2017). In this study, the authors FDM printed 3D honeycomb structures using wheat flour dough. The authors produced a linear decrease in rupture strength by printing structures with variable macro- and micro-porosities ranging 27% to 60%. The authors also presented an approach for introducing micro-porosity using coaxial extrusion nozzle to create air bubbles down to 100 µm in diameter. On another note, Derossi et al. elucidated the effect of relative density on the structural hardness using 3D FDM printing (A. Derossi, Caporizzi, Paolillo, et al., 2020). For this study, a wheat flour dough formulation was used which was composed of wheat flour (62 g/100 g on weight bases w.b.), olive oil (6 171 g/100 g w.b.), sodium chloride (1 g/100 g w.b.) and distilled water (31 g/100 g w.b.). The structures were printed using an internal cube-shaped pores enclosed in a parallelepiped structure at 6 different structures with varying porosity fraction from 18 to 54%. Using compression analysis, results showed a reduction in hardness of the 3D printed structures where the hardness was reduced from 289 N to 84 N for the relative densities of 0.569 and 0.401, respectively.

For the design of mechanical properties, Piovesan et al. presented a combined 3D printing and FEM approach to texture wheat flour dough (Piovesan et al., 2020). The

authors elucidated the correlation between the Young's modulus of the cellular structure (as a proxy for textural properties) and the structural properties. In this study, a comparison was conducted between data obtained from compression tests and predicted textural properties from FEM simulations. This comparison was performed to enable the future design of structures with desired textural properties. The authors used a cookie dough recipe composed of wheat flour (48.43%), sugar (9.69%), polydextrose (9.69%), margarine (24.21%), egg protein powder (2.42%), water (4.84%), emulsifier panodan (0.48%), and vanilla sugar (0.24%). 3D printing and FEM simulations were performed on 3D open-cell honeycomb periodic structures with variable cell sizes, wall thicknesses, and number of cells. Most importantly, the results showed an independency of the structure's Young's modulus on the wall thickness and cell size where a linear decrease occurred with respect to the increase in sample porosity (Piovesan et al., 2020). This suggests that the targeted design of structures to achieve desired levels of Young's modulus can be achieved only through the modulation of material properties and porosity. Also, the authors showed that the final porosity of the printed structures must be considered during simulation to achieve high precision in the prediction of the textural properties.

1.3 Post-processing and thermal stabilization

FDM or material extrusion 3D printing is the most used technique in the texturing of food or starch-based structures. However, it is mostly used in the food sector as a cold extrusion technique. Consequently, process compatible post-processing methods are required to induce the necessary physiochemical changes for production level integration. With regards to texture development and consumption of starch-based foams, physiochemical changes including dehydration, starch gelatinization, and recrystallization are essential (Lagrain et al., 2012; Ratnayake & Jackson, 2008). In addition, low water activity and microbial growth are important for storage stability of starch-based products. Thus, post-processing and thermal stabilization techniques are often used for starch-based materials subsequent to 3D printing.

The use of post-processing methods for starch-based structures in conjunction with 3D printing is challenging as they can induce structural deformations and can change the 3D printed features (He et al., 2020; Keerthana et al., 2020; Pereira et al., 2021; Fan Yang et al., 2019). Still a limited quantity, studies are incorporating various post-processing techniques in their approach for 3D printing of starch-based structures. The

studies mainly focus on textural development while investigating the structural and geometrical induced effects in relation to the material's composition. The used post-processing methods include frying, steaming, and baking as well as freeze- and microwave-drying (Antonio Derossi et al., 2018; Feng et al., 2020; Z. Liu, Zhang, et al., 2018; Z. Liu & Zhang, 2021; Martínez-Monzó et al., 2019; E. Pulatsu et al., 2020; Severini et al., 2016; Fan Yang, Zhang, & Liu, 2018; Zhao et al., 2021). The mentioned approaches are primarily used after printing where the development of in-line controlled thermal stabilization is still limited.

Oven-drying or baking of 3D printed starch-based structures is the most investigated post-processing method found in literature. For this post-processing technique, the output results are defined by the material constituents, physiochemical transitions, hydration level, structural configuration, and processing conditions (Feng et al., 2020). For 3D printing, the structures should geometrically resist post-processing induced deformations. Thus, most studies focus on resolving shape and structural stability through formulation control and by the inclusion of additives in the form of stabilizing agents (He et al., 2020; Kim et al., 2019). Concerning the effect of material constituents on printing quality after post-processing, Kim et al. characterized the influence of increasing hydrocolloid concentration in a wheat flour-based dough formulation (Kim et al., 2019). 4 different MC and XG concentrations of 0.5, 1, 2, and 3 g/100 g on dough basis were used. The hydrocolloid containing formulations were compared to the control formulation in terms of geometrical stability after baking at 170 °C for 15 min. During baking, results showed that the exclusion of hydrocolloids led to structural collapse of the printed structures during thermal stabilization. Besides, the incorporation of MC did not improve the structural stability after baking. Contrarily, the addition of XG improved the shape retention after baking. The study highlighted the influence of formulation control on printing quality with the integration of post-processing and thermal stabilization after 3D printing.

Also, different studies focus on elucidating the relationship between the baking performance of 3D printed starch-based structures with printing parameters. Serevini et al. investigated the evolution of the output geometry and relative density of printed wheat flour dough after baking (Severini et al., 2016). The authors printed simple cylindrical structures of 17mm diameter and 25mm height while varying the relative density and layer thickness of the printed structures. The structures were FDM 3D

printed using a dough of 100% wheat flour with a hydration level of 54 g/100 g of dry materials. In this study, the printed structures were baked at 200 °C. The study showed that, for all printed starch-based structures, the overall morphological and geometrical attributes remained after baking while various deformations occurred during thermal physiochemical transitions. A decrease in the designed geometrical dimensions of the printed structures occurred due to mass transfer during drying. Furthermore, the study showed that an increase in the targeted relative density occurred. The results obtained from several studies showed that post-processing induced discrepancies of geometrical and structural parameters must be considered during the design process of the cellular structures.

1.4 Thesis objectives and outline

Starch-based products like bread are cellular solids which are produced through a series of random physical and chemical processes (Zghal et al., 2002). Thus, the process-induced structure is generally heterogeneous (Silva et al., 1995). Due to lower sensitivity during mastication compared to analytical characterization, structural heterogeneity presents no deterministic concerns in terms of consumption. On the other hand, the complete determination and elucidation of correlations and causality between sensory, structure, and texture is still a challenge facing researchers in both theoretical and applied area of texture studies (Gao et al., 2018; Alina Surmacka Szczesniak, 1986; Scheuer et al., 2016). FDM 3D printing is introduced as a tool for standardization of textures and for localization of flavor/aroma active compounds. Considering its operational fundamentals, 3D printing can provide new insights in the elucidation of texture and sensory perception relationships. Consequently, new 3D printing texture processing methods are required.

First step in the adoption of 3D printing for the texturing of foods and starch-based materials is evaluating the material-process interaction. Printing quality or printability analysis is based on elucidating the geometrical behavior of printed structures with respect to the material constituents and viscoelastic rheological behavior. Much research was performed on characterizing the printing quality of different food systems with material extrusion 3D printing. However, various research limitations as well as knowledge and development gaps were identified. First, most research is performed on complex material systems which limits the correlation between the printing quality and the material constituents contributing to the flow and rheological behavior of the

printed food systems (Álvarez-Castillo et al., 2021; Chen et al., 2019; Keerthana et al., 2020; Y. Liu et al., 2019; Z. Liu et al., 2019; Phuhongsung et al., 2020; Sager et al., 2021; Severini et al., 2018; Theagarajan et al., 2020). As a consequence, obtaining general causality of printing quality attributes on material constituents or rheological behavior often fails.

Also, limitations regarding the approach for evaluating the printing quality are evident in previous research. Studies have carried out comprehensive characterization of the relation between the material composition and printing quality while neglecting the quantitative identification of morphological features and induced defects. As an example, several studies have used visual assessment to discuss the printing stability and resolution of 3D printed food structures (Z. Liu et al., 2017; Fanli Yang et al., 2018; M. Zhang et al., 2017) while other studies use mechanical instruments (Fan Yang, Zhang, Prakash, et al., 2018). The use of imaging was introduced in prior investigations where off line and non-automated techniques based on 3D scanning and camera imaging for geometry identification were used (Kim et al., 2017; Z. Liu, Bhandari, et al., 2018).

Both, dual extrusion and thermal stabilization techniques combined with FDM 3D printing were introduced for food texturing in published literature. Dual extrusion and deposition is mainly used for the creation of multi-material food structures (Gholamipour-Shirazi et al., 2020; Nachal et al., 2019; Periard et al., 2007; J. Sun, Peng, et al., 2015; Tan et al., 2018). This approach is useful for switching materials to fabricate specific features. For example, Liu et al. presented a dual extrusion 3D food printing method for the creation of complex food structures from starch- and fruit-based material systems (Z. Liu, Zhang, et al., 2018). As mentioned, this technique is frequently used for multi-material integration where flavor or taste design aspects are not considered. On another note, thermal stabilization techniques are used in the form of post-processing of 3D printed structures. Different post-processing techniques applied in literature include freeze and microwave drying, frying, steaming, and heating (Z. Liu, Bhandari, et al., 2018; Z. Liu & Zhang, 2021; E. Pulatsu et al., 2020; Severini et al., 2016; Fan Yang et al., 2019; L. Zhang et al., 2018; Zhao et al., 2021). Post-processing is used in literature for texture development where the in-line integration of thermal stabilization during 3D printing is not considered. Also, targeting specific material transitions, controlling of mass transfer and of base material properties was

not performed in literature. Therefore, FDM 3D printing is yet to be used for the combined control of structure and flavor design through an integrated texturing, flavor/aroma localization, and thermal stabilization approach.

The adaptation of 3D printing in texture modulation is newly applied and is not yet comprehensively researched. This adaptation is founded on the understanding of micro- and macro-structural behavior and mechanical properties of cellular food foams (Attenburrow et al., 1989; Guessasma et al., 2008, 2011; Jang et al., 2008; Robin et al., 2011; Zghal et al., 2002). 3D printing studies found in literature on the modulation of food textures relies on the manipulation of textures using structures with 2D periodic open cells. In addition, the texture modulation is often performed by the variation of material compositions, internal structure patterns, and post-processing techniques (A. Derossi, Caporizzi, Oral, et al., 2020; Kim et al., 2019; Lille et al., 2020; L. Liu et al., 2019; Y. Liu et al., 2019; Z. Liu & Zhang, 2021; Pereira et al., 2021; Varghese et al., 2020; Fan Yang et al., 2019). Only few and very recent studies characterizes the relationship between textural properties and structural parameters such as the pore geometry, cell wall sizes and cell count (A. Derossi, Caporizzi, Paolillo, et al., 2020; Piovesan et al., 2020; Vancauwenberghe et al., 2018). Furthermore, all studies focus on modulation aspect regardless to the development of an approach for designing food structures to target specific textural properties. Finally, through all technological advances and obtained knowledge, all studies are generally focused on the modulation of the textural properties in the elastic regime only without characterizing the large deformation stress-strain behavior.

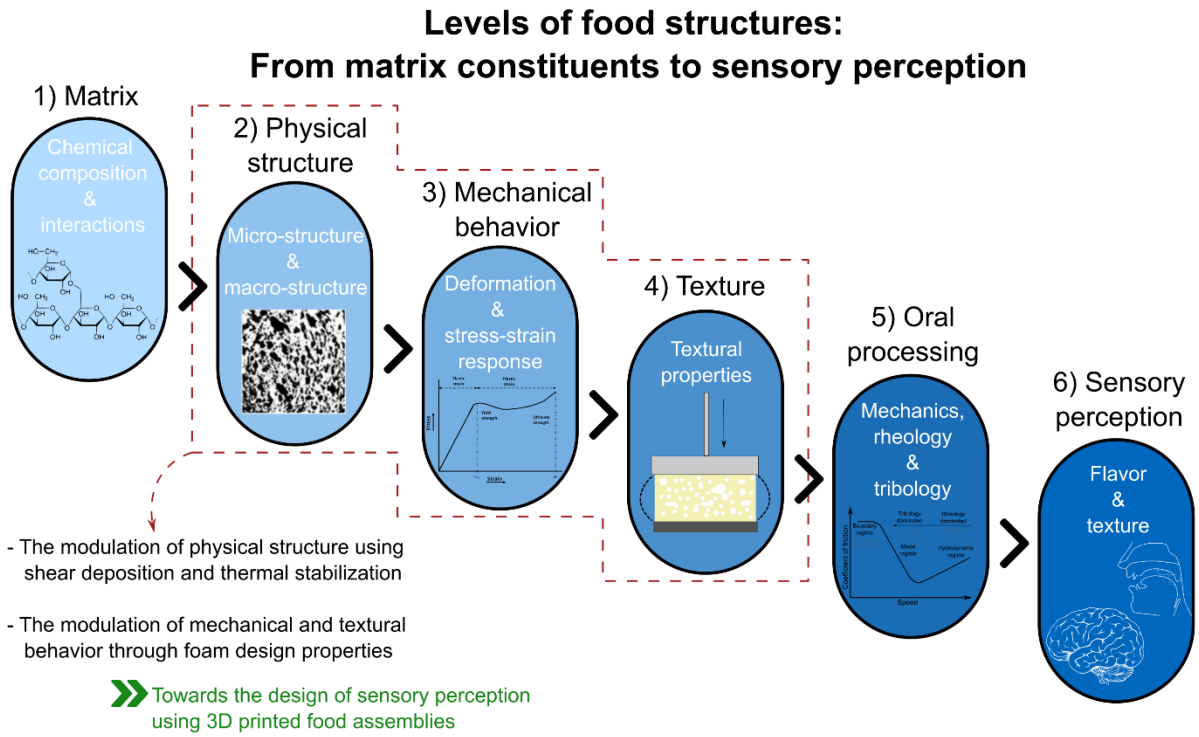

Figure 1-6: Illustration of the different levels of cellular food foam structures and its modulation using 3D printing.

Based on the identified research and development gaps concerning 3D printing and texture modulation of starch-based matrices, the following methodology-driven thesis was conceptualized and developed. The thesis is structured as follows:

I. Development of an in-line camera-based methodology for the assessment of printing quality during 3D printing. Using a morphological image processing approach, post-printing geometrical attributes as well as viscoelastic induced defects are quantitatively identified and studied on starch-based morphologies.

II. Establishment of a 3D printing methodology for the combined design of textures and localization of taste distributions in starch-based structures. This 3D printing method is developed as the controlled structuring of food textures incorporating precise local aroma or taste distributions will enable the elucidation of texture-flavor interactions as well as the control of the sensory perception of foods. In-line NIR thermal stabilization technique are introduced for printability improvement, geometrical stabilization, and moisture control. The presented method is utilized in a sensory contrast study where defined concentration gradients of sodium chloride are spatially printed in food textures.

III. Applied texture design and modulation of starch-based textures using 3D printing and in-line thermal stabilization.
    a. Formulation of a generalized hardness design formula for the 3D printing closed-cell starch-based foams using analytical texture analysis and FEM simulations. For thermal stabilization and moisture control during printing, in-line attenuation of base material's properties is developed based on NIR thermal stabilization. The developed texturing approach will enable the evolution of texture modulation to texture design where the production of cellular food structures with specifically targeted textural properties can be performed.
    b. Extension of modulation applications using 3D printing in the large-strain deformation regime. Characterization of relations between structure and stress-strain behavior of closed-cell starch-based foams are presented. A 3D printing-stabilization method is applied and optimized for targeting heat induced physiochemical material transitions.

1.5 Methods

This section of the PhD dissertation contains the methods and approaches used for characterizing the raw materials as well as for elucidating the behavior of the 3D printed starch-based structures. Also, modifications of the printer through in-line monitoring and thermal stabilization are described in this section.

Raw materials characterization

The protein and moisture contents of the raw ingredients were characterized following the American Association of Cereal Chemistry international standards (AACCi) 46-16 and 44-01, respectively. The detailed description is mentioned in sections 2.2, 2.3, 2.4, and 2.5.

3D printing setup and modifications

All printing trials and experiments were performed using a modified X400 V3 (German RepRap GmbH, Feldkirchen, Germany). The printer modifications were performed for the printing plate, extruders and for the integration the in-line NIR thermal stabilization systems. The commonly used build plate's polyetherimide (PEI) sheet was replaced by a Build Tak 3D printing surface (Build Tak, New Jersey, USA) for increased material adhesion. The original plastic extruder of the printer was replaced by 2 progressive

cavity pumps (PCP) deposition systems (Vipro-head3 and Vipro-head5) purchased from ViscoTec (ViscoTec GmbH, Töging, Germany). The Vipro-head3 and Vipro-head5 pumps have theoretical flow rates of 0.3 to 3.3 mL/min and 0.5 to 6 mL/min, respectively. The discrepancy in the flow rates between both used pumps were accounted for in the printer's firmware.

Printing models were modeled using SolidWorks (Dassault Systèmes, Vélizy-Villacoublay, France). Regarding the slicing software, simplfy3D (simplify3D, Ohio, USA) was used to generate the machine G-code files.

A NIR spot heater was mechanically integrated on the print head. The 150 W NIR spot heater was purchased from Optron (Optron GmbH, Garbsen, Germany) with a variable output power. The used NIR-emitter has a peak wavelength of approximately ~0.98 µm. The attached lens has a 6 mm spot diameter at a focal length of 17 mm. Considering the interface, a control unit was used as a link between the heater and the 3D printer which directly controls the heating power through the printer's firmware/software communication. The specific heating approach, selected power and movement speed of the heater are described in detail in sections 2.3, 2.4 and 2.5 of the dissertation.

Image processing

For the analysis of the printing behavior of starch-based systems, two Basler cameras acA1920-155µc (Basler AG, Ahrensburg, Germany) were used. The cameras have a megapixel resolution of 1920 x 1200 and equipped with identical Kowa LM16HC lenses with fixed focal lengths of 16 mm and a focus range of 300 mm. Both cameras were mounted directly on the printer, one on the extruder head (for the top view) while the other on the periphery of the build plate (for the side view). Separate scripts were used for analyzing the top and side view of the printed structures. MATLAB was used to develop the analysis scripts using its pre-existing imaging libraries and functions. The full description of the developed imaging algorithms is mentioned in section 2.2.

FEM modelling and simulations

ANSYS Workbench 2020 R1 (ANSYS, Inc., Pennsylvania, USA) was used for all simulations performed in this dissertation (sections 2.4 and 2.5). All developed models were discretized using a maximum mesh size of 800 µm that gave more than 130000 tetrahedron elements for a designed unit cell volume of 8 cm3. For all simulations, a

transient structural analysis was used. Double compression simulations were performed at 10% deformation and 0.5 mm/s vertical velocity which corresponds to the TPA analysis settings. All models were solved using a time step of 0.5 s for a total double compression time of 20 s. For defining the material properties (density and Young's modulus) in the material model, TPA test were performed on printed bulk structures (0% porosity) of the used materials under quasi-static conditions at room temperature and a low-strain rate of 0.025 1/s.

Rheological analysis

To determine the rheological and viscoelastic behavior of the 3D printing inks, an AR-G2 rheometer (TA instruments, West Sussex, UK) was used. Wheat flour dough samples were characterized using a parallel crosshatched plate geometry with a diameter of 4 cm with a gap of 1 mm. For the gluten-free 3D printing inks, a DIN single -gap concentric cylinders geometry was used with a conical rotor of 14 mm radius and a 1 mm clearance to the wall and bottom. The rheological approaches, settings and variables are presented in all of the articles presented in this dissertation (sections 2.2, 2.3, 2.4 and 2.5).

Texture profile analysis

To characterize the textural properties as well as the stress-strain behavior of the 3D printed structures, a Texture Analyzer type TA.TX. plus (Stable Micro Systems Ltd., Godalming, UK) was used. A 50 Kg measuring cell was used for all TPA experiments. In addition, all compression trials were performed at a trigger force of 0.05N and at a test speed of 0.5 mm/s. Measurements were conducted at a room temperature of 18 ± 2 ºC. Moreover, the compression trials were performed using an uncoated 25 mm cylindrical probe. For 3D printed samples with a surface area larger than 400 mm^2, a 50 mm circular platen was used. Finally, further testing details and settings are explained in sections 2.3, 2.4 and 2.5 of the dissertation

2 Results

2.1 Summary of peer-reviewed articles

Within the results section, a summary of each thesis peer-reviewed article is provided. Afterwards, full copies of the articles are presented.

3D printing and additive manufacturing of cereal-based materials: Quality analysis of starch-based systems using a camera-based morphological approach

Adapting 3D printing for structuring of starch and cereal-based systems is ambitious due to the materials' thixotropic and pseudoplastic behavior during extrusion and viscoelastic post-printing response leading to structural collapse and various defects. Therefore, to ensure printing precision, the material-process interactions were investigated. An in-line camera-based image processing method was developed to characterize the geometrical quality, structural stability and defects during printing to be used for material selection. This developed method was used to evaluate output width, length, height, area fraction, delay indices and drag/oozing artifacts of the printed geometries. Also, structural collapse and slumping behavior were characterized. Moreover, the printability method was used to monitor and elucidate the printability of two starch-based material systems (gluten-containing and gluten free) at various hydration levels. Relations between the geometrical and rheological parameters were elucidated. For printing gluten-containing systems, the formation of the complex gluten network act as structural stabilization element. On the other hand, the connected protein network induces adhesive discrepancies and drag effects during 3D printing with respect to the used hydration level. Furthermore, over-extrusion occurs due to structural deformation and yield hysteresis behavior during extrusion. Finally, geometrical attributes and viscoelastic defects were established for the first time. A better understanding of the material’s compatibility and limitations with 3D printing was obtained.

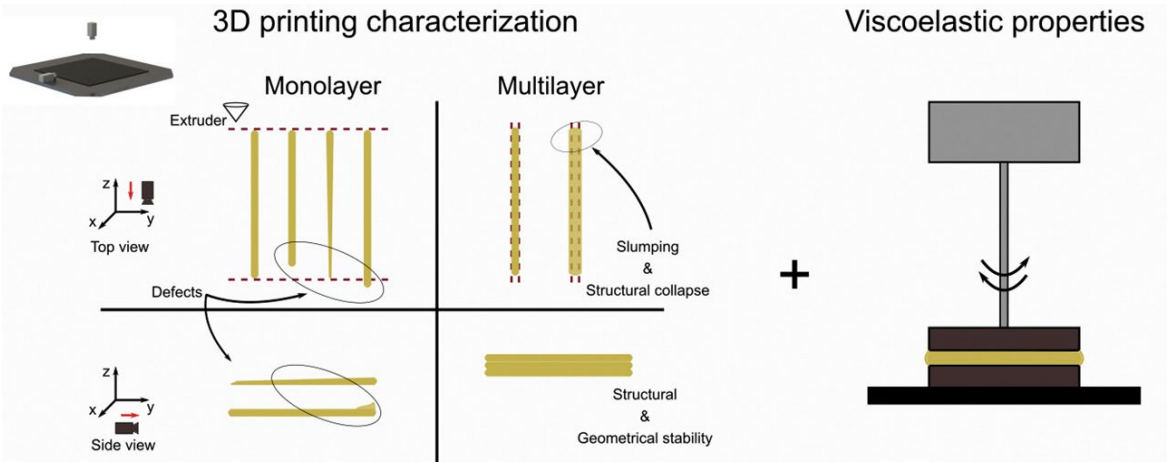

Figure 2-1: Quality analysis of 3D printed starch-based geometries through in-line camera acquisition/processing and shear-rheometry

Sensory design in food 3D printing – Structuring, texture modulation, taste localization, and thermal stabilization

Using 3D printing as a processing method for designing and modulating of food sensory profiles and as a tool for elucidating texture-taste release interactions is possible through precise texture creation and taste localization. A 3D printing method was developed for achieving a combined control over texture modulation and taste distribution of starch-based textures. This was achieved through the integration of dual extrusion/deposition and in-line NIR thermal stabilization. Dual extrusion was used as one nozzle deposits the base material while the other localizes the local taste distributions. An automatically tunable in-line NIR heating system was used for printability improvement, geometrical stabilization, and moisture control. This presented method was applied and characterized in a saltiness contrast study. To illustrate, the contrast study was performed using the developed 3D printing approach to systematically study the influence of inhomogeneous taste distribution on sensory perception. Defined concentration gradients of sodium chloride were site-specifically incorporated and locally resolved in 3D printed starch-based food textures. Ultimately, the study showed that through a sufficiently strong sensory contrast, the inhomogeneous spatial distribution of sodium chloride caused saltiness enhancement using 3D printing.

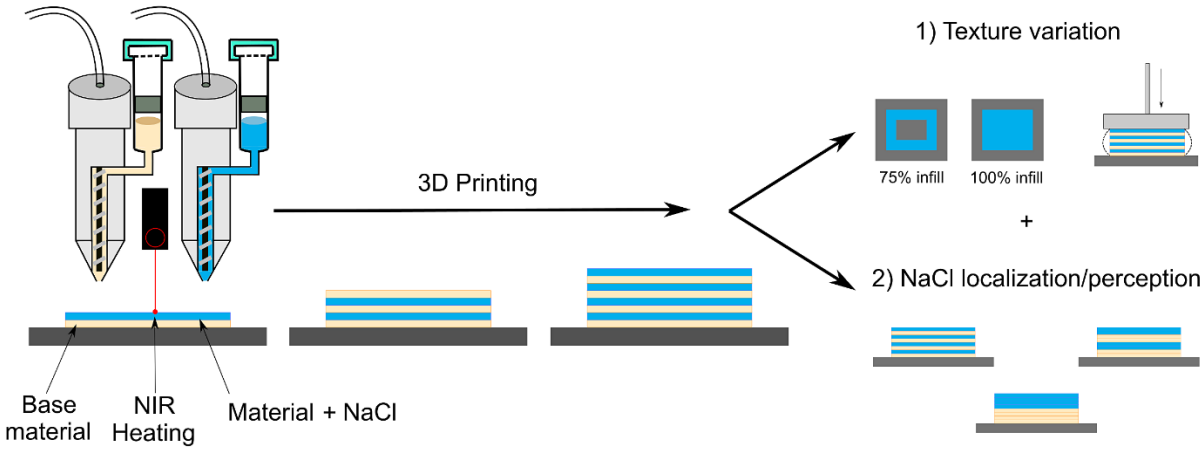

Figure 2-2: A combined texture modulation and taste localization 3D printing method for sensory control and for elucidation texture-taste interactions

Hardness targeted design and modulation of food textures in the elastic-regime using 3D printing of closed-cell foams in point lattice systems

Structuring of starch-based textures using 3D printing technology allows for the native control over layer-based properties instead of bulk structural properties. Thus, the control of pore size, distribution and percentage inside food material systems is attainable due to the dimensional precision and accuracy of the technology. Consequently, the design of specific textural perceptions is viable by the appropriate choice of mechanical properties and the manipulation of porosity, cell structure, and cell configuration of the 3D printed foams. A HT-PFM was developed to extend the texture modulation using 3D printing for the production of structures with specifically targeted textural properties. The hardness formula was developed using 3 closed-cell starch-based configurations. A 3D printing-thermal stabilization method was developed using an integrated layer-based NIR stabilization method for actively modulating the base material's properties. FEM transient mechanical simulations and analytical compressive analysis were used to characterize the dependency of the printed foam's hardness and Young's modulus on the close-cell configuration, porosity, and base material's properties. The hardness design formula was developed for the elastic-regime in relation to the chosen Young's modulus, porosity, and designed geometry. Finally, by assessing the obtained hardness design formula, measurements showed comparable results to the FEM simulations and the 3D printed structures.

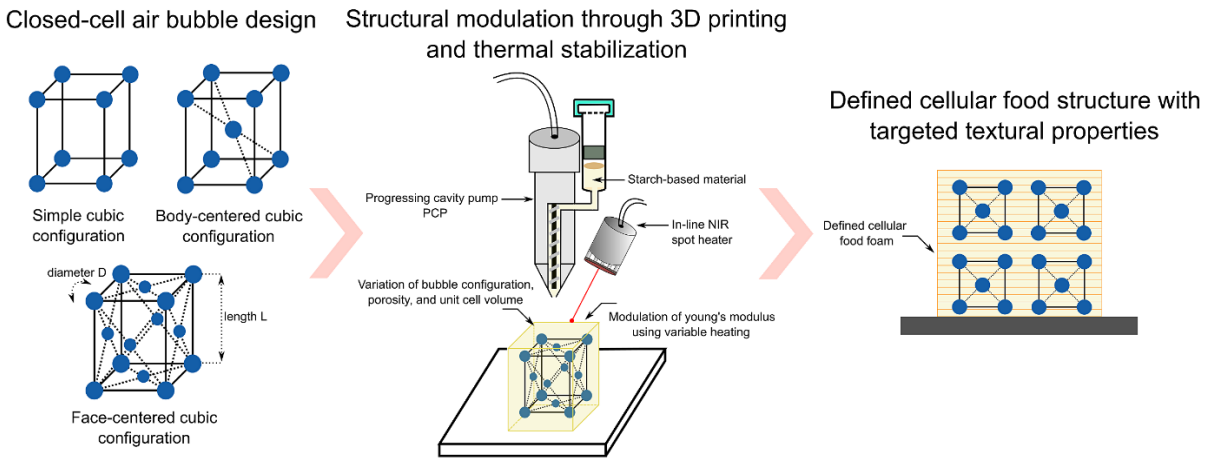

Figure 2-3: A combined texture modulation and thermal stabilization 3D printing method for creating closed-cell structures with designed textural properties

Texture modulation of starch-based closed-cell foams using 3D printing: deformation behavior beyond the elastic regime

Through the characterization and understanding of the comprehensive deformation behavior, controlling the textural perception of starch-based cellular foams is possible. Considering the macro-structure of cellular foams, the base material, cellular configuration, relative density, and pore distribution influences the mechanical characteristics and deformation behavior. Moreover, the mechanical properties and deformation behavior defines the mastication performance and thus, influencing the textural perception. Regarding the micro-structure of starch-based materials, inducing of physiochemical transitions such as protein denaturation and starch gelatinization is required for functionality. The developed HT-PFM was used to 3D print closed-cell cellular configurations with specific hardness levels. For the modulation of starch-based textures, the macro-structure was varied using 3D printing and the large-deformation stress-strain profiles were analyzed. Furthermore, the strain rate and viscoelastic response of printed cellular structures were analyzed. Results showed that the compressive yield strength can be modulated using the in-line NIR thermal stabilization. In addition, the compressive yield strength can be further altered by porosity incorporation. Also, the location, size, and number of air bubbles influences the response of the cellular structures in the plateau and strain locking regimes. Modulation of the micro-structure was achieved during 3D printing by inducing starch gelatinization using a time-temperature approach through in-line NIR stabilization.

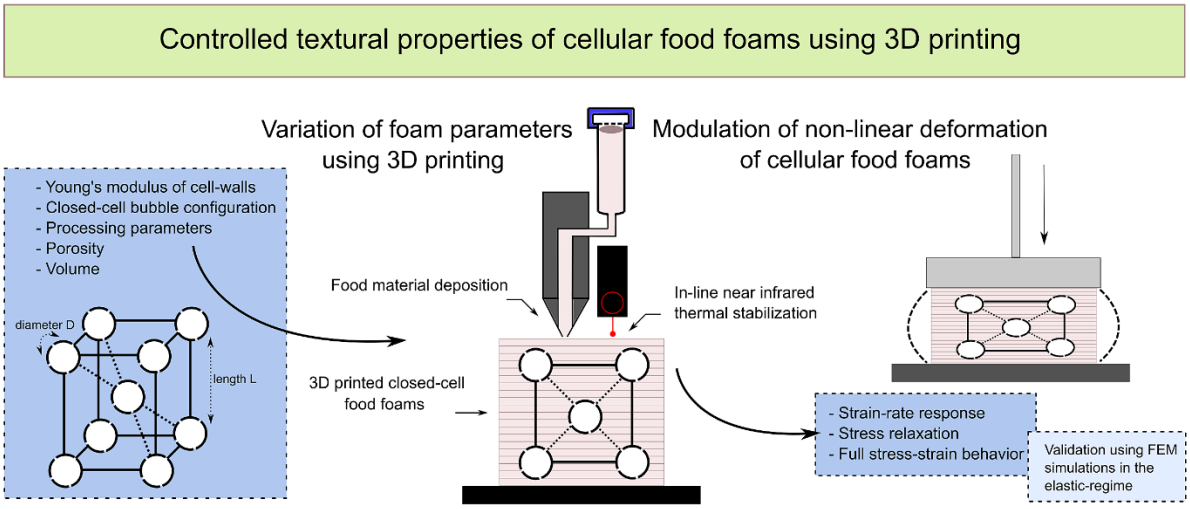

Figure 2-4: Investigation of linear and non-linear stress-strain behavior of 3D printed and thermally stabilized starched-based closed-cell foams

2.2 3D printing and additive manufacturing of cereal-based materials: Quality analysis of starch-based systems using a camera-based morphological approach

Fahmy, A. R., Becker, T., & Jekle, M. (2020). 3D printing and additive manufacturing of cereal-based materials: Quality analysis of starch-based systems using a camera-based morphological approach. Innovative Food Science & Emerging Technologies, 63 (April), 102384. https://doi.org/10.1016/j.ifset.2020.102384

Authorship contribution

A.R. Fahmy: Methodology, Investigation, Formal analysis, Resources, Data curation, Writing - original draft, Visualization. **M. Jekle**: Methodology, Conceptualization, Funding acquisition, Writing - review & editing, Supervision. **T. Becker**: Conceptualization, Funding acquisition

Innovative Food Science and Emerging Technologies 63 (2020) 102384

Contents lists available at ScienceDirect

Innovative Food Science and Emerging Technologies

journal homepage: www.elsevier.com/locate/ifset

3D printing and additive manufacturing of cereal-based materials: Quality analysis of starch-based systems using a camera-based morphological approach

Ahmed Raouf Fahmy, Thomas Becker, Mario Jekle*

Technical University of Munich, Chair of Brewing and Beverage Technology, Research Group Cereal Technology and Process Engineering, 85354 Freising, Germany

ARTICLE INFO

Keywords:
3D cereal printing
Viscoelastic materials
Morphological image processing
Bread
Material extrusion

ABSTRACT

Structural control over cereals' crumb matrix is achievable using 3D printing. The manipulation of the cellular structure including void fraction, pore size, geometry, and distribution is achievable by resolving large structures into finite layers. However, investigating the applicability of material extrusion for printing starch and cereal-based systems is of great interest due to the behavior of the thixotropic and pseudoplastic materials during extrusion and their viscoelastic post-printing geometric response. In this study, we use an on-board camera system composed of top- and side-view cameras to characterize the post-printing geometrical attributes of two cereal-based systems, which comprise of wheat flour dough and wheat starch-egg white protein blends. This quantitative method uses image processing techniques to obtain morphological dimensional parameters. Furthermore, the induced defects involving printing delays and under-extrusion are influenced by the material's yielding behavior. Over-extrusion defects are dominant in printing wheat flour dough due to the network formation of gluten which caused the collapse of the uppermost layer. Moreover, the structural collapse behavior for the printing ink systems is obtained concerning the hydration level of the dry components. For the first time, the quality behaviors and dimensional attributes were quantitatively studied using on-board imaging and analysis of 3D printed cereal-based morphologies.

1. Introduction

Additive manufacturing (AM) is a term used to identify the manufacturing processes performed by 3 dimensional (3D) printing through layer-by-layer construction. 3D printing is an AM technique used for the fabrication of a wide range of structures and complex geometries from 3D model data. AM offers the fabrication of intended designs and constructions in consecutive layers to form a 3 dimensional (3D) structure (Gibson, Rosen, & Stucker, 2010; Ruan et al., 2008; Wegrzyn, Golding, & Archer, 2012). The 3D printing working principle is extremely important as it enables the high precision fabrication of complex customized geometries, reduction of waste, and personalization of the process (Dankar, Haddarah, Omar, Sepulcre, & Pujolà, 2018; Kamran & Saxena, 2016; Ngo, Kashani, Imbalzano, Nguyen, & Hui, 2018; Sun, Zhou, Yan, Huang, & Lin, 2016). The use of 3D printing technology in food fabrication allows for custom tailoring of nutrition, flavor manipulation as well as texture control; where the other traditional processing techniques fail to achieve (Sun et al., 2015, 2016; Zhang, Liu, Bhandari, & Wang, 2017). Despite the great number of researches carried out on food 3D printing applications, no quantitative data has been shown regarding the printing defects. Also, no quantitative methods have been proposed to investigate the interactions of viscoelastic food materials with the fabrication process and their viscoelastic induced defects.

Different researches were conducted regarding the applicability of using different food formulations with material extrusion 3D printing. The different food formulations are smoothie combination of fruits and vegetables, fish surimi gel, processed cheese, encapsulated plant cells into pectin-based inks, and cereal-based matrices containing probiotics (Le Tohic et al., 2016; Severini, Derossi, Ricci, Caporizzi, & Fiore, 2018; Vancauwenberghe et al., 2017; Wang, Zhang, Bhandari, & Yang, 2017; Zhang, Lou, & Schutyser, 2018). However, these systems are mainly viscous, and it is questionable if food matrices with medium elastic properties can be used to print structures which require high precision such as 3D periodic cellular structures. In material extrusion 3D printing of thermoplastics, the viscoelastic material properties are influenced by various nozzle temperatures to obtain quality prints for printable materials such as polylactic acid (PLA), nylon (PA) or

* Corresponding author.
E-mail address: mjekle@tum.de (M. Jekle).

https://doi.org/10.1016/j.ifset.2020.102384
Received 30 January 2020; Received in revised form 21 April 2020; Accepted 13 May 2020
Available online 19 May 2020

acrylonitrile butadiene styrene (ABS). On the other hand, these temperature settings are not applicable for printing cereal-based materials. Also, 3D printing software offers different routines to overcome printing defects such as over-extrusion (stringing or oozing) by extruder retraction, wipe, and coasting settings. Often, the settings are calibrated according to the filament extruding principles such as Direct or Bowden designs. Accordingly, good knowledge of the induced defects of printing viscoelastic materials needs to be established for different extruding principles (syringe- or screw-based). This enhances the proper adaptation of such 3D printing routines for improved printing quality of real texture models of cereal-based materials. In contrast, for 3D printing of structured fluids such as cereal-based materials or (other food constituents), the effects of the fluid-flow behavior, the pre- and post-extrusion material properties, and the material-process interaction on the printing quality are inadequately investigated. Consequently, the evaluation of the material's printability and the optimization of the printing process often fail.

Different researches have carried out comprehensive studies about the relation between the material composition and printing quality neglecting the morphological identification and printing quality standardization. For example, Liu, Zhang, Bhandari, and Yang (2016) use visual assessment of printed potatoes structures to discuss the printing stability and resolution. Moreover, Yang, Zhang, Prakash, and Liu (2018) uses mechanical instrument such as Vernier caliper. Furthermore, Derossi, Caporizzi, Azzollini, and Severini (2016), Kim, Bae, and Park (2017) and Severini, Derossi, and Azzollini (2016) directly use 3D structures involving gravity and other secondary effects to obtain the relationship between the geometrical stability, viscoelastic properties, and the printing parameters, which initially should have been investigated on planar designs. Finally, Liu, Bhandari, Prakash, Mantihal, and Zhang (2019) study the evaluation of the printability of multicomponent gel system of carrageenan-xanthan-starch using material extrusion printing, where the authors present a non-automated geometrical evaluation technique based on camera systems. Though, they did not consider all geometrical aspects of the printed designs such as the length/width stability and the induced defects.

Consequently, there is no research presenting quantitative data or morphological identification methods used for assessing geometrical aspects and printing defects after printing. In this paper, we present an on-board camera-based method for quantitative geometry and defects evaluation for 3D printing of food material systems which hasn't been proposed before. We also assess the geometrical attributes and printing defects of two cereal-based material systems comprising of wheat flour and wheat starch/egg-white protein with varying water contents. The aim of using such quantitative approach is to identify important geometrical parameters and viscoelastic induced defects during 3D printing. The primary aim of using two different cereal systems, is to simulate a high range of material properties and their interaction with the printing process, thus affecting the geometrical and structural stability of the printed designs. The important geometrical aspects, which are essential for understanding the behavior of structured fluids and the contribution of viscoelastic properties during material extrusion 3D printing were established. Here, we are using two cameras to capture the side and top views of the build plate. We used this method on single lines to evaluate output width, length, height, extruded area fraction, delay indices and drag/oozing artifacts. Moreover, the stacks of lines with different heights (number of layers) are used to characterize the slumping behavior and overall structural stability. The intention behind this study is to combine it with the full fluid-flow behavior and material properties characterization of pre- and post-extrusion states, to serve as a foundation for obtaining printability prediction models for 3D printing of viscoelastic food materials and textures. In addition to obtaining quantitative information about the geometry and defects, this camera-based method can be used to identify and characterize the localization and geometrical aspects of primary and secondary materials in dual-extrusion applications. This can be done by adding color-based segmentation techniques. For future investigations, the presented method can be modified and incorporated in online detection systems for closed loop control of the printer settings during 3D printing operations.

2. Materials and methods

2.1. Raw materials

We used two different material systems to investigate the geometrical aspects of the printed geometries. German commercial wheat flour Type 550 (Rosenmühle, Landshut, Germany) was used to prepare high elasticity food material systems with varying water content. For the low elasticity material systems, wheat starch was provided by Kröner Stärke, Ibbenbüren, Germany. And egg-white protein was purchased from Bulk Powders online, Germany. The flour had a moisture content of 11.7 ± 0.10% (n = 3) with a protein content of 10.62% (n = 1) in the dry mass. The moisture content of the starch was 13.17 ± 0.16% (n = 3) with a protein content of 0.27% (n = 1) in the dry mass. The egg-white protein had a moisture content of 6.96 ± 0.04% (n = 3) and a protein content of 83.42% (n = 1) in the dry mass. The moisture and protein contents were determined following the American Association of Cereal Chemistry international standards (AACCi) 44-01 and 46-16, respectively. The material analyses were performed in triplicates.

2.2. Preparation of cereal-based inks

A total of 10 mixtures, with 50 g each, were prepared. The prepared mixtures consist of five hydrated flour dough systems (F) and five hydrated wheat starch-egg white protein paste systems (SE). For the SE materials, the ratio of starch to protein is 85:15 to show a reasonable composition compared to wheat flour constituents (Goesaert et al., 2005; Jekle, Mühlberger, & Becker, 2016). For the hydration of the dry components, distilled water was used with five different concentrations of 50, 55, 60, 70, and 80 g/100 g of the total sample weight for both the F and SE material systems. To prepare the mixture, a Z-type kneader was used at 63 rpm. Considering the SE systems, 1 min pre-mixing step was used to mix the dry components before adding water. For both material systems, water with the corresponding concentration was added and the material was kneaded for 10 min. Afterward, the material was removed from the kneading bowl, placed in a plastic beaker and covered using PARAFILM (Bemis Company Inc., Wisconsin, USA). Then, it was left to rest at room temperature for 15 min until the preparation of the paste extruder is completed. All materials were prepared, printed, and measured in triplicates and repeated three times. In this paper, SE and F denote the mixture type and the numbers 50, 55, etc. denote the water content. For example, the F50 corresponds to the wheat flour mixed with water content of 50 g/100 g of the dry material.

2.3. Material characterization

Oscillatory measurements were used to characterize the viscoelastic properties of the cereal-based inks using an AR-G2 rheometer (TA instruments, New Castle, USA). For the F mixtures, a parallel cross-hatched plate geometry (Ø 4.0 cm) was used with a 1 mm gap. For the SE mixtures, a DIN concentric cylinders' geometry was used with a conical rotor of 14 mm radius and a 1 mm clearance to the wall and bottom. The measuring geometries use a Peltier plate temperature system, which was adjusted to a constant temperature of 21 °C throughout all measurements. We placed the samples and the gap was adjusted. Afterward, excess material was removed, and the exposed transversal surface was treated with paraffin oil to avoid water loss. The materials were allowed to stay for 15 min to imitate the exact resting time before printing. Then, an oscillatory frequency test was conducted at a constant deformation of 0.01%, which is within the material's linear

viscoelastic region (determined in advance) with a frequency ranging from 0 to 10 Hz. The fundamental viscoelastic properties of the cereal-based inks were characterized and compared at 1 Hz. The rheological analysis was performed in triplicate.

2.4. 3D printing setup, geometries and printing parameters

The X400 V3 (German RepRap GmbH, Feldkirchen, Germany) was used for printing the cereal-based material systems. The heat bed was disabled; hence printing was conducted at room temperature of approx. 21 ± 2 °C with no thermal stabilization method used. Also, the commonly used build plate's polyetherimide (PEI) sheet was replaced by Build Tak 3D print surface (Build Tak, Maplewood New Jersey, USA), to increase the material adhesion to the build plate. The simplify3D slicing software (simplify3D, Ohio, USA) was used to generate the machine G-code files by following the Cartesian coordinates of the lines and stacks. The printed structures were modeled using SolidWorks (Dassault Systèmes, Vélizy-Villacoublay, France) and then converted to STL extensions for 3D printing. For extruding the mixtures, a Vipro-head 3 extruder (ViscoTec GmbH, Töging, Germany) was used, which is a progressive cavity pump (PCP) extruder. To ensure a stable flow rate of the material into the extruder, the material is transported to the dosing unit using an air pressure system employing five bars coupled to a paste injection cartridge. Moreover, Luer-Lock (standard small scale fluid fittings including hypodermic syringes) tapered nozzles with 0.84 mm diameter were coupled to the extruder head (Enanv, Medical, Ab, & Bertling, 2010).

Before printing, the build plate was manually leveled using a set of four corner setscrews with the aid of an inductive proximity sensor (OMKQN Hugong Group Co., Shanghai Shi, China). The sensor was directly mounted on the print head and connected to the printer's control board. We use bed leveling to ensure a constant distance between the extruder and build plate throughout the printing process. In Table 1, the height of the layer was chosen to be the same as the nozzle diameter of 0.84 mm for all the printed designs. This height was chosen to avoid protrusion effects perpendicular to the deposition direction in the case of close proximity to the build plate (Hao et al., 2010; Zhang et al., 2017). Also, the height was chosen to avoid droplet formation for viscous materials due to the surface tension or line deformations for elastic materials in the case of higher distances (Hao et al., 2010; Zhang et al., 2017). The model length and width were chosen as 100 mm and 0.84 mm, respectively. The choice of the model length was arbitrary. On the other hand, decreasing the model's width led to inconsistencies in the deposited lines. For all materials, single lines were printed to investigate the different geometrical stability aspects as well as printing defects. Also, stacks of lines up to five layers were printed to investigate the slumping and collapse behavior of the different material systems.

The extrusion amount depends on the geometry of the extruder, as well as the board configuration, the firmware, and the slicing software settings. To calibrate the extrusion amount, the micro-stepping mode was set to quarter steps while the feed-rate and the number of steps were kept at 60 mm/s and 300 steps/mm, respectively. There are three major parameters that control the conversion of the extrusion rate in simplify3D software. There parameters are the filament diameter, the printing speed, and the extrusion multiplier. Defining the extrusion multiplier as the main determinant of the extrusion rate, the filament diameter and the printing speed were set 0.5 mm and 4 mm/s, respectively, to reduce the amount of possible configuration.

To characterize the effect of varying material properties on printing quality due to the increase and decrease in water contents of the mixtures, we optimized the extrusion multiplier for the SE and F mixtures depending on the SE60 and F60 respectively. Using the imaging method described in Section 3.2, the calibration process was properly carried out. The multiplier was varied from 30% to 80% with a step size of 10%. A single line was printed for each step in triplicates (and repeated three times), and a top-view photo was analyzed. The criteria for choosing the correct extrusion multiplier was according to the width of the lines, thus eliminating over and under-extrusion which was indicated by higher and lower output width respectively.

Table 1
Model and simplify3D input dimensions for the lines and stacks.

	Line (L)	Stack2 (S2)	Stack3 (S3)	Stack4 (S4)	Stack5 (S5)
No. of layers	1	2	3	4	5
Single layer height mm	0.84				
Total height mm	0.84	1.68	2.52	3.36	4.20
Length mm	100				
Width mm	0.84				

3. Quality assessment method development

3.1. Camera system integration

Two cameras were used for the on-board analysis of the printed structures from the top and side views. From Basler AG (Ahrensburg, Germany), the two Basler cameras acA1920-155uc with a megapixel resolution 1920 × 1200, were mounted on the printer with one directly on the periphery of the build plate (side-view SiV) while the other on the extruder head (top-view ToV). For both cameras, Kowa LM16HC lenses were used. The lenses have fixed focal lengths of 16 mm with a focus range of 300 mm. Two 2835 SMD LED strips with attached frosted diffusers from Renkforce electronic, Hirschau, Germany, were used as the main light source. Aluminum rail profiles were fixed to the printing head to act as an overhead light source for both cameras.

3.2. Image analysis algorithm

Both image analysis and processing algorithms for the top and side views were done using MATLAB with its existing libraries and functions. We used a LEGO cube of 15.62 mm in width and 31.44 mm in length as a reference object for detecting the spatial resolution depending on the instantaneous field of view, for all the printing experiments as shown in Fig. 1. To ensure a stable focus, contrast, and brightness of the obtained images while maintaining the same camera settings, all lines and stacks were printed at the same position on the build plate with respect to the printer's origin. For all experiments, we obtained images of the reference object at the exact printing location relative to the side-view camera. For the top view analyses of each print, we obtain two images at the same height once relative to the LEGO cube and once relative to the printed samples to ensure the calculations are done at the same spatial resolution.

After printing each model, we used MATLAB to analyze the side and top views. We first use the weighted average luminous model to convert the images to grayscale. For the RGB channels of each pixel, the following equation is used to calculate the perceived luminance: $0.299R + 0.587G + 0.114B(1)$, where the variables (R, G, B) correspond

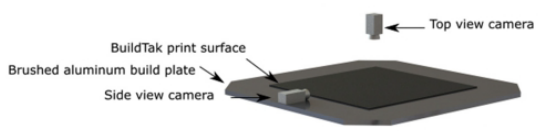

Fig. 1. Schematic of the integrated camera system with the printing platform in isometric view.

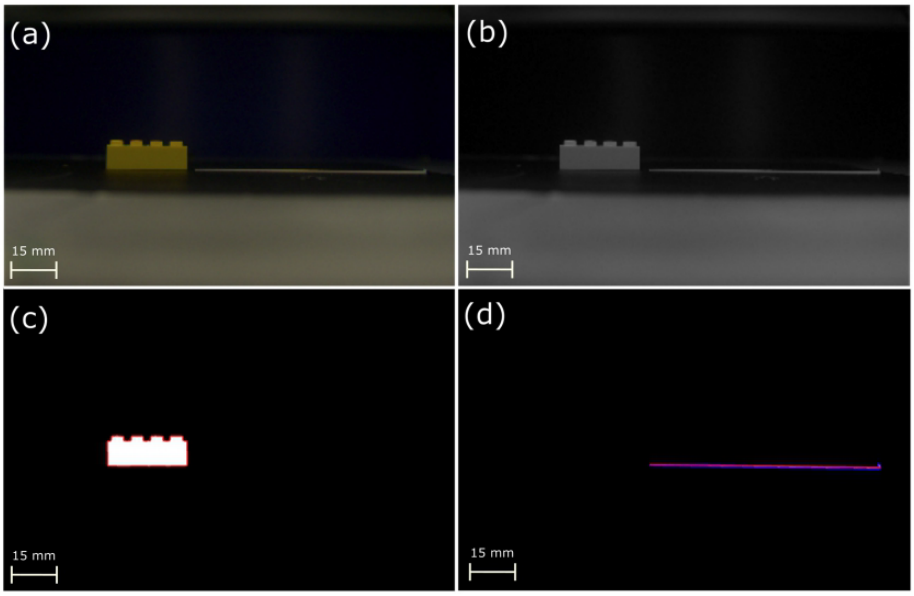

Fig. 2. Side-view of a line of starch-egg white protein blend with 50 g/100 g water addition and reference object: (a) original image; (b) grayscale image; (c) segmented reference object with boundary detection; (d) segmented printed line with boundary detection and length extraction.

to the levels of red, green, and blue in 8 bits (Anderson, Motta, Chandrasekar, & Stokes, 1996). Furthermore, a threshold value was obtained based on the aggregate histogram for the purpose of black and white conversion. To obtain the black and white images, clustering-based image thresholding was performed using Otsu's method (Otsu, 1979). After thresholding, a size-based segmentation was performed using a flood fill algorithm to isolate the image components for further pixel-based analysis as shown in Fig. 2. The boundary or edge detection and bounding box technique of the reference object, which employs a rotating calipers design (Toussaint, 1983) is used to calculate the spatial resolution.

After obtaining the spatial resolution using the reference object, a boundary detection algorithm was used on the printed lines. This approach uses the Moore-Neighbor tracing algorithm, which was modified by Jacob's stopping criteria (Gonzalez, Woods, & Eddins, 2004). The extruded length (L_{ext}) and its fraction or percentage (L_f) were calculated after detecting the x- and y-positions of the boundaries' extremities corresponding to the shortest length between the two matrix points using the following equations: $L_{ext} = \sqrt{(x_2 - x_1)^2 + (y_2 - y_1)^2}$ (2) and $L_f = (L_{ext}/L_{input}) * 100$ (3). The coordinates (x_1, x_2, y_1, y_2) corresponds to the planar positions of the two detected matrix pixels denoting the length extremities while (L_{input}) is the theoretical line length. We denote the width distribution and height distribution across the length of the extruded line as ($W_d(x)$) and ($H_d(x)$) respectively. The width distribution and height distribution were obtained along the columns of the boundaries' matrix by row operation from the top and side view respectively. From the width and height distribution functions, the average width (W_{avg}) and height (H_{avg}) across the line were obtained depending on the number of sampled points. The end-line form index (I_{ooze}) was obtained by isolating the last 2 cm of the line (with respect to the actual extrusion output) and computing the theoretical area (A_{TI}) of the region using the obtained average height (H_{avg}). Trapezoidal integration was performed on the height distribution to obtain the area of the isolated region (A_I). In addition, the end-line form index (I_{ooze}) was evaluated using the following equation: $I_{ooze} = (A_I/A_{TI}) * 100$ (4). We denote the stable width and height corresponding to 50 mm in the middle of the printed lines, where the beginning and the end of extrusion regions are eliminated as (W_s) and (H_s) respectively. The stable width and height were obtained by isolating the areas of under-extrusion and ooze corresponding to the beginning and the end of the required printed lines respectively. In isolation, the average width and height were obtained with respect to the sampled points of the boundary. The fractions (W_f, H_f) of both the stable width and height were obtained using the following equations: $W_f = (W_s/W_{input}) * 100$ (5) and $H_f = (H_s/0.84) * 100$ (6). Finally, the response length index ($I_{response}$), which corresponds to the difference between the start of the line and the position of the stable width, was attained by a recursive inquiry for the spatial discrepancy.

4. Results and discussion

4.1. Under-extrusion and initial delay

During the printing process, the planar lines are printed between a spatially resolved initial coordinate and a termination point. At this termination point, the extrusion process is concluded depending on the model allocation in the slicing software. Subsequently, the extruder returns automatically to the printer's origin by moving directly opposite to the extrusion/printing direction. In the process of extrusion, stress is applied to the material as the pressure gradient must be achieved to trigger the material deposition. To initiate the flow of yielding fluids during extrusion, the deformation of the internal structure and the yield point of the material must be reached (Lewis, 2006; Lewis, Smay, Stuecker, & Cesarano, 2006).

Fig. 3(a) and (b) show the evolution of the extruded lengths of the printed cereal-based inks with respect to the number of the deposited layers. Considering the deposition of a single layer, the extruded lengths of the SE systems were observed to lie between 80.6 ± 4.6 mm for SE55 and 88 ± 2.1 mm for SE80. The F systems showed lower extruded lengths at low hydration levels with 58.3 ± 6.2 mm for F50 and 91 ± 2 mm for F80. As an intrinsic property of the materials, the yield strength is the stress needed in order to reach the material's yield point. We consider the material's static yield strength as the cross-over point between the elastic and viscous components due to pseudoplastic

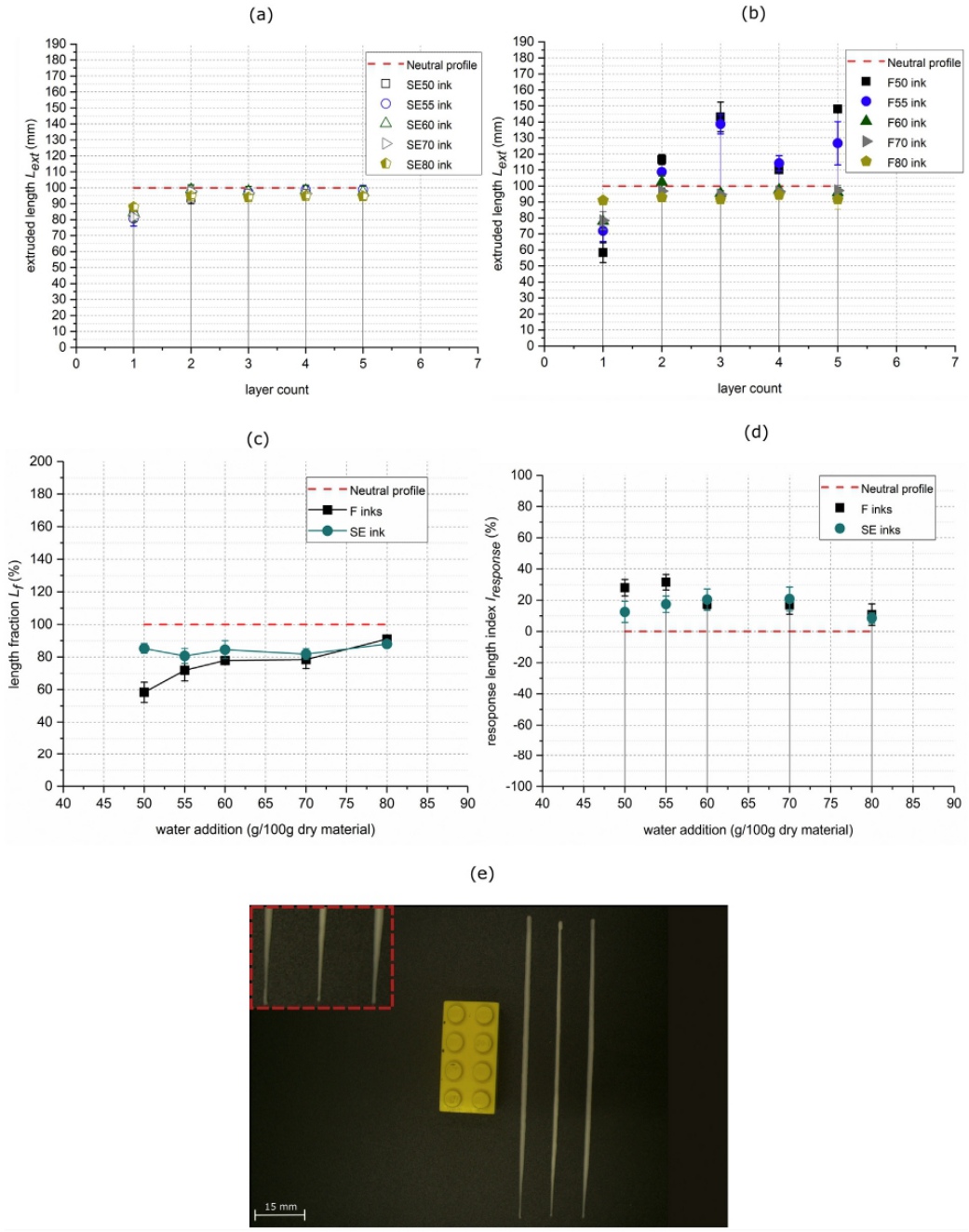

Fig. 3. Extruded length L_{ext} and length fraction L_f of starch-egg white protein and flour systems: (a) extruded length of starch-egg white protein systems at different layer counts (n = 3); (b) extruded length of flour systems at different layer counts (n = 3); (c) first layer length fraction index of starch-egg white protein and flour systems at different hydration levels (n = 3); (d) first layer response length index (delay percentage for reaching the stable input width) of starch-egg white protein and flour systems at different hydration levels (n = 3); (e) top-view of SE60 showing initial delay in width of planar lines.

behavior (Sad, 2008; Sun & Gunasekaran, 2009; Wilson, Cross, Peak, & Gaharwar, 2017). By reducing the hydration level of the printing inks, the static yield strength increases, which leads to a time delay in the beginning of the extrusion process. Fig. 3(c) shows that the time delay occurs in the beginning of the deposited planar lines. Furthermore, the insufficient adhesive force between the deposited material and the build plate may increase the specified delay. In addition, the slicing applications synchronize the axes movement with the extrusion process without considering any material incurred delays due to static yielding or insufficient adhesion. The variation between the F and the SE

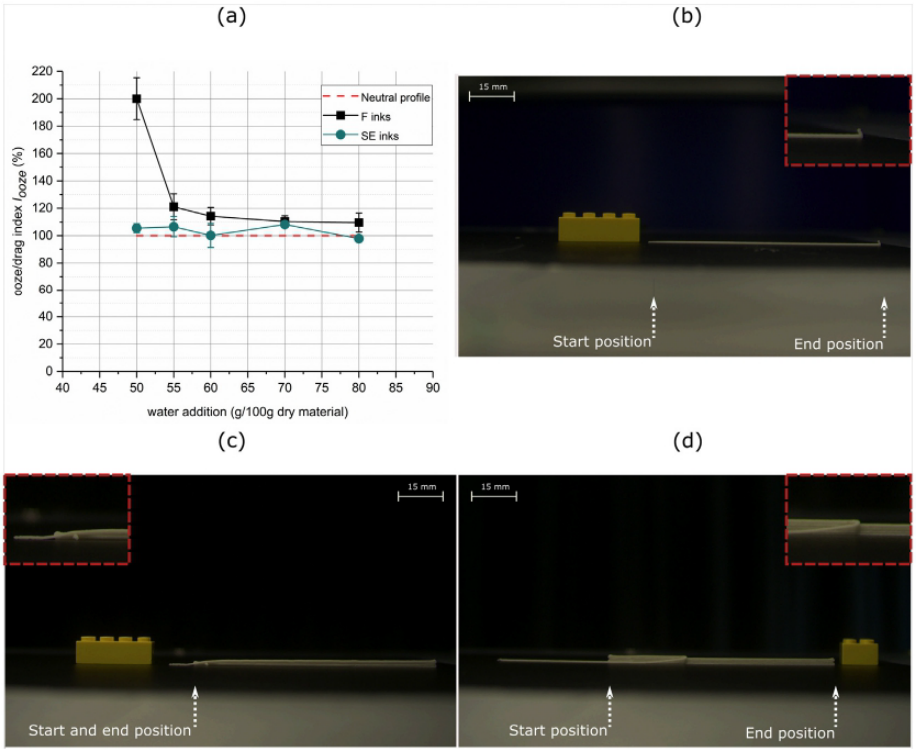

Fig. 4. The effect of drag/ooze behavior reflected on planar lines and stacks: (a) ooze/drag index I_{ooze} for starch-egg white protein and flour systems at different hydration levels; (b) SiV of starch-egg white protein blend with 60 g/100 g water addition planar line showing over-extrusion at the termination point; (c) SiV of four layers stack of flour dough with 55 g/100 g water addition showing stretch behavior; (d) SiV of five layers stack of flour dough with 55 g/100 g water addition showing stretch and layer collapse behavior.

systems at the same hydration levels, which is shown in Fig. 3(c) and (d), can be the resultant of the higher viscos and elastic components of the F systems, shown in Fig. 5. The increase of storage and loss modulus influences the initiation of the deposition process of the PCP extruder where the material-extrusion interaction is not yet fully understood. Furthermore, the adhesion properties of the F systems are influenced by the hydration state of the gluten network (Van Velzen, Van Duynhoven, Pudney, Weegels, & Van der Maas, 2003). For the SE systems, by increasing the number of layers (with a stability of ~95 mm) during the further deposition cycles, the delay was covered with material from the consecutive layers. But the mentioned effect of length correction affects the height of the structures at the areas affected by under-extrusion.

As shown in Fig. 3(d) and (e), the under-extrusion effect was not exclusive to the extruded length but was also observed in the width of the planar lines. Hence, over damped width profiles occur. Therefore, more time is required after the beginning of the extrusion to reach the stable input width, indicating a low material response. Consequently, the delay in reaching the input width shows that the deposition process started before the pressure equivalent to the flow rate (extrusion multiplier) was reached. Furthermore, under-extrusion is more pronounced for planar printing. As an example, this effect would be visible when the extrusion stops for crossing an open space. This occurs during dual extrusion or dual-component printing and during thermal stabilization of individual layers. In Section 4.3, we discuss the rheological behavior of the materials obtained and the viscoelastic properties.

4.2. Over-extrusion

Toward the end of the printing process, the stoppage of the deposition occurs as the applied stress decreases more than the materials' dynamic yield strength (considering structural hysteresis). Retraction in 3D printing is the process whereby the filament of the material is recoiled opposite to the direction of the deposition. This is usually considered as a pressure relief mechanism for the prevention of dripping or oozing. Considering PCP extrusion where a die/nozzle is attached, the pressure is commonly developed at different stages of pressure-driven and drag flow. In particular, the effect of retraction in PCP extrusion is still not analyzed. Accordingly, retraction, and coast settings were disabled to investigate the effects of over-extrusion without considering second-order effects. Furthermore, coasting enables pressure relief inside the extruder for a particular distance before the end of the deposition.

From the analysis of the end point using trapezoidal integration, the end of the deposition did not occur immediately leading to over-extrusion/ooze of the material as shown in Fig. 4(b). Due to the structural deformation of the material systems, hysteresis occurs, which causes a decrease in the materials' yield strength (Puisto, Mohtaschemi, Alava, & Illa, 2015; Radhakrishnan, Divoux, Manneville, & Fielding, 2017). Consequently, this behavior leads to a delay in the stoppage of the materials' deposition with respect to the time required to reach the pressure equilibrium. Fig. 4(a) shows the ooze/drag index with respect to the hydration level of both the SE and F systems. The index of the SE inks was observed to fluctuate around the theoretical profile over the hydration level range. We observed an over-extrusion of maximum 8.2 ± 2.3% for the SE70 material and 100 ± 15.3% for the F50 material.

In addition to the yield strength hysteresis for the F systems, the material is dragged with the extruder after the end of the deposition due

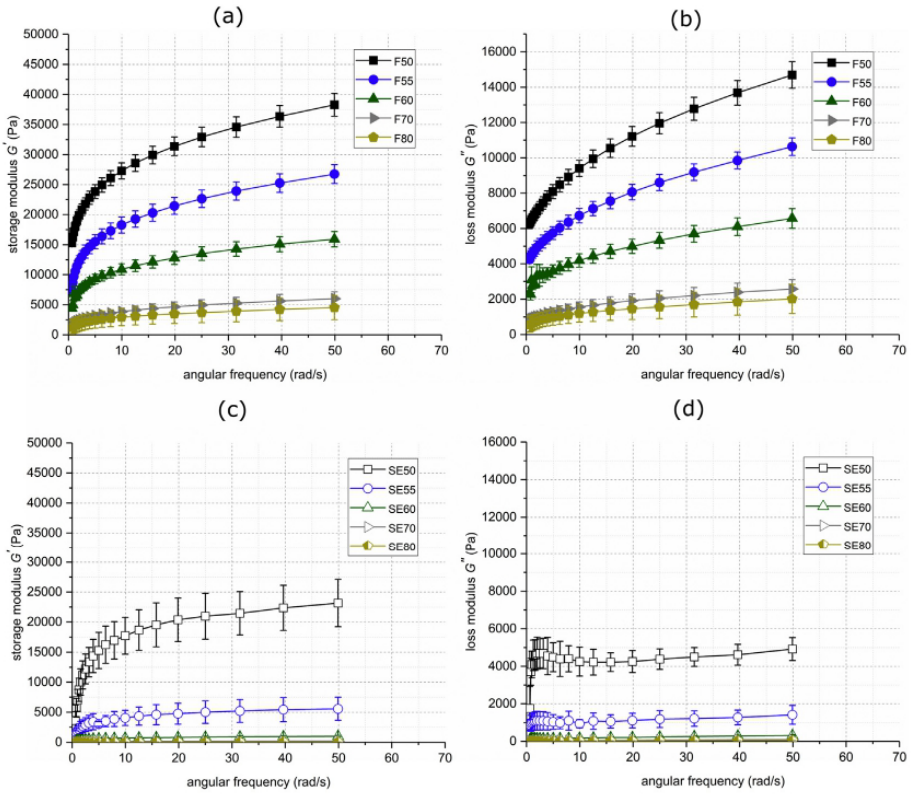

Fig. 5. Frequency sweep of flour and starch-egg white protein systems within 0–50 rad/s at 21 °C: (a) elastic component of flour inks; (b) viscous component of flour inks; (c) elastic component of starch-egg white protein inks; (d) viscous component of starch-egg white protein inks.

to the formation of the complex gluten network during kneading of the wheat flour dough. This contributes to the strength of the developed protein network. But a logarithmic decrease in the ooze/drag index I_{ooze} (R^2 = 0.99) was observed without considering the potential structural deformation due to the shear forces applied during the different phases of extrusion. Moreover, the dragging effect observed in the F systems causes the extensional deformation in the longitudinal direction while compressing the transversal direction. Therefore, if the longitudinal tensile force acting on the material exceeds the ultimate tensile strength of the material, then stoppage of the deposition process is achieved.

In the process of printing the multi-layered stacks, the starting points were optimized for faster printing to simulate a realistic printing approach. This optimization causes the printing to be carried out in sweeping meanders. In a sweeping meander routine, the end point of one layer becomes the starting point of the consecutive one. Therefore, the stoppage of the extrusion process was in the direction of the home position for the even-layered stacks in contrast to the odd-layered stacks where the stoppage occurs in opposite to the direction of the home position. From Fig. 4(c) and (d); we have that for the even-layered stacks, a slight increase in the extruded length of the F50 and F55 inks compared to the theoretical profile of 100 mm which is caused by the elongation of the uppermost layer. For even layered stacks, the longitudinal tensile force applied by the extruder was opposed by the adhesive force between the material and the build plate. On the other hand for the F systems, the printing of odd-layered stacks produce higher lengths due to the collapse of the last deposited layer as shown in Fig. 4(d). In this case, the longitudinal force applied by the extruder was opposed by the adhesive force between the individual layers of the material. Fig. 3(b) shows the fluctuation of the extruded length depending on the end point direction. Here, the adhesive force between the individual extruded layers (odd-layered stacks) is lower than the adhesive force between the material and the build plate (even-layered stacks). The stretch and drag behavior observed in the stacks of F50 and F55 inks shows a stability dependency on the direction of the extrusion. Consequently, adhesive discrepancy arises when printing wheat flour dough at low hydration levels. In conclusion, the printing of the wheat flour dough due to the presence of gluten leads to over-extrusion depending on the network strength and movement direction. And subsequently, it leads to other higher-order effects, affecting the geometrical stability of the printed structures.

4.3. Structural stability, collapse and slumping behavior

The increase in water content of the material, influences the fundamental viscoelastic properties. First, it induces different interactions with the 3D printer specifically for the extruder and the printing platform. Second, it induces different geometrical effects and influences the macro-structural behavior of the printed structures.

The increase in water content from 50 g up to 80 g/100 g of the dry material for both the F and SE systems leads to the decrease in the viscous $G``$ and elastic $G`$ moduli over the input frequency profile. In Fig. 6(c) and (d), the moduli of the cereal-based inks decreases logarithmically (R^2 = 0.99) at different orders of magnitudes with the linear increase in the water content. The decrease in the overall complex modulus of the material with respect to the water addition, which indicates the structural softening, hinders the geometrical stability of the printed stacks regardless of the structural deformation, which occurs during extrusion. With the non-gluten-containing SE material

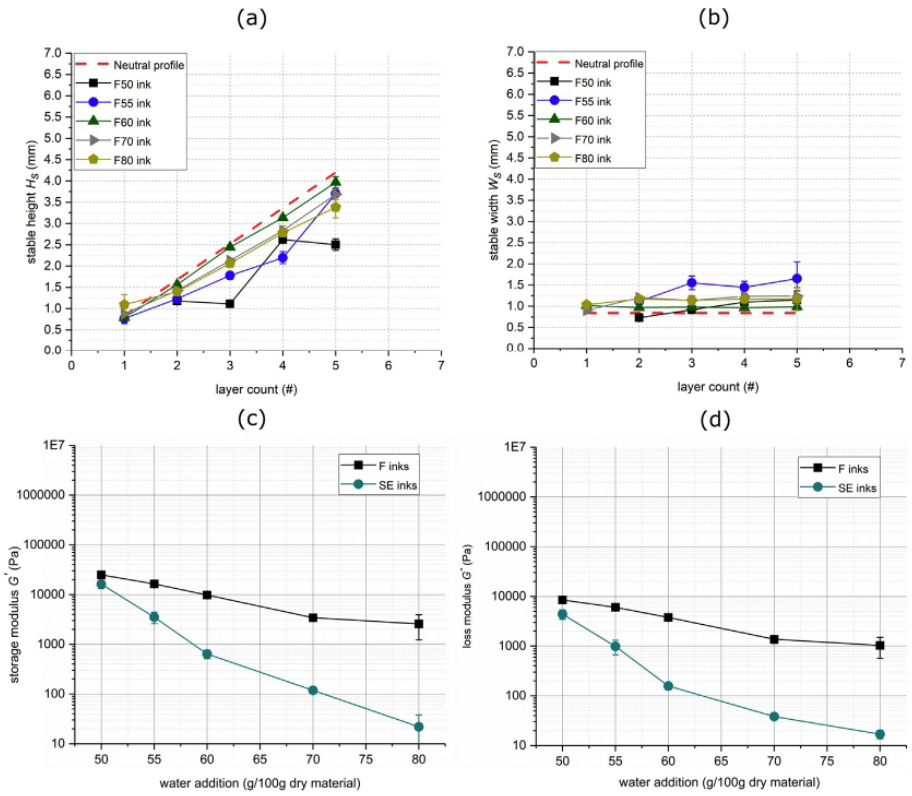

Fig. 6. Stacking performance of flour inks: (a) stable height of printed stacks up to five layers; (b) stable width of printed stacks up to five layers; (c) elastic component of flour and starch-egg white protein inks at 1 Hz; (d) viscous component of flour and starch-egg white protein inks at 1 Hz.

systems, the high decrease in the elasticity and viscosity shows softening of the internal structure which can be considered as a dilution effect (Meerts, Cardinaels, Oosterlinck, Courtin, & Moldenaers, 2017). This is typically better for easier extrusion of the materials while causes printed structures to collapse with the increasing number of layers (Liu et al., 2016; Zhang et al., 2017). The presence of gluten in the wheat flour formulations, allows for the bound water phase to play an important structural role as it is absorbed by the starch granules and it hydrates the proteins to from the gluten network (Meerts et al., 2017). This positively contributes to the stability of the printed structures with the increasing number of layers.

From the analysis of the stable heights and widths for both systems, the F60 showed approximately the same height and width as the theoretical input profile. On the contrary, the F70 and F80 materials show signs of slumping with a maximum deviation from the input design at five layers reaching 87.6 ± 3.8% and 80.5 ± 7.4%, respectively. In addition, both materials were dominated by the collapse of the top layer, which was the product of the drag behavior caused by over-extrusion discussed previously in Section 4.2. In the view of the SE material systems, all mixtures have a high increase in the width of the printed stacks. This indicates the structural collapse under the applied hydrostatic pressure due to layering as shown in Fig. 7(b) and (c). Considering the width of the printed stacks, SE50, SE55 and SE60 showed saturation of the output width upon the printing of three or more layers. Fig. 7(c) shows the slumping behavior of a five layered stack of SE70. Thus, at higher water contents under the enforced hydrostatic pressure, the lower layers flow in the transverse direction (xy-directions) with all the layers merging simultaneously. This is due to the absence of gluten as the main structural ingredient. The yield strength and overall complex modulus of the material was high enough to maintain the quality of the planar shape and prevent the layers from merging. The deformation caused in the longitudinal direction (z-direction) increases the distance between the extruder and the printing platform. In Fig. 7(d), by increasing the distance between the deposited line and the previous layers causes the last layer to form a waveform pattern with a certain oscillation frequency resembling the liquid rope coiling or fluid buckling effect associated with the linear movement of the extruder (Maleki, Habibi, Golestanian, Ribe, & Bonn, 2004). Considering the steady coiling effect, the viscous fluid falls into a stagnant reservoir following four distinct regimes viscous, gravitational, inertia-gravitational, and inertial. This is based on fluid properties and boundary conditions such as flow height and flow rate (Cruickshank & Munson, 1981; Ribe, Habibi, & Bonn, 2011). Contrary to the steady coiling, during 3D printing, the extruder or the print head moves with a constant velocity. This constant velocity creates a drag regime of the viscous material where the restoring gravitational force and destabilizing reaction forces determine the recoil frequency (Blount & Lister, 2011). Finally, in terms of the structural stability for the printed constructs, the results indicate that the uses of gluten as a structural element are essential to lower the slumping behavior after printing. This is highlighted in the significant increase in the width of the printed SE systems as compared to the F systems.

5. Conclusion

With the purpose of assessing the 3D printing quality and geometrical attributes of cereal-based materials, two material systems were used comprising of wheat flour dough and wheat starch/egg-white

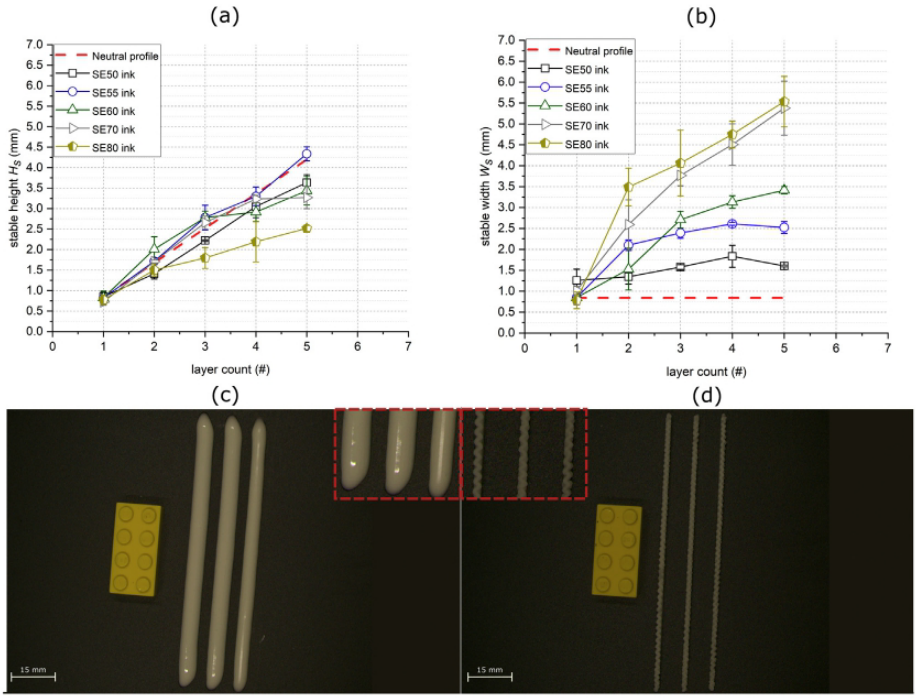

Fig. 7. Stacking performance of the starch-egg white protein inks: (a) stable height of printed stacks up to five layers; (b) stable width of printed stacks of up to five layers; (c) ToV of five layered stack of starch-egg white protein blend with 70 g/100 g water addition showing slumping behavior; (d) ToV of five layered stack of starch-egg white protein blend with 50 g/100 g water addition showing wavy top layers.

protein blends with varying water contents. These were chosen to simulate a high range of material properties and their interaction with the printing process. A quantitative morphological imaging method using two cameras to capture the side and top-view of the printing platform was used coupled with staple autonomous imaging scripts. The imaging analysis was used on printed planar lines and stacks to establish and analyze geometrical aspects that are essential for understanding the behavior of structured fluids and the contribution of viscoelastic properties during material extrusion 3D printing. While a high yield strength is a desirable post-printing attribute for retaining shape stability, the results show that reducing the hydration level of the dry components and increasing the yield strength leads to under-extrusion or a delay at the beginning of the extrusion process. On the other hand, over-extrusion occurred at the end of extrusion due to the yield hysteresis behavior, transitioning from static to dynamic yield strength due to structural deformation. In the gluten-containing systems, the printed lines were dragged with the extruder. This is because of the formation of the complex gluten network during kneading of the wheat flour dough and it is contributed to the network strength. This effect leads to adhesive discrepancies depending on the movement directions and hydration of the gluten network. The presence of the gluten network during printing, depending on the hydration level and input energy during pre-processing, act as a structural stabilization element. On the other hand, the presence of the gluten network may impose geometrical defects in the output prints due to the molecular structure and the interactions within the network. Finally, the geometrical attributes and viscoelastic properties' governed defects for printing cereal-based materials were established. They were quantified for the first time and can be coupled with post-printing thixotropic/pseudoplastic behavior characterization. We obtained a better understanding of the material's compatibility/limitations with material extrusion 3D printing. Furthermore, the 3D printing on-board morphological monitoring, can be used to characterize the effects of additional printing settings. This includes the retraction and coasting effects on the output quality for efficient selection of the printing parameters. Also, during cereal-based foam printing, the presented method can be used for the in-line analysis of layer-based infill patterns and output internal structures in terms of pore structure, density, and distribution.

Declaration of competing interest

The authors declare that they have no known competing financial interests or personal relationships that could have appeared to influence the work reported in this paper.

Acknowledgements

This IGF Project of the FEI (20385N) is supported via AiF within the program for promoting the Industrial Collective Research (IGF) of the German Ministry of Economic Affairs and Energy (BMWi), based on a resolution of the German Parliament.

References

Anderson, M., Motta, R., Chandrasekar, S., & Stokes, M. (1996). Proposal for a standard default color space for the internet—sRGB. In: *Proc. IS&T/SID 4th color imaging conf.: Color science, systems applications.* (pp. 238–246).

Blount, M. J., & Lister, J. R. (2011). The asymptotic structure of a slender dragged viscous thread. *Journal of Fluid Mechanics, 674*, 489–521. https://doi.org/10.1017/S0022112011000085.

Cruickshank, J. O., & Munson, B. R. (1981). Viscous fluid buckling of plane and axisymmetric jets. *Journal of Fluid Mechanics, 113*(April 2006), 221–239. https://doi.org/10.1017/S0022112081003467.

Dankar, I., Haddarah, A., Omar, F. E. L., Sepulcre, F., & Pujolà, M. (2018). 3D printing technology: The new era for food customization and elaboration. *Trends in Food Science & Technology, 75*(March), 231–242. https://doi.org/10.1016/j.tifs.2018.03.018.

Derossi, A., Caporizzi, R., Azzollini, D., & Severini, C. (2016). Application of 3D printing for customized food. A case on the development of a fruit-based snack for children. *Journal of Food Engineering*. https://doi.org/10.1016/j.jfoodeng.2017.05.015.

Enanv, S. I. S., Medical, H., Ab, S., & Bertling, S. (2010). *International standard ISO 80369-1. 2004*.

Gibson, I., Rosen, D. W., & Stucker, B. (2010). Introduction and basic principles. *Additive manufacturing technologies: Rapid prototyping to direct digital manufacturing* (pp. 20–35). . https://doi.org/10.1007/978-1-4419-1120-9_1.

Goesaert, H., Brijs, K., Veraverbeke, W. S., Courtin, C. M., Gebruers, K., & Delcour, J. A. (2005). Wheat flour constituents: How they impact bread quality, and how to impact their functionality. *Trends in Food Science and Technology, 16*(1–3), 12–30. https://doi.org/10.1016/j.tifs.2004.02.011.

Gonzalez, R. C., Woods, R. E., & Eddins, S. L. (2004). Digital image processing using matlab. *System*https://doi.org/10.1109/IEMBS.2011.6091204.

Hao, L., Mellor, S., Seaman, O., Henderson, J., Sewell, N., & Sloan, M. (2010). Material characterisation and process development for chocolate additive layer manufacturing. *Virtual and Physical Prototyping, 5*(2), 57–64. https://doi.org/10.1080/17452751003753212.

Jekle, M., Mühlberger, K., & Becker, T. (2016). Starch-gluten interactions during gelatinization and its functionality in dough like model systems. *Food Hydrocolloids, 54*, 196–201. https://doi.org/10.1016/j.foodhyd.2015.10.005.

Kamran, M., & Saxena, A. (2016). A comprehensive study on 3D printing technology. *MIT International Journal of Mechanical Engineering, 6*(2), 63–69. Retrieved from https://www.researchgate.net/publication/310961474.

Kim, H. W., Bae, H., & Park, H. J. (2017). Classification of the printability of selected food for 3D printing: Development of an assessment method using hydrocolloids as reference material. *Journal of Food Engineering, 215*, 23–32. https://doi.org/10.1016/j.jfoodeng.2017.07.017.

Le Tohic, C., O'Sullivan, J. J., Drapala, K. P., Chartrin, V., Chan, T., Morrison, A. P., ... Kelly, A. L. (2016). Effect of 3D printing on the structure and textural properties of processed cheese. *Journal of Food Engineering*. https://doi.org/10.1016/j.jfoodeng.2017.02.003.

Lewis, J. A. (2006). Direct ink writing of 3D functional materials. *Advanced Functional Materials, 16*(17), 2193–2204. https://doi.org/10.1002/adfm.200600434.

Lewis, J. A., Smay, J. E., Stuecker, J., & Cesarano, J. (2006). Direct ink writing of three-dimensional ceramic structures. *Journal of the American Ceramic Society, 89*(12), 3599–3609. https://doi.org/10.1111/j.1551-2916.2006.01382.x.

Liu, Z., Bhandari, B., Prakash, S., Mantihal, S., & Zhang, M. (2019). Linking rheology and printability of a multicomponent gel system of carrageenan-xanthan-starch in extrusion based additive manufacturing. *Food Hydrocolloids, 87*, 413–424. https://doi.org/10.1016/j.foodhyd.2018.08.026.

Liu, Z., Zhang, M., Bhandari, B., & Yang, C. (2016). Impact of rheological properties of mashed potatoes on 3D printing. *Journal of Food Engineering*. https://doi.org/10.1016/j.jfoodeng.2017.04.017.

Maleki, M., Habibi, M., Golestanian, R., Ribe, N. M., & Bonn, D. (2004). Liquid rope coiling on a solid surface. *Physical Review Letters, 93*(21), https://doi.org/10.1103/PhysRevLett.93.214502.

Meerts, M., Cardinaels, R., Oosterlinck, F., Courtin, C. M., & Moldenaers, P. (2017). The impact of water content and mixing time on the linear and non-linear rheology of wheat flour dough. *Food Biophysics, 12*(2), 151–163. https://doi.org/10.1007/s11483-017-9472-9.

Ngo, T. D., Kashani, A., Imbalzano, G., Nguyen, K. T. Q., & Hui, D. (2018). Ngo - 3D printing a review of materials methods applications and challenges.pdf. *Composites Part B: Engineering, 143*, 172–196. https://doi.org/10.1016/j.compositesb.2018.02.012.

Otsu, N. (1979). A threshold selection method from gray-level histograms. *IEEE Transactions on Systems, Man, and Cybernetics, 9*(1), 62–66. https://doi.org/10.1109/TSMC.1979.4310076.

Puisto, A., Mohtaschemi, M., Alava, M. J., & Illa, X. (2015). Dynamic hysteresis in the rheology of complex fluids. *Physical Review E - Statistical, Nonlinear, and Soft Matter Physics, 91*(4), https://doi.org/10.1103/PhysRevE.91.042314.

Radhakrishnan, R., Divoux, T., Manneville, S., & Fielding, S. M. (2017). Understanding rheological hysteresis in soft glassy materials. *Soft Matter, 13*(9), 1834–1852. https://doi.org/10.1039/c6sm02581a.

Ribe, N. M., Habibi, M., & Bonn, D. (2011). Liquid rope coiling. *Annual Review of Fluid Mechanics, 44*(1), 249–266. https://doi.org/10.1146/annurev-fluid-120710-101244.

Ruan, J., Sparks, T. E., Fan, Z., Stroble, J. K., Panackal, A., & Liou, F. (2008). A review of layer based manufacturing processes for metals. *Solid freeform fabrication symposium. January. Solid freeform fabrication symposium* (pp. 233–245).

Sad, N. (2008). Determining the yield - Importance and shortcomings. *Food Processing, 35*, 143–149.

Severini, C., Derossi, A., & Azzollini, D. (2016). Variables affecting the printability of foods: Preliminary tests on cereal-based products. *Innovative Food Science and Emerging Technologies, 38*, 281–291. https://doi.org/10.1016/j.ifset.2016.10.001.

Severini, C., Derossi, A., Ricci, I., Caporizzi, R., & Fiore, A. (2018). Printing a blend of fruit and vegetables. New advances on critical variables and shelf life of 3D edible objects. *Journal of Food Engineering, 220*, 89–100. https://doi.org/10.1016/j.jfoodeng.2017.08.025.

Sun, A., & Gunasekaran, S. (2009). Yield stress in foods: Measurements and applications. *International Journal of Food Properties, 12*. https://doi.org/10.1080/10942910802308502.

Sun, J., Peng, Z., Zhou, W., Fuh, J. Y. H., Hong, G. S., & Chiu, A. (2015). A review on 3D printing for customized food fabrication. *Procedia Manufacturing, 1*, 308–319. https://doi.org/10.1016/j.promfg.2015.09.057.

Sun, J., Zhou, W., Yan, L., Huang, D., & Lin, L.y. (2016). Extrusion-based food printing for digitalized food design and nutrition control. *Journal of Food Engineering*, 1–11. https://doi.org/10.1016/j.jfoodeng.2017.02.028.

Toussaint, G. T. (1983). Computing largest empty circles with location constraints. *International Journal of Computer and Information Sciences, 12*(5), 347–358. https://doi.org/10.1007/BF01008046.

Van Velzen, E. J. J., Van Duynhoven, J. P. M., Pudney, P., Weegels, P. L., & Van der Maas, J. H. (2003). Factors associated with dough stickiness as sensed by attenuated total reflectance infrared spectroscopy. *Cereal Chemistry, 80*(4), 378–382. https://doi.org/10.1094/CCHEM.2003.80.4.378.

Vancauwenberghe, V., Mbong, V. B. M., Vanstreels, E., Verboven, P., Lammertyn, J., & Nicolai, B. (2017). 3D printing of plant tissue for innovative food manufacturing: Encapsulation of alive plant cells into pectin based bio-ink. *Journal of Food Engineering*, 1–11. https://doi.org/10.1016/j.jfoodeng.2017.12.003.

Wang, L., Zhang, M., Bhandari, B., & Yang, C. (2017). Investigation on fish surimi gel as promising food material for 3D printing. *Journal of Food Engineering*, 1–8. https://doi.org/10.1016/j.jfoodeng.2017.02.029.

Wegrzyn, T. F., Golding, M., & Archer, R. H. (2012). Food layered manufacture: A new process for constructing solid foods. *Trends in Food Science and Technology, 27*(2), 66–72. https://doi.org/10.1016/j.tifs.2012.04.006.

Wilson, S. A., Cross, L. M., Peak, C. W., & Gaharwar, A. K. (2017). Shear-thinning and thermo-reversible nanoengineered inks for 3D bioprinting. *ACS Applied Materials and Interfaces, 9*(50), 43449–43458. https://doi.org/10.1021/acsami.7b13602.

Yang, F., Zhang, M., Prakash, S., & Liu, Y. (2018). Physical properties of 3D printed baking dough as affected by different compositions. *Innovative Food Science and Emerging Technologies*. https://doi.org/10.1016/j.ifset.2018.01.001 (March 2017).

Zhang, L., Lou, Y., & Schutyser, M. A. I. (2018). *3D printing of cereal-based food structures containing probiotics. 18(August)*, 14–22.

Zhang, M., Liu, Z., Bhandari, B., & Wang, Y. (2017). 3D printing: Printing precision and application in food sector. *Trends in Food Science & Technology*, 564–574. https://doi.org/10.1016/j.tifs.2017.08.018.

2.3 Sensory design in food 3D printing – Structuring, texture modulation, taste localization, and thermal stabilization

Fahmy, A. R., Amann, L. S., Dunkel, A., Frank, O., Dawid, C., Hofmann, T., Becker, T., & Jekle, M. (2021). Sensory design in food 3D printing – Structuring, texture modulation, taste localization, and thermal stabilization. Innovative Food Science & Emerging Technologies, 72 (August), 102743. https://doi.org/10.1016/j.ifset.2021.102743

Authorship contribution

A.R. Fahmy: Methodology, Investigation, Formal analysis, Resources, Data curation, Writing - original draft, Visualization. **L.S. Amann**: Methodology, Investigation, Formal analysis, Resources, Data curation, Writing - original draft, Visualization. **A. Dunkel**: Methodology. **O. Frank**: Methodology, Writing - review & editing, Supervision. **C. Dawid**: Supervision. **T. Hofmann**: Conceptualization, Funding acquisition. **T. Becker**: Conceptualization, Funding acquisition. **M. Jekle**: Methodology, Conceptualization, Funding acquisition, Writing - review & editing, Supervision.

Innovative Food Science and Emerging Technologies 72 (2021) 102743

Contents lists available at ScienceDirect

Innovative Food Science and Emerging Technologies

journal homepage: www.elsevier.com/locate/ifset

Sensory design in food 3D printing – Structuring, texture modulation, taste localization, and thermal stabilization

Ahmed Raouf Fahmy [a,1], Laura Sophie Amann [b,1], Andreas Dunkel [c], Oliver Frank [b], Corinna Dawid [b], Thomas Hofmann [b], Thomas Becker [a], Mario Jekle [a,*]

[a] Technical University of Munich, TUM School of Life Sciences, Chair of Brewing and Beverage Technology, Research Group Cereal Technology and Process Engineering, Weihenstephaner Steig 20, 85354 Freising, Germany
[b] Technical University of Munich, TUM School of Life Sciences, Chair of Food Chemistry and Molecular Sensory Science, Lise-Meitner-Strasse 34, 85354 Freising, Germany
[c] Leibniz-Institute for Food Systems Biology at the Technical University of Munich, Lise-Meitner-Strasse 34, 85354 Freising, Germany

ARTICLE INFO

Keywords:
3D cereal printing
Sensory contrast
Inhomogeneous distribution
Saltiness enhancement
Infrared stabilization
Food printing

ABSTRACT

Most 3D printing studies of foods deal with the feasibility and modulation of textures independent of flavor design aspects. As a cornerstone for the combined control over texturing and taste distribution, a 3D printing method for starch-based food textures was developed in a pioneering approach using dual extrusion coupled with focused on-board near infrared (NIR) heating for thermal stabilization. The developed method facilitated the design of hydrated starch-egg white powder-systems in reproducible printing configurations. To systematically study the influence of inhomogeneous taste distribution on sensory perception, it was applied in a saltiness sensory contrast study. For the first time, defined concentration gradients of sodium chloride were spatially printed in food textures. Comparable textural properties at the same infill levels were achieved for all printed structures with different sodium localizations. Furthermore, the inhomogeneous spatial distribution of sodium chloride caused saltiness enhancement. This 3D structuring, taste localization coupled with thermal stabilization (3D SLTS) methodology enables the elucidation of texture-taste release interactions.

1. Introduction

Food layered manufacture (FLM) is a food production process where the processing of food is implemented using electro-mechanical based additive manufacturing (AM) approach. To illustrate, additive manufacturing or 3D printing is a process where structures are built layer-by-layer from 3D models. The most commonly used 3D printing technology in the food sector for its ability to structure highly viscous pastes or materials is the fused deposition modeling (FDM) technique which relies on extrusion and deposition principles (ASTM-International, 2012). Moreover, the introduction of rapid prototyping (RP) and additive manufacturing in food production gives the advantage of customization and personalization over traditional processing (Wegrzyn, Golding, & Archer, 2012). Due to the accuracy and precision of the 3D printing technology, complex food structures can be produced incorporating customized textures, tailored nutrition, and functional ingredients (Derossi, Caporizzi, Azzollini, & Severini, 2018; Lille, Nurmela, Nordlund, Metsä-Kortelainen, & Sozer, 2018; Y. Liu et al., 2019; Zhenbin Liu, Zhang, & Yang, 2018; Sun, Zhou, Yan, Huang, & Lin, L. ya., 2018; Vancauwenberghe et al., 2018, 2019; Zhang, Lou, & Schutyser, 2018). Concerning the development of AM technologies in the production of food systems such as bread, 3D printing can be used to eliminate structural heterogeneity. This structural variability affects reproducibility which impedes the understanding of mechanistic relationships (Zghal, Scanlon, & Sapirstein, 2002). By slicing bulk structures into individual layers, the control over aeration, cellular structure, mechanical properties, and distribution of taste is achievable (Fahmy, Becker, & Jekle, 2020, 2021). Therefore, 3D printing technology has the potential of being applied in the texture and taste design as well as a tool for understanding the texture and taste relationships in food- and cereal-based material systems and structures. However, several technological developments regarding structuring, localization, and on-board thermal stabilization are required to take full advantage of 3D printing in food applications (Baiano, 2020).

* Corresponding author.
E-mail address: mjekle@tum.de (M. Jekle).
[1] A. R. Fahmy and L. S. Amann contributed equally to this work as first authors.

https://doi.org/10.1016/j.ifset.2021.102743
Received 21 April 2021; Received in revised form 22 June 2021; Accepted 22 June 2021
Available online 24 June 2021

The sensory perception during food consumption depends not only on the concentrations of odor- and taste-active compounds but also on the texture of food matrix (Tournier, Sulmont-rossé, & Guichard, 2007). The possibility of targeted analysis and control of the sensory perception of foods is confined due to limited knowledge about texture-taste interactions. Particularly, the sensory activity can hardly be predicted by the integral overall concentration if taste compounds are heterogeneously distributed in complex food matrices. Thus, it could be shown that inhomogeneous spatial distribution of taste-active compounds causes intensified sensory perception (Konitzer et al., 2013; Noort, Bult, Stieger, & Hamer, 2010; Noort et al., 2012). Noort et al. (Noort et al., 2010) investigated the effects of local concentration gradients of sodium chloride in layered bread on the perceived saltiness intensity. For this purpose, starch-protein layers with varying NaCl contents were stacked in alternating fashion before baking. They reported a significant saltiness enhancement of bread with high NaCl contrasts between layers compared to bread with homogeneous NaCl distribution, allowing up to 28% sodium reduction while maintaining saltiness intensity. The enhancement of salty taste has been ascribed mainly to the sensory contrast and to a small extent to a faster sodium release (Konitzer et al., 2013; Noort et al., 2010; Noort et al., 2012). In these previous studies, a precise positioning of spatial concentration gradients was not possible. The studies were performed with conventional manufacturing techniques on sparsely defined food matrices. To systematically investigate the effect of taste distribution on the sensory perception, new texturing approaches are necessary that achieve highly defined and reproducible texture construction. For this purpose, our study presents an approach which utilizes dual extrusion 3D printing for structuring matrix textures with spatial localization of sensory-active compounds. The method enables the production of highly defined starch-based material systems with targeted incorporation of locally resolved concentration gradients of sodium chloride.

For all food systems, the manipulation of sensory perception through the combined structure and flavor design using 3D printing is yet to be technologically integrated and functionally investigated. Without consideration for the flavor design aspects, most available studies are focused on the feasibility of texture design of foods through 3D printing (Jonkers, Van Dommelen, & Geers, 2020; Le Tohic et al., 2018; Y. Liu et al., 2019; Phuhongsung, Zhang, & Devahastin, 2020; Vancauwenberghe et al., 2018). As an example, Liu et al. (Liu et al., 2019) 3D printed variable textural properties for milk protein composite gels by changing the protein concentration. On the other hand, Vancauwenberghe et al. (Vancauwenberghe et al., 2018) obtained variable textural properties through honeycomb porosity control using varying number of cells and pore sizes. By moving forward from the isolated texture variability research, the combined control over texture and taste distribution, which is developed in this study using dual extrusion, can be a step forward for the coupled manipulation of texture and taste.

For printing of some types of gel systems, thermal stabilization or post-processing is not required for functionality or geometrical stability. On the other hand, for other foods such as starch-based systems, induced heat transitions for thermal stabilization are important for post-printing geometrical stability and consumption (He, Zhang, & Fang, 2020). Considering highly consumed staple products incorporating starch and protein contents, heat stabilization is required for inducing physiochemical changes such as protein denaturation, starch gelatinization and dehydration for storage stability in terms of low water activity and microbial growth. Different 3D food printing studies included thermal stabilization as post-processing in the form of microwave drying, baking, steaming, frying and other methods (He et al., 2020; Lille et al., 2018; Zipeng Liu, Chen, Zheng, Xie, & Chen, 2020; Pulatsu, Su, Lin, & Lin, 2020; Yang, Zhang, Prakash, & Liu, 2018, Yang, Zhang, & Liu, 2019). On the other hand, the on-board integration of thermal stabilization solutions is missing in food printing studies. The term on-board denotes the electromechanical integration of the heating system into the 3D printing system which can lead to the exclusion of post-processing after food printing. Moreover, the optimized coupling between 3D printing and an on-board thermal stabilization solution can enable layer-based heating, targeted or local heating, and automatic material-based heating optimization. The presented method incorporates a focused on-board near infrared (NIR) stabilization system for geometric stabilization and for achieving process-independent, precisely defined, and reproducible matrix textures.

To utilize the developed 3D printing method with integration of structuring, localization, and thermal stabilization, a saltiness sensory contrast study was carried out. In this approach, local NaCl distributions were spatially printed in hydrated wheat starch-egg white powder-mixtures using alternating layers with different configurations to investigate the influence of inhomogeneous NaCl distribution on sensory perception. Each layer of the printed structures was individually and automatically stabilized using a NIR spot heater before printing the subsequent layer. This automatic heating method was used to thermally and geometrically stabilize the material to reduce diffusion and mechanical deformation. Texture profile analyses were used to investigate possible textural discrepancies between the single and dual extruded structures. The actual sodium content of the samples and different layers was quantified by means of ion chromatography. The starch-based samples with inhomogeneous spatial distribution of sodium were evaluated by human sensory analyses. Finally, the combination of existing knowledge concerning texturing and the successful localization of spatial NaCl concentration gradients can be a milestone for future elucidation of mechanistic texture-taste interactions which was not possible before.

2. Materials and methods

2.1. Raw materials

A material system composed of hydrated wheat starch and egg white powder was used for 3D printing. The wheat starch was provided by Kröner-Stärke GmbH (Ibbenbüren, Germany). The hen egg white powder was purchased from Bulk Powders (Colchester, United Kingdom). For sensory analyses, an egg white powder with a lower salt content was obtained from FunCakes (Wormer, The Netherlands). According to the methods of the American Association of Cereal Chemists international (AACCi), the moisture content (AACCi 44–01) and protein content (AACCi 46–16) were determined. The wheat starch had a moisture content of 13.98 ± 0.17% ($n = 3$) and a protein content of 0.27% ($n = 1$; dry mass), and a NaCl content of 0.058 ± 0.001% (n = 3; dry mass). The egg white powders had a moisture content (n = 3) of 6.88 ± 0.03% (Bulk Powders) and 8.49 ± 0.21% (FunCakes), a protein content (n = 1; dry mass) of 83.42% (Bulk Powders) and 82.87% (FunCakes), and a NaCl content (n = 3; dry mass) of 6.46 ± 0.06% (Bulk Powders) and 3.34 ± 0.07% (FunCakes).

2.2. Chemicals

The purity grade of chemicals was pro analysi (p.a.) unless noted otherwise. The following chemicals were commercially obtained: Patent Blue V calcium salt (Glentham Life Sciences Ltd., Corsham, United Kingdom), ethanol (VWR International, Fontenay-sous-Bois, France), methanol (HPLC grade; J. T. Baker, Griesheim, Germany), sodium chloride (Sigma-Aldrich GmbH, Steinheim, Germany), D-sucrose (Carl Roth GmbH & Co. KG, Karlsruhe, Germany), caffeine (Merck KGaA, Darmstadt, Germany), monosodium L-glutamate (Alfa Aesar, Ward Hill, USA), ferulic acid and L-lactic acid (Fluka GmbH, Neu-Ulm, Germany). Water for mixture preparation, extraction, dilution steps, and analysis was purified using a Milli-Q Reference A+ Water Purification System (Merck Millipore, Darmstadt, Germany). Evian® water, a commercially available table water with low mineral content, was used for sensory analysis.

2.3. Desalination of egg white powder by means of ultrafiltration

A portion (7.5 g) of egg white powder (FunCakes, Wormer, The Netherlands) was homogenized in 250 mL ethanol/water (20/80, *v*/v) with an Ultra-Turrax (12,000 rpm, 1 min). The suspension was filled in a Vivacell 250 static gas pressure ultrafiltration concentrator (Sartorius AG, Göttingen, Germany) equipped with a Vivacell 250 polyethersulfone membrane (5 kDa) that was preconditioned by rinsing the membrane with deionized water (3 × 200 mL). After sealing, nitrogen pressure (3.5 bar) was applied by means of an air pressure controller. During filtration, the Vivacell 250 device was agitated (100 rpm, room temperature) on an orbital shaker (type 3005, GFL, Burgwedel, Germany). The retentate was taken up in 20% aqueous ethanol solution (200 mL) and was once more ultrafiltered under pressure (3.5 bar). This washing step was repeated twice. After filtration, the retentate was removed from the ultrafiltration device and the membrane was washed with deionized water to recover absorbed material. Afterwards, the solubilized retentate was lyophilized. The different batches of desalted egg white powder were combined and homogenized (3 h) using a Turbula® shaker mixer (WAB, Muttenz, Switzerland).

2.4. Preparation of printing materials

All starch-protein systems are displayed in Table 1. A total of 11 different starch-based blends was used which consisted of hydrated wheat starch-egg white powder-mixtures (SE) or hydrated wheat starch-desalted egg white powder-mixtures (SDE). The ratio of wheat starch to (desalted) egg white powder was kept at 85:15 (*w*/w) for all printing mixtures (Goesaert et al., 2005; Jekle, Mühlberger, & Becker, 2016). The overall NaCl content of the mixtures is listed in Table 1 and is given in g/100 g on dry material (starch and egg white powder) to provide values that are comparable with other studies which express the NaCl content in g/100 g on flour basis.

A Z-type kneader (63 rpm) was used to prepare the different mixtures. A pre-mixing step (1 min) was used to mix the dry ingredients before adding aqueous NaCl solutions. For the dyed mixtures, Patent Blue V calcium salt (50 mg) was added to the solutions and stirred on a magnetic stirrer (5 min). After adding the solutions, the mixture was kneaded (10 min), placed in a plastic beaker which was covered using Parafilm (Bemis Company Inc., Wisconsin, USA), and left to rest (30 min, room temperature) until the preparation and assembly of both extruders was completed. Concerning the characterization, printability, and textural analyses experiments, the mixtures were prepared and measured in triplicates. Throughout this paper, the naming scheme or abbreviations mentioned in Table 1 was used to denote the different mixtures.

Table 1
Constituents and sodium chloride content of the hydrated wheat starch-egg white powder-mixtures (SE) and the hydrated wheat starch-desalted egg white powder-mixtures (SDE) for 3D printing.

Abbreviations	Description	Wheat starch (g) – (desalted) egg white powder (g) – aqueous solution (g) – food dye (g)	NaCl content (g/100 g dry material)
SE60	SE without NaCl	85–15–60–0	0.66 ± 0.05 ^{e}
SE60-Med	SE + medium NaCl	85–15–60–0	1.92 ± 0.08 ^{c}
SE60-Hi	SE + high NaCl	85–15–60–0	3.07 ± 0.12 ^{a}
SE60-DYE	SE + dye	85–15–60–0.05	0.63 ± 0.05 ^{e}
SE60-Hi-DYE	SE + high NaCl + dye	85–15–60–0.05	3.13 ± 0.11 ^{a}
SDE102	SDE without NaCl	85–15–102–0	0.16 ± 0.02 ^{f}
SDE96-Med	SDE + medium NaCl	85–15–96–0	1.20 ± 0.13 ^{d}
SDE94-Hi	SDE + high NaCl	85–15–94–0	2.44 ± 0.20 ^{b}
SDE102-DYE	SDE + dye	85–15–102–0.05	0.19 ± 0.02 ^{f}
SDE96-Med-DYE	SDE + medium NaCl + dye	85–15–96–0.05	1.11 ± 0.11 ^{d}
SDE94-Hi-DYE	SDE + high NaCl + dye	85–15–94–0.05	2.46 ± 0.20 ^{b}

NaCl content is expressed in mean ± standard deviation. Means with unequal letters (a - f) are significantly different ($p < 0.05$).

2.5. 3D printing setup, process, and experiments

For this study, an X400 V3 3D printer (German RepRap GmbH, Feldkirchen, Germany) was used for printing the starch-based material systems. For all printing experiments, a nozzle diameter of 0.84 mm, a printing speed of 10 mm/s, and an extrusion width/height of 0.84 mm were used. The detailed printing setup including pre-printing calibration was mentioned in our previous study regarding a method development for cereal printing quality analysis (Fahmy et al., 2020). For extrusion and deposition of the mixtures, two progressive cavity pumps (PCP) based extruders were used. Both extruders were purchased from ViscoTec GmbH (Töging, Germany) which are identical except for the pumping chamber size (rotor and stator). The Vipro-head3 and Vipro-head5 extruders have theoretical flow rates of 0.3 to 3.3 mL/min and 0.5 to 6.0 mL/min, respectively. Also, the mentioned flow rates depend on the viscoelastic properties of the extruded materials and the primary flow pressure developed inside the extruder. After conducting the optimization experiments (Fahmy et al., 2020), the extrusion multiplier for the primary extruder (Vipro-head3) was set to 29% while 12% for the secondary extruder (Vipro-head5). Concerning the on-board NIR stabilization, a variable output power 150 W spot heater was used (Optron GmbH, Garbsen, Germany). The used NIR-emitter has a peak wavelength of approximately ~0.98 µm. A control unit was used to interface between the heater and the 3D printer. The heating power is controlled through a variable DC input of 0 to 10 V which is then mapped on the printer's firmware to a pulse width modulation (PWM) of 0 to 213 (0 to

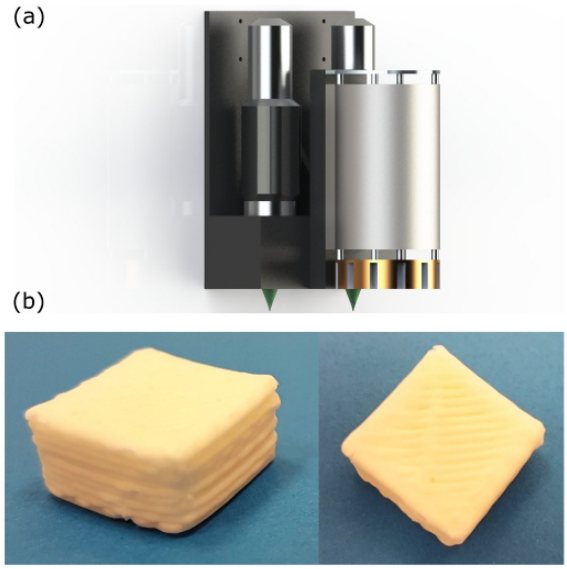

Fig. 1. Printing head and images of a 3D printed cuboid: (a) 3D rendering of the mounting system including the dual PCP extruders, and NIR spot heater; (b) images of a 3D printed sample at 100% infill with localized sodium using dual extrusion and NIR heating.

12 V corresponds to PWM or 0 to 255).

As shown in Fig. 1, a mounting system was printed using PLA to accommodate both extruders sideways while the spot heater was mounted in the perpendicular direction. With respect to the primary extruder, the secondary extruder was mounted with an offset of 80 mm in the x-direction while the spot heater was mounted with an offset of 40 mm and 30 mm in the x- and y-directions, respectively. The offset of the secondary extruder was accounted for in the printer's firmware. Layer- and tool-change G-code scripts were used, where the offsets were accounted for, to accommodate the layer-based heating routines. These scripts were executed during layer changes, whether there is a tool change or not, to insure a uniform layer-based heating and thermal stabilization.

For the printing of the starch-protein-based structures, a cuboid design of 15.0 × 15.0 × 7.5 mm (L × W × H) was used. The infill of all cuboids was 100% for the sensory and chemical analyses. While for the textural analysis, 75% infill cuboids with a middle square cutout beside the 100% infill were used to simulate the different levels of textural properties. The two infill levels were chosen for determining the textural properties produced by dual extrusion compared to single extrusion and to identify and characterize any possible defects arising from the usage of a dual extrusion system. As shown in Fig. 2, five different layer configurations were used for printing the cuboid design at adaptable printing settings. Two designs with homogeneous distribution of sodium chloride were printed using a single extruder (configuration: full a and b). The other designs incorporated a heterogeneous distribution of sodium using dual extrusion with the SE and SDE mixtures (Table 1) acting as the base material. For the 4/4 design shown in Fig. 2, the first four layers (bottom layers) were printed using the SE60 and SDE102 (Table 1) while the top 4 layers (top layers) were printed using the mixtures containing sodium chloride. The 2/2 and 1/1 designs were printed using a similar approach like the 4/4 design but with alternating dual or single layers, respectively.

2.6. Material characterization and printability experiments

The viscoelastic properties of the different mixtures were characterized using oscillatory measurements on an AR-G2 rheometer (TA instruments, New Castle, USA) coupled with a DIN concentric cylinder. The measurement geometry had a rotor radius of 14 mm and the gap clearance was set to 1 mm. A constant temperature (21 °C) was used through a Peltier plate system. 7 g samples were placed in the measuring cylinder, and the gap was adjusted to 1 mm. A 15 min of resting time was allowed, to replicate the extruder preparation before printing. In addition, a frequency sweep was used at a constant strain of 0.01. The chosen strain level was determined prior to the frequency tests (results not shown) using a strain sweep to characterize the material's linear viscoelastic region. A frequency ranging from 0 to 10 Hz was used. All printed mixtures were measured in triplicate. Furthermore, the onset gelatinization temperature of 58.96 ± 0.44 °C was measured using differential scanning calorimetry (DSC) and the base material (SE60). The DSC measurement was performed according to the method described by Paulik et al. (Paulik et al., 2019).

Since the addition of the sodium solutions and the ultrafiltration process affect the hydration and rheological properties of the starch-based blends and the egg white protein, respectively (Ferreira Machado et al., 2007; Mmadi, Amza, Wang, & Zhang, 2014; Thammasena, Fu, Liu, & Liu, 2020), hydration tests in the form of frequency sweeps were performed. The purpose of the hydration tests was to obtain comparable viscoelastic properties to ensure a similar printing performance between the different mixtures.

A camera-based approach was used to characterize the printing performance of the different starch-based blends used in the present study. This quality characterization approach was presented in a previous study by Fahmy et al. (Fahmy et al., 2020). The quality characterization was performed on lines and stacked lines. The lines were used to characterize the geometric stability of the material formulations. The stacked lines were used to assess the collapse/slumping and the overall

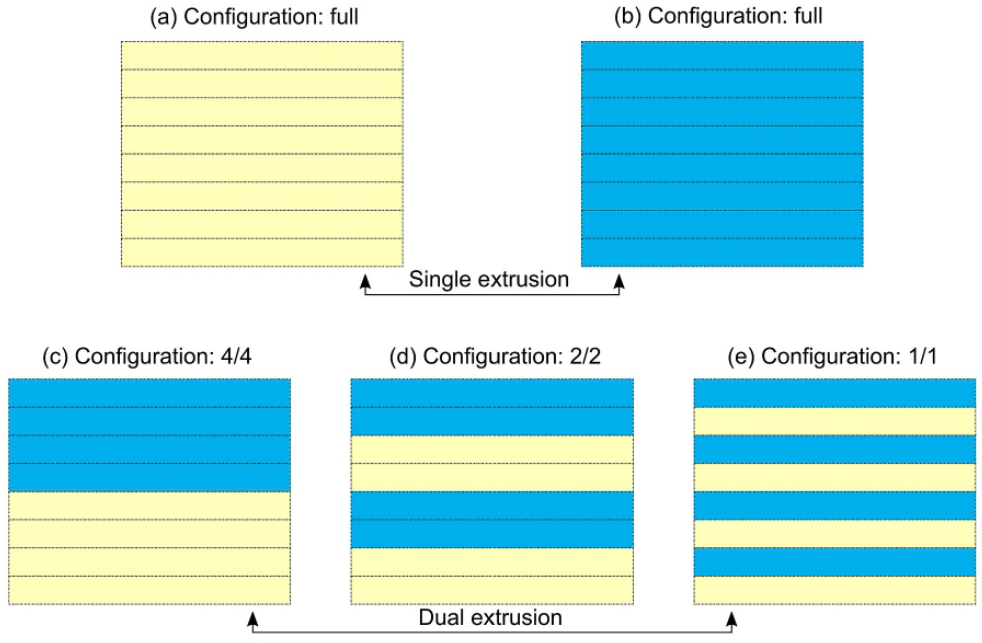

Fig. 2. Schematic diagram of the 3D printed layer configurations: (a) full configuration without dye or sodium addition; (b) full configuration with dye or/and sodium addition; (c) 4/4 configuration with alternating layers of 4; (d) 2/2 configuration with alternating layers of 2; (e) 1/1 configuration with single alternating layers.

structural stability (Fahmy et al., 2020). Geometrical parameters such as the output width, length, and height are extracted and processed autonomously with respect to the input parameters as a point of reference. Other aspects are evaluated such as pre-defined viscoelastic induced defects in the form of over-, under-extrusion, and structural collapse parameters. All measurements were performed with and without NIR heating. All mixtures were printed using a single extruder and measured in triplicate.

2.7. Thermal stabilization

An on-board NIR spot heater was used for thermally stabilizing the printed starch-based structures. The NIR spot heater is composed of a single lamp and a reflector heating system. It has a focal length of 17 mm and a spot diameter of 6 mm, as shown in Fig. 3. The heater was directly connected with the 3D printer's board, as mentioned in Section 2.5, which does not allow for controlling the heater's state, power, or movement in parallel to the printing process. Therefore, a layer-based stabilization approach was used. After each layer is printed, the heating process takes place then the printing is resumed.

For all printed layers, the heater distance was set at the focal length of the reflector (17 mm). A square function was implemented to cover the square's surface area. The square function has a period equivalent to the spot diameter and a phase shift of $-45°$ to insure uniform heating across the surface area.

To select the heating parameters, the heating profiles were measured at different power settings (data not shown). Also, the temperature inside the bottom layer of the printed structures was quantified to evaluate the heat cycles and temperature profiles during printing. For all temperature measurements, a K-type thermocouple was used with a data acquisition device 16-Bit USB DAQ (NI USB-6210) using a LabVIEW software (National Instruments, Texas, USA). The thermocouple was placed approximately at a height of ~0.5 mm of the first layer (middle of bottom layer). A heating power of 32% and movement speed of 13 mm/s (heating time of 4.4 s) for the 100% infill was chosen based on a resultant moisture content level of 41.02 ± 0.28%. Moreover, the speed was calibrated for the material systems with increased hydration to reach the same output moisture level. To obtain a constant moisture content for both printed infill levels (100% and 75%), the heating speed was varied from 9 to 15 mm/s with a step size of 1 mm/s. The different heating speeds were applied to cuboids of 90% infill with grid internal structures. The moisture content of the printed cuboids was measured, according to the AACCi 44–01 standard, at different heater movement speeds to characterize the relation between the heating speed and the occurring moisture loss. Then, to investigate the dependency of moisture loss on the infill variation, the moisture content was measured as the infill was varied between 100 and 80% with a step size of 5% while the heating speed was kept constant at 13 mm/s. Based on the relation between the heating speed, infill, and moisture content, linear regressions were used to obtain a speed calibration equation: $s = ((172.54 - i)/6.385)$ (1). Where **s** is the movement speed [mm/s] and **i** is the infill level (%). Using the mentioned equation, the 75% infill cuboids were printed using a heating speed of 15.34 mm/s (heating time of 3.8 s) to obtain a similar moisture content (compared to the 100% infill) of 40.89 ± 0.79%. In this study, the heating speed calibration was done without consideration for the heat induced transitions of the starch and egg white protein. Finally, all temperature measurements were done in triplicate.

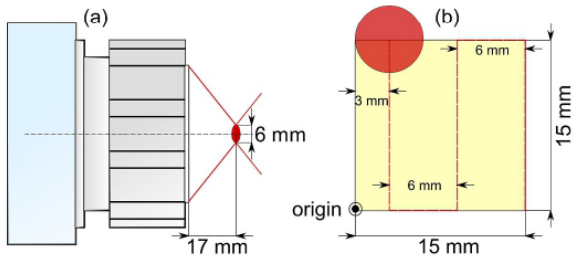

Fig. 3. Schematic diagram of the heating source and process: (a) side view of NIR spot heater and installed reflector with spot diameter of 6 mm; (b) top view of heating routine using a square wave function.

2.8. Texture profile analysis

The textural properties of the printed starch-based systems were characterized using a Texture Analyzer type TA.TX. plus (Stable Micro Systems Ltd., Godalming, UK) with a 50 kg measuring cell. The compression test was performed using an uncoated 25 mm PMMA stamp. A single double compression test was used at a test speed of 2 mm/s and a trigger force of 0.05 N. All the samples were compressed to 10% of its original height at room temperature of 18 ± 2 °C. The test was performed on a full configuration (Fig. 2) of 75% (middle square cutout) and 100% infill using the SE and SDE mixtures, shown in Fig. 2 and Table 1, respectively. The measured forces were recorded with respect to the change in time and distance. To obtain the engineering Young's modulus E, the force-distance curves were converted into stress-strain using the following equation: $\sigma/\varepsilon = ((F/A)/(\Delta H/H))$ (2) (Attenburrow, Goodband, Taylor, & Lillford, 1989; Beer Jr., DeWolf, & Mazurek, 2011). Where $\boldsymbol{\sigma}$ is the stress [Pa], $\boldsymbol{\varepsilon}$ is the strain, **F** is the resultant force [N], **A** is the surface area [m^2], **H** is the sample height [m], and $\boldsymbol{\Delta H}$ is lateral deformation [m]. A linear regression was used to obtain the engineering Young's modulus E from the linear section of the stress-strain curve with a coefficient of regression higher than 0.95. From the force-displacement curve of the double compression-decompression cycle, the following textural attributes were determined: hardness (HA), cohesiveness (CO), and resilience (RE). The hardness was extracted from the peak force of the first cycle. Moreover, the cohesiveness was defined as the area ratio of the second compression to the first compression. Finally, the resilience was represented as the ratio of energies equivalent to the ratio of decompression and compression cycles (Kramer & Szczesniak, 1973; Peleg, 2019). All texture measurements were done in triplicates.

2.9. Extraction of mixtures and printed samples

All raw materials, the starch-based blends in all compositions (cf. Table 1), and 3D printed samples in all layer configurations (Fig. 2) were extracted in order to quantify the sodium content. Prior to extraction, the stained inhomogeneous samples were separated in stained and unstained layers based on visual identification and analyzed individually. A portion (0.5 g) of the separated layers was extracted as detailed in the following but with an aliquot of 3.5 mL methanol/water (70/30, *v*/v). A portion (1.0 g) of each sample was placed in a bead beater tube (CK28_15 mL, Bertin Instruments, Montigny-le-Bretonneux, France) filled with ceramic balls (2.8 mm i. d.). An aliquot (7 mL) of methanol/water (70/30, v/v) was added. The samples were homogenized (6400 rpm, 3 cycles, 30 s each with 30 s breaks, 10 °C) using a bead beater (Precellys Evolution, Bertin Instruments, Montigny-le-Bretonneux, France) and extracted at an orbital shaker (500 rpm, 60 min, room temperature). After centrifugation (4000 rpm, 10 min), the supernatant was removed. The residue was extracted two more times (methanol/water, 70/30, v/v, 7 mL) in the same way as detailed above. The combined supernatants were evaporated to dryness under nitrogen. The remaining extract was dissolved in water and membrane-filtered (0.45 μm). Appropriate dilutions were prepared with water before analysis using High Performance Ion Chromatography (HPIC). The extraction was performed in biological triplicates.

2.10. Quantitative analysis of sodium by means of High-Performance Ion Chromatography

Sodium was quantified by means of HPIC using an ICS-2000 ion chromatography system (Dionex GmbH, Idstein, Germany) with an AS-AP autosampler, an eluent generator equipped with an eluent generator cartridge methanesulfonic acid EGC III MSA, a cation self-regenerating suppressor CSRS 500 (2 mm, suppressor current: 6 mA), and a digital conductivity detector DS6. System control and data processing were carried out using Chromeleon software (version 7.2, Dionex GmbH, Idstein, Germany). The quantification was performed using an external calibration with sodium standard solutions ranging from 1.4 to 175 mg/L. Aliquots (2 μL) were injected into the ICS-2000 apparatus equipped with a Dionex IonPac CS19 analytical column (4 μm, 2 × 250 mm) and a Dionex IonPac CG19 guard column (2 × 50 mm). Chromatography was performed at 30 °C with isocratic elution of aqueous methanesulfonic acid (7 mmol/L) at a flow rate of 0.25 mL/min. The quantitative data is given as the mean of triplicates.

2.11. Analytical sensory experiments

2.11.1. General conditions

All sensory sessions were performed in an air-conditioned sensory room separated into single booths at 20–22 °C. The light was adjusted to yellow to mask visual differences between the samples. The panelists used nose clips to avoid cross-modal interactions with odor-active compounds. The sensory panel consisted of 16 experienced human assessors (aged 24–31 years) who had given informed consent to participate in the sensory tests of the present investigation and have no history of known aroma and taste disorders.

2.11.2. Panel training

The panelists were trained to recognize and evaluate the taste of supra-threshold solutions of following taste compounds in bottled water to become familiar with the taste language used: NaCl (20 mmol/L) for salty taste, D-sucrose (20 mmol/L) for sweet taste, L-lactic acid (20 mmol/L) for sour taste, caffeine (2 mmol/L) for bitter taste, monosodium L-glutamate (6 mmol/L) for umami taste, and tannic acid (0.05%) for puckering-astringent. Furthermore, the panelists were accustomed to the starch-based food matrix and trained to distinguish between a sample with 1.0 g/100 g NaCl on dry material (= %) and samples with different NaCl contents (1.1%, 1.2%, 1.3%, 1.5%, 1.7% and 2.0%) by means of two-alternative forced choice (2-AFC) tests. For this one-sided paired comparison test, mixtures were prepared with wheat starch, low salt egg white powder (FunCakes), and aqueous NaCl solutions in a composition of 53.125/9.375/37.5 (*w*/w/w). The NaCl content in the samples is given based on the weight of dry materials (= 100%). The starch-based blends were baked in baking tins (50 × 20 × 20 mm, L × W × H) at 230 °C for 10 min. The samples were left to cool for 2 h and stored in airtight freezer bags at 4 °C until the next day. The crust was removed, and the crumb was separated into cubes (7.5 × 7.5 × 7.5 mm, L × W × H) before sensory analysis. To train the panelists, the 2-AFC tests were performed three times.

2.11.3. Saltiness evaluations of 3D printed samples

Before sensory analysis, the 3D printed samples were stored vacuum-packed at −22 °C for maximum 3 days. The perceived saltiness of 3D printed samples with homogeneous and heterogeneous spatial sodium distribution which had the same overall sodium content was compared in 2-AFC tests. For this two-sided paired comparison test, each panelist got a homogeneous sample with medium sodium content (SE60-Med or SDE96-Med) and an inhomogeneous sample consisting of layers without sodium addition (SE60 or SDE102) and layers with high sodium content (SE60-Hi or SDE94-Hi). The inhomogeneous samples in the three different layer configurations, 1/1, 2/2, and 4/4 (Fig. 2), were compared to the homogeneous sample in individual 2-AFC tests.

2.11.4. Procedure of two-alternative forced choice tests

The saltiness evaluation of the samples was carried out by means of 2-AFC tests. In this paired comparison test, the panelists received two covered beakers encrypted by a three-digit random number containing different samples (7.5 × 7.5 × 7.5 mm, L × W × H). To eliminate interfering carry-over effects, the panelists rinsed their mouths with bottled water between tasting of the samples. The panelists were instructed to indicate which of the two samples tasted saltier according to the forced choice method. The statistical evaluation of the 2-AFC tests was performed according to significance tables for one-sided and two-sided paired comparison tests in accordance with ISO 5495 (*ISO 5495: Sensory Analysis – Methodology – Paired Comparison Test. Geneva, Switzerland: International Organization for Standardization*, ISO 5495, 2005). The tables outline the minimum number of correct answers that is required to achieve a significant difference with a specified number of panelists on a level of significance α. Depending on the number of correct answers, the significance level α was determined. All p values ≤ 0.05 were judged as significant.

2.12. Statistics

One-way ANOVA and Tukey's pair-wise comparison, with the significance level set at $p < 0.05$, were used to analyze differences between sodium and NaCl contents. All data and statistical analyses were performed using MATLAB (The MathWorks Corporation, Natick, USA) and OriginPro 2020 (OriginLab Corporation, Northampton, USA).

3. Results and discussion

3.1. Rheological properties and printing performance

Printability tests of 2 different cereal-based systems coupled with rheological characterization were performed at different hydration levels in previous studies (Fahmy et al., 2020; Fahmy, Becker, & Jekle, 2018; Fahmy, Becker, & Jekle, 2019). The base material/mixture used in the presented study (SE60), with a hydration level of 60 g/100 g of dry material, was selected based on its geometric stability and low induced defects during printing. To obtain comparable geometric stability for the printed cuboids of the desalted egg white powder and the different sodium concentrations, the viscoelastic properties were measured through frequency sweeps at different hydration levels (Section 2.4). The hydration levels were varied from 90 to 110 g/100 g of dry material with a step size of 2 g/100 g of dry material according to preliminary tests (not shown). The hydration levels were increased until comparable viscoelastic properties (compared to the base material) were reached. The addition of the 50 mg of Patent Blue V calcium salt was not considered for the rheological hydration tests as there was no significant difference in the observed viscoelastic properties compared to the addition of the sodium base solution.

The viscous component or loss modulus was considered as the point of reference for obtaining the hydration levels for the other mixtures containing the sodium solutions as well as the desalted egg white powder. For reflecting the viscous properties of the materials, the loss modulus was considered over the storage modulus to obtain comparable viscous response of all materials during extrusion and deposition. Furthermore, the flow index could not be considered as the reference for obtaining the hydration levels due to the variation of the shear thinning behavior caused by the functional changes that were introduced by the desalination process, freeze drying, and the different sodium concentrations. For the stock (without sodium) desalted egg white powder mixture SDE102, a hydration level of 102 g/100 g of dry material was observed which corresponds to the same viscosity level of the base SE60 material as shown in Fig. 4. For the medium and high sodium concentration mixtures, the hydration levels were determined as 96 g/100 g SDE96-Med and 94 g/100 g SDE94-Hi of dry material, respectively, for the same viscous levels as the SE60 mixture. An increase in the hydration

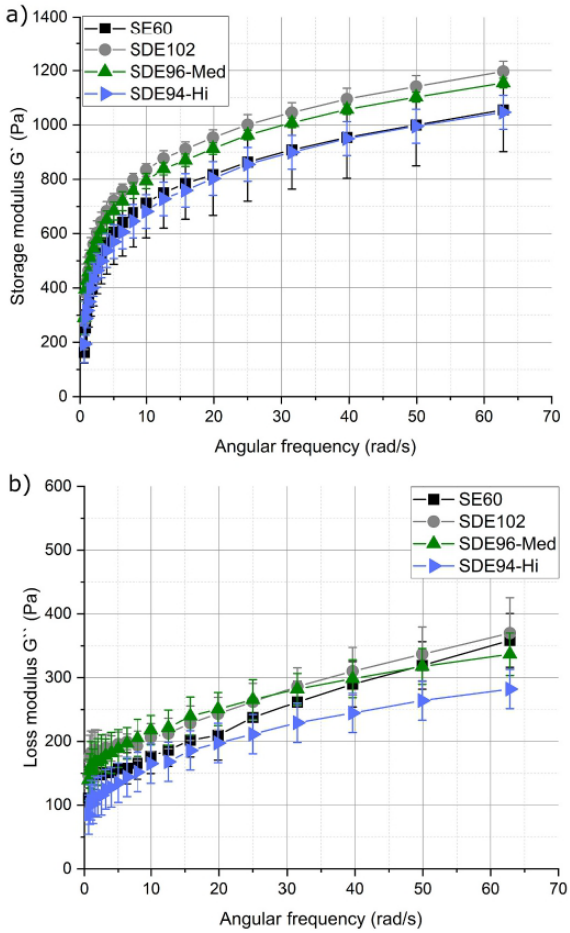

Fig. 4. Frequency sweep of the starch-based blends SE60, SDE102, SDE96-Med, and SDE94-Hi mixtures within 0 and 62 Hz at 21 °C: (a) elastic component; (b) viscous component.

for the SDE mixtures can be contributed to the alteration of the protein's particle microstructure and the protein's hydration properties after the ultrafiltration-desalination (Thammasena et al., 2020). Also, the protein solubility in the purified water compared to the different saline concentration affects the protein-protein and protein-solvent interactions which influences the physiochemical properties and thus the functional properties such as the viscoelastic response of the material (Ferreira Machado et al., 2007; Kakalis & Regenstein, 1986). Depending on the type and content of the present salts in the medium, they affect the electrostatic interactions among the macromolecules through ionic forces and are sufficient to change the conformation of the proteins (Fennema, 1993; Kinsella, 1982). Consequently, the material functionality of the starch-based mixtures is highly influenced by the presence of sodium in different concentrations (Jekle, Necula, Jekle, & Becker, 2019).

After determining the hydration levels for the desalted egg white powder mixtures, the printing quality of the mixtures was analyzed. The dimensional parameters and defects were determined using the on-board camera-based morphological approach as shown in Section 2.6. The approach was used during printing of the lines/stacks before and after the NIR heating. The aim is to highlight the improvement in structural stability of the printed structures after heating, also to detect any heating induced defects which could influence the structural and textural properties of the printed cuboids.

All output geometrical properties were analyzed and compared to the neutral profile which represents the optimal values of the given parameters. Considering the printed lines and stacks without heating, all materials show signs of slumping or structural collapse with the increasing number of layers, as shown in Fig. 5(a) and (b). The output extruded height (Fig. 5a) for all mixtures decreases from the target value starting from the 3rd layer onwards with the maximum deviation at the 5th layer for the SDE94-Hi mixture with an output height of 3.24 ± 0.03 mm. Compared to the neutral profile at the 5th layer with 4.2 mm in height, the deviation maxes out at approximately 22.8%. This effect indicates the structural collapse under the increasing applied hydrostatic pressure due to the increase in height. Moreover, shown in Fig. 5 (b), all mixtures show a high increase in the width of the printed structures while the optimal width should remain 0.84 mm according to the nozzle diameter under ideal material conditions. For all mixtures, an increase in the extruded width is observed at the deposition of a single layer. This effect can be contributed to the constriction of the nozzle's tip which induces a binding force acting on the material before deposition. The viscoelastic flow of the material causes a die swell phenomenon to occur where the deposited diameter is larger than the channel size (Wang, 2012). This increase can affect the precision of sodium localization if an area-based localization is performed where the local concentration of sodium is located beside or within the base material. On the other hand, for the layer-based approach presented in this study, the die swell effect should not affect the planar localization of the sodium component. Moreover, the maximum deviation of the output width of 1.8 ± 0.3 mm which represents an approximately ~114% increase than the neutral profile for the SE60 mixture at 4 layers. This shows a material flow from the top to the bottom layers in the direction of the gravitational forces. The flow of material between layers under hydrostatic pressure would pose a problem in the localization of the sodium containing mixtures which could nullify the localization of the sodium component. Consequently, the increase in width and decrease in height of all mixtures highlights the importance of a layer-based material stabilization.

The trials involving layer based NIR heating show a large improvement in the height and width performance, as illustrated in Fig. 5(a) and (b). Each layer is autonomously stabilized using the spot heater before the deposition of the consecutive layer. The heat and mass transfer during the localized heating process in the form of temperature increase and moisture loss increases the overall complex modulus of the material towards gelation (results not shown). This increases the yield point for the materials while exposed to the hydrostatic pressure from the height increase during layering of the materials which results on a more stable structure resistant to slumping or structural collapse. Regarding the width of the extruder mixtures with the respect to the increase in deposited layers, results show a fluctuation of maximum ~12% situated around the optimal value of 0.84 mm. Finally, the height of all mixtures increased towards the neutral profile compared to the non-heating trials. The maximum deviation of the SDE94-Hi mixture improved by approximately ~14% (absolute value) with a deviation of ~8.8% represented by a height of 3.8 ± 0.2 mm at 5 layers compared to the 4.2 mm of the optimal or theoretical value.

While short IR wave lengths influence the penetration depths, long-wave radiation is essential regarding the mount of transferred energy to the material (Skjöldebrand, Ellbjär, Andersson, & Eriksson, 1988). To illustrate, when the cereal matrix is exposed to infrared waves, the radiation is absorbed, reflected, or scattered. The absorption intensities of the radiative energy are highly dependent on the matrix constituents as well as the radiation's wave length (Riadh, Ahmad, Marhaban, & Soh, 2015). Consequently, the amount of absorbed radiation as well as the received energy is specific to the cereal matrix and heating setup that was used in this study.

To enumerate the effect of the local NIR layer-based heating method,

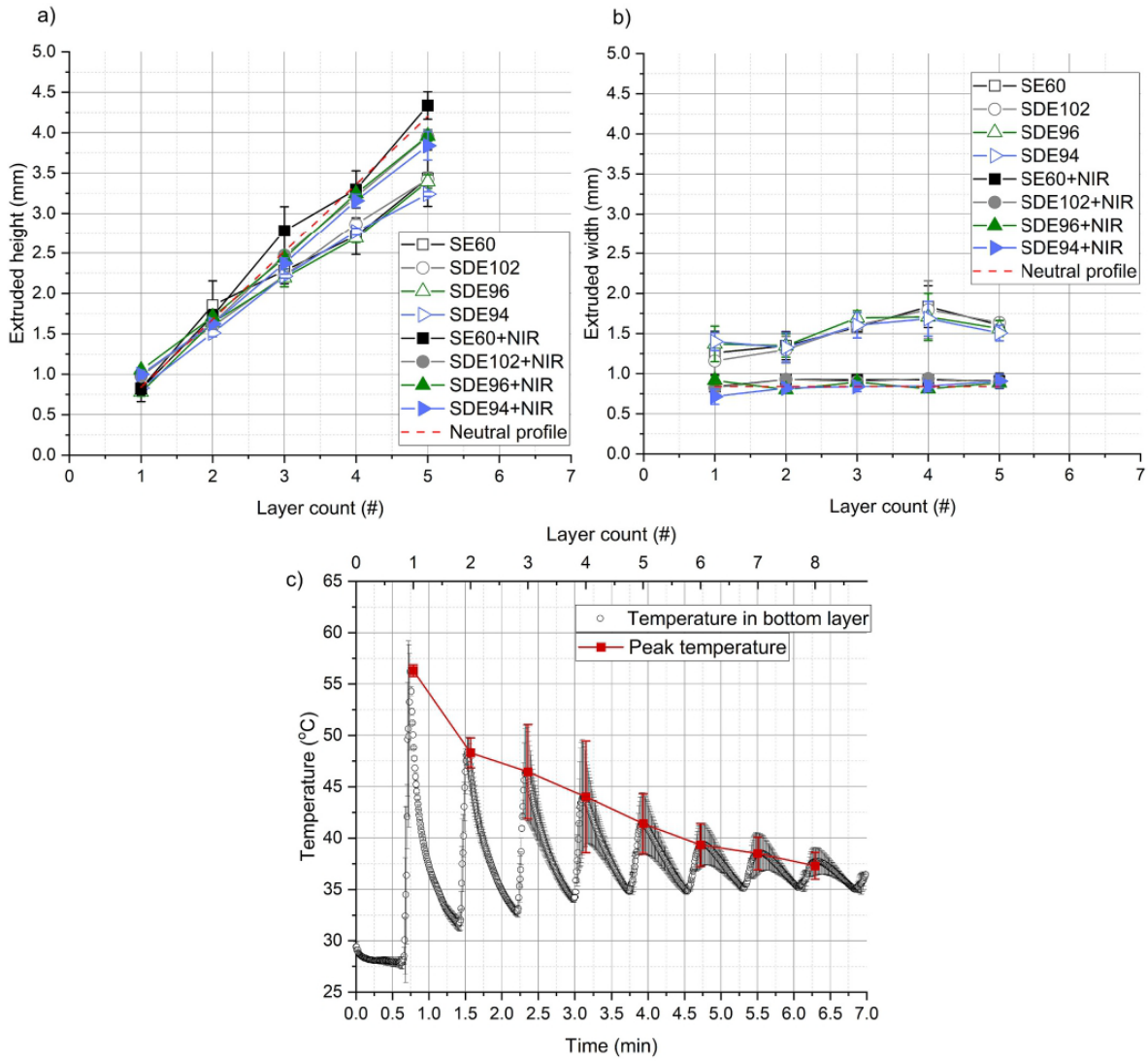

Fig. 5. Printing performance of the printing mixtures and in-line temperature measurements: (a) extruded height of printed stacks up to five layers; (b) extruded width of stacks up to five layers; (c) temperature cycle during printing with respect to the elapsed time and peak temperature recorded during each layer deposition (std $n = 3$).

the heat transmission was measured inside a single layer and through multiple layers. The surface area of the cuboids was decreased to 10.0 × 10.0 mm but the same layer thickness and structure height was maintained to reduce the printing time while keeping the same heat profiles as the other printing experiments. As shown in Fig. 5(c), the thermal stabilization of each layer consists of heating and cooling cycle. The heating region occurs where the NIR spot is incident to the thermocouple's location. The peak temperature is reached depending on the power and movement speed of the heater corresponding to the amount of time the spot diameter takes to move a length of 6 mm. The cooling cycle represents the heating of other regions followed by the printing of the consecutive layers. Because of this cyclic behavior, the lower layers receive more energy compared to the upper layers. Therefore, a heterogeneous distribution of moisture is expected to occur across the different layers resulting in a concentration gradient of water content along the thickness direction. Regarding the heat induced transformations, a peak temperature of approximately ~120 °C was measured at the top of the layer (at the focal length of the heater). Using the DSC approach (Section 2.6), the peak gelatinization temperature was observed to be 91.3 °C (extrapolating to the NIR's heating rate). Therefore, this resultant secondary heating cycles that increases proportional to the structure's height means that the heat induced transformation of the starch and protein is different across the layers. Consequently, the mechanical properties are expected to vary across the layers and the structural/textural properties are the resultant of the response of all layers. Furthermore, the concentration gradient of moisture is time dependent where moisture equilibrium occurs with the increase in storage duration. To elucidate the time dependency of moisture equilibrium, the bottom layers of 9 samples were separated directly after printing. Then, 3 samples were measured directly while the

other samples were stored for 1 and 2 days at −22 °C. The sample layers that were measured directly after printing showed a decrease of ~4.5% of the total moisture content compared to the overall moisture content of the cuboids (Section 2.6). After 24 h of storage, the moisture content equilibrated to just a decrease of ~0.3% from the final moisture content. Consequently, the results showed that the sensory tests were conducted where the internal deviations of the moisture content between layers is negligible and thus, moisture content-dependent textural discrepancies are avoided.

3.2. Textural properties

The textural properties of the printed designs and the localized layer configurations were of general interests. Therefore, double compression tests were conducted under quasi-static conditions in the linear deformation regime to texturally characterize the printed cuboids (Section 2.8). Also, the compression tests were used to calibrate the printing process with regards to the operation of the dual PCP extrusion design. The testing and calibration process were of outmost importance to this study as similar or comparable textural properties are required to ensure that the textural differences between the different layer configurations do not influence the results of the sensory analysis so that the results are solely dependent on the localization of the sodium inside the structures.

According to preliminary testing (results not shown), two main factors had an influence on the textural properties and thus they were of great interest to define. First, are the designed offsets in the cartesian coordinates between both custom extruders. Offsets and deviations in the layer height due to the small deviations in the z-axis did not show any influence on the textural properties in the elastic regime. To illustrate, the texture of cereal foams in the elastic regime is mainly dominated by the effective area as well as the relative density (Gibson, 1989; Lorna J. Gibson & Ashby, 1999). The overall height difference due to the propagation of uncertainty in the layer thickness does not affect the texture if the relative density remains constant. Finally, the offsets in the x- and y-axes resulted in high deviations in the output cuboid geometry and textural properties. In relation to the textures, the planar offsets were adjusted until low deviations were achieved. The second influence on the textural properties is derived from the slicing parameters and printing settings. This stems from the material difference contained in both extruders as well as the different flow ratings of both extruders (refer to Section 2.5). The shear rate applied on each material system is different due to the difference in rotor sizes between the extruders and the variability in the flow index or the rate of change of viscosity with respect to the applied shear rate. The flow index variability is a resultant of the functional changes that have arisen from the desalination process, freeze drying, and the different sodium concentrations. The mentioned dependencies affect the deformation of the material micro-structure during extrusion which in turn leads to different output base material properties between both extruders for all localized layer configurations.

To address the dual extrusion induced textural variability, first a constant moisture content (for all layer configurations) was attained through the heating speed optimization method mentioned in Section 2.7. Second, the full configuration (using SE60 and SDE102) was printed using a single extruder (Vipro-head3) controlled with a single set of extrusion and printing settings such as speed, flowrate, etc. On the other hand, full configurations of the sodium containing mixtures were printed using the extruder (Vipro-head5) since in printing the localized layer configuration of 1/1, 2/2, and 4/4 this extruder is used for depositing the sodium containing layers. For this extruder, the slicing/printing settings were adjusted with respect to the output hardness of the printed cuboids for both infills of 75% and 100%. The hardness of the cuboids was compared for all printed full configurations from both extruders and the extrusion settings for the Vipro-head5 extruder were adjusted until there was no significant difference observed. After setting and calibrating the extrusion settings for all mixtures, the cuboids in 75% and 100% infills were printed with the configurations shown in Fig. 2 for the egg white powder mixture SE60 and for the desalted egg white powder mixture SDE102. Fig. 6 shows the measured textural properties for the SE60 mixture for both infills and all configurations. As shown, comparable textural properties were achieved between the different printed configurations. Consequently, textural deviations between all configurations were eliminated to ensure no influence occurs in the sensory analyses.

3.3. Sodium diffusion in layered samples

Applying the developed 3D printing method, samples with inhomogeneous NaCl distribution were printed in three configurations, 1/1, 2/2, and 4/4 (Fig. 2), consisting of undyed layers without NaCl addition and dyed layers with NaCl addition. The actual sodium content within the different sample layers was quantified to determine whether sodium ions diffuse during the 3D printing and heating process and subsequent storage (cf. Fig. 7). The sodium content of the samples before and after the printing and heating process differ because the sodium content is given based on the fresh weight of the samples and moisture evaporates during the heating process.

In the first approach, a hydrated wheat starch-egg white powder-mixture (SE60) was the base material. The mixture SE60 was used for layers without NaCl addition and SE60-Hi-DYE for layers with NaCl addition (Table 1). The initial sodium concentration ratio between the layers was ~1:5 for all configurations (Fig. 7a). After 3D printing, heating, and storage, the remaining sodium concentration ratio was ~1:2.5 in case of configuration 4/4 and a sodium concentration equilibrium was reached in case of configuration 1/1 and 2/2 (Fig. 7b). This is caused by sodium diffusion from the high to the low salt layers.

In the second and third approach, the base material consisted of a hydrated wheat starch-desalted egg white powder-mixture (SDE102) resulting in a lower sodium content in the layers without NaCl addition compared to the first approach. The difference of approach two and three is the amount of NaCl addition. In both approaches, layers without NaCl addition were printed with mixture SDE102 and layers with NaCl addition were printed with SDE96-Med-DYE in approach two and with SDE94-Hi-DYE in approach three (Table 1). In the second approach, the initial sodium concentration contrast was ~1:7 (Fig. 7c). As a result of sodium diffusion during the 3D printing and heating process and storage, the ratio was reduced to ~1:5 in case of configuration 4/4 and to ~1:1.3 in case of configuration 1/1 and 2/2 (Fig. 7d). In the third approach, the initial sodium concentration ratio between the layers was ~1:15 (Fig. 7e). Due to sodium diffusion, it decreased to ~1:6.4 in case of configuration 4/4, to ~1:4.1 in case of configuration 2/2, and to ~1:3.2 in case of configuration 1/1 (Fig. 7f). Consequently, a large NaCl concentration gradient had to be applied to obtain samples with sodium concentration contrast at the time of sensory evaluation.

Salt diffusion was also reported in literature for layered bread with inhomogeneous NaCl distribution with findings that are comparable with the present study. During fermentation, baking, cooling and storage at ambient temperature, the initial salt concentration ratios of 1:5 and 1:11 of a bread with 1.5 g/100 g NaCl on flour basis were reduced to ~1:2.2 and ~ 1:3.1, respectively (Noort et al., 2010).

The approaches one and three were applied in sensory experiments (Section 3.5) but with uncolored samples. The food colorant was merely added to the high salt starch-based blends of the analysis samples to support the visual layer identification. Patent Blue V calcium salt was used as a food colorant to not alter the sodium content of the printing blends. This was also proven by sodium quantification in mixtures that only differed in addition of dye because no significant difference ($p > 0.05$) occurred between SE60 and SE60-DYE, SE60-Hi and SE60-Hi-DYE, SDE102 and SDE102-DYE, as well as between SDE94-Hi and SDE94-Hi-DYE (Table 1).

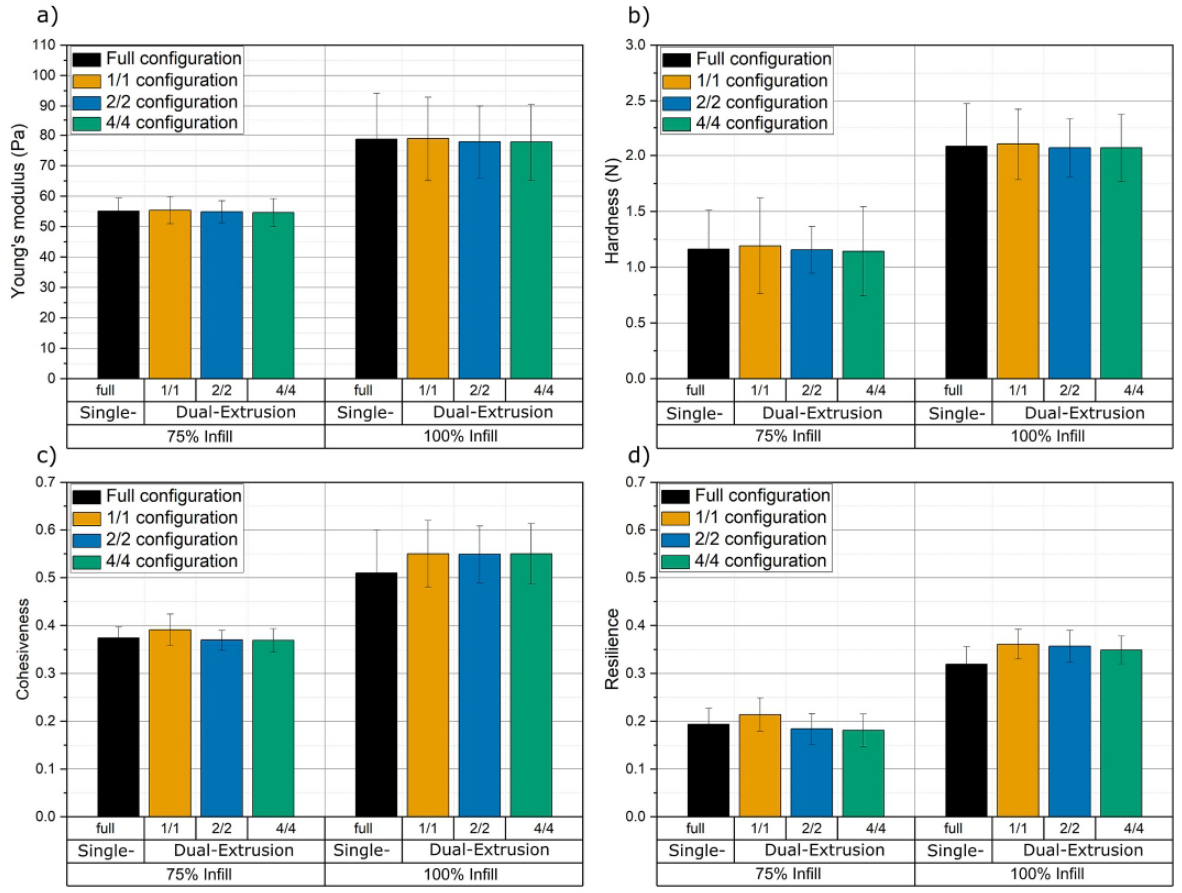

Fig. 6. Texture profile analysis of the 3D SLTS printed configurations from SE mixtures with 75% and 100% infills for all printed configurations: (a) young's modulus; (b) hardness; (c) cohesiveness and (d) resilience.

3.4. Differentiation of samples with variable NaCl contents

To determine the lowest perceivable salt taste difference, the saltiness of a sample with 1.0 g/100 g NaCl on dry material (= %) was assessed in 2-AFC tests in comparison to samples with 1.1%, 1.2%, 1.3%, 1.5%, 1.7%, and 2.0% NaCl, respectively. The samples containing 1.2% NaCl and more were rated significantly saltier ($p = 0.005$ for 1.2% and $p \leq 0.001$ for 1.3%, 1.5%, 1.7%, and 2.0%) than the 1.0% NaCl reference sample. The sample containing 1.1% NaCl could not be significantly distinguished ($p = 0.12$) from the reference sample, thus making 0.2% NaCl the lowest detectable difference for the sensory panel.

3.5. Effect of inhomogeneous spatial distribution of sodium on saltiness perception

By means of 2-AFC tests, the perceived saltiness of 3D printed samples with inhomogeneous spatial sodium distribution in three different layer configurations 1/1, 2/2, and 4/4, was compared to a reference sample with homogeneous distribution containing the same overall sodium chloride content.

In the first sensory experiment, the mixture SE60-Med was used for the homogeneous reference sample and mixtures SE60 and SE60-Hi for the inhomogeneous samples (Table 1). The overall NaCl content of the homogeneous reference sample (1.92 ± 0.08 g/100 g dry material) was not significantly different ($p > 0.05$) from that of the inhomogeneous samples (1.87 ± 0.05 g/100 g dry material). The sensory panel could not distinguish the homogeneous sample from the inhomogeneous samples of all layer configurations in terms of saltiness ($p \geq 0.5$). The reason for this could be that, at the moment of sensory evaluation, the NaCl concentration gradient between the different layers was too low (ratio ~ 1:2.5) to result in a perceivable effect on saltiness in case of configuration 4/4 and not existent in case of configuration 2/2 and 1/1 because sodium diffusion occurred (Section 3.3). Noort et al. (Noort et al., 2010) reported similar findings in a study with inhomogeneous distribution of NaCl in layered bread. NaCl concentration contrasts of ~1:2.2 and ~ 1:3.1 in breads did not result in a significant difference in the perceived saltiness intensity compared to a homogeneous bread with the same overall NaCl content of 1.5% based on flour.

Previous studies revealed that the saltiness enhancement also depends on the overall NaCl content. The relative saltiness enhancement was strongest at the lowest overall NaCl content (Noort et al., 2010). Because of this, the overall NaCl content was decreased in the second sensory evaluation of the present study by using desalted egg white powder in the 3D printed mixtures. The homogeneous sample consisted of mixture SDE96-Med and the inhomogeneous samples of SDE102 and SDE94-Hi (Table 1). The overall NaCl content of the homogeneous sample (1.20 ± 0.13 g/100 g dry material) was not significantly different ($p > 0.05$) from that of the inhomogeneous samples (1.30 ±

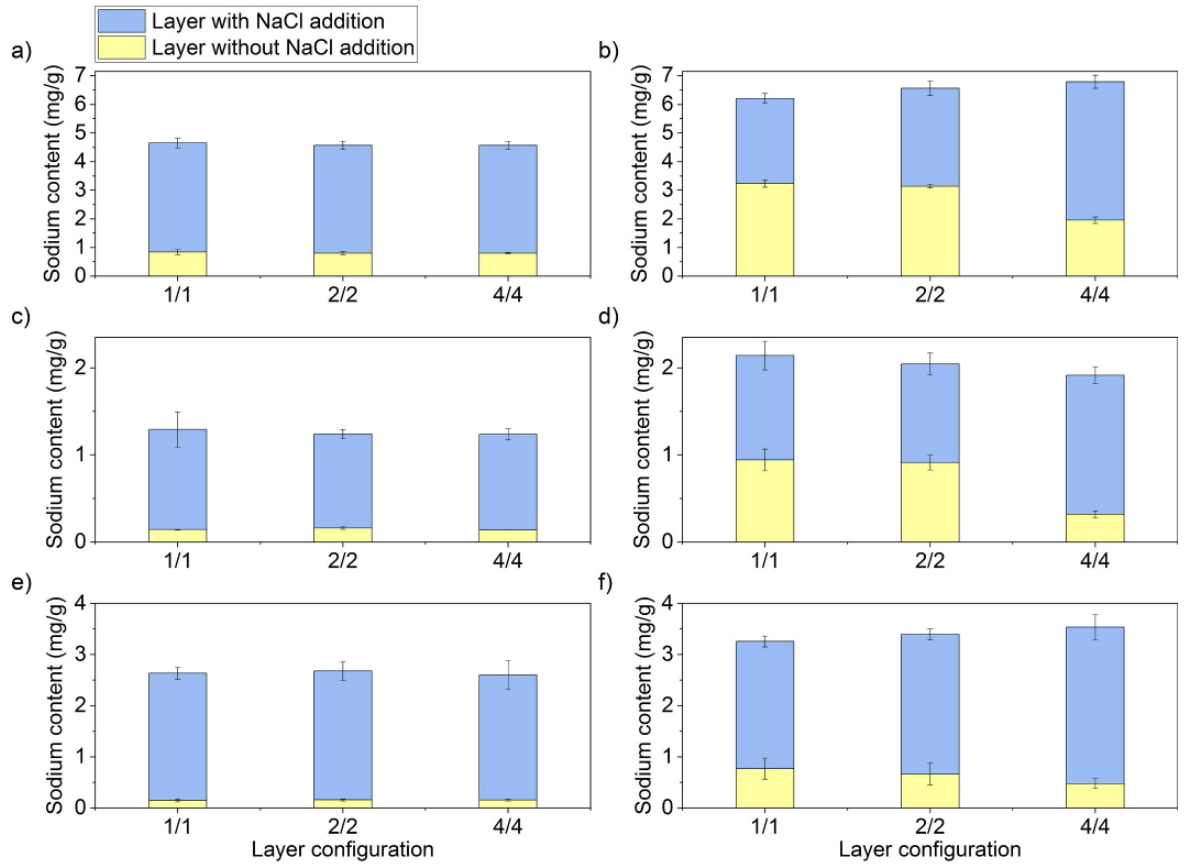

Fig. 7. Sodium content in different sample layers before and after the 3D printing and heating process and storage: (a) starch-based blends consisting of SE60 and SE60-Hi-DYE; (b) 3D printed sample consisting of SE60 and SE60-Hi-DYE; (c) starch-based blends consisting of SDE102 and SDE96-Med-DYE; (d) 3D printed sample consisting of SDE102 and SDE96-Med-DYE; (e) starch-based blends consisting of SDE102 and SDE94-Hi-DYE; and (f) 3D printed sample consisting of SDE102 and SDE94-Hi-DYE.

0.10 g/100 g dry material). Besides, the lowest perceivable difference of the sensory panel was 0.2 g/100 g NaCl on dry material as shown in Section 3.4. During the sensory evaluation, the inhomogeneous samples of all three configurations were perceived significantly saltier than the homogeneous reference sample ($p = 0.026$). This demonstrates that, at an overall NaCl content of ~1.3 g/100 g dry material, a sodium concentration ratio of ~1:6 in case of configuration 4/4, of ~1:4 in case of configuration 2/2, and of ~1:3 in case of configuration 1/1 (Section 3.3) is sufficiently strong to enhance the saltiness perception in layered 3D printed samples. The saltiness enhancement could be attributed to a small extent to an accelerated sodium release from the food matrix, but to a higher extent to the sensory contrast, because alternating stimuli of low and high sodium concentration prevent taste adaption and thus, are more intensively perceived than a continuous stimulus (Konitzer et al., 2013; Noort et al., 2010; Noort, Bult, & Stieger, 2012).

The effect of saltiness enhancement due to spatial NaCl heterogeneity in the 3D printed samples could be applied for sodium reduction in real life products while maintaining the perceived saltiness intensity. Sodium diffusion from the high to the low NaCl layers reduces the initial NaCl concentration ratios. Therefore, high NaCl concentration gradients must be applied while, at the same time, the overall NaCl content must stay at a low level to ensure an enhancement of saltiness perception by inhomogeneous spatial NaCl distribution. To reduce the effect of diffusion in future applications, configuration pattern other than layer configurations could be used where the ratio of the printing blends with and without salt addition is not balanced but concentrated spots are site-specifically introduced in matrix without salt addition.

4. Conclusion

A 3D printing method was developed that combines texturing, localization, and focused on-board near infrared stabilization of food systems. This 3D SLTS technique enables the production of hydrated starch-egg white powder-material systems in reproducible textural configurations. For the first time, defined NaCl concentration gradients were site-specifically incorporated and locally resolved in 3D printed starch-based food textures. The inhomogeneous spatial sodium chloride distribution caused saltiness enhancement, provided that the sensory contrast was sufficiently strong and the overall NaCl content at a low level. The evolved 3D printing method has the potential to be utilized in the development of healthier products due to sodium reduction without compromising saltiness intensity. Furthermore, the combination of texturing and targeted localization of spatial concentrations gradients could be applied to elucidate not only texture-taste interactions but also texture-aroma interactions. This can be a step forward to customize 3D printed food by systematically influencing texture, taste, and aroma to achieve ideal sensory profiles.

Declaration of Competing Interest

The authors declare that they have no known competing financial interests or personal relationships that could have appeared to influence the work reported in this paper.

Acknowledgements

This research was funded by the Deutsche *Forschungsgemeinschaft* (DFG, German Research Foundation) - 405072578.

References

ASTM-International. (2012). Standard terminology for additive manufacturing technologies. In *ASTM F2792-10e1 Standard, Vol ASTM F2792-10e1 Standard*. ASTM International. http://www.ciri.org.nz/nzrma/technologies.html.

Attenburrow, G. E., Goodband, R. M., Taylor, L. J., & Lillford, P. J. (1989). Structure, mechanics and texture of a food sponge. *Journal of Cereal Science, 9*(1), 61–70. https://doi.org/10.1016/S0733-5210(89)80024-4

Baiano, A. (2020). 3D printed foods: A comprehensive review on technologies, nutritional value, safety, consumer attitude, regulatory framework, and economic and sustainability issues. *Food Reviews International, 00*(00). https://doi.org/10.1080/87559129.2020.1762091. Taylor & Francis.

Beer, F. P., Jr., DeWolf, E. R. J., & Mazurek, D. F. (2011). *Statics and mechanics of materials* (1st ed.). McGraw-Hill.

Derossi, A., Caporizzi, R., Azzollini, D., & Severini, C. (2018). Application of 3D printing for customized food. A case on the development of a fruit-based snack for children. *Journal of Food Engineering, 220*, 65–75. https://doi.org/10.1016/j.jfoodeng.2017.05.015

Fahmy, A., Becker, T., & Jekle, M. (2018). 3D printing of cereal-based materials: On the relation between rheology and printability. In , *18. AACCI Annual Meeting Cereals & Grains*.

Fahmy, A. R., Becker, T., & Jekle, M. (2019). Flow behavior analysis for 3D printing of starch- based systems : Morphological imaging and multiple stage extrusion characterization through a rheometry imitation approach. In *33rd EFFoST International Conference*.

Fahmy, A. R., Becker, T., & Jekle, M. (2020). 3D printing and additive manufacturing of cereal-based materials: Quality analysis of starch-based systems using a camera-based morphological approach. *Innovative Food Science & Emerging Technologies, 63* (April), 102384. https://doi.org/10.1016/j.ifset.2020.102384

Fahmy, A. R., Becker, T., & Jekle, M. (2021). *Design and modulation of food textures using 3D printing of closed-cell foams in point lattice systems*. DECHEMA - Jahrestreffen Lebensmittelverfahrenstechnik.

Fennema, O. R. (1993). *Food chemistry (2nd editio)*. Marcel Dekker Inc.

Ferreira Machado, F., Coimbra, J. S. R., Garcia Rojas, E. E., Minim, L. A., Oliveira, F. C., & Sousa, R. (2007). Solubility and density of egg white proteins: Effect of pH and saline concentration. *LWT - Food Science and Technology, 40*(7), 1304–1307. https://doi.org/10.1016/j.lwt.2006.08.020

Gibson, L. J. (1989). Modelling the mechanical behavior of cellular materials. *Materials Science and Engineering A, 110*(C), 1–36. https://doi.org/10.1016/0921-5093(89)90154-8

Gibson, L. J., & Ashby, M. F. (1999). *Cellular-Solids-Structure-and-Properties-Cambridge-Solid-State-Science-Series-.pdf* (p. 510). https://books.google.pt/books/about/Cellular_Solids.html?id=lySUr5sn4N8C&source=kp_cover&redir_esc=y.

Goesaert, H., Brijs, K., Veraverbeke, W. S., Courtin, C. M., Gebruers, K., & Delcour, J. A. (2005). Wheat flour constituents: How they impact bread quality, and how to impact their functionality. *Trends in Food Science and Technology, 16*(1–3), 12–30. https://doi.org/10.1016/j.tifs.2004.02.011

He, C., Zhang, M., & Fang, Z. (2020). 3D printing of food: Pretreatment and post-treatment of materials. *Critical Reviews in Food Science and Nutrition, 60*(14), 2379–2392. https://doi.org/10.1080/10408398.2019.1641065

ISO 5495. (2005). *Sensory Analysis – Methodology – Paired Comparison Test. Geneva, Switzerland: International Organization for Standardization*. https://www.iso.org/standard/31621.html.

Jekle, M., Mühlberger, K., & Becker, T. (2016). Starch-gluten interactions during gelatinization and its functionality in dough like model systems. *Food Hydrocolloids, 54*, 196–201. https://doi.org/10.1016/j.foodhyd.2015.10.005

Jekle, M., Necula, A., Jekle, M., & Becker, T. (2019). Concentration dependent rate constants of sodium substitute functionalities during wheat dough development. *Food Research International, 116*(August), 346–353. https://doi.org/10.1016/j.foodres.2018.08.047

Jonkers, N., Van Dommelen, J. A. W., & Geers, M. G. D. (2020). Experimental characterization and modeling of the mechanical behavior of brittle 3D printed food. *Journal of Food Engineering, 278*, 109941. https://doi.org/10.1016/j.jfoodeng.2020.109941

Kakalis, L. T., & Regenstein, J. M. (1986). Effect of pH and salts on the solubility of egg white protein. *Journal of Food Science, 51*(6), 1445–1447. https://doi.org/10.1111/j.1365-2621.1986.tb13830.x

Kinsella, J. E. (1982). Structure and functional properties of food proteins. In J. J. C. P. P. Fox (Ed.), *Food proteins (pp. 72–85)*. Applied Science Published.

Konitzer, K., Tabea, P., Oliveira, P., Arendt, E., Koehler, P., & Hofmann, T. (2013). Kinetics of sodium release from wheat bread crumb as affected by sodium distribution. *Journal of Agricultural and Food Chemistry, 61*, 10659–10669. https://doi.org/10.1021/jf404458v

Kramer, A., & Szczesniak, A. S. (Eds.). (1973). *Texture measurement of foods* (1st ed.). Netherlands: Springer. https://doi.org/10.1007/978-94-010-2562-1.

Le Tohic, C., O'Sullivan, J. J., Drapala, K. P., Chartrin, V., Chan, T., Morrison, A. P., … Kelly, A. L. (2018). Effect of 3D printing on the structure and textural properties of processed cheese. *Journal of Food Engineering, 220*, 56–64. https://doi.org/10.1016/j.jfoodeng.2017.02.003

Lille, M., Nurmela, A., Nordlund, E., Metsä-Kortelainen, S., & Sozer, N. (2018). Applicability of protein and fiber-rich food materials in extrusion-based 3D printing. *Journal of Food Engineering, 220*, 20–27. https://doi.org/10.1016/j.jfoodeng.2017.04.034

Liu, Y., Yu, Y., Liu, C., Regenstein, J. M., Liu, X., & Zhou, P. (2019). Rheological and mechanical behavior of milk protein composite gel for extrusion-based 3D food printing. *Lwt, 102*, 338–346. https://doi.org/10.1016/j.lwt.2018.12.053

Liu, Z., Zhang, M., & Yang, C. (2018). Dual extrusion 3D printing of mashed potatoes/strawberry juice gel. *Lwt, 96*, 589–596. https://doi.org/10.1016/j.lwt.2018.06.014

Liu, Z., Chen, H., Zheng, B., Xie, F., & Chen, L. (2020). Understanding the structure and rheological properties of potato starch induced by hot-extrusion 3D printing. *Food Hydrocolloids*, 105812. https://doi.org/10.1016/j.foodhyd.2020.105812

Mmadi, M., Amza, T., Wang, Y. C., & Zhang, M. (2014). Effect of desalination on physicochemical and functional properties of duck (Anas plotyrhyncus) egg whites. *Advance Journal of Food Science and Technology, 6*(6), 784–791. https://doi.org/10.19026/ajfst.6.111

Noort, M. W. J., Bult, J. H. F., & Stieger, M. (2012). Saltiness enhancement by taste contrast in bread prepared with encapsulated salt. *Journal of Cereal Science, 55*(2), 218–225. https://doi.org/10.1016/j.jcs.2011.11.012

Noort, M. W. J., Bult, J. H. F., Stieger, M., & Hamer, R. J. (2010). Saltiness enhancement in bread by inhomogeneous spatial distribution of sodium chloride. *Journal of Cereal Science, 52*(3), 378–386. https://doi.org/10.1016/j.jcs.2010.06.018

Paulik, S., Yu, W. W., Flanagan, B., Gilbert, R. G., Jekle, M., & Becker, T. (2019). Characterizing the impact of starch and gluten-induced alterations on gelatinization behavior of physically modified model dough. *Food Chemistry, 301*, 125276. https://doi.org/10.1016/j.foodchem.2019.125276

Peleg, M. (2019). The instrumental texture profile analysis revisited. *Journal of Texture Studies, 50*(5), 362–368. https://doi.org/10.1111/jtxs.12392

Phuhongsung, P., Zhang, M., & Devahastin, S. (2020). Influence of surface pH on color, texture and flavor of 3D printed composite mixture of soy protein isolate, pumpkin, and beetroot. *Food and Bioprocess Technology, 13*(9), 1600–1610. https://doi.org/10.1007/s11947-020-02497-8

Pulatsu, E. T., Su, J., Lin, J., & Lin, M. (2020). Factors affecting 3D printing and post-processing capacity of cookie dough. *Innovative Food Science and Emerging Technologies, 102316*. https://doi.org/10.1016/j.ifset.2020.102316

Riadh, M. H., Ahmad, S. A. B., Marhaban, M. H., & Soh, A. C. (2015). Infrared heating in food drying: An overview. *Drying Technology, 33*(3), 322–335. https://doi.org/10.1080/07373937.2014.951124

Skjöldebrand, C., Ellbjär, C., Andersson, C. G., & Eriksson, T. S. (1988). Optical properties of bread in the near-infrared range. *Journal of Food Engineering, 8*(2), 129–139. https://doi.org/10.1016/0260-8774(88)90059-3

Sun, J., Zhou, W., Yan, L., Huang, D., & Lin, L. ya.. (2018). Extrusion-based food printing for digitalized food design and nutrition control. *Journal of Food Engineering, 220*, 1–11. https://doi.org/10.1016/j.jfoodeng.2017.02.028

Thammasena, R., Fu, C. W., Liu, J. H., & Liu, D. C. (2020). Evaluation of nutrient content, physicochemical and functional properties of desalted duck egg white by ultrafiltration as desalination. *Animal Science Journal, 91*(1), 1–9. https://doi.org/10.1111/asj.13339

Tournier, C., Sulmont-rossé, C., & Guichard, E. (2007). Flavour perception: Aroma, taste and texture interactions. *Food, 1*, 246–257.

Vancauwenberghe, V., Delele, M., Vanbiertvliet, J., Aregawi, W., Verboven, P., & Lammertyn, J. (2018). Model-based design and validation of food texture of 3d printed pectin-based food simulants. *Journal of Food Engineering, 231*, 72–82. https://doi.org/10.1016/j.jfoodeng.2018.03.010

Vancauwenberghe, V., Mbong, V. B. M., Vanstreels, E., Verboven, P., Lammertyn, J., & Nicolai, B. (2019). 3D printing of plant tissue for innovative food manufacturing: Encapsulation of alive plant cells into pectin based bio-ink. *Journal of Food Engineering, 263*, 454–464. https://doi.org/10.1016/j.jfoodeng.2017.12.003

Wang, K. (2012). Die swell of complex polymeric systems. In J. De Vicente (Ed.), *Viscoelasticity - From Theory to Biological Applications (1st ed., issue 1, pp. 77–96)*. IntechOpen. https://doi.org/10.5772/50137.

Wegrzyn, T. F., Golding, M., & Archer, R. H. (2012). Food layered manufacture: A new process for constructing solid foods. *Trends in Food Science and Technology, 27*(2), 66–72. https://doi.org/10.1016/j.tifs.2012.04.006

Yang, F., Zhang, M., & Liu, Y. (2019). Effect of post-treatment microwave vacuum drying on the quality of 3D-printed mango juice gel. *Drying Technology, 37*(0), 1757–1765. https://doi.org/10.1080/07373937.2018.1536884

Yang, F., Zhang, M., Prakash, S., & Liu, Y. (2018). Physical properties of 3D printed baking dough as affected by different compositions. *Innovative Food Science & Emerging Technologies, 49*, 202–210. https://doi.org/10.1016/J.IFSET.2018.01.001

Zghal, M. C., Scanlon, M. G., & Sapirstein, H. D. (2002). Cellular structure of bread crumb and its influence on mechanical properties. *Journal of Cereal Science, 36*(2), 167–176. https://doi.org/10.1006/jcrs.2001.0445

Zhang, L., Lou, Y., & Schutyser, M. A. I. (2018). 3D printing of cereal-based food structures containing probiotics. *Food Structure, 18*(August), 14–22. https://doi.org/10.1016/j.foostr.2018.10.002

2.4 Hardness targeted design and modulation of food textures in the elastic-regime using 3D printing of closed-cell foams in point lattice systems

Fahmy, A. R., Vogt, U. T., Jekle, M., & Becker, T. (2022). Hardness targeted design and modulation of food textures in the elastic-regime using 3D printing of closed-cell foams in point lattice systems. Journal of Food Engineering, 320 (May), 110942. https://doi.org/10.1016/j.jfoodeng.2022.110942

Authorship contribution

A.R. Fahmy: Methodology, Investigation, Formal analysis, Resources, Data curation, Writing - original draft, Visualization. **U.T. Vogt**: Investigation, Formal analysis, Data curation. **M. Jekle**: Methodology, Conceptualization, Funding acquisition, Writing - review & editing, Supervision. **T. Becker**: Conceptualization, Funding acquisition.

Journal of Food Engineering 320 (2022) 110942

Contents lists available at ScienceDirect

Journal of Food Engineering

journal homepage: www.elsevier.com/locate/jfoodeng

Hardness targeted design and modulation of food textures in the elastic-regime using 3D printing of closed-cell foams in point lattice systems

Ahmed Raouf Fahmy [a], Ulrike T. Vogt [a], Mario Jekle [b,*], Thomas Becker [a]

[a] Technical University of Munich, TUM School of Life Sciences, Chair of Brewing and Beverage Technology, Research Group Cereal Technology and Process Engineering, 85354, Freising, Germany
[b] University of Hohenheim, Institute of Food Science and Biotechnology, Department of Plant-based Foods, 70599, Stuttgart, Germany

ARTICLE INFO

Keywords:
Texture design
Closed-cell foam
3D food printing
Texture simulation
Hardness modulation
In-line heating

ABSTRACT

Recently, 3D printing has become an innovative technique in the structuring and modulation of food textures. The objective is to systematically extended 3D food printing to allow the production of cellular structures with specifically targeted textural properties. This study presents an approach for 3D printing structures with predefined hardness. As a step in the foundation of textural design, parameter fitting of 3D printed foams and finite element simulations was used to obtain a generalized hardness design formula for the 3D printing of closed-cell foams. Structures incorporating spherical bubbles arranged in point lattice cubic configurations were printed at different porosity levels. A complete 3D printing-stabilization method was applied with an integrated on-board layer-based heating and optimized for targeting heat induced material transitions to actively modulate the material's mechanical properties. FEM simulations were performed at different Young's moduli adjusted using variable heating speeds where the results showed an independency of hardness on the foam configuration and the distance between the closed-cell bubbles. Comparable hardness results were observed between the 3D printed and simulated samples where the same exponential decrease behavior was achieved. The hardness design formula was developed in relation to the material's Young's modulus, porosity, and printed geometry. The performance of the obtained relation showed comparable results to the FEM simulations and the 3D printed structures.

1. Introduction

The mechanical and textural properties of solid cellular food foams are determined by the foaming/structuring process, the mechanical properties of the constitutive material, the relative density, and the foam's microstructure (Gibson, 1989; Zghal et al., 2002). Typical structural imperfections are associated with the traditional structuring processes such as non-periodic ordering of cells, defects, and non-uniformity of cell walls. The inherited structural heterogeneity affects the foam's reproducibility and impacts its sensory characteristics (Gao et al., 2018; Guessasma and Nouri, 2015; Wang et al., 2006, 2011; Zghal et al., 2002). This paves the path for the integration of 3D printing in the texturing of cellular foods due to its accuracy, precision, reproducibility, and control over layer-based properties. As an additive manufacturing technique, 3D printing supports the precise manipulation of aeration, mechanical properties, and cellular structure for the design and modulation of customized textures (Derossi et al., 2020a, 2020b; Jonkers et al., 2020; Pereira et al., 2021; Phuhongsung et al., 2020a; Sun et al., 2015; Vancauwenberghe et al., 2018a; Wegrzyn et al., 2012). For all solid food products, the textural properties are essential in influencing the sensory perception. Moreover, the most relevant textural behavior influencing the sensory experience of solid foods are the resistance, fracture, springiness, and cohesiveness (Chen and Rosenthal, 2015). The adaptation of 3D printing in texture and hardness manipulation as well as in forming or structuring of cellular foods is newly yet extensively researched, which is founded on the comprehension of the microstructural effects on the mechanical properties of food foams (Attenburrow et al., 1989; Guessasma et al., 2008; Jang et al., 2008; Robin et al., 2011; Zghal et al., 2002).

Ultimately, from an innovative perspective, 3D printing has the potential to evolve from a textural modulation technique to a true behavior designing method. This will allow the production of cellular food structures with specifically chosen deformation behavior to alter the textural properties and sensory perception. Prior to texture design and

* Corresponding author.
E-mail address: mario.jekle@uni-hohenheim.de (M. Jekle).

https://doi.org/10.1016/j.jfoodeng.2022.110942
Received 23 July 2021; Received in revised form 28 December 2021; Accepted 4 January 2022
Available online 7 January 2022

modulation using 3D printing, the elucidation of the interaction between food-based materials and 3D extrusion printing is of interest for the optimization of specific material and process parameters (Wilms et al., 2021). Many studies can be found in literature focusing on the investigative-driven optimization of material-process interaction using rheological investigations, behavioral modelling, predictive models, and quantitative printing-quality analysis techniques (Derossi et al., 2020a, 2020b; Fahmy et al., 2020, 2019b, 2019a; Guo et al., 2019; Kim et al., 2017; Lille et al., 2018; Liu et al., 2019a, 2019b; Paolillo et al., 2021; Sun et al., 2018; Vancauwenberghe et al., 2018b; Wang et al., 2018; Wilms et al., 2021; Yang et al., 2019; Yang et al., 2018b; Yang et al., 2018a). Moreover, for 3D food printing applications and studies, investigations concerning material behavior and printing quality serves as a foundation for material selection. Most studies found in literature focus on the applicability and modulation of food textures using different compositions, pre-processing, printing settings, infill patterns, and post-processing techniques (Liu et al., 2019a; Park et al., 2019; Phuhongsung et al., 2020b, 2020a). As an example, Le Tohic et al. showed that the shear stress and heat applied during printing lowered the textural properties of printed cheese compared to the untreated formulation (Le Tohic et al., 2018). Only few and very recent studies focus on the controlled attenuation of structural parameters such as porosity structure, cell count, and cell sizes (Derossi et al., 2020a, 2020b; Vancauwenberghe et al., 2018a). And thus, the modelling and modulation of food textures using 3D printing was investigated and established. On the contrary, the parameter design of structures targeting specific textural properties is yet to be explored.

The main objective of this study was to obtain a hardness-targeted phenomenological foam model (HT-PFM) based on parameter fitting for the design and prediction of 3D printed food textures in the elastic regime. This allows for a transition from texture modulation using 3D printing to a parametric design approach for the prediction and digital design of hardness. A complete texture creation method was applied where the 3D printing process incorporates on-board local heating, thus eliminating the need for post-processing (Fahmy et al., 2021). The local thermal stabilization technique enables targeted heat induced material transitions for the manipulation of the bulk material's mechanical properties. This study was conducted on 3 variable porosity closed-cell foam designs which were 3D printed with spherical bubbles arranged in point lattice configurations. To ensure structural stability and geometrical accuracy during printing, a printability study was performed on two starch-based material systems using an on-board camera approach. The starch-based material systems were formulated at different concentrations of methylcellulose MC. One material formulation was chosen for printing the closed-cell foam designs based on its printability performance.

Furthermore, the inclusion of the material influence in the hardness-targeted formula was performed using a heating-based variation technique of the Young's modulus. Finite element (FEM) simulations and texture profile analysis (TPA) in the elastic regime were performed to characterize the hardness and develop the hardness equation. There are 3 main scientific objectives behind the use of FEM simulations in the presented study. First, to characterize the effect of the structural design of the closed-cell foam (bubble size, porosity, cell wall size, and distribution) on the Hardness in the elastic regime. The simulations were performed alongside analytical measurements using 3D printing and textural TPA analysis to ensure that there aren't any propagated structural defects occurring during printing, which would be indicated by an increase in the difference or divergence of the results. Second, the FEM simulations were used to develop a hardness formula depending on 3 design variables which are the material's Young's modulus, design porosity, and printed surface area. The hardness formula development was based on parameter fitting of the hardness behavior using multiple simulation levels. Third, the formula's hardness prediction and design performance were assessed using FEM simulations combined with 3D printing. Specific hardness values were selected, and the possible design parameters were generated using the developed equation. The parameters generated from the equation were simulated and used for printing where the performance of the equation/formula was assessed. Finally, this research can be a milestone in the foundation of food texture design for 3D printing applications where design parameters can be determined for a specific output hardness.

2. Materials and methods

2.1. Raw materials

For this study, two material systems composed of hydrated wheat starch-egg white protein (EWP) and hydrated wheat starch-soy protein (SPI) were used. Both material systems were used with increasing concentration of methyl cellulose (MC). Wheat starch was provided by Kröner Stärke, Ibbenbrünen, Germany. The egg-white protein concentrate and soy protein isolate were purchased from Bulk Powders online, Germany. The MC was purchased from Sigma-Aldrich Chemie GmbH, Taufkirchen, Germany. The moisture content of the starch was 13.98 ± 0.17% (n = 3) with a protein content of 0.27% (n = 1) in the dry mass. The egg-white protein had a moisture content of 6.96 ± 0.04% (n = 3) and a protein content of 83.42% (n = 1) in the dry mass. The soy protein isolate had a moisture content of 6.79 ± 0.21% (n = 3) and a protein content of 88.75% (n = 1) in the dry mass. The protein and moisture contents were measured following the American Association of Cereal Chemistry international standards (AACCi) 46-16 and 44-01, respectively. All material analyses were performed in triplicates.

2.2. Material preparation

With an increasing concentration of MC, 5 mixtures were prepared for each material system. For both material systems, the ratio of starch to protein was kept to 85:15 to show an equitable composition comparable to wheat flour constituents (Goesaert et al., 2005; Jekle et al., 2016). Two hydration levels were used, one hydration level for each material system. For the EWP material systems, a hydration level of 35.48% was used of the total mass ratio. Moreover, for the SPI material systems, a hydration level of 50% was used of the total mass ratio. Based on the dry ingredients, 0.5, 1.0, 2.0, and 3.0% of MC were added. Table 1 shows the mixtures composition for the used material systems. Moreover, to keep the ratio of dry ingredients to water content constant, the wheat starch was replaced by the MC amount for both material systems. A z-type kneader was used at 63 rpm to prepare the mixtures. A 1 min pre-mixing step was used to mix the dry ingredients before adding the distilled water. After adding the distilled water, the mixtures were kneaded for 10 min. Thereafter, the mixtures were removed from the kneading bowl and directly placed into the printing cartridges then covered using PARAFILM (Bemis Company Inc., Wisconsin, USA). The cartridges were rested at room temperature for 15 min during the preparation of the printer's extruder. All materials were prepared three times and for each preparation, the 3D printing and measurements were performed in triplicates.

2.3. 3D printing setup

A X400 V3 printer (German RepRap GmbH, Feldkirchen, Germany) was used to print the starch-based material systems. The printer was coupled with a simplify3D slicing software (simplify3D, Ohio, USA) for the generation of the machine G-code files. In addition, the printer was equipped with 2 cameras (side and top views) for analyzing the printing quality of any food printing inks (Fahmy et al., 2020). Considering the paste extruder, we used one miniature progressive cavity pump (PCP) purchased from ViscoTec GmbH, Töging, Germany. The PCP extruder (Vipro-head3) has a flow rate rating of 0.3–3.3 mL/min depending on the printing settings as well as the viscoelastic properties of the extruded materials. Finally, for the on-board layer-based stabilization of the

Table 1
Mixtures composition for both material systems composed of wheat starch-egg white protein and wheat starch-soy protein.

Material system	MC concentration	Wheat starch		Protein		Methylcellulose		Distilled water	
		Mass ratio (%)	Amount (g)	Mass ratio (%)	Amount (g)	Mass ratio (%)	Amount (g)	Mass ratio (%)	Amount (g)
EWP	0.0%	54.84	42.50	9.68	7.50	0.00	0.00	35.48	27.50
EWP	0.5%	54.52	42.25	9.68	7.50	0.32	0.25	35.48	27.50
EWP	1.0%	54.19	42.00	9.68	7.50	0.65	0.50	35.48	27.50
EWP	2.0%	53.55	41.50	9.68	7.50	1.29	1.00	35.48	27.50
EWP	3.0%	52.90	41.00	9.68	7.50	1.94	1.50	35.48	27.50
SPI	0.0%	42.50	42.50	7.50	7.50	0.00	0.00	50.00	50.00
SPI	0.5%	42.25	42.25	7.50	7.50	0.25	0.25	50.00	50.00
SPI	1.0%	42.00	42.00	7.50	7.50	0.50	0.50	50.00	50.00
SPI	2.0%	41.50	41.50	7.50	7.50	1.00	1.00	50.00	50.00
SPI	3.0%	41.00	41.00	7.50	7.50	1.50	1.50	50.00	50.00

printed closed-cell foams, a variable output power 150 W near-infrared (NIR) spot heater was used. The heating power was controlled through pulse width modulation (PWM) which was mapped to a 10 V DC output of the printer. The detailed printing setup and pre-printing calibration can be found in our previous study concerning printing quality analysis for starch-based materials (Fahmy et al., 2020).

2.4. Lattice designs

To develop a hardness-targeted design and prediction model for 3D printing, we used 3 closed-cell foam designs based on a 3D point lattice system. The 3 foam forms were formulated based on a cubic lattice design with spherical bubbles. Hereby, the 3 closed-cell foam structures were designed, FEM simulated and 3D printed to investigate and validate the foam's structural independency of deformation in the elastic regime (Gibson, 1989; Gibson and Ashby, 1999; Zghal et al., 2002). As shown in Fig. 1a, a simple cubic design SC with 8 bubbles, a body-centered cubic design BCC with 9 bubbles, and a face-centered cubic design FCC with 14 bubbles were designed and modeled using SolidWorks (Dassault Systèmes, Vélizy-Villacoublay, France). The SC design incorporates 8 bubbles on the corners of the cubic lattice (Dunlap, 2018; Galperin, 2014). The BCC and FCC designs also incorporate 8 bubbles on the corners in addition to 1 in the center and 6 on the faces of the cubic lattice, respectively. All structural models were designed, FEM simulated, and 3D printed at 5 porosity levels of 0, 2.5, 5, 10, and 15% by increasing the bubbles' diameter while keeping the printed volume constant. The 3 bubble configurations were printed in a cubic unit cell volume $V_{unit\ cell}$ of 8 cm^3 with a surface area of 400 mm^2 and a height of 20 mm, Fig. 1b. To develop and validate the hardness design model, the bubble configurations were also designed with a surface area of 1600 mm^2 and 6400 mm^2.

Furthermore, 3 main parameters were used for the parametric modelling of each cubic lattice design. One independent design parameter which is the cubic unit cell volume $V_{unit\ cell} = 8$ cm^3 and two dependent design parameters which are the segment length l_s (distance between two consecutive corner bubbles) and the spherical bubble diameter d_{bubble}. The dependent design parameters were computed according to a set of trigonometric equations, depending on the printed cell volume, to avoid protrusion and coalescence of the air bubbles. To determine the permissible range of the dependent parameters (l_s and

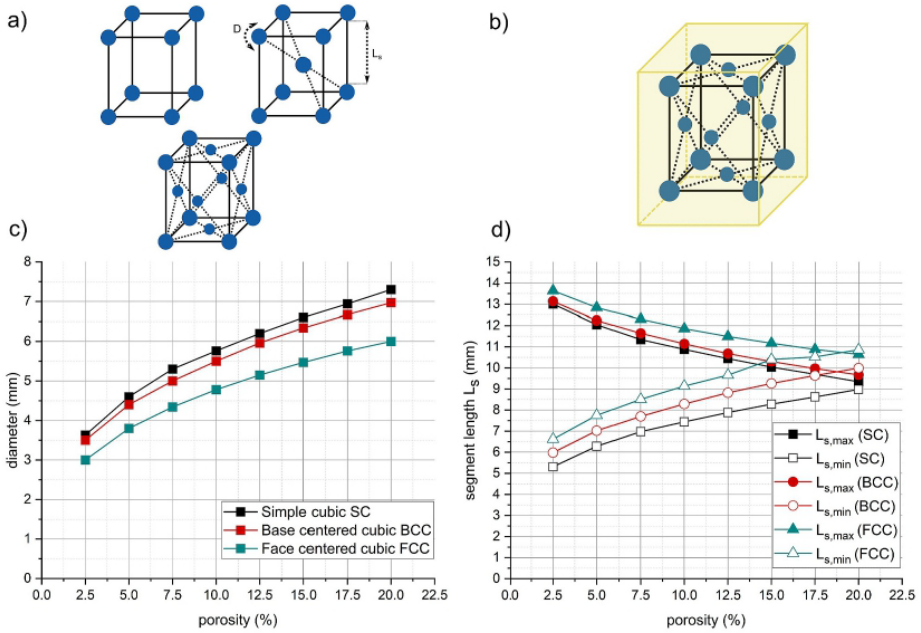

Fig. 1. Design and parameter definition of cubic lattice structures: a) schematic illustration of simple cubic SC, body-centered cubic BCC, and face-centered cubic FCC designs; b) schematic illustration of a face-centered cubic FCC unit lattice structure; c) bubble diameter of cubic designs for an 8 cm^3 unit cell cube; d) minimum and maximum permissible segment lengths of cubic designs for an 8 cm^3 unit cell cube.

d_{bubble}) with respect to the chosen unit cell volume, the nozzle diameter d_{nozzle} which is 840 μm was considered in the calculations of the dependent parameters. For all configurations, the bubble diameter was calculated as a function of the printed unit cell volume as well as the targeted porosity P and the number of bubbles N (the configuration indicator). The bubble diameter was computed according to the following equation: $d_{bubble} = 2^* \sqrt[3]{\frac{3^* V_{unit\ cell}{}^* P^* 10^{-2}}{4\pi^* N}}$ (2.1).

The maximum segment length was estimated for all configurations to avoid protrusion of the bubbles outside the printed cube and was calculated according to the following equation: $l_{s,max} = \sqrt[3]{V_{unit\ cell}} - 2d_{nozzle} - d_{bubble}$ (2.2). To enumerate, the maximum segment length must lie within the 2 radii of bubbles, 2 bubble wall thicknesses, and a side of the printed cube. The minimum segment length was considered to avoid coalescence or merging of the bubbles. For the SC design, the segment length must not decrease than the wall thickness of 2 bubbles as the bubbles are located only on the lattice corners. The minimum segment length for the SC bubble configuration was computed using the following equation: $l_{s,min} = 2d_{nozzle}$ (2.3). Since the BCC configuration features a central bubble equidistance from all corner bubbles, the segment length must not decrease to allow the coalescence of the corner bubbles with the central bubble. Therefore, the minimum segment length was computed according to the following equation: $l_{s,min} = 2(d_{nozzle} + 2d_{bubble})/\sqrt{3}$ (2.4). Considering the FCC configuration, in addition to the corner bubbles, there are 6 bubbles located in the center of the cube faces. Consequently, the segment length must not decrease to allow the coalescence of the corner bubbles with the face-centered bubbles. Thus, the minimum segment length for the FCC configuration was calculated according to this equation: $l_{s,min} = 2(d_{nozzle} + 2d_{bubble})/\sqrt{2}$ (2.5).

We computed the bubble diameter, maximum, and minimum segment lengths for the 3 design configurations with respect to the selected porosities. The computation was carried out for a cubic unit cell volume of 8 cm^3. The determination of the maximum and minimum segment lengths was carried out to establish the permissible length selection range for each design with respect to the porosity and printed volume. Illustrated in Fig. 1c, for all bubble configurations, the area between the maximum and minimum segment length which is considered as the permissible region for the segment length selection to avoid bubble protrusion and coalescence for a given unit cell volume. The intersection of the maximum and minimum lengths marks the design limitation for length selection where to increase this limit, one must increase the unit cell volume. Finally, Fig. 1c shows the decrease of bubble diameter between the SC, FCC, and BCC designs which is attributed to the increase in the bubble amount for a chosen porosity level.

Following the parametric modelling of the 3 designs, the closed-cell structures were modeled using SolidWorks (Dassault Systèmes, Vélizy-Villacoublay, France). For each of the 3 closed-cell designs, 2 models were created. One model for the cube (at 100% infill) and another for the spherical bubble configuration. The obtained general and specific equations for the bubble configurations were defined in SolidWorks to specify the relationship and boundaries between the bubble diameter, segment length and cube volume. As shown in Fig. 2a, to model the closed-cell structures, an assembly file was created and both designed models (cube and bubble configuration) were imported. Moreover, the bubble configuration was centered inside the cube and a combine function was applied to subtract the spherical bubbles from the cube model. Consequently, a closed-cell structure was created containing spherical air bubbles where the porosity and bubble configuration are defined using the obtained equations.

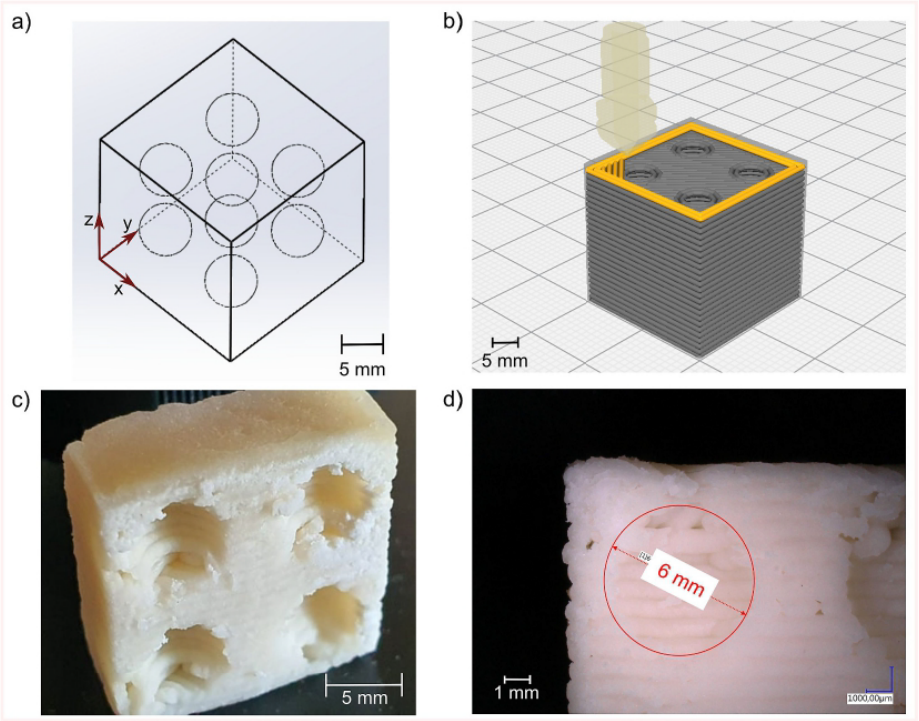

Fig. 2. 3D model and printed structures using hydrated wheat starch-soy protein mixture: a) 3D design of closed-cell spherical bubbles in SC configuration; b) sliced model and printing path of a structure with SC bubble configuration; c) 3D printed structure with SC bubble configuration at d_{bubble} = 6 mm and l_s = 10 mm. d) bubble diameter measurement using light microscopy.

2.5. Rheology, printability, and material selection

An AR-G2 rheometer (TA instruments, New Castle, USA) was used to characterize the viscoelastic properties of the printed mixtures (Table 1) using a combination of oscillatory and shear measurements. All rheological measurements were done using a DIN concentric cylinders geometry with a conical rotor of 14 mm radius and a 1 mm gap to the housing wall and bottom surface. A strain sweep was conducted to determine the linear viscoelastic region (LVER). In addition, we used frequency sweep measurements at a strain of 0.01% to obtain the complex shear, storage, and loss moduli of the mixtures. Flow measurements between the range of 0.01 and 100/s was applied to characterize the shear thinning behavior of both material systems with respect to the MC concentration. All measurements were conducted at a constant temperature of 21 °C through a Peltier plate system. All printed mixtures were measured in triplicate.

To develop a phenomenological regression model for foam hardness design of 3D printed constructs, we decided to select one material which presents the best printing performance compared to the other mixtures (Table 1). A good printing performance would ensure good geometrical and structural stability for maintaining bubble perseverance during printing and to reduce the uncertainty in the output porosity. Considering the printability assessment of the material systems, an on-board image analysis approach was applied. This approach consists of two cameras (top and side views) which are coupled with an image analysis algorithm for characterizing the overall post-printing quality in terms of geometrical stability and viscoelastic inherited defects. The top and side view cameras are used to monitor geometrical and defect parameters on printed one-layer lines and multi-layer stacks. The used camera-based approach was presented in our previous study regarding a quality analysis approach for starch- and cereal-based materials (Fahmy et al., 2020). All measurements were printed in triplicate.

2.6. Mechanical testing

A texture analyzer type TA. TX. plus (Stable Micro Systems Ltd, Godalming, UK) was used to measure the hardness and textural properties of the printed closed-cell foam configurations. For all TPA experiments, a 50 Kg measuring cell was used. A double compression test was applied at a trigger force of 0.05N and a test speed of 0.5 mm/s. All measurements were conducted at room temperature of 18 ± 2 °C. To measure the printed samples of 400 mm^2 surface area, the compression tests were performed using an uncoated 25 mm cylindrical probe. For the printed samples of 1600 and 6400 mm^2, a 50 mm circular platen was used. All printed samples were compressed to 10% of their original height and the measured forces were recorded with respect to the change in distance. Moreover, from the force-displacement behavior of the compression and decompression cycles, the hardness (N) was obtained as the peak force of the first compression cycle. Finally, the texture measurements were done in triplicates.

2.7. Near infrared NIR heating

For stabilizing the printed closed-cell foam configurations, an on-board NIR spot heater (Optron GmbH, Garbsen, Germany) was used. The NIR heater is composed of a single NIR lamp and a focusing reflector. It has a spot diameter of 6 mm at a focal length of 17 mm. A layer-based heating approach was used as the heating process isn't controllable in parallel to the printing process. Thus, after printing each layer, the heating process takes place then the printing of the consecutive layer is resumed. The 17 mm height between the heater and printed layers was kept constant for all layers. Since the 6 mm heating spot diameter is smaller than the surface area of the printed structures, a square function for movement was implemented to heat the layer's surface area uniformly (Fahmy et al., 2021). The square function has a period equivalent to the spot diameter to avoid heating overlap of the same area. To include the base material's response in the hardness-targeted model, the variation and manipulation of the material's properties was conducted using a variable thermal stabilization technique. The variation of thermal stabilization was accomplished using a constant heating power of 32% and a variable heater movement speed according to the material infill. Consequently, a variable absorbed energy occurs, inducing different thermal transitions in the printed material and thus, promoting variable mechanical properties for the base material. Furthermore, this was performed to ensure a constant moisture content (measured according to AACCi 44-01 standard) independent of the porosity and to vary the young's modulus of the bulk material (section 3.1).

2.8. FEM modelling and simulation

To simulate the hardness of the closed-cell foam structural configurations, we used ANSYS Workbench 2020 R1 (ANSYS, Inc., Pennsylvania, USA). The SolidWorks models were converted to a Parasolid extension format and imported to ANSYS DesignModeler. A mesh sensitivity analysis (not shown) was performed on tetrahedrons simplex category elements on the modeled unit cell structure where the elements (size and count) were chosen after convergence of the results. The designed models were discretized using a maximum mesh size of 800 μm that gave more than 130000 tetrahedron elements for a designed unit cell volume of 8 cm^3. For all simulations, a transient structural analysis was chosen. As a general solution setup for the modeled configurations, the bottom surface of the structures was taken as a fixed boundary. Moreover, the top surface of the structures was taken as a displacement boundary where the load was applied. A 10% double compression deformation with a 0.5 mm/s vertical velocity was implemented on the top surface corresponding to the applied TPA measurements. The models were solved using a time step of 0.5 s for a total double compression time of 20 s. A Poisson's ration of 0.1 was applied for all simulations. The applied young's modulus was chosen depending on the applied thermal stabilization speed and porosity which is further clarified in section 3.1. The measurements to obtain the material properties (density and Young's modulus) for the updated model under quasi-static conditions at room temperature and a low-strain rate of 0.025 1/s. Finally, for the development of the hardness formula a cost function was not considered for the optimization of the design parameters. The dependency of the FEM model on each design parameter was simulated (section 3) through a parametric sweep. This approach was chosen to characterize the dependency of hardness on each design parameter which would serve better for textural elucidation as well as when designing the model and material selection for 3D printing applications. The FEM analysis was done using a 64-bit, 3.00 GHz Intel® Core™ i7-9700F CPU, 32 Gb RAM, NVIDIA GeForce RTX 2060 super GPU, and Windows 10 Professional computer.

2.9. Data analysis and hardness model development

The computation of equations, data analysis and regression fitting for the simulated and mechanically tested closed-cell foams were done using MATLAB R2020a (MathWorks, Massachusetts, USA) and OriginPro 2020 (OriginLab Corporation, Massachusetts, USA). Moreover, Fig. 3 presents a schematic diagram for the hardness model development. First, material selection was performed based on the analysis of printing behavior and quality (Fahmy et al., 2020). Second, the Young's modulus was varied using a selected heating speeds at 100% infill and measured using the TPA. The obtained Young's moduli were used to simulate the hardness of the closed-cell structures and compare the results with analytical findings. Third, by obtaining comparable results, the dependency of hardness on the Young's modulus, porosity, and sample volume was simulated. Fourth, regression analysis was used to determine the hardness model. Finally, the hardness model was validated using 3D printing and TPA measurements.

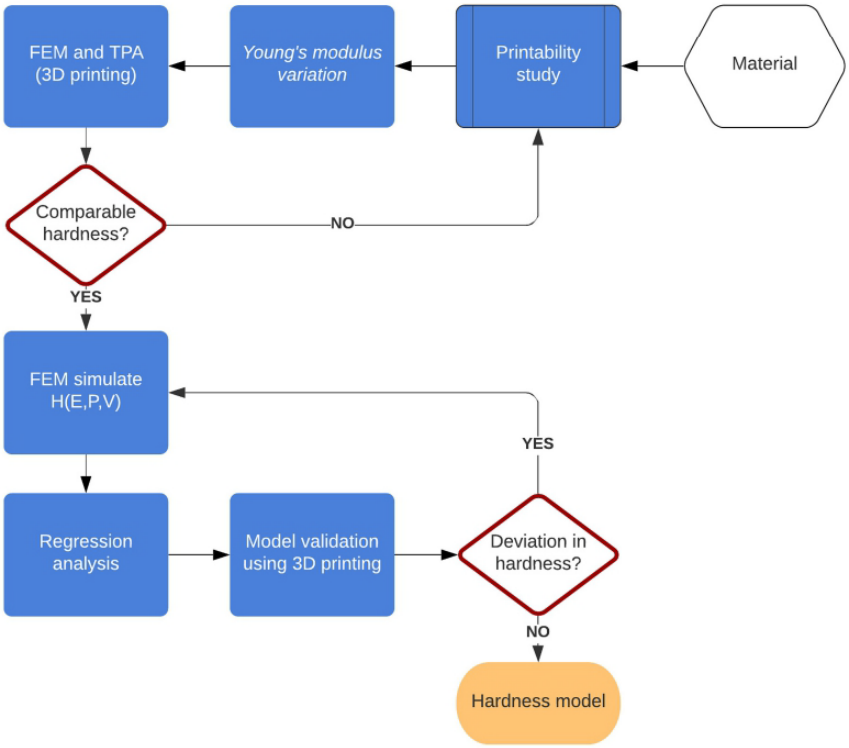

Fig. 3. Flowchart illustrating the development process of the hardness model.

3. Results and discussion

3.1. Process control for material manipulation and thermal stabilization

To select the base material for printing the closed-cell foam configurations, we first measured the rheological properties of the different mixtures (Appendix A). The oscillatory tests showed a linear increase in the overall complex shear modulus at a frequency of 10 Hz for both material systems with the increase in MC concentration ($R^2 = 0.98$). The egg white protein containing mixtures showed higher levels of storage and loss moduli compared to the soy protein containing mixtures. Based on that increase, theoretically, the increase in structural stability after printing was possible as the gain in the complex modulus meant an increment in resistance to the applied hydrostatic pressure and capillary forces (Fahmy et al., 2018, 2019b, 2020; Liu et al., 2019b; M'Barki et al., 2017). From the printing results, a better structural stability was not observed for both material systems with the increase in MC concentration as shown in Fig. 4. This can be contributed to the increase in the flow behavior index for both material systems with the increase in MC concentration (Appendix A). According to literature, an increase in the flow behavior index leads to an increase in the applied shear rate (inducing an increase in structural deformation) during extrusion which is justified by the Weissenberg-Rabinowitsch correction of the Newtonian drag flow for non-parabolic velocity profiles (Morrison, 2001).

Considering both material systems, minor levels of viscoelastic induced defects like over-, under-extrusion, and drag effect (Fahmy et al., 2020) were observed (Appendix A). As shown in Fig. 4b, the soy protein containing material systems showed a stable height with respect to the increasing number of layers. On the other hand, the egg-white protein containing material systems showed slumping behavior with the increase in the number of deposited layers. Consequently, the wheat starch-soy protein material system without the addition of MC was chosen for the printing of the closed-cell foam configurations.

The textural properties of the printed closed-cell foam structures as well as their stress-strain behavior in the elastic regime are dependent on the variability of the moisture content and the base material's Young's modulus. Thus, to reach a point comparison between the different porosity levels, the moisture content must remain constant for all porosities while the variability in the Young's modulus can be accounted for in the FEM simulation. By keeping the moisture content constant, the influence of the material properties and, in this specific study, the Young's modulus can be presented in the hardness prediction model. Maintaining a constant layer-based heating speed leads to a decrease in moisture content in the printed foam at increasing porosities as shown in Fig. 5b. This is due to the decrease in the amount of deposited material while the output heating energy is kept constant.

For obtaining a constant moisture content of the printed foams, we developed a heating speed modulation function with respect to the foam porosity. The heating power was kept constant as mentioned in section 2.7. For the reduction of printing time, grid structures with 90% porosity were printed instead of the closed-cell configurations as the moisture content is dependent on the relative density and independent of the foam structure. The heating speed was varied from 9 mm/s (540 mm/min) to 15 mm/s (900 mm/min) with a step size of 2 mm/s (120 mm/min) and the moisture content of the printed grid structures was recorded as shown in Fig. 5a. The moisture content increased with the increase in heating speed as the amount of energy received by the structures was reduced. Furthermore, to obtain a relation between the moisture content m and heating speed v, we fitted the increase behavior with a linear regression ($R^2 = 0.95$): $m = 0.87v + 18.98$ (3.1). From the obtained regression, we observed a change in heating speed of $v = 1.06\ mm/s$ representing a 1% change in the moisture content. Moreover,

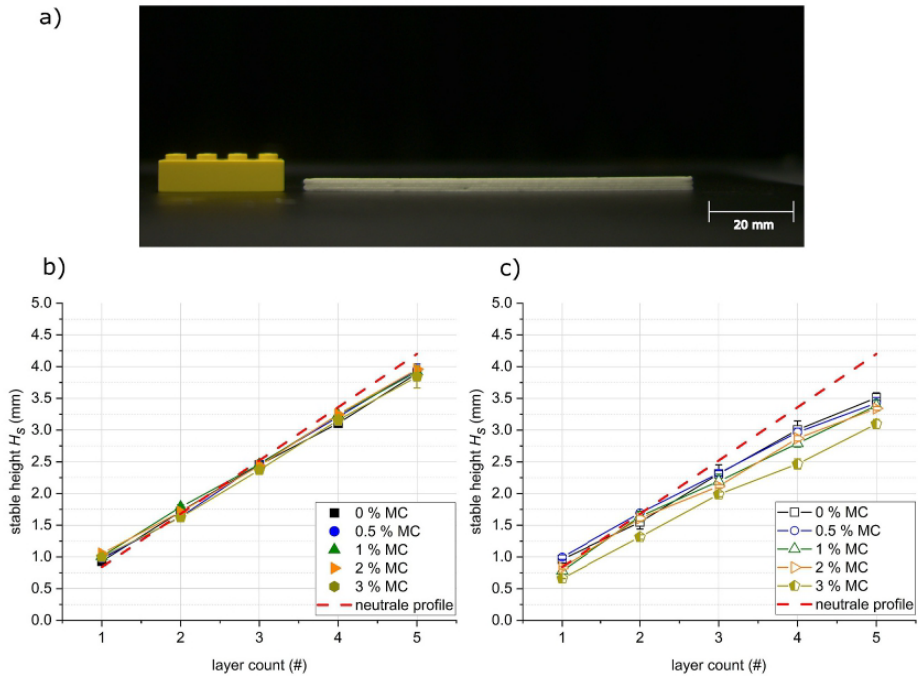

Fig. 4. Printability analysis of hydrated wheat starch soy protein and wheat starch egg-white protein with different MC concentrations using on-board cameras: a) side view of printed wheat starch-soy protein with 0% MC (3 layers); b) analyzed stable height of wheat starch-soy protein mixtures with 5 MC concentrations (n = 3); c) analyzed stable height of wheat starch-egg white protein mixtures with 5 MC concentrations (n = 3).

as shown in Fig. 5b, the moisture content was measured at a constant speed with respect to the change in porosity to develop a relation between porosity P or infill $I = 100 - P$. Consequently, a porosity-dependent heating speed modulation function was obtained: $v = \frac{100-P-182.65}{-6.36}$ (3.2). By using the obtained heat speed modulation function, an average moisture content of 47.99 ± 0.10% was achieved for the closed-cell configurations at all chosen porosity levels as shown in Fig. 5b. From the development approach of this speed calibration method, only the overall moisture content of the printed structures was considered. Thus, the moisture content gradient over the structure thickness which occurs due to the heat transmission through multiple layers was not considered for this study.

3.2. Textural analysis and simulation in the linear elastic regime

The Young's modulus is varied throughout the experiments to simulate 3D printing of different material systems. With using the heating speed modulation function, the overall moisture content was kept constant (section 3.1). Consequently, the Young's modulus was changing due to the varying heat transitions of starch and protein with the different applied heating energies. This presents an approach for varying the base material properties while keeping the material constituents the same. The heating speeds (shown in Table 2) were calculated for the selected porosity levels using equation (3.2). To measure the Young's modulus at variable heating speeds, 100% infill cubes were printed with the same unit cell volume as the foam configurations (section 2.4). The calculated heating speeds were applied to the printed cubes (n = 3) to simulate different heat induced material transitions. Then, the Young's modulus of the 100% infill cubes was measured using the TPA. The double compression force-distance behavior was converted to the engineering stress and engineering strain using the sample surface area and change in height, respectively. Presented in Table 2, the Young's modulus of the base material at the applied heating speeds was obtained as the rising slope of the first compression cycle.

Fig. 6a shows the obtained Young's modulus with respect to the applied heating speeds. Exponential decay of the Young's modulus was observed with the increase in heating speed. A heating speed-dependent Young's modulus modulation function was obtained by using an exponential regression ($R^2 = 0.98$) presented by the following equation: $E = (1.31 * 10^{12})e^{-v/3.5.7} + 66.37$ (3.3). The obtained equation was used as a determinant of the base material's Young's modulus depending on the printed porosity and can be used for the modulation of the Young's modulus with the selected heating speed. As this equation represents the base material's Young's modulus, it doesn't serve as a determinant of the closed-cell foam's Young's modulus. Consequently, the obtained Young's moduli were used as the materials' moduli in the FEM simulation to simulate the hardness with respect to the used heating speed.

Achieving comparable results between the FEM simulations and 3D printing is the foundation for the digital design and modulation of textures with respect to the material properties, porosity, and geometry constraints. For the designed porosities of 0, 2.5, 5, 10, and 15% of the 3 closed-cell foam configurations (SC, BCC, and FCC), the obtained Young's moduli were applied in the FEM simulation. In Fig. 6b, the simulation results showed an exponential decrease in hardness with the increase in porosity. There was no observed dependency of hardness on the cubic lattice bubble configuration. Also, the hardness behavior showed no dependency on the segment length between the bubbles (Gibson, 1989; Gibson and Ashby, 1999). TPA measurements of the 3D printed foams at the different design porosities showed the same exponential decrease behavior of hardness as the FEM simulation. The obtained hardness for the printed configurations and porosities range from an average of 17.20 ± 2.40 to 1.86 ± 0.45 N at 0 and 15% porosity levels, respectively. The deviation between printing and simulation, yet the same observed decrease behavior, can be attributed to the inherited

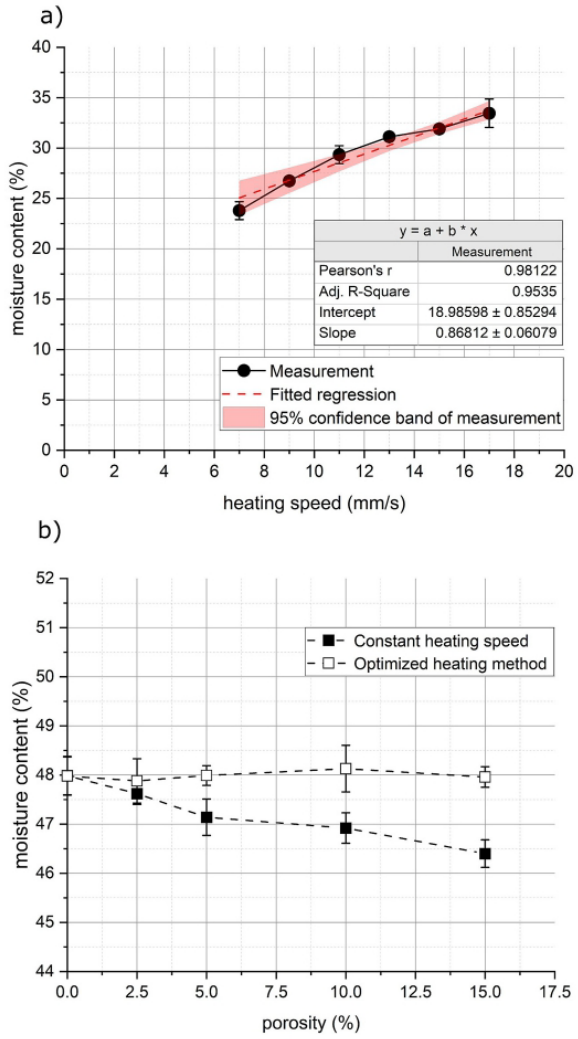

Fig. 5. Porosity-dependent moisture control of printed structures: a) moisture content in relation to the applied heating speed; b) obtained moisture content while using a constant heating speed versus using porosity dependent heating speed approach.

Table 2
Calculated heating speeds for the different porosities to obtain a porosity-independent moisture content in addition to the measured Young's modulus of the base material at 100% infill for the design porosities of the closed-cell foam configurations (n = 3).

Calculated heating speed v		Measured material Young's modulus E
(mm/s)	(mm/min)	(kPa) at P = 0%
13.00	780	524.0 ± 45.5
13.39	803	248.4 ± 20.0
13.78	827	180.3 ± 4.7
14.57	874	92.8 ± 7.2
15.36	921	74.4 ± 1.7

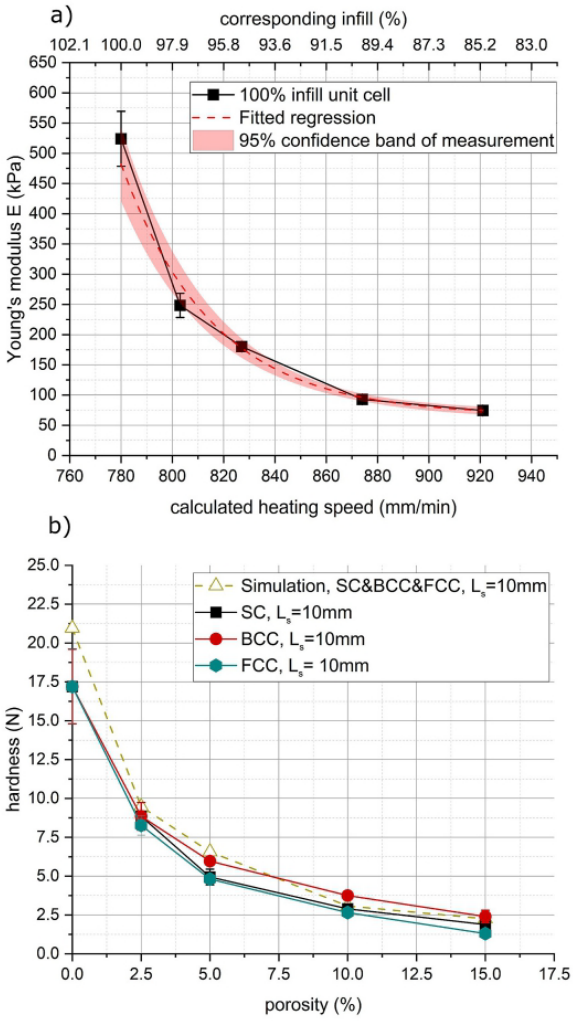

Fig. 6. TPA measurement and FEM simulation of Young's modulus and hardness in the elastic region under quasi-static conditions using double compression at 10% deformation; a) measured Young's modulus of 100% infill unit cells at 5 calculated heating speed levels; b) measured and simulated hardness of cubic designs with variable porosities and elastic moduli with a constant segment length of 10 mm.

structural defects propagated from the 3D printing and heating uncertainties. In addition, printing and heating induced irregularities can affect the geometrical accuracy and the resultant porosity, which are not addressed in this study. Most important, Fig. 6b shows that through the Young's modulus modulation technique during 3D printing, comparable hardness levels can be achieved to reflect the FEM simulations.

3.3. Hardness targeted texture design

The main objective of this study was to develop a hardness-targeted formula for 3D printing applications which can be used for hardness determination or prediction. The hardness design equation was developed under a set of measurement and boundary conditions. First, to generalize the hardness design equation for all 3D printed closed-cell structures, the regression was confined to the elastic regime. This is due to the configuration-dependent stress-strain behavior in the plastic

plateau and densification regimes which few preliminary results showed (results not shown). Second, the developed hardness design equation was based on 10% uniaxial compression under quasi-static conditions at low strain rates. Third, the hardness relations with the design parameters were obtained through FEM simulations, then verified using 3D printing and in-line modulation of the Young's modulus coupled with mechanical TPA measurements. And finally, since a configuration independency of foam was found (section 3.2), all simulations were performed on the SC bubble lattice configuration.

Obtaining a HT-PFM for 3D printing which represents the hardness of a unit cell $H_{unit\ cell}$ with respect to the 3 design parameters which are the used material's Young's modulus E, the porosity P, and the printed unit cell volume $V_{unit\ cell}$ was accomplished on several steps or development levels. First, we obtained a relation between the base material's hardness and Young's modulus irrespective of porosity and at a constant volume and surface area of 8 cm^3 and 400 mm^2, respectively. The hardness was simulated at 0% porosity while conducting a parametric sweep for the Young's modulus in 10 data points obtained from equation (3.3). By simulating the variation of the Young's modulus, a linear increase in hardness occurred with the increase in Youngs' modulus. The hardness was observed to increase from 2.97 to 19.28 N at a range of Young's modulus from 74.35 to 482.14 kPa, respectively. We used a linear regression ($R^2 = 1$) to present the relationship between hardness and Young's modulus: $H_{400\ mm^2} = 0.04E - (2.49 * 10^{-12})$ (3.4). By substituting equation 3.3 into 3.4, we obtained a material dependent relation between the output hardness and 3D printing heating speed: $H_{400\ mm^2} = (5.22 * 10^{-14})e^{-s/35.7} + 2.66$ (3.5).

Second, after obtaining the dependency of the hardness on the material's Young's modulus, we incorporated the dependency on the foam porosity at a constant unit cell volume and surface area of 8 cm^3 and 400 mm^2, respectively. As shown in Fig. 7a, the hardness was simulated at variable porosities ranging from 0 to 60% while incorporating the porosities used in the 3D printing trials (section 3.2). Similarly, the hardness was simulated using a parametric sweep for the Young's modulus in 10 data points obtained from equation (3.3). Then, linear regressions ($R^2 = 1$) were used to fit the hardness and Young's modulus relation at the simulated porosities as shown in Fig. 7a. In Fig. 7b, the derivative of

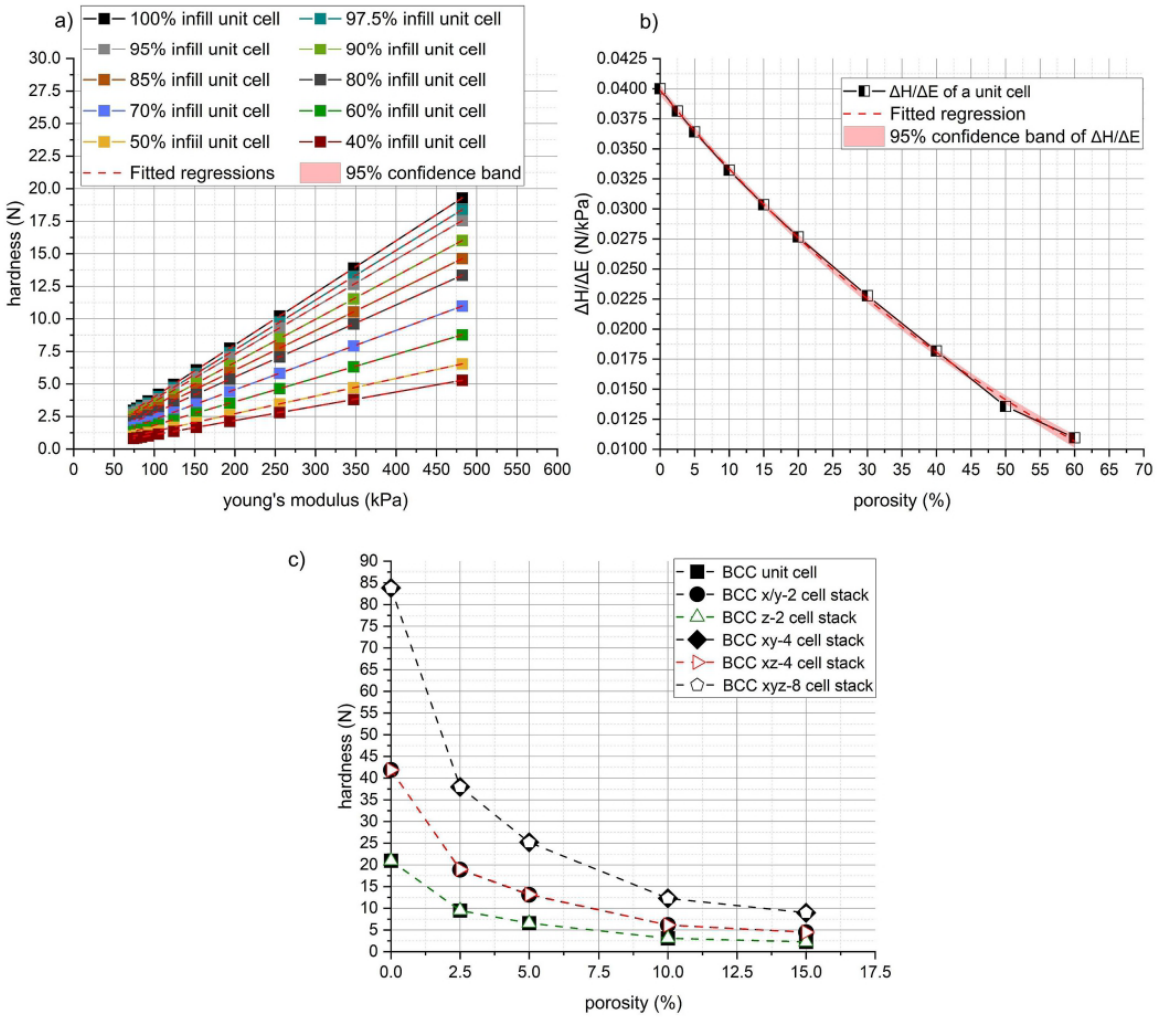

Fig. 7. Regression analysis for obtaining a hardness PFM with Yong's modulus and foam porosity as predictors: a) linear regression analysis of simulated hardness of body-centered cubic unit cell ($R^2 = 1$); b) exponential decay regression of the derivative of simulated hardness with respect to Young's modulus ($R^2 = 0.99$); c) simulated hardness of body-centered cubic BCC bubble design with increasing number of unit cells in x-, y-, and z-axes.

hardness with respect to the Young's modulus was calculated for all porosities. This presents the decrease in the rate of change of hardness with the Young's modulus with respect to the increase in porosity. Moreover, an exponential decrease was observed in the rate of change of hardness. Shown in Fig. 7b, we used an exponential regression to fit the obtained derivative of hardness ($R^2 = 0.99$): $\frac{\Delta H_{unit\ cell}}{\Delta E} = 0.055e^{-P_{70.76}} - 0.015$ (3.6). By substituting equation 3.6 into 3.4, the dependency of hardness on the material's Young's modulus and printed porosity was obtained: $H_{unit\ cell} = (3.8 * 10^{-8}) - 0.015E + 0.055Ee^{-P_{70.76}}$ (3.7).

Third, to obtain a generalized regression HT-PFM, we had to include the influence of the unit cell volume on the hardness of the 3D printed structures. Thus, we simulated the influence of volume increase on hardness by stacking unit cell of equivalent volume (8 cm^3) in x-, y-, and z-directions. The simulation was implemented while increasing the bubble diameter to keep a constant porosity level while increasing the volume. As shown in Fig. 7c, it was observed that the increase in the number of cells in the z-direction had no influence on the hardness. To enumerate, there was no observed influence of the model's thickness on the hardness. On the contrary, as illustrated in Fig. 7c, we observed that the increase in unit cells in x- and y-direction lead to an increase in the structural hardness at all porosity levels. Specifically, the simulation showed that hardness is dependent on the effective reaction surface area were the structural deformation takes place. Therefore, the influence of the unit cell volume shouldn't be considered, but rather only the influence of the effective area as the hardness is independent on unit cell thickness while dependent on the effective area.

Forth and finally, we included the influence of the unit cell area on the hardness in the regression model. In Fig. 8, 3 area data points of 400, 1600, and 6400 mm^2 were added to the previous simulation to illustrate the hardness dependency on the 3 design parameters represented by the unit cell area, the material's Young's modulus, and the porosity. Then,

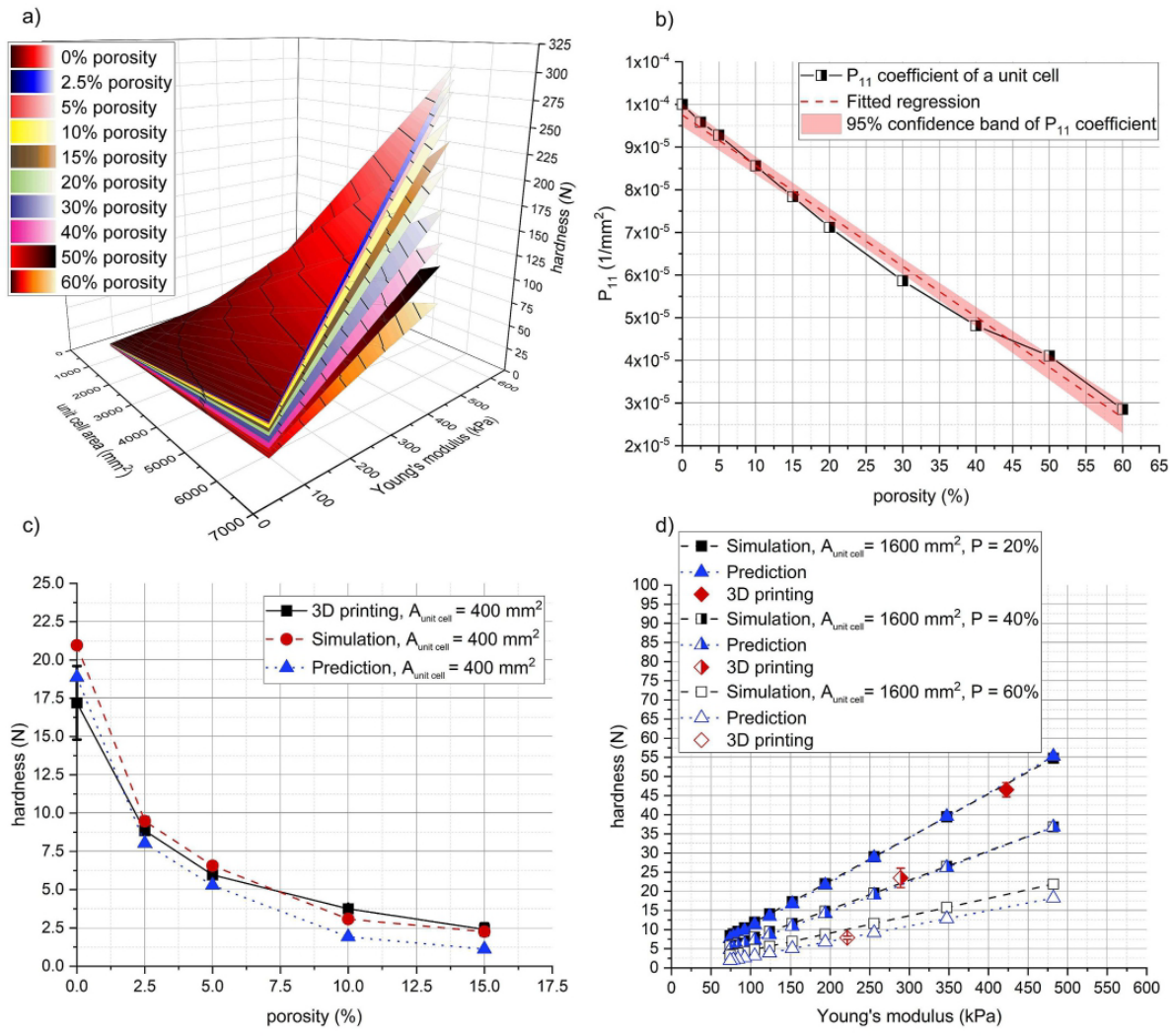

Fig. 8. Regression analysis for obtaining a hardness phenomenological foam model PFM with Yong's modulus, foam porosity, and unit cell area as predictors: a) simulated hardness of body-centered cubic with variable porosity; Young's modulus, and unit cell area; b) linear regression of the rate of change of hardness with respect to the change in the product of Young's modulus and unit cell area with variable porosity ($R^2 = 0.98$); c) measured, simulated, and model predicted hardness at variable porosities with constant unit cell area $A_{unit\ cell} = 400\ mm^2$; d) measured, simulated, and model predicted hardness at variable Young's moduli, porosities of $P = 20, 40, 60\%$, and at a constant unit cell area of $A_{unit\ cell} = 1600\ mm^2$.

polynomial surface fitting ($R^2 = 0.98$) was used to fit the relationship between hardness, Young's modulus, and cell area for the different porosities in the form of $H_{cell} = p_0 + p_{10}A_{unit\ cell} + p_{01}E + p_{20}A^2_{unit\ cell} + p_{11}EA_{cell}$ (3.8). Shown in Fig. 8b, we obtained the partial derivative of hardness with respect to the product of the Young's modulus and the unit cell area for all porosity levels. Considering the other polynomial coefficients, an average was taken with respect to all porosity levels. Moreover, as shown in Fig. 8b, a linear regression ($R^2 = 0.98$) was used to characterize the decrease in the partial derivative with the increase porosity: $p_{11} = \frac{\Delta H_{unit\ cell}}{\Delta E \Delta A_{unit\ cell}} = (9.75 * 10^{-5}) - (1.82 * 10^{-6})P$ (3.9). By substituting equation 3.9 into 3.8, we obtained a generalized HT-PFM for the hardness-based design, modulation and prediction of 3D printed textures: $H_{unit\ cell} = -1.23 + (8.24 * 10^{-5})A_{unit\ cell} + (7.1 * 10^{-4})E + (1.15 * 10^{-8})A^2_{unit\ cell} + (1.2 * 10^{-6})EPA_{unit\ cell}$ (3.10).

To investigate the performance of the obtained hardness formula, the same design parameters obtained in section 3.2 were used to predict the hardness obtained from the FEM simulation and the mechanically tested 3D printed closed-cell foams. Fig. 8c shows the performance of formula 3.10 when used as a hardness predictor compared to the simulation and 3D printing. In addition, we used the regression model to design the hardness for a unit cell area of 1600 mm^2 at 3 porosity levels of 20, 40, and 60% with variable Young's modulus. As illustrated in Fig. 6d, we simulated the foam hardness for the same input parameters used in the design model which showed similar hardness results with small deviations at high porosity levels or low hardness levels. For further model characterization, we printed BCC closed-cell foam structures at the same unit cell area of 1600 mm^2 at the same 3 porosity levels (20, 40, and 60%) to verify the hardness obtained from the regression model as well as the FEM simulation that is illustrated in Fig. 8d. The structures were printed at 3 Young's modulus values of 442.7, 289.0, and 221.6 kPa for porosity levels of 60, 40, and 20, respectively. The variation of the Young's modulus was performed according to the moisture content and the Young's modulus modulation approach described in section 3.1. As shown in Fig. 8d, the hardness of the 3D printed closed-cell structures coincided with the hardness obtained from the regression model and the FEM simulations at the selected design and material parameters.

As a result, the developed HT-PFM presented in formula 3.10 represents a relation of hardness dependency on the printed material's Young's modulus, unit cell area, and porosity. According to the obtained results and comparisons, the regression model can be used for parametric design targeting specific hardness for 3D printed closed-cell food foams by controlling the material's Young's modulus, printed area, and porosity. Solutions for the printed geometry $A_{unit\ cell}$, porosity P, and material design E tailored for a specific required hardness can be achieved by solving the regression models as in indeterminate linear Diophantine equation with lower and upper bounds on variables using well established algorithms.

4. Conclusion

In this study, we developed a model for the design and prediction of hardness for 3D printed closed-cell foams. The model development was achieved using a complete 3D texturing method coupled with FEM simulations. This 3D printing method incorporates on-board thermal stabilization technique which allows targeted heat induced material transitions for the manipulation of the material's mechanical properties (Fahmy et al., 2021). The hardness model was developed in the elastic deformation regime at quasi-static loading conditions using simulations in relation to the material's Young's modulus, porosity, and printed surface area. The Young's modulus of the base material can be actively controlled using the developed in-line NIR heating technique. Furthermore, in the elastic regime, results showed no relation between the designed closed-cell configuration, printed volume and hardness. A linear increase in hardness was observed with respect to the increase of the base material's Young's modulus. Finally, the performance of the obtained relation showed comparable results to the FEM simulations and the 3D printed structures. Using the obtained hardness relation combined with the Young's modulus tailoring thermal technique, specific closed-cell foam structures can be designed for targeted hardness grades.

Credit author statement

A.R. Fahmy: Methodology, Investigation, Formal analysis, Resources, Data curation, Writing – original draft, Visualization. **U.T. Vogt:** Investigation, Formal analysis, Data curation. **M. Jekle:** Methodology, Conceptualization, Funding acquisition, Writing – review & editing, Supervision. **T. Becker:** Conceptualization, Funding acquisition.

Declaration of competing interest

The authors declare that they have no known competing financial interests or personal relationships that could have appeared to influence the work reported in this paper.

Acknowledgments

This research was funded by the Deutsche Forschungsgemeinschaft (DFG, German Research Foundation) - 405072578.

Appendix

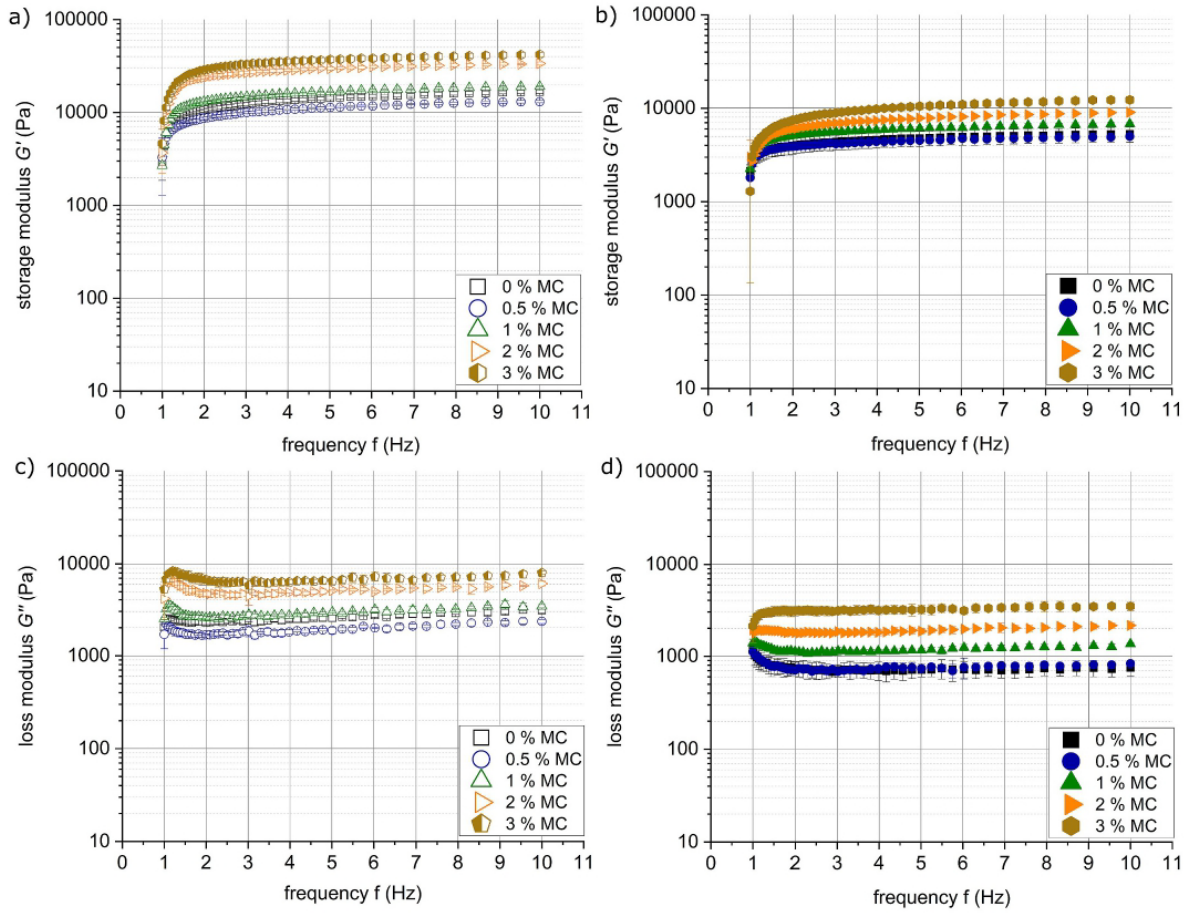

Appendix Fig. 1. Frequency sweep of the material systems containing egg-white protein and soy protein at different MC concentrations with a frequency range of 1–10 Hz: a) storage modulus of the material containing egg-white protein; b) storage modulus of the material containing soy protein; c) loss modulus of the material containing egg-white protein; d) loss modulus of the material containing soy protein.

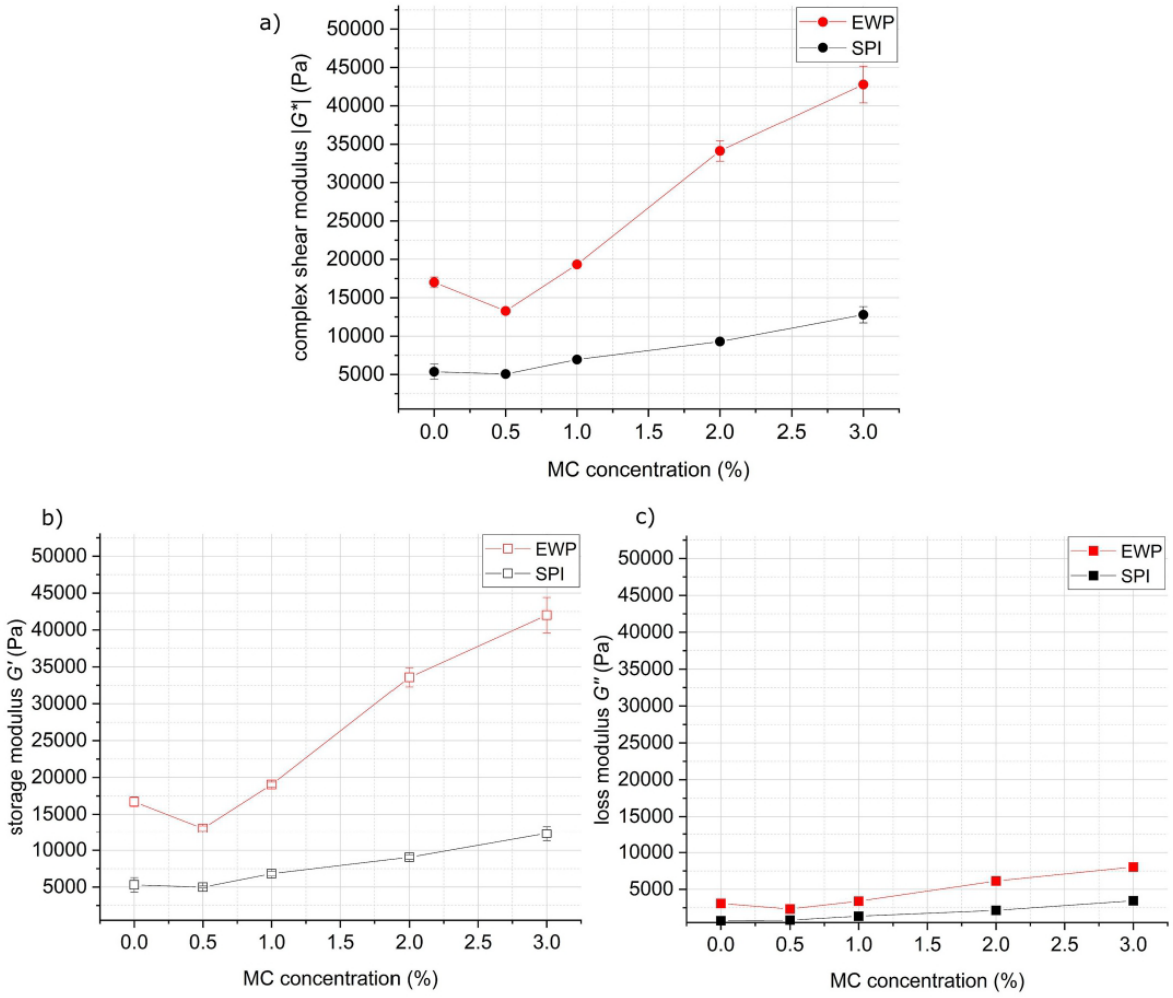

Appendix Fig. 2. Frequency sweep extracted rheological properties at 10 Hz of the material systems containing egg-white protein and soy protein with respect to the MC concentration: a) complex shear modulus of the egg-white protein (EWP) materials versus the soy protein (SPI) materials; b) storage modulus of the egg-white protein materials versus the soy protein materials; c) loss modulus of the egg-white protein materials versus the soy protein materials.

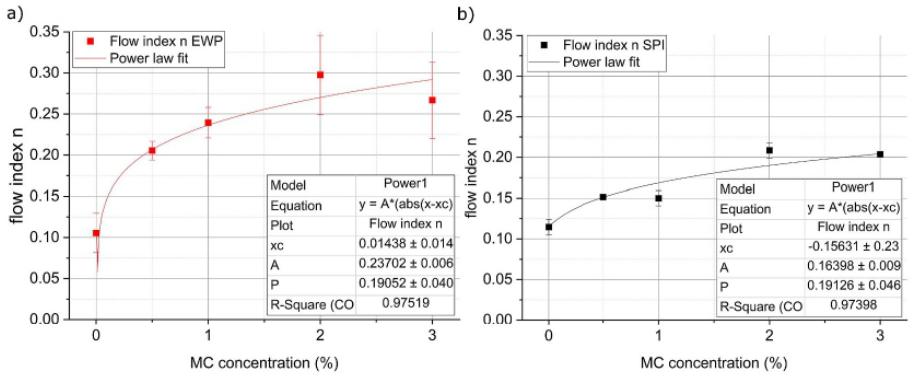

Appendix Fig. 3. Flow behavior index of the material systems containing egg-white protein and soy protein with respect to the MC concentration: a) power law fit of the flow index for the material containing egg-white protein; b) power law fit of the flow index for the material containing soy protein.

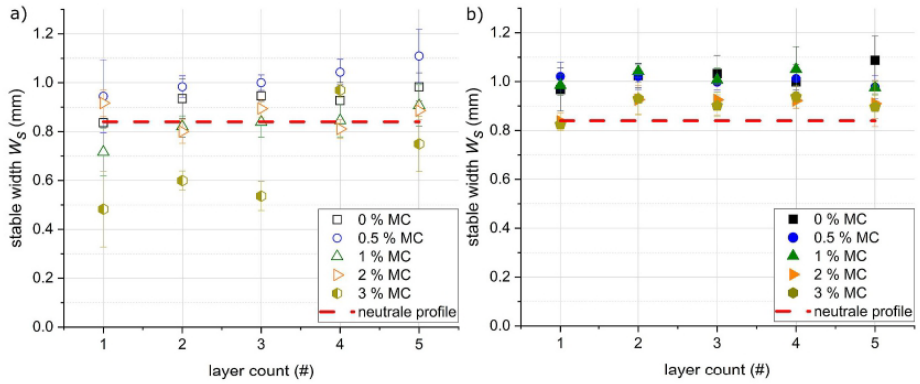

Appendix Fig. 4. Printability analysis of hydrated wheat starch-soy protein and wheat starch-egg white protein with different MC concentrations using top-view camera: a) analyzed stable width of wheat starch-soy protein mixtures with 5 MC concentrations (n = 3); b) analyzed stable width of wheat starch-egg white protein mixtures with 5 MC concentrations (n = 3).

References

Attenburrow, G.E., Goodband, R.M., Taylor, L.J., Lillford, P.J., 1989. Structure, mechanics and texture of a food sponge. J. Cereal. Sci. 9, 61–70. https://doi.org/10.1016/S0733-5210(89)80024-4.

Chen, J., Rosenthal, A., 2015. Food texture and structure. In: Modifying Food Texture: Novel Ingredients and Processing Techniques. Elsevier Ltd., pp. 3–24. https://doi.org/10.1016/B978-1-78242-333-1.00001-2

Derossi, A., Caporizzi, R., Paolillo, M., Severini, C., 2020a. Programmable texture properties of cereal-based snack mediated by 3D printing technology. J. Food Eng. 289, 110160. https://doi.org/10.1016/j.jfoodeng.2020.110160.

Derossi, A., Paolillo, M., Caporizzi, R., Severini, C., 2020b. Extending the 3D food printing tests at high speed Material deposition and effect of non-printing movements on the final quality of printed structures. J. Food Eng. 109865. https://doi.org/10.1016/j.jfoodeng.2019.109865.

Dunlap, R.A., 2018. Novel microstuctures for solids. In: Acta Universitatis Agriculturae et Silviculturae Mendelianae Brunensis.

Fahmy, A., Becker, T., Jekle, M., 2018. 3D Printing of cereal-based materials: on the relation between rheology and printability. In: AACCI Annual Meeting Cereals & Grains 18 (London).

Fahmy, A.R., Amann, L.S., Dunkel, A., Frank, O., Dawid, C., Hofmann, T., Becker, T., Jekle, M., 2021. Sensory design in food 3D printing – structuring, texture modulation, taste localization, and thermal stabilization. Innovat. Food Sci. Emerg. Technol. 72, 102743. https://doi.org/10.1016/j.ifset.2021.102743.

Fahmy, A.R., Becker, T., Jekle, M., 2020. 3D printing and additive manufacturing of cereal-based materials: quality analysis of starch-based systems using a camera-based morphological approach. Innovat. Food Sci. Emerg. Technol. 63, 102384. https://doi.org/10.1016/j.ifset.2020.102384.

Fahmy, A.R., Becker, T., Jekle, M., 2019a. 3D Printing of starch-based systems: morphological imaging and flow behavior characterization of multiple stage extrusion through a rheometry imitation approach. In: 33rd EFFoST International Conference (Rotterdam, Netherlands).

Fahmy, A.R., Becker, T., Jekle, M., 2019b. Flow behavior analysis for 3D printing of starch- based systems : morphological imaging and multiple stage extrusion characterization through a rheometry imitation approach. In: 33rd EFFoST International Conference (Rotterdam, Netherlands).

Galperin, Y., 2014. Introduction to Modern Solid State Physics.

Gao, J., Wang, Y., Dong, Z., Zhou, W., 2018. Structural and mechanical characteristics of bread and their impact on oral processing: a review. Int. J. Food Sci. Technol. 53, 858–872. https://doi.org/10.1111/ijfs.13671.

Gibson, L.J., 1989. Modelling the mechanical behavior of cellular materials. Mater. Sci. Eng. A 110, 1–36. https://doi.org/10.1016/0921-5093(89)90154-8.

Gibson, L.J., Ashby, M.F., 1999. Cellular-Solids-Structure-and-Properties-Cambridge-Solid-State-Science-Series-.pdf.

Goesaert, H., Brijs, K., Veraverbeke, W.S., Courtin, C.M., Gebruers, K., Delcour, J.A., 2005. Wheat flour constituents: how they impact bread quality, and how to impact their functionality. Trends Food Sci. Technol. 16, 12–30. https://doi.org/10.1016/j.tifs.2004.02.011.

Guessasma, S., Babin, P., Valle, G. Della, Dendievel, R., 2008. Relating cellular structure of open solid food foams to their Young's modulus: finite element calculation. Int. J. Solid Struct. 45, 2881–2896. https://doi.org/10.1016/j.ijsolstr.2008.01.007.

Guessasma, S., Nouri, H., 2015. Compression behaviour of bread crumb up to densification investigated using X-ray tomography and finite element computation. Food Res. Int. 72, 140–148. https://doi.org/10.1016/j.foodres.2015.03.038.

Guo, C.F., Zhang, M., Bhandari, B., 2019. A comparative study between syringe-based and screw-based 3D food printers by computational simulation. Comput. Electron. Agric. 162, 397–404. https://doi.org/10.1016/j.compag.2019.04.032.

Jang, W., Kraynik, A.M., Kyriakides, S., 2008. On the Microstructure of Open-Cell Foams and its Effect on Elastic Properties, vol. 45, pp. 1845–1875. https://doi.org/10.1016/j.ijsolstr.2007.10.008.

Jekle, M., Mühlberger, K., Becker, T., 2016. Starch-gluten interactions during gelatinization and its functionality in dough like model systems. Food Hydrocolloids 54, 196–201. https://doi.org/10.1016/j.foodhyd.2015.10.005.

Jonkers, N., Dommelen, J.A.W. Van, Geers, M.G.D., 2020. Experimental characterization and modeling of the mechanical behavior of brittle 3D printed food. J. Food Eng. 278, 109941. https://doi.org/10.1016/j.jfoodeng.2020.109941.

Kim, H.W., Bae, H., Park, H.J., 2017. Classification of the printability of selected food for 3D printing: development of an assessment method using hydrocolloids as reference material. J. Food Eng. 215, 23–32. https://doi.org/10.1016/j.jfoodeng.2017.07.017.

Le Tohic, C., O'Sullivan, J.J., Drapala, K.P., Chartrin, V., Chan, T., Morrison, A.P., Kerry, J.P., Kelly, A.L., 2018. Effect of 3D printing on the structure and textural properties of processed cheese. J. Food Eng. 220, 56–64. https://doi.org/10.1016/j.jfoodeng.2017.02.003.

Lille, M., Nurmela, A., Nordlund, E., Metsä-Kortelainen, S., Sozer, N., 2018. Applicability of protein and fiber-rich food materials in extrusion-based 3D printing. J. Food Eng. 220, 20–27. https://doi.org/10.1016/j.jfoodeng.2017.04.034.

Liu, Y., Yu, Y., Liu, C., Regenstein, J.M., Liu, X., Zhou, P., 2019a. Rheological and mechanical behavior of milk protein composite gel for extrusion-based 3D food printing. LWT (Lebensm.-Wiss. & Technol.) 102, 338–346. https://doi.org/10.1016/j.lwt.2018.12.053.

Liu, Z., Bhandari, B., Prakash, S., Mantihal, S., Zhang, M., 2019b. Linking rheology and printability of a multicomponent gel system of carrageenan-xanthan-starch in extrusion based additive manufacturing. Food Hydrocolloids 87, 413–424. https://doi.org/10.1016/j.foodhyd.2018.08.026.

M'Barki, A., Bocquet, L., Stevenson, A., 2017. Linking rheology and printability for dense and strong ceramics by direct ink writing. Sci. Rep. 7, 1–10. https://doi.org/10.1038/s41598-017-06115-0.

Morrison, F.A., 2001. Understanding Rheology, eighteenth ed. Oxford University Press, New York.

Paolillo, M., Derossi, A., Van Bommel, K., Noort, M.W.J., Severini, C., 2021. Rheological properties, dispensing force and printing fidelity of starchy-gels modulated by concentration, temperature and resting time. Food Hydrocolloids 117. https://doi.org/10.1016/j.foodhyd.2021.106703.

Park, S.M., Kim, H.W., Park, H.J., 2019. Callus-based 3D printing for food exemplified with carrot tissues and its potential for innovative food production. J. Food Eng. https://doi.org/10.1016/j.jfoodeng.2019.109781, 109781.

Pereira, T., Barroso, S., Gil, M.M., 2021. Food texture design by 3D printing: a review. Foods 10, 320. https://doi.org/10.3390/foods10020320.

Phuhongsung, P., Zhang, M., Devahastin, S., 2020a. Influence of surface pH on color, texture and flavor of 3D printed composite mixture of soy protein isolate, pumpkin, and beetroot. Food Bioprocess Technol. 13, 1600–1610. https://doi.org/10.1007/s11947-020-02497-8.

Phuhongsung, P., Zhang, M., Devahastin, S., 2020b. Investigation on 3D printing ability of soybean protein isolate gels and correlations with their rheological and textural properties via LF-NMR spectroscopic characteristics. LWT (Lebensm.-Wiss. & Technol.) 122, 109019. https://doi.org/10.1016/j.lwt.2020.109019.

Robin, F., Dubois, C., Curti, D., Schuchmann, H.P., Palzer, S., 2011. Effect of wheat bran on the mechanical properties of extruded starchy foams. Food Res. Int. 44, 2880–2888. https://doi.org/10.1016/j.foodres.2011.06.041.

Sun, J., Peng, Z., Zhou, W., Fuh, J.Y.H., Hong, G.S., Chiu, A., 2015. A review on 3D printing for customized food fabrication. Procedia Manuf. 1, 308–319. https://doi.org/10.1016/j.promfg.2015.09.057.

Sun, J., Zhou, W., Yan, L., Huang, D., Lin, L. ya, 2018. Extrusion-based food printing for digitalized food design and nutrition control. J. Food Eng. 220, 1–11. https://doi.org/10.1016/j.jfoodeng.2017.02.028.

Vancauwenberghe, V., Delele, M., Vanbiertvliet, J., Aregawi, W., Verboven, P., Lammertyn, J., 2018a. Model-based design and validation of food texture of 3d printed pectin-based food simulants. J. Food Eng. 231, 72–82. https://doi.org/10.1016/j.jfoodeng.2018.03.010.

Vancauwenberghe, V., Verboven, P., Lammertyn, J., Nicolaï, B., 2018b. Development of a coaxial extrusion deposition for 3D printing of customizable pectin-based food simulant. J. Food Eng. 225, 42–52. https://doi.org/10.1016/j.jfoodeng.2018.01.008.

Wang, C., Dai, S., Tanner, R.I., 2006. On the compressibility of bread dough. Korea-Australia Rheol. J 18, 127–131.

Wang, L., Zhang, M., Bhandari, B., Yang, C., 2018. Investigation on fish surimi gel as promising food material for 3D printing. J. Food Eng. 220, 101–108. https://doi.org/10.1016/j.jfoodeng.2017.02.029.

Wang, S., Austin, P., Bell, S., 2011. It's a maze: the pore structure of bread crumbs. J. Cereal. Sci. 54, 203–210. https://doi.org/10.1016/j.jcs.2011.05.004.

Wegrzyn, T.F., Golding, M., Archer, R.H., 2012. Food Layered Manufacture: a new process for constructing solid foods. Trends Food Sci. Technol. 27, 66–72.

Wilms, P., Daffner, K., Kern, C., Gras, S.L., Schutyser, M.A.I., Kohlus, R., 2021. Formulation engineering of food systems for 3D-printing applications – a review. Food Res. Int. 148, 110585. https://doi.org/10.1016/j.foodres.2021.110585.

Yang, Fanli, Zhang, M., Bhandari, B., Liu, Y., 2018a. Investigation on lemon juice gel as food material for 3D printing and optimization of printing parameters. LWT - Food Sci. Technol. (Lebensmittel-Wissenschaft -Technol.) 87, 67–76. https://doi.org/10.1016/j.lwt.2017.08.054.

Yang, F., Zhang, M., Fang, Z., Liu, Y., 2019. Impact of processing parameters and post-treatment on the shape accuracy of 3D-printed baking dough. Int. J. Food Sci. Technol. 54, 68–74. https://doi.org/10.1111/ijfs.13904.

Yang, Fan, Zhang, M., Prakash, S., Liu, Y., 2018b. Physical properties of 3D printed baking dough as affected by different compositions. Innovat. Food Sci. Emerg. Technol. 49, 202–210. https://doi.org/10.1016/J.IFSET.2018.01.001.

Zghal, M.C., Scanlon, M.G., Sapirstein, H.D., 2002. Cellular structure of bread crumb and its influence on mechanical properties. J. Cereal. Sci. 36, 167–176. https://doi.org/10.1006/jcrs.2001.0445.

2.5 Texture modulation of starch-based closed-cell foams using 3D printing: Deformation behavior beyond the elastic regime

Fahmy, A. R., Jekle, M., & Becker, T. (2022). Texture modulation of starch-based closed-cell foams using 3D printing: Deformation behavior beyond the elastic regime. Journal of Texture Studies, 1-17. https://doi.org/10.1111/jtxs.12729

Authorship contribution

A.R. Fahmy: Methodology, Investigation, Formal analysis, Resources, Data curation, Writing - original draft, Visualization. **M. Jekle**: Methodology, Conceptualization, Funding acquisition, Writing - review & editing, Supervision. **T. Becker**: Conceptualization, Funding acquisition.

Received: 7 July 2022 | Revised: 22 September 2022 | Accepted: 1 October 2022
DOI: 10.1111/jtxs.12729

RESEARCH ARTICLE

Journal of Texture Studies WILEY

Texture modulation of starch-based closed-cell foams using 3D printing: Deformation behavior beyond the elastic regime

Ahmed Raouf Fahmy[1] | Mario Jekle[2] | Thomas Becker[1]

[1]Technical University of Munich, TUM School of Life Sciences, Chair of Brewing and Beverage Technology, Research Group Cereal Technology and Process Engineering, Freising, Germany

[2]University of Hohenheim, Institute of Food Science and Biotechnology, Department of Plant-based Foods, Stuttgart, Germany

Correspondence
Ahmed Raouf Fahmy, Technical University of Munich, TUM School of Life Sciences, Chair of Brewing and Beverage Technology, Research Group Cereal Technology and Process Engineering, Freising, Germany.
Email: ahmed.fahmy@tum.de

Funding information
Deutsche Forschungsgemeinschaft, Grant/Award Number: 405072578

Abstract

3-dimensional printing is a novel processing method used for the design and manipulation of food textures. The systematic characterization and modulation of 3D printed food textures is imperative for the future design of sensory profiles using additive manufacturing. For 3D printed closed-cell food foams, the clarification of the deformation behavior in relation to design parameters is of interest for the processing of customized food textures. For this reason, we studied the deformation behavior of 3D printed and thermally stabilized closed-cell starch-based foams beyond the elastic regime. Periodic spherical bubble configurations at different porosity levels were used to modulate the deformation behavior of the printed foams. From a processing perspective, the integration of in-line thermal stabilization was used to eliminate post-processing and to control the moisture content of the starch-based system. Compression analysis combined with FEM simulations were performed to characterize the strain rate dependency of textural properties, the stress relaxation, and the foam's stress–strain behavior with respect to the design porosity and bubble distribution. Results showed that the stress relaxation is solely dependent on cell wall properties while different stress–strain regimes showed distinct dependencies on design parameters such as bubble size and distribution. Consequently, the precise control of the large deformation behavior of foods using 3D printing is challenging due to the superposition of structural and geometrical dependencies. Finally, through the presented approach, the structure-deformation relations of 3D printed closed-cell food structures are adequately described.

KEYWORDS
3D food printing, closed-cell foam, large-deformation behavior, texture design, texture modulation

1 | INTRODUCTION

Food texture design and modulation using 3-dimensional (3D) printing is based on the precise manipulation of food micro- and macro-structure. The adoption of 3D printing in the texture manipulation of foods is performed using a food layered manufacturing approach (FLM) where structures are constructed layer-by-layer. Using 3D geometrical models, 3D printing is used to construct complex structures and geometries by a layer-based deposition of the design geometrical and structural elements (Godoi et al., 2016; Lipton et al., 2010; Sun,

This article was published on AA publication on: 12 October 2022.

Peng, et al., 2015a; Sun, Zhou, et al., 2015b; Wegrzyn et al., 2012). While different 3D printing technological approaches are currently used for food processing, fused deposition modeling (FDM) is the most commonly utilized FLM technique which operates through material extrusion and deposition (ASTM-International, 2012). Moreover, FDM is applied in food printing applications such as in the modulation of food textures due to its compatibility with highly viscous food pastes (Chen et al., 2019; Derossi, Caporizzi, Paolillo, et al., 2020; Gholamipour-Shirazi et al., 2020; Liu & Zhang, 2021; Mantihal et al., 2020; Phuhongsung et al., 2020; Vancauwenberghe et al., 2018, 2019). Compared to the traditional processing of food textures, this approach enables the precise processing and fabrication of customized textures. In addition, FDM can facilitate the elucidation of textural dependencies and material-structure-processes relationships (Fahmy, Amann, et al., 2021; Fahmy, Becker, et al., 2021; Liu & Zhang, 2021; Pereira et al., 2021). By characterizing textural dependencies and deformation behavior through 3D printing, controlling the perception of food textures is possible and thus the design of sensory profiles is enabled.

The overall deformation behavior of cellular foods is defined by the base material properties, the relative density, the foam's cellular structure, and the applied structuring process. Moreover, the deformation behavior influences the mechanical and textural properties of cellular food foams. Prior to the structuring and post-processing, the food microstructure is determined through the raw materials' chemical structure and interactions as well as through the pre-processing conditions. Furthermore, the macrostructure is initially resolved and affected by the microstructure. Textures of cereals and food foams in general are scientifically defined as the manifestation and interaction of mechanical, structural, and surface properties (Szczesniak, 2002). The mechanical properties including textures of starch-based foams influences both the deformation and mastication behaviors of such cellular structures and thus affecting their sensory profile (Wang et al., 2011). The mastication process, which is correlated to the deformation behavior, influences the foam's nutritional characteristics (Takahashi et al., 2009). Therefore, controlling and designing the textural perception of starch-based cellular foams using 3D printing can be performed by the control over the base material's properties and the modulation of the foam's micro- and macro-structure.

Considering the manipulation of the cellular structure using 3D printing, many studies focus on the modulation of textures using multiple infill variations and relative densities (Derossi, Caporizzi, Oral, et al., 2020; Derossi, Caporizzi, Paolillo, et al., 2020; Lille et al., 2020; Liu et al., 2018; Pereira et al., 2021; Phuhongsung et al., 2020; Piovesan et al., 2020; Varghese et al., 2020; Zhao et al., 2021; Zhu et al., 2021). Most studies focus on the modulation and the characterization of the deformation behavior in the elastic regime. However, few articles highlight the mechanical and sensory behavior of 3D printed food structures beyond the textural properties in the elastic regime (Jonkers et al., 2020; Lille et al., 2020; Shahbazi et al., 2021a, 2021b). The study performed by Lille et al. modulated the fracture force of periodic open-cell structures (describing the cutting force needed to break the sample) by varying the 3D printed food formulation (Lille et al., 2020). Modulation of the fracture force was not performed by varying the design parameters of the cellular structures such as the design porosity and pore distribution. Moreover, the authors attempted to correlate the analytical findings with sensory analysis with respect to the printed food formulation. Jonkers et al. presented a modeling approach for predicting the full stress strain behavior of food structures printed using selective laser sintering (Jonkers et al., 2020). For the sintered dense food structures, the authors showed a 3D constitutive model which incorporates inelastic deformation and allows for high non-linearity. Furthermore, the study presented by Shahbazi et al. showed a new approach for the structuring of personalized food through the application of 3D printing of casein-based Pickering emulsion (Shahbazi et al., 2021a, 2021b). The authors studied the tribological behavior of the structured analogs through oral tribology and rheometry measurements. To conclude, extending the characterization and modulation of the structure-dependent deformation behavior in the large-strain non-linear regime in relation to the cellular design properties is essential for designing variable texture profiles through 3D printing. This importance arises as the larger-strain behavior is the main determinant of the cellular food's mastication performance and sensory perception.

This study was performed on three 3D printed closed-cell foam configurations using spherical bubbles in simple, body-centered, and face-centered cubic designs. The foam configurations were 3D printed using a starch-based material system composed of hydrated wheat starch and soy protein. The three starch-based foam configurations were printed using a cubic design of 8 cm^3 in volume, irrespective of the foam porosity. Moreover, the simple cubic design consisted of eight corner bubbles and the body-centered design consisted of eight corner bubbles with an additional bubble located at the center of the printed cubic structure. Furthermore, the face-centered design incorporated a total of 14 bubbles consisting of eight corner bubbles and six bubbles located at the center of each cube face. For this investigation, design and heating parameters were modulated for 3D printing of closed-cell structures to achieve pre-determined hardness levels (Fahmy et al., 2022). A 3D printing method for texture creation was used incorporating in-line NIR heating for moisture control and for modulating the base material's Youngs' modulus (Fahmy, Amann, et al., 2021). Measurements that were performed using analytical texture profile analysis (TPA) were compared with finite element (FEM) simulations to verify the precision of the printed structures. Also, the comparison between TPA analyses and FEM simulations was performed to investigate and eliminate any inherited geometrical defects during the printing process which might affect the textural and mechanical response during loading. First, the strain rate dependency of the textural properties was investigated at variable applied deformation rates. Second, the viscoelastic response of the 3D printed cellular structures was investigated using stress relaxation measurements with the application of the Peleg-Normand model (Peleg & Normand, 1983). Third, the large-strain deformation behavior was investigated using compressive analysis with respect to cellular design, relative density, and base material's Young's modulus. The stress–strain behavior including yielding, plateau, and densification

TABLE 1 Wheat starch-soy protein material system composition used for 3D printing of closed-cell structures

	Wheat starch		Protein		Distilled water	
Material system	Mass ratio (%)	Amount (g)	Mass ratio (%)	Amount (g)	Mass ratio (%)	Amount (g)
SPI	42.50	42.50	7.50	7.50	50.00	50.00

regimes of the 3D printed cellular structures were characterized using a phenomenological foam model (PFM) presented by Goga et al. which applies a macroscopic-level modeling approach (Goga & Hučko, 2016). Finally, structure-deformation relations were obtained with respect to the base material's properties, applied heating, and cellular design configuration and porosity.

2 | MATERIALS AND METHODS

2.1 | Raw materials

One material system composed of hydrated wheat starch and soy protein isolate was used for the 3D printing of the different closed-cell foam configurations. The soy protein isolate was purchased from Bulk Powders (Colchester, United Kingdom). The wheat starch was provided by Kröner-Stärke GmbH (Ibbenbüren, Germany). The protein and moisture contents were determined according to the methods of the American Association of Cereal Chemists international (AACCi) 46–16 and 44–01, respectively. The wheat starch had a moisture content of 13.98 ± 0.17% ($n = 3$) and a protein content of 0.27% ($n = 1$; dry mass). The soy protein isolate had a moisture content of 6.79 ± 0.21% ($n = 3$) and a protein content of 88.75% ($n = 1$; dry mass). The material analyses were performed in triplicates.

2.2 | Material preparation

To modulate and characterize the texture, deformation, and stress–strain behavior of 3D printed closed-cell structures, one starch-based mixture was used. Measurement of the printing quality and geometrical stability of the starch-based material was performed using an approach based on in-line camera-based analysis and rheological characterization which was proposed in earlier articles (Fahmy et al., 2019, 2020). The specific choice of the material formulation was based on the characterization of printing quality and performance presented in our previous study which presents an approach for designing closed-cell food foams for achieving specific hardness levels (Fahmy et al., 2022). In this study, the same material formulation is used to investigate the strain rate dependency of the textural properties for the purpose of textural modulation using 3D printing. Also, to investigate the viscoelastic response and large-strain deformation behavior and their dependency of the foam's structure as well as the foam's relative density. Hereby, we used a mixture of hydrated wheat starch and soy protein isolate (SPI). For showing a comparable composition to wheat flour constituents, the starch to protein ratio was kept to 85:15. The hydration level of the dry components was 50% of the total mass ratio (Fahmy et al., 2022). Table 1 shows the mixture composition for the used material system.

For the preparation of the starch-based mixture, a z-type kneader was used at 63 rpm. First, a pre-mixing step of 1 min was performed to mix the dry ingredients. Second, the water was added, and the mixture was kneaded for 10 min at a room temperature of 18 ± 2°C. Following the kneading process, the mixture was removed, placed directly in the printing cartridges, covered using PARAFILM (Bemis Company Inc., Wisconsin), and rested for 15 min at room temperature until the preparation of the used progressive cavity pump (PCP) extruder is completed. As the PCP extruder consists of a stator and a stepper controlled rotor, the preparation includes the assembly of both within the extruder's housing forming the progressing cavity. Directly after assembling the main extruder's components, the material-containing cartridge is attached. The starch-based material was prepared in triplicates. Furthermore, for each material preparation, 3D printing, and measurements were performed in triplicates.

2.3 | 3D printing setup and designs

For printing the starch-based closed-cell structures, an X400 V3 3D printer (German RepRap GmbH, Feldkirchen, Germany) was used. For generating the machine G-code files, simplify3D slicing software (simplify3D, Ohio) was used. All printing experiments were performed using a conical nozzle of 0.84 mm in diameter, at a printing speed of 10 mm/s, and at an extrusion width\height of 0.84 mm. A detailed description of the printing setup and the pre-printing calibration process was mentioned in our previous study which investigates the printing quality of starch-base material systems using a camera-based morphological approach (Fahmy et al., 2020). For the transport and deposition of the material, a progressing cavity pump (PCP) was used in all printing experiments (ViscoTec GmbH, Töging, Germany). The PCP (Vipro-head3) has a theoretical flow rate range of 0.3–3.3 ml/min. The flow rate of the pump depends on the printing settings as well as the rheological-viscoelastic properties and flow behavior of the printed material. Moreover, a near-infrared (NIR) spot heater (Optron GmbH, Garbsen, Germany) was used for the in-line thermal stabilization of the printed structures. The variable output 150 W spot heater is equipped with a NIR-emitter that has a peak wavelength of approximately ~0.98 μm. Through a control unit that was used as an interface between the heater and the 3D printer, the heating power is controlled through pulse width modulation (PWM). To control the heating power, the PWM was mapped to a 10 V DC output of the 3D printer. Furthermore, all printed structures were printedat room temperature

of approx. 21 ± 2.0°C and then thermally stabilized in a layer-based approach using the NIR spot heater (Fahmy, Amann, et al., 2021). Finally, a detailed description of the thermal stabilization process can be found in section 2.5.

To modulate and characterize the textural properties and the stress–strain behavior of 3D printed starch-based structures, three closed-cell foam designs were used. For generalizing the results of all analyses, all designs which were digitally constructed, and 3D printed are considered as unit-cells that can be assembled longitudinally and transversely to obtain larger closed-cell structures (Fahmy et al., 2022). For all designs, a cubic structure with a volume of 8 cm^3, a surface area of 400 mm^2 and a height of 20 mm was chosen. The three closed-cell designs were composed of spherical bubbles arranged in point-lattice configurations which are simple, body-centered, and face-centered cubic designs (Fahmy et al., 2022). The simple cubic SC design is composed of eight bubbles while the body-centered BCC and the face-centered FCC designs are composed of nine and 14 bubbles respectively. The SC design incorporates the eight bubbles on the corners of the cubic lattice. The BCC design incorporates eight corner bubbles with a central bubble located in the spatial center of the cubic structure. Furthermore, the FCC design also incorporates the eight corner bubbles like the SC and BCC designs with the addition of six bubbles located at the centers of the cubic structure's faces. For all designs, the distance between the corner bubbles was chosen to be 10 mm throughout the 3D printing trials. All cellular configurations were 3D printed at five porosity levels of 0, 2.5, 5, 10, and 15% while keeping the printed volume constant. To illustrate, the printed designs were printed at the same volume and porosity, which leads to different bubble sizes due to the difference in bubble quantity between the three configurations. Finally, the full parametric modeling of the printed designs was presented in our previous study concerning the hardness targeted design of 3D printed closed-cell foams (Fahmy et al., 2022).

2.4 | Texture profile analysis and mechanical characterizations

To characterize the deformation behavior of all printed closed-cell structures, a TA. TX. plus Texture Analyzer (Stable Micro Systems Ltd, Godalming, UK) was used. TPA tests were performed using a 50 Kg measuring cell. To apply the compression analysis on all printed structures, a 50 mm cylindrical probe was used. All measurements were conducted at room temperature of 18 ± 2.0°C. To characterize the textural properties of the closed-cell structures and their strain rate dependency, double compression tests were applied at 10% deformation, a trigger force of 0.05 N, and at variable strain rates. The double compression tests were performed at five strain rate levels which are 0.5, 1.25, 2.5, 3.75, and 5/s. To characterize the viscoelastic response of the closed-cell foams, stress relaxation measurements were performed at a strain of 0.5%. The strain was applied and kept constant for 30 s, where the force profile was measured as a function of time. For obtaining the stress–strain behavior of the closed-cell structures beyond the elastic regime, the printed structures were compressed to 80% of their original height to identify the yielding, plateau, and densification regimes. The developed force profiles were analyzed with respect to the deformation distance and time. Due to the large applied strain, the deformed cross-sectional area is required for measuring the true stress. As the in-line measurement of the deformed cross-sectional area was not possible during this study, the engineering stress was used instead of the true stress. Finally, all compression measurements were performed in triplicates.

To compute the engineering Young's modulus E_{eng} from the double compression test, the engineering stress σ_{eng} and strain ε_{eng} were obtained from the measured force-distance curves using the following equation: $\sigma_{eng}/\varepsilon_{eng} = ((F/A)/(\Delta H/H))$ (2.1), where the F is the measured force (N), A is the sample cross-sectional area (m^2), H is the sample height (m), and the ΔH is the lateral deformation (m) (Attenburrow et al., 1989; Beer et al., 2011; Roylance, 1996). From the initial engineering stress–strain linear behavior, the engineering Young's modulus E_{eng} was obtained using a linear regression with a regression coefficient higher than 0.95. The textural properties were characterized from the force-displacement curve of the double compression tests. The following attributes were determined as a function of the closed-cell bubble configuration, porosity, and the applied strain rate: hardness (H) which was defined as the first compression cycle's peak force, cohesiveness (C) which was defined as the area ratio of the second to the first compression, and resilience (R) which was defined as the ratio of energies equivalent to the ratio of decompression and compression cycles (Peleg, 2019; Szczesniak, 1963).

For elucidating the stress relaxation behavior of the printed closed-cell foam configurations, the viscoelastic response was characterized using the Peleg-Normand model (Peleg & Normand, 1983). Through the normalized relaxation curves presented by the Maxwell model for stress relaxation, the stress relaxation curves were normalized in the form of: $(\sigma_{eng\_0} * t)/(\sigma_{eng\_0} - \sigma(t)) = k_1 + k_2 t$ (2.2), where σ_{eng_0} is the initial stress (Pa), σ(t) is the instantaneous decay stress (Pa) with respect to time t (s). The k_1 (s) and k_2 are the Peleg-Normand constants. They represent the intercept and slope of the regression obtained by the normalized stress with respect to time. To further illustrate, the constant k_1 quantifies the initial rate of decay of the developed compressive stress (described as the initial rate of relaxation). Moreover, the constant k_2 describes the extent of relaxation. Which quantifies the residual stress as time tends to infinity. In this study, another calculated parameter %SR (%) was used to characterize the stress relaxation behavior of the printed closed-cell configurations (Hatcher et al., 2008). The parameter %SR provides a comparative measurement of the viscoelastic behavior at an arbitrary time: $\%SR = \left(\sigma_{eng\_0} - \sigma_{eng\_t}/\sigma_{eng\_0}\right) * 100$ (2.3), where σ_{eng_0} is the initial stress (Pa) and σ_{eng_t} is the stress at an arbitrary time t (Pa). Furthermore, %SR = 100% for an ideal viscous behavior presented by an ideal liquid while for an ideal elastic behavior of an elastic solid %SR = 0%. For this study, the %SR was calculated at time t = 20 s (Figure 1).

To characterize the compressive stress–strain behavior of the 3D printed closed-cell foam configurations, a phenomenological foam model (PFM) presented by Goga et al. was used (Goga & Hučko, 2016). Phenomenological foam models are developed using a macroscopic level modeling approach. For modeling at the

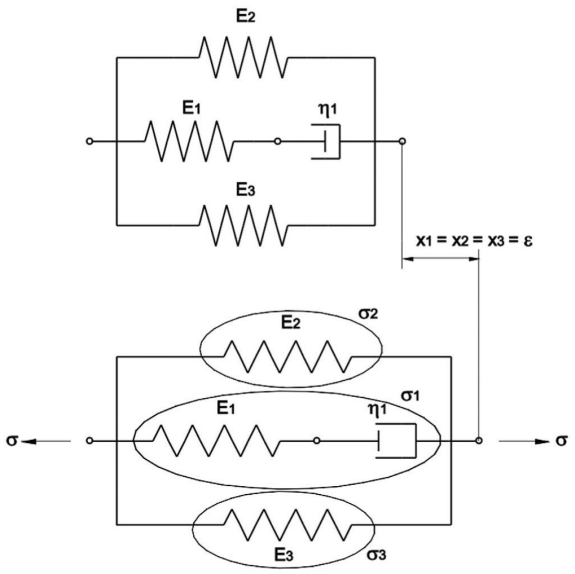

FIGURE 1 Goga PFM rheological model for cellular solids (Goga & Hučko, 2016). The serial Maxwell model (spring E_1 and damper η_1) represents the linear elastic region of the stress–strain behavior. The strain locking (plateau) and densification regimes are modeled as springs (E_2 and E_3, respectively) in parallel configuration to the Maxwell model

macroscopic level, the foam's macroscopic behavior can be elucidated by a set of constitutive equations where the foam is assumed to be a continuum (Avalle et al., 2007; Goga & Hučko, 2016; Liu & Subhash, 2004). This approach focuses on describing the deformation behavior (shape of compressive stress–strain) using appropriate mathematical descriptors during the establishment of the constitutive equations (Goga & Hučko, 2016). The PFM presented by Goga et al. (Goga PFM) is applicable for all cellular solids having the same characteristic response during compression (like foams and honeycombs) which is characterized by three regimes: a linear elastic regime, a stress plateau and a densification or strain locking region (Gibson, 1989; Gibson & Ashby, 1999). The linear elastic regime corresponds to the elastic bending of the cell walls while the plateau and strain locking (densification) regimes correspond to the plastic yielding (or elastic buckling depending on the constitutive foam material) and to the collapse of cells, respectively. The Goga PFM models each region separately using a rheological model which determines the influence of all parameters in relation to the compressive stress–strain behavior. The linear region is modeled using a Maxwell model which consists of a linear spring E_1 and a viscous damper η_1 in series. For the plateau region, a linear spring E_2 is connected in parallel to the Maxwell model. Finally, considering the densification or strain locking region, it is characterized by a strong non-linear increase behavior which is modeled as a non-linear spring E_3 in parallel to the Maxwell model. Regarding the relationship between the resultant stresses and strain(Goga & Hučko, 2016), the Goga model can be denoted as: $\sigma(\epsilon) = e^{-\left(\frac{E_1}{\eta_1}\right)\epsilon}\left(-1+e^{-\left(\frac{E_1}{\eta_1}\right)\epsilon}\right)\eta_1 + \left(E_2+\gamma(1-e^{\epsilon})^h\right)\epsilon$ (2.4). The presented model contains five parameters (E_1, η_1, E_2, γ, and h) which represents stresses and all of them are positive except the E_2 which represents the slope direction of the plateau regime. The parameter h is a dimensionless parameter which is usually four or six (Goga & Hučko, 2016). For this study, the young's modulus was characterized using the double compression tests. Thus, this study focuses on characterizing and comparing the damping coefficient η which corresponds to the yielding behavior of the foam, the plateau stiffness E_p which represents the inclination, and the densification coefficient γ. The objective is to characterize the dependency and behavior of such parameters in relation to the modulation of the base material's properties, the relative density or porosity, and the bubble configuration.

2.5 | In-line near infrared NIR heating

An in-line thermal stabilization approach was used for heat treating the printed closed-cell configurations during the 3D printing process. A NIR spot heater composed of one NIR lamp and a focusing reflector was used. A detailed description of the heater properties and interface was mentioned in section 2.3. The spot heater is equipped with a lens which resulted in a 6 mm spot diameter at a focal length of 17 mm. For all printing trials, the heat treatment was applied at the focal length of 17 mm.

A layer-based heating approach was adopted for the thermal stabilization of the printed structures (Fahmy, Amann, et al., 2021). After 3D printing of one layer, the heating process is applied then the printing of the subsequent layer is performed. As mentioned in section 2.3, the surface area of the printed structures is 400 mm^2 where the effective surface area of the NIR spot is smaller which is approx. ~113 mm^2. For this reason and to uniformly heat the surface area of the printed structures, a square function for the movement of the NIR spot was applied (Fahmy, Amann, et al., 2021). The square function has a period which is equivalent to the spot diameter, but with a phase shift of $-45°$. The function's period was chosen so that the application of heat is performed once per surface location. For all printed structures, the heating power was kept constant at 32%, regardless of the design porosity or bubble configuration. On the other hand, the movement speed of the heating spot was adjusted depending on the structure porosity to maintain the same moisture content for all printed structures. The moisture content of the printed and thermally treated structures was measured according to the AACCi 44–01 standard.

2.6 | FEM modeling and simulation

ANSYS Workbench 2020 R1 (ANSYS Inc., Pennsylvania) was used to simulate the developed stresses, deformation behavior and hardness of the designed closed-cell configurations. FEM simulations of the cellular designs were compared to TPA results to justify the precision of the printed structures (Fahmy et al., 2022). In addition, the simulations were used to highlight the differences in the developed stresses between the different bubble configurations. To simulate the

designed structures, the models were imported to the ANSYS Design-Modeler as a Parasolid extension format. For obtaining the structural deformation and hardness, a transient structural analysis was performed. Prior to the transient mechanical simulations, a mesh sensitivity analysis (results not shown) was performed on the designed unit cell structures to determine the element size and count. The analyses were performed using a tetrahedron simplex geometry where the element size and count were chosen after the convergence of the model's hardness value. For a designed model volume of 8 cm^3, the discretization was performed using a maximum mesh size of 800 μm that resulted in more than 130,000 tetrahedron elements. Regarding the transient solution setup and boundary conditions, the load was applied on the top surface of the structure as it was considered as a displacement boundary. Moreover, as an accurate representation of the TPA compression analysis, the bottom surface of the structure was taken as a fixed boundary. A 1 mm/s vertical velocity was set for the top surface or the displacement boundary while the double compression deformation was set to 10%. A total compression duration of 20 s was applied, and the models were solved using a time step of 0.5 s. The Young's modulus and density that were applied in the linear elastic model were measured using the TPA using the bulk material (without the inclusion of porosity). The measurements were performed under quasi-static conditions at room temperature of 18 ± 2.0°C and at a low strain rate of 0.025/s. The base material's Young's modulus was applied depending on the attenuation of in-line thermal stabilization speed which is clarified in section 3 (Fahmy et al., 2022). For all simulated structures, a low Poisson's ratio of 0.1 was applied to the material model. Only the linear elasticity was considered for all simulations while viscoelasticity was not considered. The transient mechanical simulations were performed using a 64-bit, 3.00 GHz Intel Core i7-9700F CPU, 32 Gb RAM, NVIDIA GeForce RTX 2060 super GPU, and Windows 10 Professional computer.

2.7 | Data analysis

The computation of equations, data analysis and regression fitting for the simulated and the mechanically tested closed-cell foams were performed using MATLAB R2020a (MathWorks, Massachusetts) and OriginPro 2020 (OriginLab Corporation, Massachusetts). Furthermore, for the regression fitting of all obtained parameters, both linear and exponential regressions were fitted and the coefficients of determination R^2 were compared. The behavior of all obtained parameters was identified by either one of the mentioned regressions depending on a higher coefficient of determination.

3 | RESULTS AND DISCUSSION

3.1 | Modulation of deformation and stress–strain behaviors

The mechanical and deformation behavior of processed elastomeric cellular foams is highly dependent on the base material properties, the geometry, and the foam's relative density (Avalle et al., 2007; Gibson, 1989; Gibson & Ashby, 1999; Jang et al., 2008; Zghal et al., 2002). Ensuring a high accuracy of the printed starch-based cellular configurations is of outmost importance for eliminating viscoelastic induced defects during printing which lead to geometrical and thus textural deviations from the designed structures. And thus, high precision is required during printing to ensure comparable and even equivalent geometry and porosity to the designed closed-cell bubble configurations. For this reason, two hierarchical stages of quality assessment were performed.

The two quality characterization stages include the printing quality characterization of the base material and the accuracy assessment of the printed porosities. First, to assess the printability of the used starch-based material, a camera-based morphological approach was used which we described in details in our previous studies (Fahmy et al., 2019, 2020). This method assesses the printability by comparing geometrical dimensions of printed structures to design parameters. Also, the method assesses key defect parameters with respect to the viscoelastic behavior of cereal- and starch-based materials. Using the mentioned approach, the printing quality of the wheat starch-soy protein (SPI) material (Table 1) used for printing the closed-cell bubble configurations was compared to other starch-based material systems in our previous study (Fahmy et al., 2022). The used SPI material formulation (Table 1), compared to the other characterized material formulations, showed in a previous study the highest geometrical accuracy and stability (Fahmy et al., 2022). Second, to assess the accuracy of the printed porosities, a FEM simulation approach was used instead of x-ray microtomography (Fahmy et al., 2022). A comparison between the hardness obtained from TPA analyses and FEM simulations is performed where comparable hardness results indicate comparable porosity levels between the designed and printed structures.

Prior to investigating the textural, deformation, and stress–strain behavior of the three designed closed-cell configurations, the hardness was measured using a double compression TPA test and compared to FEM simulations. The TPA measurements and FEM simulations were performed and compared at specific designed porosity-dependent hardness values. In our previous study regarding hardness-targeted design of 3D printed structures, we developed an equation (hardness-targeted PFM) which enables the design of printing parameters with respect to specified hardness values: $H_{unit\ cell} = -1.23 + \left(8.24 * 10^{-5}\right) A_{unit\ cell} + \left(7.1 * 10^{-4}\right) E + \left(1.15 * 10^{-8}\right) A^2_{unit\ cell} + \left(1.2 * 10^{-6}\right) EPA_{unit\ cell}$ (3.1), where $H_{unit\ cell}$ is the selected hardness for the printed structure (N), $A_{unit\ cell}$ is the effective compression area (mm^2), P is the design porosity (%), and the E is the base material's young's modulus (kPa) (Fahmy et al., 2022). To determine the accuracy of the printed porosities through comparing the hardness obtained from TPA measurements and FEM simulations, shown in Table 2, structures which exhibit a decrease in hardness with the increase in porosity were selected using equation 3.1. As mentioned in section 2.3, the printed configurations were designed with a specific constant surface area $A_{unit\ cell}$ of 400 mm^2 and five levels of porosity which are 0, 2.5, 5, 10, and 15%. Therefore, after the computation of equation 3.1, the

TABLE 2 Base material's Young's modulus computed according to equation 3.1 with the design parameters

Porosity P	Surface area $A_{\text{unit cell}}$	Selected hardness $H_{\text{unit cell}}$	Calculated material Young's modulus E
(%)	(mm^2)	(N)	(kPa) at $P = 0\%$
0	400	14	364.2
2.5	400	12	315.4
5	400	10	249.8
10	400	7	216.5
15	400	4	148.9

base-material's Young's modulus required modulation to achieve the designed hardness levels as shown in Table 2.

For all printed porosities of the designed point lattice bubble configurations, the moisture content was kept constant and the Young's modulus was modulated using a porosity dependent equation for moisture attenuation using variable heating speeds which we presented in our previous study ($R^2 = 0.95$): $v = \frac{P-82.65}{-6.36}$ (3.2), where v is the heater movement speed (mm/s) and P is the porosity of the printed structure (%) (Fahmy et al., 2022). For obtaining the mentioned equation, structures with constant design porosity were printed and the heating speed was varied between 9 and 15 mm/s with a step size of 2 mm/s. The analyzed moisture content of the printed and heated structures showed a linear increase with respect to the increase in heating speed. A linear regression was fitted to obtain the relation between the applied heating speed and the resultant moisture content. The dependency between the resultant moisture content and the applied heating speed was shown in our previous article concerning the hardness targeted design of 3D printed closed-cell foams (Fahmy et al., 2022). A change in heating speed of $v = 1.06$ mm/s per 1% change in moisture content was observed from the obtained regression. Then, the moisture content was characterized with respect variable porosities at a constant heating speed. Furthermore, by obtaining both relations and through simple substitution, the shown porosity dependent equation for the attenuation of the moisture content was formulated (Fahmy et al., 2022). For an average moisture content of 47.79 ± 0.2% for all printed porosities, the heating speed was modulated, and the Young's moduli were characterized under quasi-static conditions using double compression tests in the elastic regime (section 2.4). As shown in our previous study (Fahmy et al., 2022), an exponential decay dependency of the young's modulus on the heating speed was observed. Moreover, a heating speed-dependent Young's modulus modulation function was obtained ($R^2 = 0.98$): $E = \left(1.31 * 10^{12}\right) e^{-v_{35.7}} + 66.37$ (3.3), where E is the modulated young's modulus (kPa). From equation 3.3, the heating speeds were calculated and applied during the in-line heating of the printed structures. The calculated heating speeds were used to modulate the base material's Young's modulus.

For simulating the compressive behavior of the closed-cell foam structures, the calculated Young's moduli were used in the FEM model, depending on the simulated porosity. As shown in Figure 2, the hardness of the printed configurations at the designed porosities were characterized and compared to the FEM simulations. From the

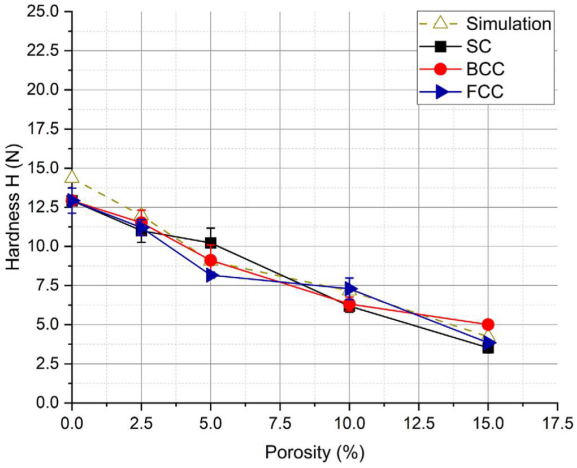

FIGURE 2 TPA measurements and FEM simulation of hardness of the 3D printed closed-cell configurations at the selected porosity levels (STD $n = 3$). Simulations of the SC, BCC and FCC configurations resulted in an equivalent hardness regression with respect to the design porosity. Thus, the presented simulation regression represents the simulation of the three closed-cell configurations

obtained results, there was no clear dependency of the hardness on the simulated or measured configuration but rather only a dependency on the porosity (Fahmy et al., 2022). This is supported by literature where the elastic deformation of cellular structures depends on the based material constituents and properties as well as the foam's relative density (Gibson, 1989; Gibson & Ashby, 1999). Both simulated and 3D printed structures showed the same decrease behavior with respect to the increase in porosity. By comparing the FEM hardness values with the characterized 3D printed structures, the average deviations for all porosity levels of the SC, BCC, and FCC were observed as 9.7 ± 3.3%, 5.5 ± 3.0%, and 6.93 ± 3.4%, respectively. The calculated deviations between simulation and printing can be related to the occurring structural defects due to heating and printing uncertainties (Fahmy et al., 2022). The inherited geometrical defects can be contributed to in-accuracies in the target porosities or in the printed volume. Finally, the relatively low deviations between 3D printing and FEM simulations show moderate accuracy in printing the designed closed-cell configurations at different porosity levels.

Elastomeric cellular foams are usually non-linear viscoelastic materials which exhibits high static and dynamic linear and viscoelastic behaviors (Alzoubi et al., 2014; Avalle et al., 2007; Gao et al., 2018; Goga & Hučko, 2016; Wu et al., 2012; Zghal et al., 2002). Moreover, most studies concerning texture modulation of 3D printed food foams do not extend their textural characterization at different strain rates (Derossi, Caporizzi, Paolillo, et al., 2020; Liu & Zhang, 2021; Pereira et al., 2021; Piovesan et al., 2020; Varghese et al., 2020). Thus, double compression tests were performed at five strain rate levels in the elastic regime to elucidate the strain rate dependent behavior of the 3D printed structures and its dependency on the structural configuration as well as the base material's young's modulus. The tests were performed for the three designed bubble configurations (SC, BCC, and FCC) where the foam's engineering Young's modulus, hardness, cohesiveness, and resilience were characterized at 10% deformation. Furthermore, to characterize the textural properties and their strain rate dependency, the tests were applied at five strain levels of 0.5, 1.25, 2.5, 3.75, and 5/s.

Figure 3 shows the porosity and strain rate dependency of the hardness and engineering Young's modulus of the BCC closed-cell configuration. Concerning the dependency of hardness and Young's modulus on the printed porosity at the strain rate level of 0.5/s, the SC, BCC, and FCC configurations showed the same decrease behavior and absolute values as verified previously using FEM simulations, as

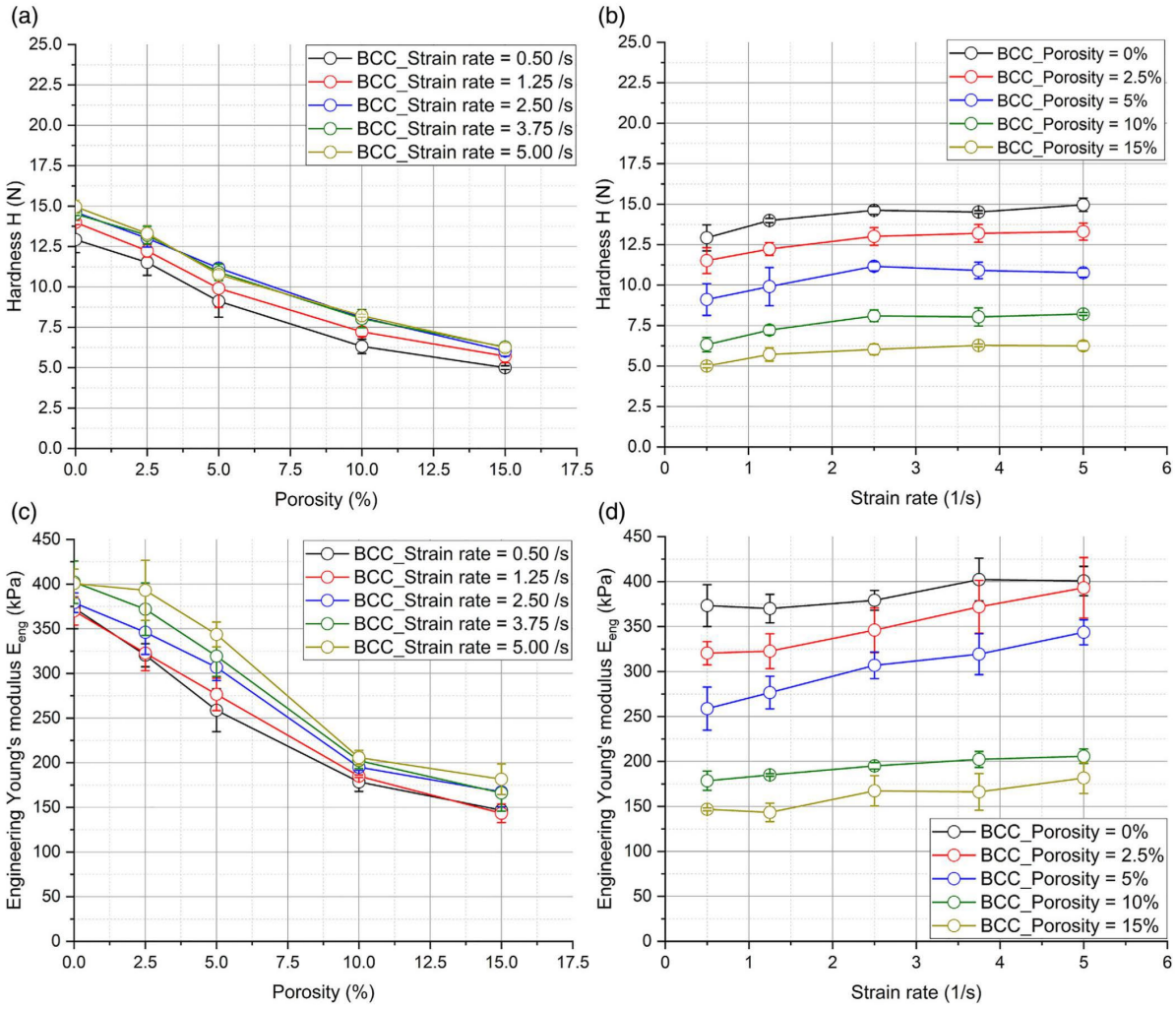

FIGURE 3 TPA measurement of porosity and strain rate dependency of the hardness and engineering Young's modulus of the body-centered cubic (BCC) bubble configuration (STD $n = 3$): (a) hardness behavior with respect to increasing porosity at different applied strain rates; (b) hardness behavior with respect to increasing strain rate at the designed porosity levels; (c) behavior of Young's modulus with respect to increasing porosity at different applied strain rates; (d) behavior of Young's modulus with respect to increasing strain rate at the designed porosity levels

illustrated in Figure 2. As shown in Figure 3a, considering the BCC configuration, an increase in the hardness decay at the different porosities was observed with respect to the applied strain rate. This can be clearly observed when plotting the hardness against the strain rate of the different printed porosities, as presented in Figure 3b. A linear increase was observed where the hardness increased from 12.9 ± 0.8 N at 0.5/s to 14.9 ± 0.4 N at 5/s for the 0% porosity while the hardness increased from 5.0 ± 0.2 N at 0.5/s to 6.3 ± 0.3 N at 5/s for the 15% porosity. The results indicate an increase of approx. ~15.5% in the hardness of the base material (0% porosity) with respect to an increase of 10 folds in the applied strain rate of deformation. At the same time, an increase of 26% was observed for the hardness of the BCC configuration at 15% porosity with respect to the same increase in the applied strain rate of deformation. Figure 3c shows a linear decrease behavior of the engineering Young's modulus with respect to the design porosity of printed closed-closed cell foams. A similar linear decrease behavior was reported by Piovesan et al. while the Young's modulus was characterized on open-cell honey comb structures (Piovesan et al., 2020). The comparable Young's modulus behavior between open- and closed-cell designs shows the independency of its decrease behavior on the pore geometry and distribution. In addition, the same behavior was observed for the SC and FCC configurations (results not shown). This eliminates the dependency of the strain rate response of hardness and engineering Young's modulus with respect to the printed configuration. As the different printed porosities are subjected to different heating speeds to modulate the base material's Young's modulus, the strain rate dependency of hardness of the base material was investigated with respect to the applied heating speed. A linear increase was observed where the hardness increased from 12.9 ± 0.8 N at 0.5/s to 14.9 ± 0.4 N at 5/s for the 13.0 mm/s heating speed corresponding to the base material of the 0% porosity while the hardness increased from 8.2 ± 0.1 N at 0.5/s to 9.8 ± 0.6 N at 5/s for the 15.4 mm/s heating speed corresponding to the base material of the 15% porosity. This indicates the same increase of approx. ~15.5% for the base material while an increase of only ~19.5% for the heating speed (15.4 mm/s) that is used for printing the structures with 15% porosity. Therefore, independent of the printed configuration, the strain rate response of hardness is dependent on the base material's mechanical properties of the cell walls superimposed by the response of the closed cells. On the contrary, the resilience and cohesiveness was observed to be dependent only on the applied strain rate where the value and increase response remained unchanged with respect to the applied heating speed, the closed-cell configuration, and the porosity. This independence of the applied heating speed can indicate that principal physiochemical transitions within the constituent components did not occur to alter the material's response Figure 4.

For characterizing the viscoelastic response of the closed-cell foam configurations, the stress relaxation spectra of the structures were investigated. The printed structures were compressed at a constant strain of 0.5% for 30 s. The developed stress profiles were recorded with respect to the relaxation time. The engineering stress-time responses were analyzed using the Peleg-Normand stress relaxation model (R^2 > 0.95) as presented previously in section 2.4. The normalized stress and model parameters were computed and compared with respect to the applied heating speed corresponding to the Young's modulus modulation of the base material. This comparison was performed to investigate the dependency of the viscoelastic response with respect to the base material's state depending on the applied NIR thermal energy. Also, the model parameters were computed and compared in relation to the printed closed-cell foam configurations at variable porosities. Consequently, the dependency of the stress relaxation response was obtained as a function of porosity and bubble lattice configuration.

Considering the stress relaxation response with respect to the applied NIR speed, the normalized stress profiles show a decrease in the linear growth with the increase in NIR heating speed, as shown in Figure 5. This indicates a decrease in the linear growth of the normalized stress with respect to the decrease in the Young's modulus of the base material (Table 2). The decrease in the linear growth of the normalized stress of the printed structures indicates an increase in the solid-like behavior with the increase of heating speed. Furthermore, the viscoelastic response decreases with the increase in heating speed and with the decrease in the base material's Young's modulus (Wu et al., 2012). Therefore, by using the in-line heating modulation method, the stress relaxation and viscoelastic response can be modulated throughout the printing process irrespective of the printed relative density.

Finally, the Peleg-Normand parameters were extracted from the slope and intercept (R^2 > 0.98) of the normalized stress profiles averaged over the number of samples ($n = 3$). To elucidate the dependency on the applied NIR heating of the base material, the parameters k_1, k_2, and %SR were plotted against the applied heating speed. As shown in Figure 6a, the %SR increases linearly ($R^2 = 0.99$) with the increase in heating speed or with the decrease in the base material's Young's modulus (Table 2). The %SR was observed to increase from 30.5 ± 0.9% at E_{eng} = 359.3 ± 13.9 kPa to 36.9 ± 3.2% at E_{eng} = 140.8 ± 3.4 kPa. This increase shows a decrease in the solid response with the increase in heating speed (lower heating energy). Which can be contributed to the decrease in mass transfer or moisture loss during heating. While most studies use the Peleg-Normand model for elucidating the stress relaxation behavior of dough, Wu et al. used the Peleg-Normand and %SR constants to study the effect of electric power of steamer on the stress relaxation of steamed breads (Wu et al., 2012). The study showed also an increase in the % SR or the solid response of the foam with respect to the steaming power. As shown in Figure 6a, both k_1 and k_2 constants of the Peleg-Normand model show a linear decrease ($R^2 = 0.99$ and $R^2 = 0.98$, respectively) with different rates in relation to the increase in heating speed. The k_1 constant was observed to decrease from 4.8 ± 0.2 s at E_{eng} = 359.3 ± 13.9 kPa to 3.3 ± 0.3 s at E_{eng} = 140.8 ± 3.4 kPa. Considering the linear decrease in k_1, the behavior indicates a decrease in the initial rate of decay of the compressive stress with the increasing heating speed. This indicates an increase in solid-like behavior and faster stress response which is also confirmed by the increase in %SR at lower applied heating speeds. Moreover, the k_2 constant was

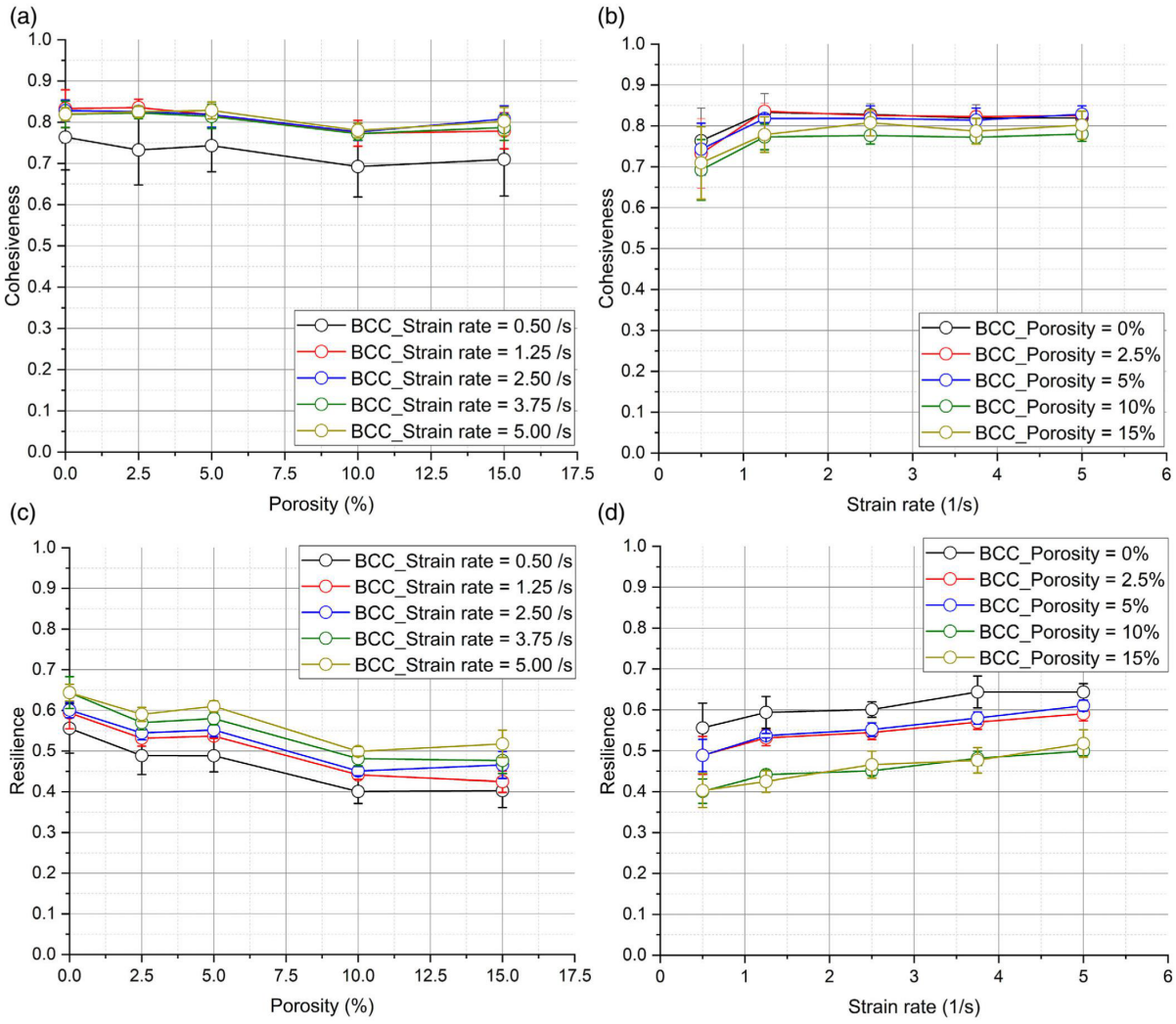

FIGURE 4 TPA measurement of porosity and strain rate dependency of the cohesiveness and resilience of the body-centered cubic (BCC) bubble configuration (STD n = 3): (a) cohesiveness behavior with respect to increasing porosity at different applied strain rates; (b) cohesiveness behavior with respect to increasing strain rate at the designed porosity levels; (c) resilience behavior with respect to increasing porosity at different applied strain rates; (d) resilience behavior with respect to increasing strain rate at the designed porosity levels

observed to decrease from 3.1 ± 0.1 at E_{eng} = 359.3 ± 13.9 kPa to 2.5 ± 0.1 at E_{eng} = 140.8 ± 3.4 kPa. Regarding the linear decrease in k_2, the rate of change is lower than that of the k_1 constant. This behavior indicates a decrease in the residual stress with respect to the decrease in Young's modulus. Finally, the results indicate that at lower heating speeds subjected to the base material, the printed material without porosity tends to possess faster response to relaxation but at the same time the residual stress of the micro-structure increases.

Regarding the dependency of the model coefficients k_1, k_2 and % SR on the closed-cell configurations and porosity levels, they showed primarily the same overall increase or decrease behavior with different decay or growth levels depending on the printed closed-cell configuration. For the SC, BCC, and FCC configurations, the initial rate of decay of the compressive stress k_1 decreases with the increase in structural porosity from 4.8 ± 0.2 s at 0% porosity to 3.1 ± 0.1 s for the SC, to 2.9 ± 0.1 s for the BCC, and to 2.9 ± 0.2 s for the FCC configuration at 15% porosity. The decrease behavior was observed to be different comparing the SC with the BCC and FCC configurations where the SC configuration shows a linear decrease (R^2 = 0.97) while both the BCC and FCC configurations show an exponential decay (R^2 = 0.99). This change of decrease behavior of the BCC and FCC configurations can be contributed to the response of the air bubbles located in the mid-section of the unit cell where the most deformation occurs contrarily to the corner distribution of bubbles in the SC configuration. The overall amount of

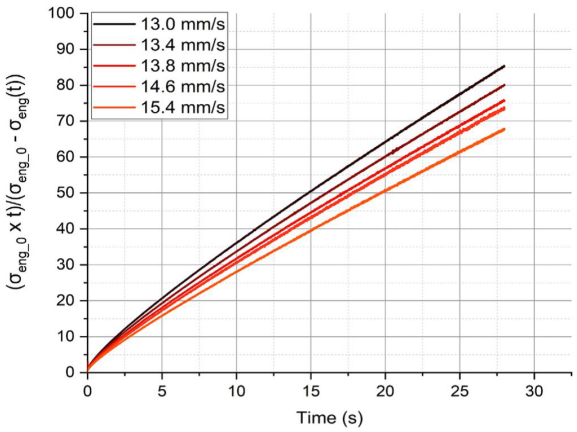

FIGURE 5 Linear regression profiles plotted using the normalized Peleg-Normand stress with respect to the stress relaxation time of the bulk material as a function of applied heating speed

decrease in the rate of decay of compressive stress indicates that the behavior of k_1 is solely dependent on the response of the base material. Regarding the mentioned findings, no literature in food research was found that attempted to study the Peleg-Normand constants in relation to the properties of highly defined pore distributions. Considering the behavior of the residual stress as denoted by k_2 constant, a similar behavior to the k_1 constant was observed. The residual stress constant was observed to decrease linearly with the increase in porosity for the SC, BCC, and FCC configurations. Comparing the dependency on the pore configuration with the dependency on the applied heating speed, it was determined that the behavior of the residual stress is also (similar to k_1) independent of the printed configuration and porosity. Finally, for the three configurations, the %SR increases with the increase in structural porosity from 30.5 ± 0.9% at 0% porosity to 37.4 ± 0.8% for the SC, to 39.4 ± 1.9 s for the BCC, and to 38.2 ± 2.2% for the FCC configuration at 15% porosity. Also, a discrepancy was observed in the increase behavior between the SC with the BCC and FCC configurations where the SC configuration shows a linear increase ($R^2 = 0.99$) while both the BCC and FCC configurations show an exponential growth ($R^2 = 0.99$). The overall amount of increase of %SR is solely dependent on the response of the base material when compared to the change in heating speed. This also indicates that the modulation of the %SR is independent of the printed configuration and porosity.

To characterize the large deformation behavior of the 3D printed closed-cell configurations, the structures were compressed to 80% of their original height. The reaction force was recorded and analyzed against the deformation distance. The engineering stresses and strains were used to analyze the stress–strain curves of the printed structures. Due to the large applied deformations, the true stresses and strains required active real-time monitoring of the sample's deformable surface area which was not possible during this study. Moreover, the obtained engineering stress–strain profiles were fitted with the mentioned Goga PFM (section 2.4).

As shown in Figure 7, the engineering stress–strain profiles were analyzed for the three printed closed-cell configurations at the increasing porosity levels (section 2.3). The illustrated profiles represent as sample of each porosity. All measured profiles show three distinct regions with two transition sites with respect to the stress behavior in relation to the increasing applied strain. The first region (as mentioned in section 2.4) is a linear region where the cell walls of the three configurations bend elastically. Considering the application of small strains (approx. $\epsilon < 0.025$), an exponential increase in stress is observed which can be assumed as an initial densification regime which occurs due to the layer-based approach of 3D printing. This effect can be explained as the initial densification or merging of the layers compressing any gaps which forms during the deposition of layers. Following the linear regime, the first transition period occurs which is the yielding of the internal structure (Gibson, 1989). Yielding occurs at the transition between elastic and plastic deformation of the cell walls where a drop or no increase in stress occurs with the increase in strain (Lu & Abbott, 2004; Roylance, 1996). As shown in Figure 7, the second region which is the plateau regime exists for all configurations in the strain range of approx. ~0.2 till ~0.4. The plateau regime shows a slight increase of stress with respect to the increase in strain for all closed-cell configurations. The increase in stress shows the contribution of air within the cells to the mechanical response of the cellular configurations. As mentioned (Gibson, 1989), closed-cells within cellular foams which are subjected to compression, their volume progressively decreases which increases the air pressure within the cell. This contribution is typical negligible at small strains or to the linear elastic behavior. On the other hand, the increase in air pressure induces a sloping stress plateau in elastomeric foams which can exhibit large deformations without rupture of the cell walls (Gibson, 1989). Thus, as shown in Figure 7, the sloping stress plateau shows that the cells within the printed cellular structures were not subjected to printing induced defects which might transition the closed nature of the cells into a connected network. Following the plateau region, the onset of densification was observed where the exponential strain locking behavior is initiated.

To elucidate the stress–strain behavior of the printed closed-cell configurations, the parameters denoting the damping or yielding coefficients η (kPa), the plateau stiffness E_p (kPa), and the densification coefficients γ (kPa) were extracted from the regression and averaged over the number of samples ($n = 3$). First, the Goga PFM parameters were investigated with respect to the material's modulated Young's modulus at 0% porosity which corresponds to the variable heating speeds (refer to Table 2). Considering the densification coefficient, it remained approx. Constant with respect to the increase of NIR heating speed or to the decrease in Young's modulus, as shown in Figure 8a. The densification coefficient was observed to be an average of 165.4 ± 2.3 kPa. This indicates that the densification regime of the printed structures is independent of the applied heat during 3D printing. In addition, the behavior of the base material during strain locking could be independent of the thermal transitions of the material's constitutive components. This is an indication that the densification behavior is solely dependent of the foam's internal structure and

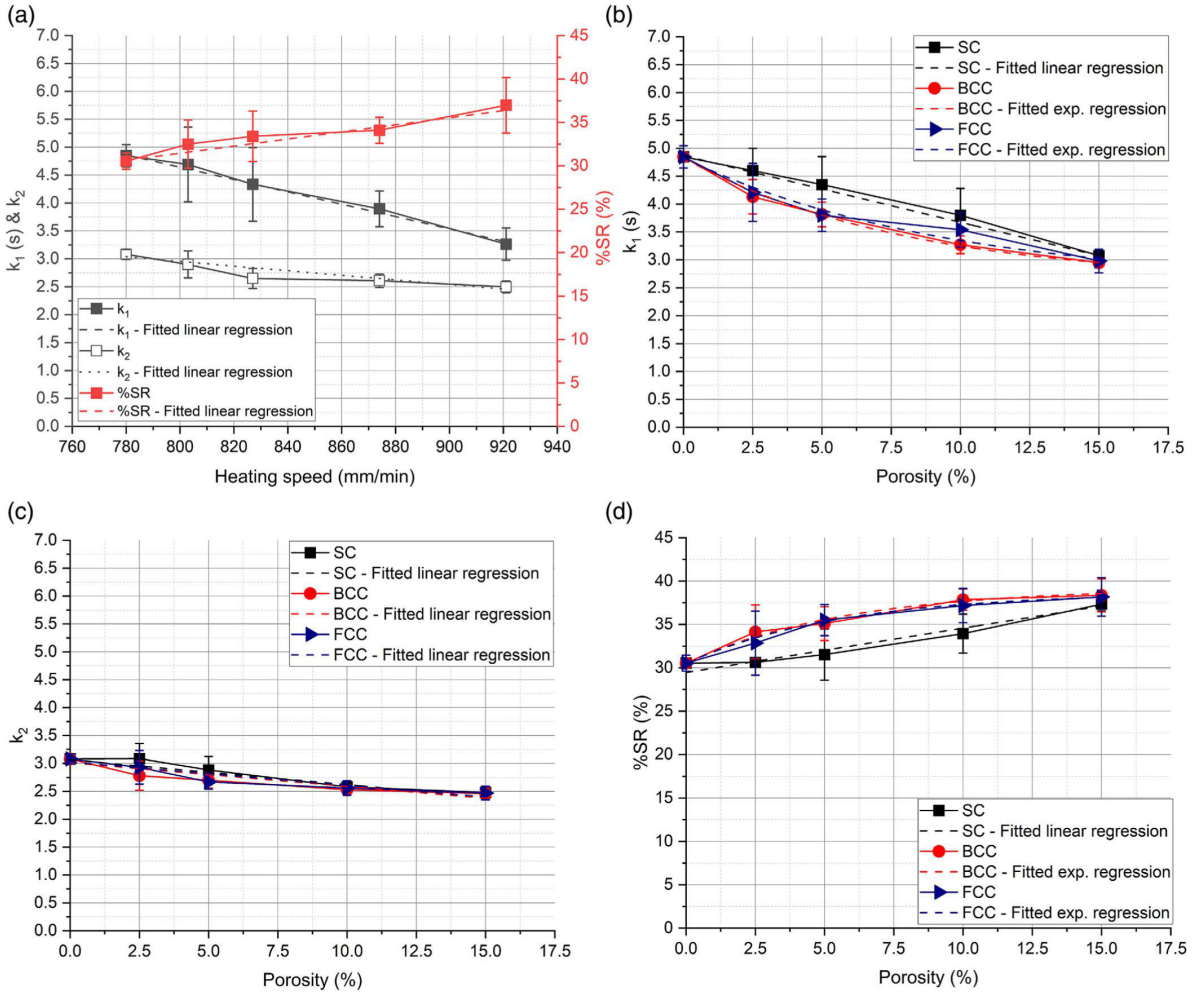

FIGURE 6 Calculated and regression fitted Peleg-Normand model parameters from stress relaxation curves with respect to varying heating speeds and porosities (STD $n = 3$): (a) change in k_1, k_2, and %SR with respect to increasing NIR heating speeds at 0% porosity (base material); (b) behavior of the k_1 intercept at increasing porosity levels for the different 3D printed closed-cell configurations; (c) behavior of k_2 slope at increasing porosity levels for the different 3D printed closed-cell configurations; (d) change in %SR with respect to increasing porosity levels for the different 3D printed closed-cell configurations

relative density. As shown in Figure 8a, unlike the densification coefficient, both the damping and plateau coefficients show an exponential decay behavior with $R^2 = 0.97$ and $R^2 = 0.9$, respectively. This decrease behavior occurs with the increase in NIR heating speed or to the decrease in base material's Young's modulus (refer to Table 2). The damping coefficient which corresponds to the compressive yield stress of the base material was observed to decrease from 44.2 ± 1.9 kPa at $E_{eng} = 359.3 \pm 13.9$ kPa to 22.9 ± 1.1 kPa at $E_{eng} = 140.8 \pm 3.4$ kPa. Thus, the compressive yield stress of the base material can be modulated using the in-line NIR heating system irrespective of the printed porosity or internal structure. Moreover, the plateau coefficient of the base material was observed to decrease from 9.34 ± 0.2 kPa at $E_{eng} = 359.3 \pm 13.9$ kPa to 1.1 ± 0.1 kPa at $E_{eng} = 140.8 \pm 3.4$ kPa. As the plateau regime of cellular foams is correlated with the type or structure of cells (open- or closed-cells) and the enclosed fluid (Gibson, 1989), the change in the plateau stiffness can be contributed to the subjected NIR thermal energy. As the heating speed decreases the heating time of the printed structure increase which increases the occurring mass transfer during NIR thermal stabilization (Dessev et al., 2011; Riadh et al., 2015). Therefore, at lower heating speeds more moisture evaporates which can increase the micro porosity within the printed structures leading to an increase in the plateau response.

Considering the dependency of the model coefficients on the closed-cell configurations and porosity levels, they showed primarily the same behavior with different decay or growth levels depending

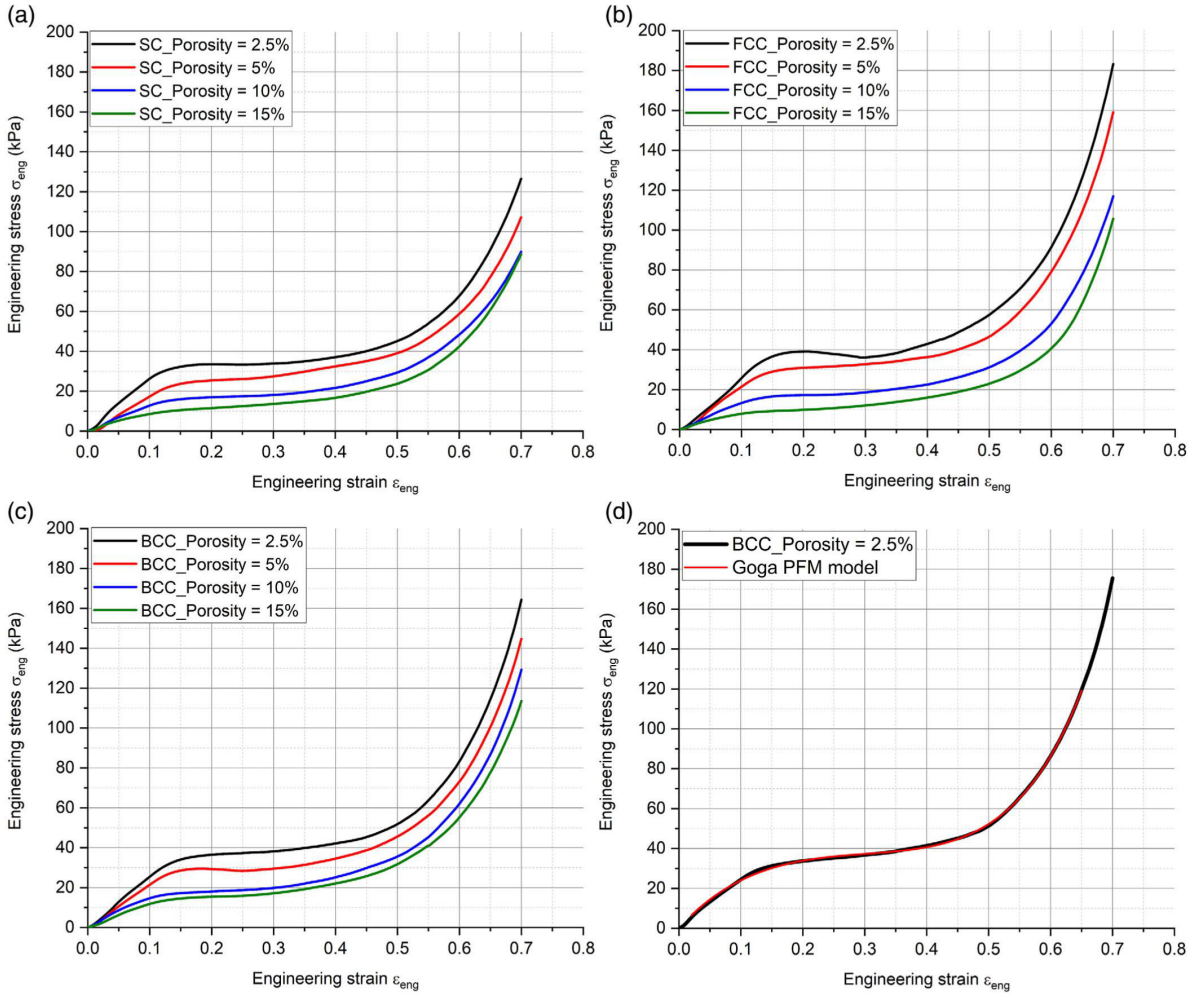

FIGURE 7 Measured engineering stress–strain profiles of the 3D printed closed-cell bubble configurations at the four design porosity levels: (a) engineering stress–strain behavior of SC bubble configuration; (b) engineering stress–strain behavior of FCC bubble configuration; (c) engineering stress–strain behavior of BCC bubble configuration; (d) engineering stress–strain behavior of BCC bubble configuration at 2.5% porosity with Goga PFM regression

on the printed closed-cell configuration. Regarding the damping coefficient or the compressive yield stress of the printed closed-cell configurations, the same exponential decrease as the base material occurs ($R^2_{avg} = 0.98$), as shown in Figure 8b. For the 15% porosity, the three configurations had a compressive yield stress of 16.8 ± 0.6 kPa for the BCC, to 11.9 ± 1.3 kPa for the SC, and to 18.1 ± 2.7 kPa for the FCC configuration. By comparing the results to the yield stress of the base material at the corresponding applied heating speed (22.9 ± 1.1 kPa), it is observed that the inclusion of porosity act as a superposition in the transition between elastic and plastic deformation. The addition of stress concentration points at the cell walls leads to a decrease in the compressive yield stress of the printed structure. Moreover, the lower yield stress of the SC configuration is due to the larger bubbles as for this configuration, the number of cells is lower at the same porosity level.

As shown in Figure 8c, the plateau stiffness showed for the three printed configurations a logarithmic growth behavior with the increase in porosity. This is contributed to the closed-cell response of the air cells to compression which increases with the increase in porosity or amount of compressed air (Gibson, 1989). Illustrated in Figure 8c, the logarithmic growth of the BCC configuration ($R^2 = 0.97$) is observed to be higher than the growth of the SC and FCC configurations ($R^2 = 0.99$ and $R^2 = 0.99$, respectively). The increase in the plateau stiffness of the closed-cell configurations is from 9.34 ± 0.2 kPa at 0% porosity to 47.4 ± 0.2 kPa for the BCC, to 31.3 ± 2.3 kPa for the SC, and to 32.3 ± 5.2 kPa for the FCC configuration. As mentioned in section 2.3, the BCC configuration has a single body-centered bubble while the air bubbles SC and FCC configurations are distributed on the lattice corners and faces. In addition, during compressive testing, the compressive load is not uniform over the

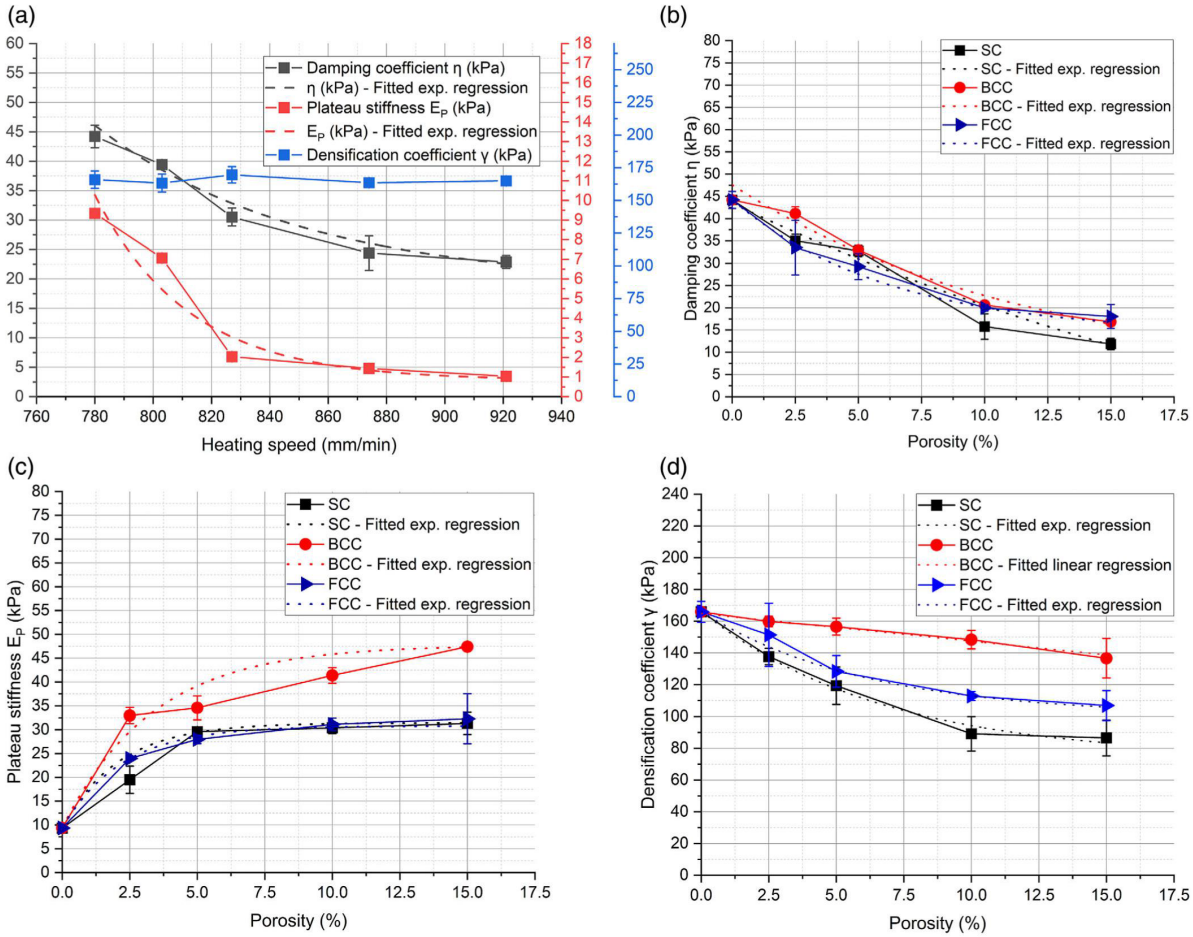

FIGURE 8 Obtained Goga PFM coefficients/stresses from the engineering stress–strain curves with respect to varying heating speeds and porosities (STD $n = 3$): (a) change in damping η, plateau E_P, and densification γ coefficients with respect to increasing NIR heating speeds at 0% porosity (base material); (b) behavior of damping coefficient η with respect to increasing porosity levels of the 3D printed closed-cell bubble configurations; (c) behavior of plateau stiffness E_P with respect to increasing porosity levels of the 3D printed closed-cell bubble configurations; (d) behavior of densification coefficient γ with respect to increasing porosity levels of the 3D printed closed-cell bubble configurations

structure's height. High friction forces act between the top surface and the probe, also high friction forces exist between the bottom surface of the structure and the base support. Thus, low deformation occurs at the structure's top and bottom surfaces (Kramer & Szczesniak, 1973; Peleg, 2019). Therefore, buckling of the middle part occurs which explains the higher registered response of the BCC's centered air bubble.

Considering the densification behavior of the closed-cell configurations, as shown in Figure 8d, a decrease occurs with respect to the increase in porosity. The porosity-modulated behavior is different comparing the BCC configuration with the SC and FCC configurations. The decrease of the densification behavior of the BCC configuration follows a linear regression ($R^2 = 0.99$) while both the SC and FCC configurations follow an exponential decay regression ($R^2 = 0.99$ and $R^2 = 0.99$, respectively). The decrease in the densification coefficient of the closed-cell configurations is from 165.9 ± 6.5 kPa at 0% porosity to 136.6 ± 12.4 kPa for the BCC, to 86.5 ± 11.3 kPa for the SC, and to 106.8 ± 9.4 kPa for the FCC configuration. The results show that the location, size, and number of air bubbles influence the response of the material in the densification regime. Comparing the SC and BCC configurations, the bubble distribution over the lattice structure is the same except for the body-centered bubble of the BCC configuration. As a consequence, the linear decrease behavior of the BCC configuration is caused by the integration of centrally located air cell where the highest deformation occurs during compressive testing. As mentioned before, the behavior of the densification coefficient is independent of the base material's Young's modulus and heating speed. Therefore, the observed decrease behavior shown in Figure 8d proves that the modulation of the densification coefficient occurs through the relative density and the bubble distribution inside the cellular structure.

4 | CONCLUSION

In this study, we extended the texture modulation using 3D printing of starch-based closed-cell foams beyond the elastic regime. We elucidated structure-deformation relations at variable strain rates and large-strain deformation. The main objective was to characterize and understand the behavior of textural properties and stress–strain parameters with respect to the base material's Young's modulus, porosity, and bubble distribution. Three closed-cell configurations were designed printed at five porosity levels. The three closed-cell spherical bubble configurations consisted of simple, base-centered, and face-centered cubic designs. Moisture control and Young's modulus modulation of used starch-based material was performed using in-line NIR thermal stabilization. To verify the precision of the printed structures, hardness levels obtained from FEM simulations and compression analysis were compared and comparable results were achieved.

Concerning the dependency of textural properties on the strain rate of deformation, results showed that the strain rate response of hardness is dependent on the base material's mechanical properties of the cell walls. This is superimposed by the response of the closed cells and porosity which is independent of the printed configuration. Also, the resilience and cohesiveness were observed to be dependent only on the applied strain rate and porosity. The increased response remained unchanged with respect to the applied heating speed and bubble configuration. For characterizing the viscoelastic response of the printed configurations, the stress relaxation spectra were measured, then the Peleg-Normand parameters were evaluated and compared. It was observed for all three configurations that the viscoelastic response is only dependent on the base material properties of the cell walls.

Regarding the stress-stain behavior of the base material, results showed that the densification coefficient remains constant with respect to the increase of NIR heating speed or to the decrease in Young's modulus. The compressive yield stress of the base material can be modulated using the in-line NIR heating system. For the closed-cell configurations, it was observed that the inclusion of porosity act as a superposition in the transition between elastic and plastic deformation. The addition of stress concentration points at the cell walls leads to a decrease in the compressive yield stress of the printed structure. The plateau stiffness showed for the three printed configurations a logarithmic growth behavior with the increase in porosity. This is contributed to the closed-cell response of the air cells to compression. a higher registered response of the BCC's centered air bubble was observed as the compressive load is not uniform over the structure's height. Therefore, buckling of the middle part occurs which explains the higher registered response of the BCC's centered air bubble. Considering the densification behavior, the porosity-modulated behavior was different comparing the BCC configuration with the SC and FCC configurations. The results showed that the location, size, and number of air bubbles influenced the response of the cellular structures in the densification regime.

AUTHOR CONTRIBUTIONS

Ahmed Raouf Fahmy: Methodology; Investigation; Formal analysis; Data curation; Writing - original draft; Visualization; Validation; Software. Mario Jekle: Methodology; Conceptualization; Funding acquisition; Supervision; Writing - review & editing; Project administration; Resources. Thomas Becker: Conceptualization; Writing - review & editing; Funding acquisition; Project administration; Resources.

ACKNOWLEDGMENTS

This research was funded by the Deutsche *Forschungsgemeinschaft* (DFG, German Research Foundation) - 405072578. Open Access funding enabled and organized by Projekt DEAL.

DATA AVAILABILITY STATEMENT

Research data are not shared.

ETHICAL STATEMENTS

Conflict of Interest: The authors declare that they have no known competing financial interests or personal relationships that could have appeared to influence the work reported in this paper or any conflict of interest.

Ethical Review: This study does not involve any human or animal testing.

Informed Consent: Not required.

ORCID

Ahmed Raouf Fahmy https://orcid.org/0000-0003-0218-9380
Mario Jekle https://orcid.org/0000-0002-2560-0040
Thomas Becker https://orcid.org/0000-0001-6842-8300

REFERENCES

Alzoubi, M. F., Abu-Ayyad, M. M., & Al-Hallaj, S. (2014). Modeling of compressiong curves of flexible polyurethane foam with variable density, chemical formulations and strain rates. *Journal of Solid Mechanical*, *6*(1), 82–97.

ASTM-International (2012). Standard terminology for additive manufacturing technologies. In *ASTM F2792-10e1 Standard, Vol ASTM F2792-10e1 Standard*. Pennsylvania: ASTM International.

Attenburrow, G. E., Goodband, R. M., Taylor, L. J., & Lillford, P. J. (1989). Structure, mechanics and texture of a food sponge. *Journal of Cereal Science*, *9*(1), 61–70. https://doi.org/10.1016/S0733-5210(89)80024-4

Avalle, M., Belingardi, G., & Ibba, A. (2007). Mechanical models of cellular solids: Parameters identification from experimental tests. *International Journal of Impact Engineering*, *34*(1), 3–27. https://doi.org/10.1016/j.ijimpeng.2006.06.012

Beer, F. P., Jr., J., E. R., DeWolf, J. T., & Mazurek, D. F. (2011). *Statics and mechanics of materials* (1st ed.). New York: McGraw-Hill.

Chen, J., Mu, T., Goffin, D., Blecker, C., Richard, G., Richel, A., & Haubruge, E. (2019). Application of soy protein isolate and hydrocolloids based mixtures as promising food material in 3D food printing. *Journal of Food Engineering*, *261*, 76–86. https://doi.org/10.1016/j.jfoodeng.2019.03.016

Derossi, A., Caporizzi, R., Oral, M. O., & Severini, C. (2020a). Analyzing the effects of 3D printing process per se on the microstructure and mechanical properties of cereal food products. *Innovative Food Science and Emerging Technologies*, *66*, 102531. https://doi.org/10.1016/j.ifset.2020.102531

Derossi, A., Caporizzi, R., Paolillo, M., & Severini, C. (2020b). Programmable texture properties of cereal-based snack mediated by 3D printing technology. *Journal of Food Engineering*, *289*, 110160. https://doi.org/10.1016/j.jfoodeng.2020.110160

Dessev, T., Jury, V., & Le-Bail, A. (2011). The effect of moisture content on short infrared absorptivity of bread dough. *Journal of Food Engineering*, *104*(4), 571–576. https://doi.org/10.1016/j.jfoodeng.2011.01.019

Fahmy, A. R., Amann, L. S., Dunkel, A., Frank, O., Dawid, C., Hofmann, T., … Jekle, M. (2021a). Sensory design in food 3D printing – Structuring, texture modulation, taste localization, and thermal stabilization. *Innovative Food Science & Emerging Technologies*, *72*, 102743. https://doi.org/10.1016/j.ifset.2021.102743

Fahmy, A. R., Becker, T., & Jekle, M. (2019). *3D printing of starch-based systems: Morphological imaging and flow behavior characterization of multiple stage extrusion through a rheometry imitation approach*. 33rd EFFoST International Conference.

Fahmy, A. R., Becker, T., & Jekle, M. (2020). 3D printing and additive manufacturing of cereal-based materials: Quality analysis of starch-based systems using a camera-based morphological approach. *Innovative Food Science & Emerging Technologies*, *63*(April), 102384. https://doi.org/10.1016/j.ifset.2020.102384

Fahmy, A. R., Becker, T., & Jekle, M. (2021b). *Design and modulation of food textures using 3D printing of closed-cell foams in point lattice systems*. DECHEMA - Jahrestreffen *Lebensmittelverfahrenstechnik*.

Fahmy, A. R., Vogt, U. T., Jekle, M., & Becker, T. (2022). Hardness targeted design and modulation of food textures in the elastic-regime using 3D printing of closed-cell foams in point lattice systems. *Journal of Food Engineering*, *320*, 110942. https://doi.org/10.1016/j.jfoodeng.2022.110942

Gao, J., Wang, Y., Dong, Z., & Zhou, W. (2018). Structural and mechanical characteristics of bread and their impact on oral processing: A review. *International Journal of Food Science and Technology*, *53*(4), 858–872. https://doi.org/10.1111/ijfs.13671

Gholamipour-Shirazi, A., Kamlow, M. A., Norton, I. T., & Mills, T. (2020). How to formulate for structure and texture via medium of additive manufacturing-a review. *Foods*, *9*(4), 497. https://doi.org/10.3390/foods9040497

Gibson, L. J. (1989). Modelling the mechanical behavior of cellular materials. *Materials Science and Engineering A*, *110*, 1–36. https://doi.org/10.1016/0921-5093(89)90154-8

Gibson, L. J., & Ashby, M. F. (1999). *Cellular-solids-structure-and-properties-cambridge-solid-state-science-series-.pdf*. (p. 510).

Godoi, F. C., Prakash, S., & Bhandari, B. R. (2016). 3d printing technologies applied for food design: Status and prospects. *Journal of Food Engineering*, *179*, 44–54. https://doi.org/10.1016/j.jfoodeng.2016.01.025

Goga, V., & Hučko, B. (2016). Phenomenological material model of foam solids. *Strojnícky Casopis – Journal of. Mechanical Engineering*, *65*(1), 5–20. https://doi.org/10.1515/scjme-2016-0001

Hatcher, D. W., Bellido, G. G., Dexter, J. E., Anderson, M. J., & Fu, B. X. (2008). Investigation of uniaxial stress relaxation parameters to characterize the texture of yellow alkaline noodles made from durum and common wheats. *Journal of Texture Studies*, *39*(6), 695–708. https://doi.org/10.1111/j.1745-4603.2008.00164.x

Jang, W., Kraynik, A. M., & Kyriakides, S. (2008). On the Microstructure of Open-Cell Foams and its Effect on Elastic Properties. *International Journal of Solids and Structures*, *45*, 1845–1875. https://doi.org/10.1016/j.ijsolstr.2007.10.008

Jonkers, N., van Dommelen, J. A. W., & Geers, M. G. D. (2020). Experimental characterization and modeling of the mechanical behavior of brittle 3D printed food. *Journal of Food Engineering*, *278*, 109941. https://doi.org/10.1016/j.jfoodeng.2020.109941

Kramer, A., & Szczesniak, A. S. (Eds.). (1973). *Texture measurement of foods* (1st ed.). Netherlands: Springer. https://doi.org/10.1007/978-94-010-2562-1

Lille, M., Kortekangas, A., Heiniö, R. L., & Sozer, N. (2020). Structural and textural characteristics of 3D-printed protein- and dietary fibre-rich snacks made of milk powder and wholegrain rye flour. *Foods*, *9*(11), 1527. https://doi.org/10.3390/foods9111527

Lipton, J., Arnold, D., Nigl, F., Lopez, N., Cohen, D., Norén, N., & Lipson, H. (2010). Mutli-material food printing with complex internal structure suitable for conventional post-processing. *21st annual international solid freeform fabrication symposium - an additive manufacturing conference, SFF 2010*. (January 2010. pp. 809–815).

Liu, Q., & Subhash, G. (2004). A phenomenological constitutive model for foams under large deformations. *Polymer Engineering and Science*, *44*(3), 463–473. https://doi.org/10.1002/pen.20041

Liu, Z., Bhandari, B., Prakash, S., & Zhang, M. (2018). Creation of internal structure of mashed potato construct by 3D printing and its textural properties. *Food Research International*, *111*(2017), 534–543. https://doi.org/10.1016/j.foodres.2018.05.075

Liu, Z., & Zhang, M. (2021). Texture properties of microwave post-processed 3D printed potato snack with different ingredients and infill structure. *Future Foods*, *3*, 100017. https://doi.org/10.1016/j.fufo.2021.100017

Lu, R., & Abbott, J. A. (2004). Force/deformation techniques for measuring texture. In *Texture in food* (Vol. 2, pp. 109–145). Amsterdam: Elsevier Inc. https://doi.org/10.1533/978185538362.2.109

Mantihal, S., Kobun, R., & Lee, B. B. (2020). 3D food printing of as the new way of preparing food: A review. *International Journal of Gastronomy and Food Science*, *22*, 100260. https://doi.org/10.1016/j.ijgfs.2020.100260

Peleg, M. (2019). The instrumental texture profile analysis revisited. *Journal of Texture Studies*, *50*(5), 362–368. https://doi.org/10.1111/jtxs.12392

Peleg, M., & Normand, M. D. (1983). Comparison of two methods for stress relaxation data presentation of solid foods. *Rheologica Acta*, *22*(1), 108–113. https://doi.org/10.1007/BF01679835

Pereira, T., Barroso, S., & Gil, M. M. (2021). Food texture design by 3D printing: A review. *Foods*, *10*(2), 320. https://doi.org/10.3390/foods10020320

Phuhongsung, P., Zhang, M., & Devahastin, S. (2020). Influence of surface pH on color, texture and flavor of 3D printed composite mixture of soy protein isolate, pumpkin, and beetroot. *Food and Bioprocess Technology*, *13*(9), 1600–1610. https://doi.org/10.1007/s11947-020-02497-8

Piovesan, A., Vancauwenberghe, V., Aregawi, W., Delele, M. A., Bongaers, E., de Schipper, M., … Nicolai, B. (2020). Designing mechanical properties of 3D printed cookies through computer aided engineering. *Foods*, *9*(12), 1804. https://doi.org/10.3390/foods9121804

Riadh, M. H., Ahmad, S. A. B., Marhaban, M. H., & Soh, A. C. (2015). Infrared heating in food drying: An overview. *Drying Technology*, *33*(3), 322–335. https://doi.org/10.1080/07373937.2014.951124

Roylance, D. (1996). *Mechanics of materials* (1st ed.). New York, NJ: Wiley & Sons.

Shahbazi, M., Jäger, H., & Ettelaie, R. (2021a). Application of Pickering emulsions in 3D printing of personalized nutrition. Part I: Development of reduced-fat printable casein-based ink. *Colloids and Surfaces A: Physicochemical and Engineering Aspects*, *622*, 126641. https://doi.org/10.1016/j.colsurfa.2021.126641

Shahbazi, M., Jäger, H., & Ettelaie, R. (2021b). Application of Pickering emulsions in 3D printing of personalized nutrition. Part II: Functional properties of reduced-fat 3D printed cheese analogues. *Colloids and Surfaces A: Physicochemical and Engineering Aspects*, *624*, 126760. https://doi.org/10.1016/j.colsurfa.2021.126760

Sun, J., Peng, Z., Zhou, W., Fuh, J. Y. H., Hong, G. S., & Chiu, A. (2015a). A review on 3D printing for customized food fabrication. *Procedia Manufacturing*, *1*, 308–319. https://doi.org/10.1016/j.promfg.2015.09.057

Sun, J., Zhou, W., Huang, D., Fuh, J. Y. H., & Hong, G. S. (2015b). An overview of 3D printing Technologies for Food Fabrication. *Food and Bioprocess Technology*, *8*(8), 1605–1615. https://doi.org/10.1007/s11947-015-1528-6

Szczesniak, A. S. (1963). Classification of textural characteristics. *Journal of Food Science*, *28*, 385–389.

Szczesniak, A. S. (2002). Texture is a sensory property. *Food Quality and Preference*, *13*(4), 215–225. https://doi.org/10.1016/S0950-3293(01)00039-8

Takahashi, T., Hayakawa, F., Kumagai, M., Akiyama, Y., & Kohyama, K. (2009). Relations among mechanical properties, human bite parameters, and ease of chewing of solid foods with various textures. *Journal of Food Engineering*, *95*(3), 400–409. https://doi.org/10.1016/j.jfoodeng.2009.05.023

Vancauwenberghe, V., Mbong, V. B. M., Vanstreels, E., Verboven, P., Lammertyn, J., & Nicolai, B. (2019). 3D printing of plant tissue for innovative food manufacturing: Encapsulation of alive plant cells into pectin based bio-ink. *Journal of Food Engineering*, *263*, 454–464. https://doi.org/10.1016/j.jfoodeng.2017.12.003

Vancauwenberghe, V., Verboven, P., Lammertyn, J., & Nicolaï, B. (2018). Development of a coaxial extrusion deposition for 3D printing of customizable pectin-based food simulant. *Journal of Food Engineering*, *225*, 42–52. https://doi.org/10.1016/j.jfoodeng.2018.01.008

Varghese, C., Wolodko, J., Chen, L., Doschak, M., Srivastav, P. P., & Roopesh, M. S. (2020). Influence of selected product and process parameters on microstructure, rheological, and textural properties of 3D printed cookies. *Foods*, *9*(7), 907. https://doi.org/10.3390/foods9070907

Wang, S., Austin, P., & Bell, S. (2011). It's a maze: The pore structure of bread crumbs. *Journal of Cereal Science*, *54*(2), 203–210. https://doi.org/10.1016/j.jcs.2011.05.004

Wegrzyn, T. F., Golding, M., & Archer, R. H. (2012). Food layered manufacture: A new process for constructing solid foods. *Trends in Food Science and Technology*, *27*(2), 66–72.

Wu, M. Y., Chang, Y. H., Shiau, S. Y., & Chen, C. C. (2012). Rheology of fiber-enriched steamed bread: Stress relaxation and texture profile analysis. *Journal of Food and Drug Analysis*, *20*(1), 133–142. https://doi.org/10.38212/2224-6614.2083

Zghal, M. C., Scanlon, M. G., & Sapirstein, H. D. (2002). Cellular structure of bread crumb and its influence on mechanical properties. *Journal of Cereal Science*, *36*(2), 167–176. https://doi.org/10.1006/jcrs.2001.0445

Zhao, Z., Wang, Q., Yan, B., Gao, W., Jiao, X., Huang, J., … Fan, D. (2021). Synergistic effect of microwave 3D print and transglutaminase on the self-gelation of surimi during printing. *Innovative Food Science and Emerging Technologies*, *67*, 102546. https://doi.org/10.1016/j.ifset.2020.102546

Zhu, S., Vazquez, I., de Azua, R., Feijen, S., Jan, A., der Goot, V., … Stieger, M. (2021). How macroscopic structure of 3D printed protein bars filled with chocolate influences instrumental and sensory texture. *LWT*, *151*, 112155. https://doi.org/10.1016/j.lwt.2021.112155

How to cite this article: Fahmy, A. R., Jekle, M., & Becker, T. (2022). Texture modulation of starch-based closed-cell foams using 3D printing: Deformation behavior beyond the elastic regime. *Journal of Texture Studies*, 1–17. https://doi.org/10.1111/jtxs.12729

3 Discussion

The use of FDM 3D printing in the fabrication of cereal- and starch-based products is a promising texturing method due to its principle of operation. Its introduction allows for higher product and structural reproducibility. For consumption, yet on a small scale, the technology can be used to personalize the fabrication of products in terms of textures, flavors, and nutrition (Godoi et al., 2016; J. Sun, Peng, et al., 2015). From a scientific and research perspective, the randomness and heterogeneity associated with the traditional texturing processes poses several challenges for elucidating and understanding fundamental material-textural-sensorial relationships. This is due to the complexity of the occurring physiochemical processes. On the other hand, 3D printing enhances the reproducibility of structures due to its principles or operation which enables the elucidation of complex relationships and the manipulation of sensory perception (Fahmy et al., 2021). The task is achieved by controlling the material's formulation and properties, the cellular properties, and the distribution of flavor/aroma active compounds.

However, FDM 3D printing is considered as an emerging technology in the manufacturing of cereal- and starch-based textures. The compatibility of the processes with cereal- and starch-based materials is not yet understood. The lack of knowledge about the material's behavior during printing presents a challenge in material selection and ingredient optimization. Also, there are still no standardized quantitative methods for characterizing the printing behavior. Moreover, the applicability of 3D printing in modulating cereal- and starch-based textures is proven in literature, but yet limited. To illustrate, taking full advantage of 3D printing in controlling the textural properties was not achieved previously. As a newly adopted technology, the technological development in localizing flavor/aroma active compounds, in thermally stabilizing structures and inducing physiochemical changes during printing is not reported in literature.

In this context and as a first step for texturing of cereal- and starch-based matrices using 3D printing, the objective of this thesis was to develop scientific-driven general approaches for material behavior evaluation, compound localization, in-line thermal stabilization, and an approach for controlling the textural properties of printed structures. Moreover, fundamental printing behavior and relations with the rheological

behavior of cereal- and starch-based matrices were determined. Research objectives also involved the characterization of the combined texturing-localization 3D printing method. Also, texture-structure relations were elucidated in the linear and non-linear regimes.

Assessment of printing quality and elucidation of material behavior

During the first adoption of FDM 3D printing in food applications, the printing quality determination was performed qualitatively using visual assessment (Periard et al., 2007). The application of qualitative determination hinders the elucidation of material behavior during printing. Also, obtaining correlations of specific geometrical attributes and induced defects with material constituents and rheological parameters was not possible qualitatively. Therefore, the material selection process was performed in a trial and error approach. During further developments, other quantitative approaches was integrated in the evaluation processes in previous literature (mentioned in section 1.4). Most methods including imaging approaches were often not integrated with the 3D printing system and non-automated. Also, the assessment lacked standardization of the printed geometries and structures where experiments were mostly performed on complex designs. Therefore, no clear identification of the geometrical and defect parameters required for quality determination was obtained. In the present study, key geometrical and induced defect parameters were identified and related to the rheological behavior using an imaging approach. An in-line dual camera approach was used for characterizing printed cereal- and starch-based morphologies. A top- and side-view cameras were used to characterize the post-printing geometrical attributes of two cereal-based material systems which comprise of wheat flour dough and wheat starch-egg white protein blends. The hydration level of both material systems was varied to simulate different rheological and viscoelastic responses. Through morphological approaches and pixel-based mathematical operations, the following parameters were autonomously quantified: output width, length, height, extrusion delay and over-extrusion parameters.

For instance, by comparing the rheological behavior with the quantified parameters, it was shown that extrusion delays occur in the beginning of the 3D printing process. Under-extrusion occurred in relation to the material's hydration level which is directly related to the material's yield strength which is supported by literature (M'Barki et al., 2017). Also, the insufficient adhesive force between the deposited material and printing

surface increases the specified delay. However, elucidation of adhesion forces between the materials and the printing surface was not performed. Moreover, a similar effect was characterized which occurs at the end of the printing process. The end of deposition does not occur immediately leading to over-extrusion. Two separate effects were considered. First, a decrease in the materials' yield strength occurs due to the subjected structural deformation of the material systems during extrusion (Puisto et al., 2015; Radhakrishnan et al., 2017). Second, through the analysis of the morphologies, on over-extrusion reaching 100 ± 15.3% was observed for the wheat flour formulation at low hydration levels while only 8.2 ± 2.3% as a maximum was observed for the gluten free material. This was contributed to the strength and formation of the complex gluten network during kneading. Considering structural stability and deformation resistance of the materials after printing, rheological measurements showed a high decrease in the elastic and viscous components for both material systems with the increase in hydration. Defined as a dilution effect (Meerts et al., 2017), the results show softening of the internal structure which reflects an easier extrusion process while increase in structure collapse and slumping behavior. Consequently, the presence of gluten in dough formulations act as a structural stabilizing element, which was reflected in the analyzed heights of the printed structures. On the other hand, the presence of gluten during 3D printing may impose geometrical defects due to the molecular structure and the interactions with the polymer network (Schiedt et al., 2013).

Furthermore, this imaging approach was used in the subsequent articles to elucidate the effect of in-line NIR heating on printing quality as well as for material selection. Finally, this approach was later used in literature for predicting the extrudability of complex food materials during printing using data-driven modelling (L. Zhang et al., 2021). However, the method was used in the present thesis on simple planar and 3D objects. By further optimization of the performed analysis, more complex structures can be recognized and characterized. This can enhance the recognition and elucidation of structure- and printing-driven defects.

An approach for the sensory design of food textures

As mentioned previously in section 1.4, dual extrusion was mainly integrated for texturing of multi-material structures (Gholamipour-Shirazi et al., 2020; Nachal et al., 2019; Periard et al., 2007; J. Sun, Peng, et al., 2015; Tan et al., 2018). This approach is useful for switching materials to fabricate specific features. However, the use of dual

extrusion was not considered before in conjunction with texture modulation for flavor or taste design aspects. As shown in section 2.3, as an objective of this thesis, a novel approach using dual extrusion and focused on-board NIR heating was developed to achieve combined control over texture and taste distribution. The developed method facilitated the design of starch-based structures in reproducible texture and taste configurations. Subsequently, the method was used in a sensory contrast study to characterize the influence of inhomogeneous taste distribution on the sensory perception. For this application, defined concentration gradients of sodium chloride were spatially localized in starch-based textures with different localization configurations or designs. In-line NIR heating was integrated within the 3D printing process to eliminate the need for post-processing or baking. The presented method was optimized for layer-based heating rather than post-printing structural heating. Layer-based heating was implemented for geometrical stabilization and reducing structural collapse or slumping during printing which was elucidated previously in section 2.2.

To print the starch-based textures with localized concentrations of sodium chloride, material selection was performed using the quality assessment method described in section 2.2. A wheat starch-egg white protein mixture (85:15 starch to protein ratio (Jekle et al., 2016)) with a hydration level of 60 g/100 g of dry material was selected based on its characterized printing performance. To achieve higher sensory contrast, desalination of the egg white powder was performed by the means of ultrafiltration. 3D printing was performed using 3 different formulations depending on the salt concentration. The first used formulation is the base material with a NaCl content of 0.16 ± 0.02 g/100 g of dry material. Second, is the medium concentration formulation with a NaCl content of 1.20 ± 0.13 g/100 g of dry material. Finally, is the high concentration formulation with a NaCl content of 2.44 ± 0.20 g/100 g of dry material. For printing the starch-based structures, a cubic design was chosen with 2 different porosity levels of 0 and 25%. A single extruder was used to print the base material while the other extruder was used to printing the sodium containing formulations. Furthermore, 3 different localization layer-based configurations were printed: 4/4 configuration with alternating layers of 4 (4 layers of base material followed by 4 layers with sodium), 2/2 configuration with alternating layers of 2, and 1/1 configuration with single alternating layers.

Results showed that the desalination process and the addition of salt solutions altered the hydration properties as well as the rheological properties (Ferreira Machado et al., 2007; Mmadi et al., 2014; Thammasena et al., 2020). As a consequence, the alteration of rheological properties and flow behavior leads to different material-process interactions (Kim et al., 2017; Godoi et al., 2016; M. Zhang et al., 2017). Thus, the hydration of the formulations was adjusted to achieve comparable rheological levels to the base material prior to desalination. The hydration adjustment was performed while keeping the sodium concentrations constant. The printability of the printed formulations was assessed with and without the integration of NIR heating. Concerning the printing quality prior to heating, results showed that structural collapse occurs with the increase in height of the structure. The formulations showed a decrease in height by approximately 22.8% and increase in width by up to 114% while at 5 layers. This showed a material flow from the top to the bottom layers in the direction of the gravitational forces. The flow of material between the deposited layers is problematic in such a localization application as it could nullify the localization of the sodium component. The inclusion of the layer-based NIR heating showed a large improvement in the structural stability. For each separately heated layer, stabilization occurs in the form of moisture loss which in turn increases the overall complex modulus of the materials. Using the layer-based heat stabilization reduced the deviation in height by 14% (absolute value) with a deviation of 8.8% (compared to 22% before). Regarding the width of the printed structures, the deviation to optimal value improved to 12% (compared to 114% before). However, due to the applied layer-based heating approach, a cyclic heating behavior occurs where lower layers of the printed structure receive more energy compared to the upper layers. Therefore, a heterogeneous distribution of moisture occurs across the height of the printed samples. As a disadvantage, this might lead to different heat induced transformations for the starch and proteins across the deposited layers.

Standardization of the textural properties was of general interest during printing of the different localized configurations of NaCl. As mentioned earlier, hydration levels were adjusted depending on the NaCl concentration. Thus, textural properties were expected to vary with respect to the printed configuration at the same heating level as the final moisture content of the structures will vary. A material-dependent moisture calibration equation was obtained. The equation was used to modulate the output heat depending on the hydration level of the printed material. Through the heat modulation

method, comparable textural properties were obtained for all printed configurations at both porosity levels. The calibration of the textural properties was essential so that textural deviations between the samples would not influence the taste perception of the printed structures. To evaluate the effect of inhomogeneous spatial distribution of sodium on saltiness perception, the printed structures were used in a two-alternative forced choice 2-AFC test. The alternative choice test is a method were n-stimuli are presented to the trained panel which a choice has to be made and in this case is the perception of saltiness. The three printed configurations (1/1, 2/2, and 4/4) were compared to a reference sample with homogeneous distribution containing the same overall NaCl concentration. The overall NaCl content of the homogeneous sample (1.2 ± 0.13 g/100 g of dry material) was not significantly different ($p > 0.05$) for that of the inhomogeneous samples (1.3 ± 0.10 g/100 g of dry material). During the sensory evaluation, the inhomogeneous samples of all three configurations were perceived significantly saltier than the homogeneous reference sample ($p = 0.026$). Which proved a successful application for 3D printing and localization approach.

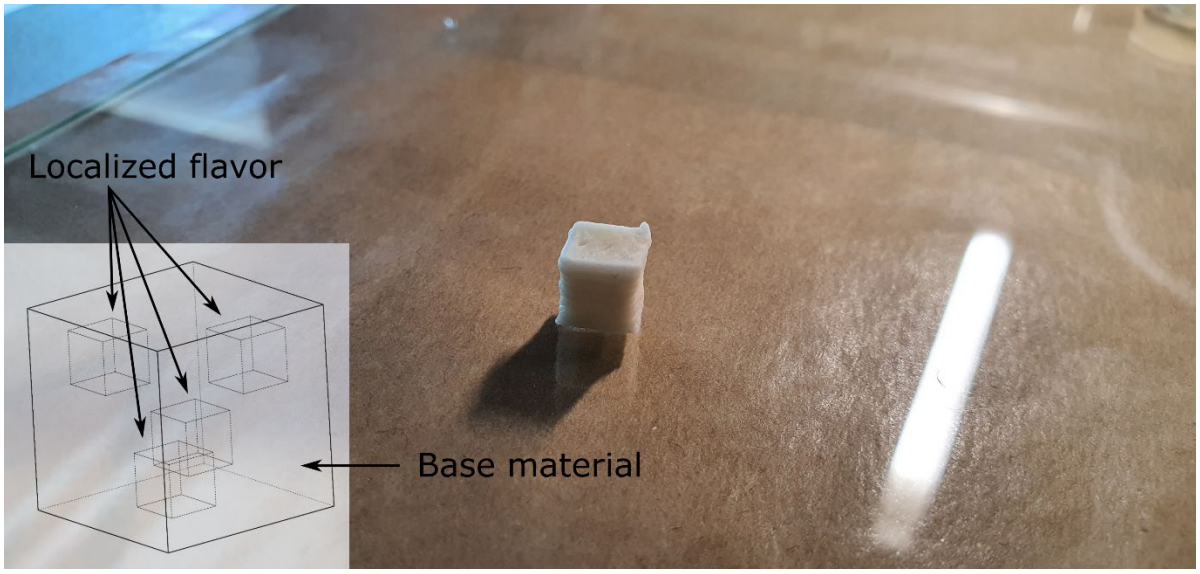

Figure 3-1: 3D printed cube of wheat starch and egg-white protein with localized flavor compound (unpublished figure).

For the use of NIR heating during 3D printing, long-wave radiation controls the amount of transferred energy to the matrix while short IR wave lengths influence the penetration depths (Skjöldebrand et al., 1988). Also, the absorption intensity of the radiative energy is highly dependent on the matrix constituents (Riadh et al., 2015). Thus, as a short coming, the characterization of the applied heat treatment is not generalized but specific for the used cereal matrix and process parameters used in this

thesis. Furthermore, during this study, the effect of NIR stabilization on the micro-structure and on the induced physiochemical transitions was not fully elucidated.

Design of textural properties using 3D printing

The study presented in section 2.3 focused on achieving control over compound distribution in starch-based structures using a combined approach of 3D printing and integrated NIR heating. The structures were printed without the consideration for achieving specific textural properties. To illustrate, the structures were designed without prior knowledge or prediction of the resultant values of the textural properties. The study in section 2.4 of this thesis expands on the objective of accomplishing the control and manipulation of the sensory perception. The main aim was to define a method or an approach for printing structures to target specific levels of textural properties, with the focus on structural hardness of closed-cell foams. The objectives were studied using analytical TPA measurements and FEM simulations by elucidating the dependency of hardness on the material properties, cellular structure, and processing parameters in the elastic regime.

As mentioned earlier in section 1.2, the textural properties of cellular structures depend on the geometry, base material properties, relative density, and pore distribution. Thus, the control over these aspects during 3D printing was crucial for the aims of this thesis. In 3D printing applications of starch-based materials, the determination of material properties is usually performed by the manipulation of the material's constituents. For instance, by increasing/decreasing the hydration of the system, by replacing material constituents, or by increasing/decreasing the concentration of certain components (Z. Liu & Zhang, 2021; Pereira et al., 2021; E. T. Pulatsu et al., 2020). The manipulation of ingredients presents a setback and a challenge during 3D printing. Varying the hydration levels or ingredient concentration affects the material's rheological response thus affecting the printing behavior. Also, applying quality assessment methods will be required to determine the material compatibility. In the present thesis, a different and more defined approach was developed for controlling the base material's mechanical properties. The approach was adopted using the integrated NIR heating. By modulating the heating energy, the Young's modulus E of the cell wall material was varied according to the transfer of mass or moisture loss. This approach was verified on textural analysis basis using the TPA.

As the modulation of the base material's Young's modulus E was performed using NIR heating, only one starch-base material was selected using the method mentioned previously in section 2.2. The printing behavior of 2 material systems were compared at different MC concentrations of 0, 0.5, 1, 2, and 3%. The chosen material was composed of wheat starch and soy protein (85:15 starch to protein ratio) with a hydration level of 100 g/100g of dry material. To develop the Young's modulus E modulation approach, cubic structures of 8000 mm^3 were printed at 0% porosity from the selected material. For the specific NIR heater that was used, the heating power was kept constant at 25% while the heating speed was varied from 9 mm/s to 15 mm/s with a step size of 2 mm/s. Then, the Young's modulus E of the printed structures was measured using the TPA. An exponential decay behavior of E (ranging from 524 ± 45.5 to 74.4 ± 1.7 kPa) was observed with respect to the increase in heating speed. Thus, an equation for E modulation using the heating speed was developed. However, as a short coming of the used method, the obtained exponential decay relation was specific for the used starch-based matrix and the used NIR heater.

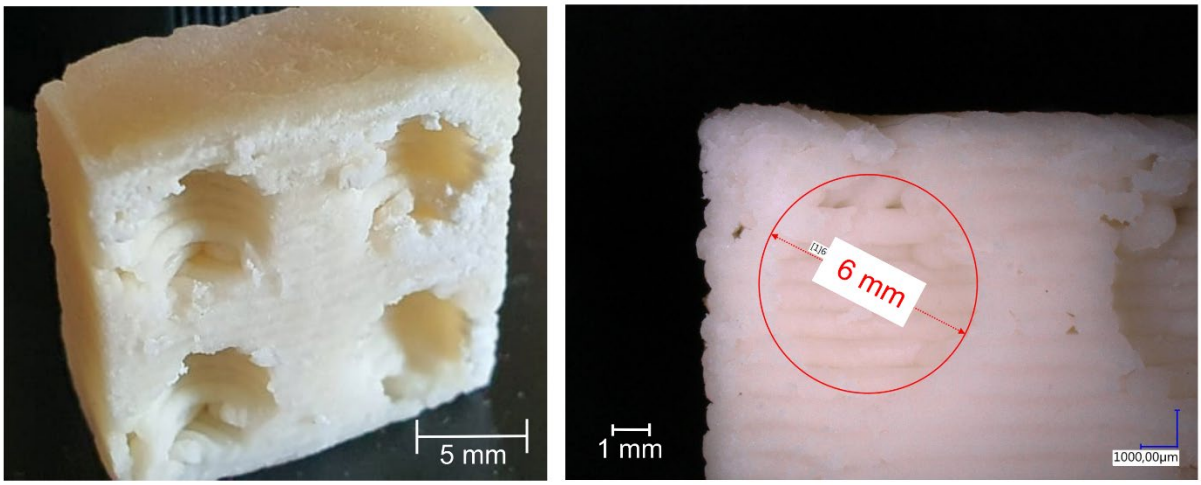

Figure 3-2: FDM 3D printed SC closed-cell design of wheat starch and soy protein.

After achieving the modulation of E for the cell wall material, the cellular structure was varied using closed-cell spherical bubbles, as shown in Figure 3-2. 3 closed-cell designs were used which are simple SC, body-centered BCC, and face-centered cubic FCC. The three designs were printed at varying volumes, surface area, and at 5 porosity levels of 0, 2.5, 5, 10, and 15%. Using a combination of compression TPA tests and FEM simulations, the relation between the base material's E, cellular design parameters, and textural properties were elucidated in the elastic regime. An exponential decay of hardness was observed with the increase of porosity and the

decrease of the base material's E. The obtained hardness for the printed configurations and porosities range from an average of 17.20 ± 2.40 to 1.86 ± 0.45 N at 0 and 15% porosity levels, respectively. The obtained E from the heating modulation method was used to simulate the deformation behavior of the printed designs. Furthermore, comparable results to the TPA were obtained. The hardness of the printed structures was independent of the bubble distribution inside the structure. Also, the cell wall size has no influence the measured hardness of the printed structures in the elastic regime. Thus, it was concluded that the hardness response in the elastic regime can be modulated only using the base material's E, the relative density, and the geometry of the printed structures.

To further illustrate the dependency of hardness on the printed geometry and cellular structure, FEM was used to simulate the dependencies of the structural hardness. Results showed that, for any printed porosity, the structural hardness is linearly related to the cell wall's E. Furthermore, the structural hardness is independent of the printed volume but rather linearly dependent on the deformable surface area. Through the elucidated material, structural, and textural relationships, an HT-PFM equation was obtained using regression fitting. By eliminating the independent variables, the hardness design equation relates the structural hardness with the porosity, Young's modulus, and effective surface area. To verify the obtained equation, hardness values were selected and the equation was solved for the design parameters with upper and lower bounds. Closed-cell cellular structures were designed and printed with the obtained parameters. By comparing the simulations with the 3D printed structures, comparable hardness values were obtained.

The presented approach and model can be used to 3D printing structures with specific hardness values. However, this is only valid for a deformation or a compression level of 10%. Further studies should be performed to extend the model for variable deformation levels in the elastic-regime. Also, the regression fitting of the structure-texture dependencies was performed without regards to the propagation of uncertainties which induces discrepancies between FEM simulations and 3D printing. This method was used to successfully print algae-based hydrogels at specific hardness levels, as shown in Figure 3-3. Furthermore, an exopolysaccharide (EPS) formed by the microalgae Chlorella sorokiniana was produced, hydrogels were formed and used

in combination with the developed phenomenological hardness model to print variable textures with pre-determined hardness levels.

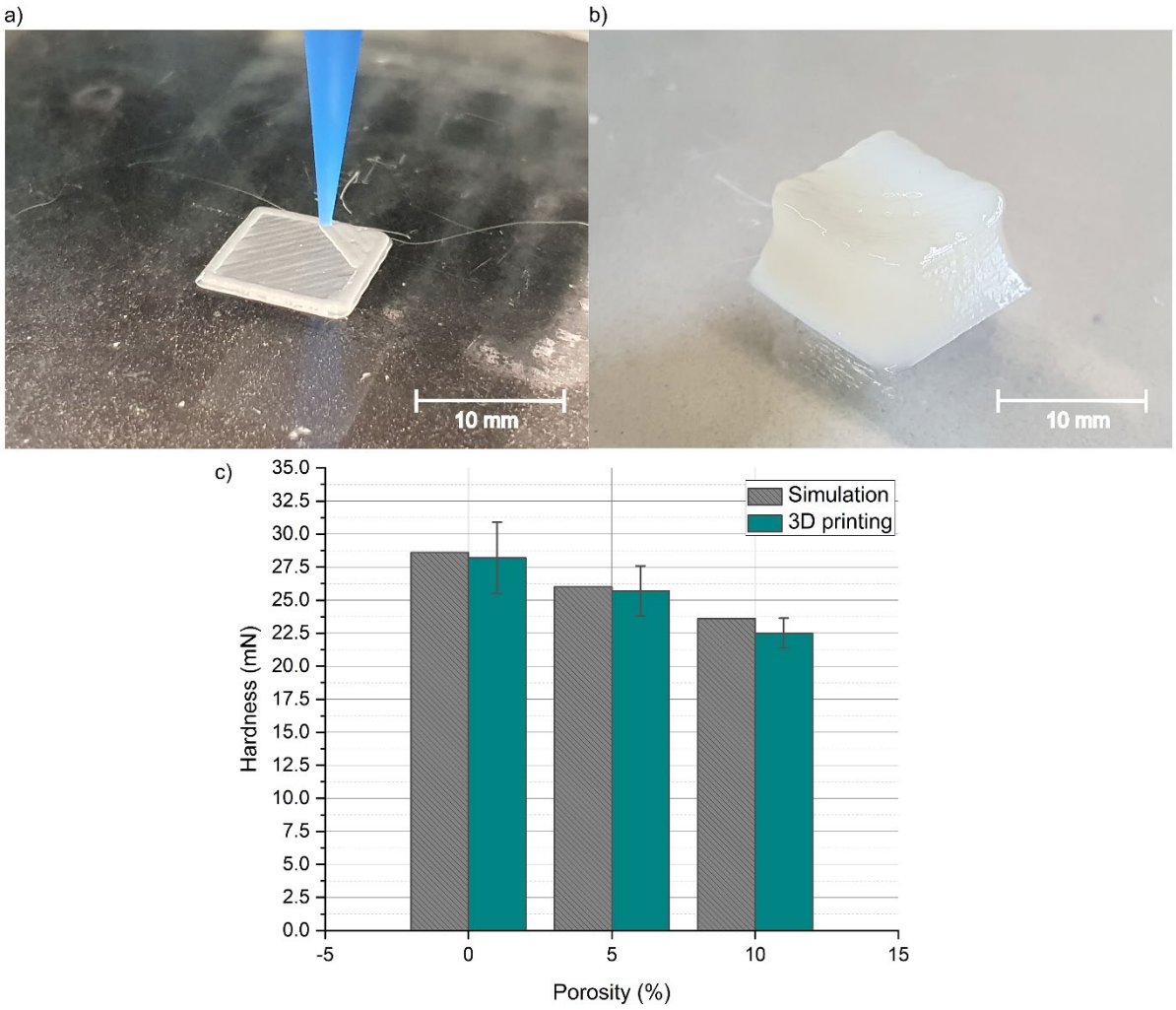

Figure 3-3: Creation of reference textures using a 3D printed biopolymer hydrogel: a) 3D printing process of the cubic structure; b) cuboid with 10% porosity using closed-cell spherical bubbles; c) hardness levels obtained from TPA and FEM simulations.

Textural modulation in the non-linear regime

Previously in section 2.4, the relationship between the material, cellular structure, and textural properties were elucidated only in the elastic regime. Also, an HT-PFM equation was obtained for designing 3D printing cellular structures with specific hardness levels. Prior, the integrated NIR heating method was used only for moisture control and for modulating the base material's Young's modulus. The objective of section 2.5 of this thesis was to extend the textural modulation in the large-strain non-linear regime. Also, another aim was to develop a NIR heating method for achieving starch gelatinization during 3D printing using layer-based heating. The same wheat

starch and soy protein starch-based matrix was selected. To control the foam's cellular structure, the same closed-cell designs (SC, BCC and FCC) were 3D printed at the same porosity levels of 0, 2.5, 5, 10, and 15%. The obtained HT-PFM (section 2.4) was used to modulate the E of the material to achieve a linear decrease hardness with respect to the increase of porosity.

Elastomeric cellular foams are usually non-linear viscoelastic materials which exhibits high static and dynamic linear and viscoelastic behaviors (Alzoubi et al., 2014; Avalle et al., 2007; Wu et al., 2012; Zghal et al., 2002). In section 2.5, the strain rate-dependent behavior, the viscoelastic response and the large-deformation stress-strain behavior of the 3D printed closed-cell foams were studied using TPA compression analysis. Most studies concerning texture modulation of 3D printed food foams do not extend their textural characterization at different strain rates (A. Derossi, Caporizzi, Paolillo, et al., 2020; Pereira et al., 2021; Piovesan et al., 2020; Varghese et al., 2020). First, the strain rate of compression was varied on 5 levels at 10% deformation (in the elastic regime) to elucidate the strain rate dependent textural behavior. The tests were applied in a strain rate range of 0.5, 1.25, 2.5, 3.75, and 5/s. Results showed that the textural strain rate response of the printed cellular structures is independent of the cellular configuration or cell distribution. Results indicates that an increase of approx. ~15.5% (from 12.9 ± 0.8 N at 0.5/s to 14.9 ± 0.4 N at 5/s) for the hardness at 0% porosity occurs with respect to an increase of 10 times in the applied strain rate of deformation. At the same time, for all cellular configurations, an increase of 26.0% (from 5.0 ± 0.2 N at 0.5/s to 6.3 ± 0.3 N at 5/s) occurs at 15% porosity with respect to the same increase in the applied strain rate. By eliminating the influence of porosity, the strain rate response was characterized depending on the E of the cell walls with respect to the applied heating at 0% porosity. A dependency of the hardness's strain rate response on the E was shown. Consequently, the analysis showed that the strain rate response of the structural hardness is dependent on the properties of the cell wall material and superimposed by the response from the closed-cells independent of the pore distribution. Contrarily, other textural properties such as the cohesiveness and resilience were observed to be only dependent on the applied strain rate and on the properties of the cell wall material.

The stress relaxation behavior of the starch-based cellular structure was investigated. A constant strain of 0.5% was applied in the compression analysis for 30s. The

engineering E-T response was analyzed using the Peleg-Normand stress relaxation model (M. Peleg & Normand, 1983). Using this analysis, the overall viscoelastic response was modulated based on the E of the cell walls (Wu et al., 2012). Results showed that the viscoelastic response have a direct relationship with the base material's E. Furthermore, the analysis (through the model coefficients) indicated that the viscoelastic response of the printed cellular structures is independent of the relative density and cellular configuration or pore distribution. Consequently, the investigation revealed that the modulation of the viscoelastic response of cellular structures can be performed using the NIR heating only thorough the modulation of the cell wall material.

Concerning the stress-strain behavior of the cellular structures at large deformation, a PFM was used to characterize 3 deformation regions of elastomeric foams (Goga & Hučko, 2016). However, for this study, the engineering stress and engineering strain was used as monitoring of the deformed cross-sectional area was not possible during compression (Jonkers et al., 2020). The yielding behavior was characterized through the damping coefficient η; the plateau regime was characterized through the plateau stress E_p while the strain locking or densification behavior was characterized through the damping coefficient γ (Goga & Hučko, 2016). The obtained stress-strain parameters were elucidated with respect to the E of the cell walls, porosity and cellular configuration. First, through the analysis of the strain-rate profiles of the printed structures, a linear increase in the E_p was observed in an ϵ range of ~0.2 till ~0.4. As Gibson et al. described, this response belongs to the closed-cells where their volume decreases which increases the air pressure within the cell (L. J. Gibson, 1989). This verified that the internal structure of the printed structures was indeed not connected. Moreover, the γ remained constant with respect to the variation of the E of the cell walls. As mentioned in section 1.2, the densification regime is described with the complete collapse of the cells in a cellular structure. Thus, the modulation of the densification regime is performed using the manipulation of the internal cellular structure irrespective of the printed material.

Unlike the γ, both the η and E_p showed an exponential decay behavior with respect to the decrease of the base material E. Thus, the compressive yield stress of the base material can be modulated using the in-line NIR heating system irrespective of the printed porosity or internal structure. As the plateau regime of cellular foams is correlated with the type or structure of cells (open- or closed-cells) and the enclosed

fluid (L. J. Gibson, 1989), the change in the plateau stiffness can be contributed to the subjected NIR thermal energy. As the heating speed decreases the heating time of the printed structure increase which increases the occurring mass transfer during NIR thermal stabilization (Dessev et al., 2011; Riadh et al., 2015). Therefore, at lower heating speeds more moisture evaporates which can increase the micro-porosity within the printed structures leading to an increase in the plateau response.

Regarding the elucidation of yielding, plateau, and densification with respect to the cellular configuration and porosity, several relationships were identified. The same exponential decay behavior was observed for η, for all configurations with respect to increasing porosity. For the 15% porosity, the 3 configurations had a compressive yield stress of 16.8 ± 0.6 kPa for the BCC, to 11.9 ± 1.3 kPa for the SC, and to 18.1 ± 2.7 kPa for the FCC configuration. By comparing the results to the yield stress of the base material at the corresponding applied heating speed (22.9 ± 1.1 kPa), it was observed that the inclusion of porosity act as a superposition in the transition between elastic and plastic deformation. The addition of stress concentration points at the cell walls leads to a decrease in the compressive yield stress of the printed structure. Moreover, the lower yield stress of the SC configuration is due to the larger bubbles as for this configuration, the number of cells is lower at the same porosity level. As for the E_p, it showed for the 3 printed configurations a logarithmic growth behavior with the increase in porosity. This is contributed to the closed-cell response of the air cells to compression which increases with the increase in porosity or amount of compressed air (L. J. Gibson, 1989). The logarithmic growth of the BCC configuration was observed to be higher than the growth of the SC and FCC configurations. This is due to the base-centered bubble located in the middle of the structure as the deformation in this region is higher (Kramer & Szczesniak, 1973). This means that by designing structures with body centered bubbles increase the structural plateau response.

For the γ, a decrease occurs with respect to the increase in porosity. However, the porosity-modulated behavior is different comparing the BCC configuration with the SC and FCC configurations. The decrease of the densification behavior of the BCC configuration followed a linear regression while both the SC and FCC configurations followed an exponential decay regression. The decrease in the densification coefficient of the closed-cell configurations was from 165.9 ± 6.5 kPa at 0% porosity to 136.6 ± 12.4 kPa for the BCC, to 86.5 ± 11.3 kPa for the SC, and to 106.8 ± 9.4 kPa for the

FCC configuration. The results showed that the location, size, and number of air bubbles influence the response of the material in the densification regime. Comparing the SC and BCC configurations, the bubble distribution over the lattice structure was the same except for the body-centered bubble of the BCC configuration. As a consequence, the linear decrease behavior of the BCC configuration was caused by the integration of centrally located air cell where the highest deformation occurs during compressive testing. As mentioned before, the behavior of the densification coefficient is independent of the base material's Young's modulus and heating speed. Therefore, the observed decrease behavior proved that the modulation of the densification coefficient occurs through the relative density and the bubble distribution inside the cellular structure. Finally, section 2.5 presented a layer-based heating method for achieving onset of starch gelatinization through the attenuation of time-temperature setting during 3D printing. The results were characterized and identified using DSC and CLSM.

Conclusion

Finally, this thesis provided a method-driven approach for 3D printing of cereal- and starch-based materials and structures. The approach was performed on a series of stages including the assessment of material behavior, the integration of thermal stabilization, the localization of taste components, and modulation of textures. Through the camera-based morphological approach, key geometrical and defects parameters were identified and related to the rheological behavior of cereal- and starch-based materials. However, several improvements are encouraged in future research. For instance, expanding the identification to more complex 3D designs as well as integrating the methodology with the printing process to enable quality-driven adjustment of the processing settings during printing. Moreover, the developed and characterized texturing-localization-stabilization method can be used for food materials to create design-driven sensory profiles by through the combination of spatial localization of aromas with the target design of textural properties. However, the correlation between the presented structure-texture information and the sensory qualities is still missing. For future research, the presented methods and structure-texture knowledge can be used to advance in the design of customized sensory perception of food foams.

4 References

Álvarez-Castillo, E., Oliveira, S., Bengoechea, C., Sousa, I., Raymundo, A., & Guerrero, A. (2021). A rheological approach to 3D printing of plasma protein based doughs. *Journal of Food Engineering*, *288*, 110255. https://doi.org/10.1016/j.jfoodeng.2020.110255

Alzoubi, M. F., Abu-Ayyad, M. M., & Al-Hallaj, S. (2014). Modeling of compressiong curves of flexible polyurethane foam with variable density, chemical formulations and strain rates. *Journal of Solid Mechanical*, *6*(1), 82–97.

Ashby, M. F. (2001). Plastic Deformation of Cellular Materials. *Encyclopedia of Materials: Science and Technology*, 7068–7071. https://doi.org/10.1016/b0-08-043152-6/01252-3

ASTM-International. (2012). Standard Terminology for Additive Manufacturing Technologies. *ASTM F2792-10e1 Standard, Vol ASTM F2792-10e1 Standard. ASTM International.*

Attenburrow, G. E., Goodband, R. M., Taylor, L. J., & Lillford, P. J. (1989). Structure, mechanics and texture of a food sponge. *Journal of Cereal Science*, *9*(1), 61–70. https://doi.org/10.1016/S0733-5210(89)80024-4

Avalle, M., Belingardi, G., & Ibba, A. (2007). Mechanical models of cellular solids: Parameters identification from experimental tests. *International Journal of Impact Engineering*, *34*(1), 3–27. https://doi.org/10.1016/j.ijimpeng.2006.06.012

Baker, J. C., & Mize, M. D. (1941). The origin of the gas cell in bread dough. *Cereal Chemistry*, *18*, 19–34.

Benning, C. J. (1969). Plastic foams: the physics and chemistry of product performance and process technology. In *Volume I: chemistry and physics of foam formation* (pp. 131–134). New York: John Wiley.

Biliaderis, C. G. (1991). The structure and interactions of starch with food constituents. *Canadian Journal of Physiology and Pharmacol- Ogy*, *69*, 60–78.

Blanshard, J. M. V. (1986). The significance of the structure and func- tion of the starch granule in baked products. *J. M. V. Blanshard, P. J. Frazier, & T. Galliard (Eds.), Chemistry and Physics of Baking. London: Royal Society of Chemistry*, 1–13.

Bloksma, A. H. (1990a). Dough structure, dough rheology, and bak- ing quality. *Cereal Foods World*, *35*, 237–244.

Bloksma, A. H. (1990b). Rheology of the breadmaking process. *Cereal Foods World*,

35, 228–236.

Bloksma, A. H., & Bushuk, W. (1988). Wheat: chemistry and technology Volume II. In *Rheology and chemistry of dough* (pp. 131–217). MN: American Asso- ciation of Cereal Chemists, Inc.

Bourne, M. C. (2002). *Food Texture and Viscosity* (Second edi). Academic Press.

Brezny, R., & Green, D. J. (1990). The effect of cell size on the mechanical behavior of cellular materials. *Acta Metallurgica et Materialia*, *38*, 2517–2526.

Campbell, G. M., Rielly, C. D., Fryer, P. J., & Sadd, P. A. (1991). The measurement of bubble size distributions in an opaque food fluid. *Transactions Ofthe Institution OfChemicalEngineers, Part C*, *69*, 67– 76.

Cauvain, S. P., & Young, L. S. (2006). *Baked Products: Science, Technology and Practice.* Wiley Online Library.

Chaffanjon, P., & Verhelst, G. (1992). An automated image analysis method for the characterisation of flexible foam cellular structure. *Cellular Polymers*, *11*, 1–17.

Chamberlain, N., & Collins, T. H. (1979). The Chorleywood bread process: the roles of oxygen and nitrogen. *Baker's Digest*, *53*(1), 18– 19, 22–24.

Chen, J., Mu, T., Goffin, D., Blecker, C., Richard, G., Richel, A., & Haubruge, E. (2019). Application of soy protein isolate and hydrocolloids based mixtures as promising food material in 3D food printing. *Journal of Food Engineering*, *261*, 76–86. https://doi.org/10.1016/j.jfoodeng.2019.03.016

Corp, G. F., & Plains, W. (1973). Training a texture profile panel. *Journal of Texture Studies*, *4*, 204–223.

Derossi, A., Caporizzi, R., Oral, M. O., & Severini, C. (2020). Analyzing the effects of 3D printing process per se on the microstructure and mechanical properties of cereal food products. *Innovative Food Science and Emerging Technologies*, *66*, 102531. https://doi.org/10.1016/j.ifset.2020.102531

Derossi, A., Caporizzi, R., Paolillo, M., & Severini, C. (2020). Programmable texture properties of cereal-based snack mediated by 3D printing technology. *Journal of Food Engineering*, *289*, 110160. https://doi.org/10.1016/j.jfoodeng.2020.110160

Derossi, Antonio, Caporizzi, R., Ricci, I., & Severini, C. (2018). Critical variables in 3D food printing. In *Fundamentals of 3D Food Printing and Applications*. Elsevier Inc. https://doi.org/10.1016/B978-0-12-814564-7.00003-1

Dessev, T., Jury, V., & Le-Bail, A. (2011). The effect of moisture content on short infrared absorptivity of bread dough. *Journal of Food Engineering*, *104*(4), 571–

576. https://doi.org/10.1016/j.jfoodeng.2011.01.019

Donovan, J. W. (1979). Phase transitions of the starch-water system. *Biopolymers*, *18*, 263–275.

Evans, I. D., & Lips, A. (1992). Viscoelasticity of gelatinized starch dispersions. *Journal of Texture Studies*, *23*, 69–86.

Evers, A. D., Baker, G. J., & Stevens, D. J. (1984). Production and measurement of starch damage in flour Part 2. Damage produced by unconventional methods. *Starch*, *36*, 350–355.

Fahmy, A. R., Amann, L. S., Dunkel, A., Frank, O., Dawid, C., Hofmann, T., Becker, T., & Jekle, M. (2021). Sensory design in food 3D printing – Structuring, texture modulation, taste localization, and thermal stabilization. *Innovative Food Science & Emerging Technologies*, *72*(August), 102743. https://doi.org/10.1016/j.ifset.2021.102743

Fahmy, A. R., Becker, T., & Jekle, M. (2020). 3D printing and additive manufacturing of cereal-based materials: Quality analysis of starch-based systems using a camera-based morphological approach. *Innovative Food Science & Emerging Technologies*, *63*(April), 102384. https://doi.org/10.1016/j.ifset.2020.102384

Fan, J., Mitchell, J. R., & Blanshard, J. M. V. (1999). A model for the oven rise of dough during baking. *Journalof Food Engineering*, *41*, 69–77.

Farrand, E. A. (1969). Starch damage and alpha-amylase as bases for mathematical models relating to flour water-absorption. *Cereal Chemistry*, *46*, 103–116.

Feng, C., Zhang, M., Liu, Z., Mujumdar, A., Wang, Y., & Chang, L. (2020). Effect of drying method on post-processing stability and quality of 3D printed rose-yam paste. *Drying Technology*, *0*(0), 1–9. https://doi.org/10.1080/07373937.2020.1851708

Ferreira Machado, F., Coimbra, J. S. R., Garcia Rojas, E. E., Minim, L. A., Oliveira, F. C., & Sousa, R. de C. S. (2007). Solubility and density of egg white proteins: Effect of pH and saline concentration. *LWT - Food Science and Technology*, *40*(7), 1304–1307. https://doi.org/10.1016/j.lwt.2006.08.020

Gao, J., Wang, Y., Dong, Z., & Zhou, W. (2018). Structural and mechanical characteristics of bread and their impact on oral processing: a review. *International Journal of Food Science and Technology*, *53*(4), 858–872. https://doi.org/10.1111/ijfs.13671

Gholamipour-Shirazi, A., Kamlow, M. A., Norton, I. T., & Mills, T. (2020). How to

formulate for structure and texture via medium of additive manufacturing-a review. *Foods*, *9*(4). https://doi.org/10.3390/foods9040497

Gibson, L. J. (1989). Modelling the mechanical behavior of cellular materials. *Materials Science and Engineering A*, *110*(C), 1–36. https://doi.org/10.1016/0921-5093(89)90154-8

Gibson, Lorna J., & Ashby, M. F. (1999). *Cellular-Solids-Structure-and-Properties-Cambridge-Solid-State-Science-Series-.pdf* (p. 510). https://books.google.pt/books/about/Cellular_Solids.html?id=IySUr5sn4N8C&source=kp_cover&redir_esc=y

Godoi, F. C., Prakash, S., & Bhandari, B. R. (2016). 3d printing technologies applied for food design: Status and prospects. *Journal of Food Engineering*, *179*, 44–54. https://doi.org/10.1016/j.jfoodeng.2016.01.025

Goga, V., & Hučko, B. (2016). Phenomenological Material Model of Foam Solids. *Strojnícky Casopis – Journal of Mechanical Engineering*, *65*(1), 5–20. https://doi.org/10.1515/scjme-2016-0001

Guessasma, S., Babin, P., Valle, G. Della, & Dendievel, R. (2008). Relating cellular structure of open solid food foams to their Young's modulus: Finite element calculation. *International Journal of Solids and Structures*, *45*(10), 2881–2896. https://doi.org/10.1016/j.ijsolstr.2008.01.007

Guessasma, S., Chaunier, L., Della Valle, G., & Lourdin, D. (2011). Mechanical modelling of cereal solid foods. *Trends in Food Science and Technology*, *22*(4), 142–153. https://doi.org/10.1016/j.tifs.2011.01.005

Guo, C. F., Zhang, M., & Bhandari, B. (2019). A comparative study between syringe-based and screw-based 3D food printers by computational simulation. *Computers and Electronics in Agriculture*, *162*(April), 397–404. https://doi.org/10.1016/j.compag.2019.04.032

Hao, L., Mellor, S., Seaman, O., Henderson, J., Sewell, N., & Sloan, M. (2010). Material characterisation and process development for chocolate additive manufacturing. *Virtual and Physical Prototyping*, *5*(2), 57–64. https://doi.org/10.1080/17452751003753212

He, C., Zhang, M., & Fang, Z. (2020). 3D printing of food: pretreatment and post-treatment of materials. *Critical Reviews in Food Science and Nutrition*, *60*(14), 2379–2392. https://doi.org/10.1080/10408398.2019.1641065

Hull, C. W., & Arcadia, C. (1984). *United States Patent (19) Hull (54) (75) (73) 21) 22*

(51) 52) (58) (56) APPARATUS FOR PRODUCTION OF THREE-DMENSONAL OBJECTS BY STEREO THOGRAPHY. https://doi.org/US005485919A

Jang, W., Kraynik, A. M., & Kyriakides, S. (2008). *On the microstructure of open-cell foams and its effect on elastic properties*. *45*, 1845–1875. https://doi.org/10.1016/j.ijsolstr.2007.10.008

Jekle, M., Mühlberger, K., & Becker, T. (2016). Starch-gluten interactions during gelatinization and its functionality in dough like model systems. *Food Hydrocolloids*, *54*, 196–201. https://doi.org/10.1016/j.foodhyd.2015.10.005

Jonkers, N., Dommelen, J. A. W. Van, & Geers, M. G. D. (2020). Experimental characterization and modeling of the mechanical behavior of brittle 3D printed food. *Journal of Food Engineering*, *278*, 109941. https://doi.org/10.1016/j.jfoodeng.2020.109941

Jordahl, J. H., Solorio, L., Sun, H., Ramcharan, S., Teeple, C. B., Haley, H. R., Lee, K. J., Eyster, T. W., Luker, G. D., Krebsbach, P. H., & Lahann, J. (2018). 3D Jet Writing: Functional Microtissues Based on Tessellated Scaffold Architectures. *Advanced Materials*, *30*(14), 1–9. https://doi.org/10.1002/adma.201707196

Keerthana, K., Anukiruthika, T., Moses, J. A., & Anandharamakrishnan, C. (2020). Development of fiber-enriched 3D printed snacks from alternative foods: A study on button mushroom. *Journal of Food Engineering*, *287*(May), 110116. https://doi.org/10.1016/j.jfoodeng.2020.110116

Kent, N. L., & Evers, A. D. (1994). Kent's technology of cereals. In *Kent's technology of cereals* (4th ed, pp. 191–217). Oxford: Elsevier.

Keunings, R., Bhavar, V., Kattire, P., Patil, V., Khot, S., Gujar, K., Singh, R., Anzalone, G. C., Zhang, C., Wijnen, B., Sanders, P. G., Pearce, J. M., Moylan, S., Whitenton, E., Lane, B., Slotwinski, J., Faludi, J., Hu, Z., Alrashed, S., … Becker, T. (2016). Application of 3D printing for customized food. A case on the development of a fruit-based snack for children. *Journal of Food Engineering*, *215*(3), 0–1. https://doi.org/10.1108/13552540710776197

Khalil, S., & Sun, W. (2007). Biopolymer deposition for freeform fabrication of hydrogel tissue constructs. *Material Science and Engineering: C*, *27*(3), 469–478. https://doi.org/10.1016/j.msec.2006.05.023

Kim, H. W., Bae, H., & Park, H. J. (2017). Classification of the printability of selected food for 3D printing: Development of an assessment method using hydrocolloids as reference material. *Journal of Food Engineering*, *215*, 23–32.

https://doi.org/10.1016/j.jfoodeng.2017.07.017

Kim, H. W., Lee, I. J., Park, S. M., Lee, J. H., Nguyen, M. H., & Park, H. J. (2019). Effect of hydrocolloid addition on dimensional stability in post-processing of 3D printable cookie dough. *Lwt*, *101*(November 2018), 69–75. https://doi.org/10.1016/j.lwt.2018.11.019

Kodama, H. (1981). Automatic method for fabricating a three-dimensional plastic model with photo-hardening polymer. *Review of Scientific Instruments*, *52*(11), 1770–1773. https://doi.org/10.1063/1.1136492

Kramer, A., & Szczesniak, A. S. (Eds.). (1973). *Texture Measurement of Foods* (1st ed.). Springer Netherlands. https://doi.org/10.1007/978-94-010-2562-1

Lagrain, B., Wilderjans, E., Glorieux, C., & Delcour, J. A. (2012). Importance of Gluten and Starch for Structural and Textural Properties of Crumb from Fresh and Stored Bread. *Food Biophysics*, *7*(2), 173–181. https://doi.org/10.1007/s11483-012-9255-2

Lanaro, M., Forrestal, D. P., Scheurer, S., Slinger, D. J., Liao, S., Powell, S. K., & Woodruff, M. A. (2017). 3D printing complex chocolate objects: Platform design, optimization and evaluation. *Journal of Food Engineering*, *215*, 13–22. https://doi.org/10.1016/j.jfoodeng.2017.06.029

Landers, R., Hubel, R., & Borgogelli, R. (2008). The Importance of Cell Structure for Viscoelastic Foams. *PU Magazine International*, 40–48.

Lille, M., Kortekangas, A., Heiniö, R. L., & Sozer, N. (2020). Structural and textural characteristics of 3D-Printed protein- and dietary fibre-Rich snacks made of milk powder and wholegrain rye flour. *Foods*, *9*(11). https://doi.org/10.3390/foods9111527

Lipton, J., Arnold, D., Nigl, F., Lopez, N., Cohen, D., Norén, N., & Lipson, H. (2010). Mutli-material food printing with complex internal structure suitable for conventional post-processing. *21st Annual International Solid Freeform Fabrication Symposium - An Additive Manufacturing Conference, SFF 2010*, *January 2010*, 809–815.

Liu, L., Meng, Y., Dai, X., Chen, K., & Zhu, Y. (2019). 3D Printing Complex Egg White Protein Objects: Properties and Optimization. *Food and Bioprocess Technology*, *12*(2), 267–279. https://doi.org/10.1007/s11947-018-2209-z

Liu, Y., Yu, Y., Liu, C., Regenstein, J. M., Liu, X., & Zhou, P. (2019). Rheological and mechanical behavior of milk protein composite gel for extrusion-based 3D food

printing. *Lwt*, *102*, 338–346. https://doi.org/10.1016/j.lwt.2018.12.053

Liu, Z., Bhandari, B., Prakash, S., Mantihal, S., & Zhang, M. (2019). Linking rheology and printability of a multicomponent gel system of carrageenan-xanthan-starch in extrusion based additive manufacturing. *Food Hydrocolloids*, *87*, 413–424. https://doi.org/10.1016/j.foodhyd.2018.08.026

Liu, Z., Bhandari, B., Prakash, S., & Zhang, M. (2018). Creation of internal structure of mashed potato construct by 3D printing and its textural properties. *Food Research International*, *111*(2017), 534–543. https://doi.org/10.1016/j.foodres.2018.05.075

Liu, Z., & Zhang, M. (2021). Texture properties of microwave post-processed 3D printed potato snack with different ingredients and infill structure. *Future Foods*, *3*(November 2020), 100017. https://doi.org/10.1016/j.fufo.2021.100017

Liu, Z., Zhang, M., Bhandari, B., & Yang, C. (2017). Impact of rheological properties of mashed potatoes on 3D printing. *Journal of Food Engineering*, *220*, 76–82. https://doi.org/10.1016/j.jfoodeng.2017.04.017

Liu, Z., Zhang, M., & Yang, C. hui. (2018). Dual extrusion 3D printing of mashed potatoes/strawberry juice gel. *Lwt*, *96*, 589–596. https://doi.org/10.1016/j.lwt.2018.06.014

Luyten, H., & van Vliet, T. (1995). Fracture properties of starch gels and their rate dependency. *Journal of Texture Studies*, *26*, 281–298.

M'Barki, A., Bocquet, L., & Stevenson, A. (2017). Linking Rheology and Printability for Dense and Strong Ceramics by Direct Ink Writing. *Scientific Reports*, *7*(1), 1–10. https://doi.org/10.1038/s41598-017-06115-0

Makino, M., Fukuzawa, D., Murashima, T., & Furukawa, H. (2017). Simulation of 3D food printing extrusion and deposition. *Nanosensors, Biosensors, Info-Tech Sensors and 3D Systems 2017*, *10167*, 1016717. https://doi.org/10.1117/12.2261409

Malone, E., & Lipson, H. (2007). Fab@Home: the personal desktop fabricator kit. *Rapid Prototyping Journal*, *13*(4), 245–255. https://doi.org/10.1108/13552540710776197

Martin, M. L., Zeleznak, K. J., & Hoseney, R. C. (1991). A mechan- ism of bread firming. I. Role of starch swelling. *Cereal Chemistry*, *68*, 498–503.

Martínez-Monzó, J., Cárdenas, J., & García-Segovia, P. (2019). Effect of Temperature on 3D Printing of Commercial Potato Puree. *Food Biophysics*, *14*(3), 225–234. https://doi.org/10.1007/s11483-019-09576-0

Meerts, M., Cardinaels, R., Oosterlinck, F., Courtin, C. M., & Moldenaers, P. (2017). The Impact of Water Content and Mixing Time on the Linear and Non-Linear Rheology of Wheat Flour Dough. *Food Biophysics*, *12*(2), 151–163. https://doi.org/10.1007/s11483-017-9472-9

Mitchell, A., Lafont, U., Hołyńska, M., & Semprimoschnig, C. (2018). Additive Manufacturing- A Review of 4D Printing and Future Applications. *Additive Manufacturing*. https://doi.org/10.1016/j.addma.2018.10.038

Mmadi, M., Amza, T., Wang, Y. C., & Zhang, M. (2014). Effect of desalination on physicochemical and functional properties of duck (Anas plotyrhyncus) Egg Whites. *Advance Journal of Food Science and Technology*, *6*(6), 784–791. https://doi.org/10.19026/ajfst.6.111

Monaco, R. Di, Cavella, S., & Masi, P. (2008). Predicting Sensory Cohesiveness, Hardness And Springiness of Solid Foods From Instrumental Measurements. *Journal of Texture Studies*, *39*, 129–149. https://doi.org/10.1111/j.1745-4603.2008.00134.x

Nachal, N., Moses, J. A., Karthik, P., & Anandharamakrishnan, C. (2019). Applications of 3D Printing in Food Processing. *Food Engineering Reviews*, *11*(3), 123–141. https://doi.org/10.1007/s12393-019-09199-8

Noort, M., Van Bommel, K., & Renzetti, S. (2017). 3D-printed cereal foods. *Cereal Foods World*, *62*(6), 272–277. https://doi.org/10.1094/CFW-62-6-0272

Noort, M., Vancauwenberghe, V., Van Bommel, K., & Verboven, P. (2017). Innovative structure design of bakery products by means of additive manufacturing (3D printing). *6th Cereals&Europe Spring Meeting*.

Otcu, G. B., Ramundo, L., & Terzi, S. (2019). State of the Art of Sustainability in 3D Food Printing. *Proceedings - 2019 IEEE International Conference on Engineering, Technology and Innovation, ICE/ITMC 2019*. https://doi.org/10.1109/ICE.2019.8792611

Paolillo, M., Derossi, A., Bommel, K. Van, Noort, M., & Severini, C. (2021). Rheological properties, dispensing force and printing fidelity of starchy-gels modulated by concentration, temperature and resting time. *Food Hydrocolloids*, 106703. https://doi.org/10.1016/j.foodhyd.2021.106703

Peleg, M., & Normand, M. D. (1983). Comparison of two methods for stress relaxation data presentation of solid foods. *Rheologica Acta*, *22*(1), 108–113. https://doi.org/10.1007/BF01679835

Peleg, Micha. (2019). The instrumental texture profile analysis revisited. *Journal of Texture Studies*, *50*(5), 362–368. https://doi.org/10.1111/jtxs.12392

Pereira, T., Barroso, S., & Gil, M. M. (2021). Food Texture Design by 3D Printing: A Review. *Foods*, *10*(2), 320. https://doi.org/10.3390/foods10020320

Periard, D., Schaal, N., Schaal, M., Malone, E., & Lipson, H. (2007). Printing food. *18th Solid Freeform Fabrication Symposium*, 564–574.

Phuhongsung, P., Zhang, M., & Devahastin, S. (2020). Investigation on 3D printing ability of soybean protein isolate gels and correlations with their rheological and textural properties via LF-NMR spectroscopic characteristics. *Lwt*, *122*(January), 109019. https://doi.org/10.1016/j.lwt.2020.109019

Piovesan, A., Vancauwenberghe, V., Aregawi, W., Delele, M. A., Bongaers, E., de Schipper, M., van Bommel, K., Noort, M., Verboven, P., & Nicolai, B. (2020). Designing Mechanical Properties of 3D Printed Cookies through Computer Aided Engineering. *Foods*, *9*(12), 1804. https://doi.org/10.3390/foods9121804

Puisto, A., Mohtaschemi, M., Alava, M. J., & Illa, X. (2015). Dynamic hysteresis in the rheology of complex fluids. *Physical Review E - Statistical, Nonlinear, and Soft Matter Physics*, *91*(4). https://doi.org/10.1103/PhysRevE.91.042314

Pulatsu, E., Su, J. W., Lin, J., & Lin, M. (2020). Factors affecting 3D printing and post-processing capacity of cookie dough. *Innovative Food Science and Emerging Technologies*, *61*(November 2019), 102316. https://doi.org/10.1016/j.ifset.2020.102316

Pulatsu, E. T., Su, J., Lin, J., & Lin, M. (2020). Factors affecting 3D printing and post-processing capacity of cookie dough. *Innovative Food Science and Emerging Technologies*, 102316. https://doi.org/10.1016/j.ifset.2020.102316

Radhakrishnan, R., Divoux, T., Manneville, S., & Fielding, S. M. (2017). Understanding rheological hysteresis in soft glassy materials. *Soft Matter*, *13*(9), 1834–1852. https://doi.org/10.1039/c6sm02581a

Ratnayake, W. S., & Jackson, D. S. (2008). Chapter 5 Starch Gelatinization. *Advances in Food and Nutrition Research*, *55*(08), 221–268. https://doi.org/10.1016/S1043-4526(08)00405-1

Riadh, M. H., Ahmad, S. A. B., Marhaban, M. H., & Soh, A. C. (2015). Infrared Heating in Food Drying: An Overview. *Drying Technology*, *33*(3), 322–335. https://doi.org/10.1080/07373937.2014.951124

Robin, F., Dubois, C., Curti, D., Schuchmann, H. P., & Palzer, S. (2011). Effect of

wheat bran on the mechanical properties of extruded starchy foams. *Food Research International*, *44*(9), 2880–2888. https://doi.org/10.1016/j.foodres.2011.06.041

Roylance, D. (2008). *Mechanical Properties of Materials*. MIT. https://doi.org/10.1109/ICT.2007.4569446

Sager, V. F., Munk, M. B., Hansen, M. S., Bredie, W. L. P., & Ahrné, L. (2021). Formulation of heat-induced whey protein gels for extrusion-based 3d printing. *Foods*, *10*(1). https://doi.org/10.3390/foods10010008

Scanlon, M. G., Dexter, J. E., & Biliaderis, C. G. (1988). Particle-size related physical properties of flour produced by smooth roll reduc- tion of hard red spring wheat farina. *Cereal Chemistry*, *65*, 486–492.

Scanlon, M. G., & Zghal, M. C. (2001). Bread structure and crumb structure. *Food Research International*, *34*, 841–864.

Scheuer, P. M., di Luccio, M., Zibetti, A. W., de Miranda, M. Z., & de Francisco, A. (2016). Relationship between Instrumental and Sensory Texture Profile of Bread Loaves Made with Whole-Wheat Flour and Fat Replacer. *Journal of Texture Studies*, *47*(1), 14–23. https://doi.org/10.1111/jtxs.12155

Schiedt, B., Baumann, A., Conde-Petit, B., & Vilgis, T. A. (2013). Short- and long-range interactions governing the viscoelastic properties during wheat dough and model dough development. *Journal of Texture Studies*, *44*(4), 317–332. https://doi.org/10.1111/jtxs.12027

Severini, C., Derossi, A., & Azzollini, D. (2016). Variables affecting the printability of foods: Preliminary tests on cereal-based products. *Innovative Food Science and Emerging Technologies*, *38*, 281–291. https://doi.org/10.1016/j.ifset.2016.10.001

Severini, C., Derossi, A., Ricci, I., Caporizzi, R., & Fiore, A. (2018). Printing a blend of fruit and vegetables. New advances on critical variables and shelf life of 3D edible objects. *Journal of Food Engineering*, *220*, 89–100. https://doi.org/10.1016/j.jfoodeng.2017.08.025

Shah, P., Campbell, G. M., McKee, S. L., & Rielly, C. D. (1998). Proving of bread dough: modelling the growth of individual bubbles. *Transactions of the Institution of ChemicalEngineers, Part C, 76*, 73–79.

Sharma, P. K. (2010). Mechanics of materials. *Technology and Health Care*, *18*(1), 49–61. https://doi.org/10.3233/THC-2010-0566

Shimiya, Y., & Yano, T. (1987). Measurements of accompanying air, specific surface

area and micropore volume of some flour particles. *Agricultural and Biological Chemistry*, *51*, 25–30.

Shimiya, Y., & Yano, T. (1988). Rates of shrinkage and growth of air bubbles entrained in wheat flour dough. *Agricultural and Biological Chemistry*, *52*, 2879–2883.

Silva, M. J., Hayes, W. C., & Gibson, L. J. (1995). The Effects Of Non-Periodic Microstructure On The Elastic Properties Of Two-Dimensional Cellular Solids. *International Journal of Mechanical Sciences*, *37*(11), 1161–1177.

Skjöldebrand, C., Ellbjär, C., Andersson, C. G., & Eriksson, T. S. (1988). Optical properties of bread in the near-infrared range. *Journal of Food Engineering*, *8*(2), 129–139. https://doi.org/10.1016/0260-8774(88)90059-3

Soulaka, A. B., & Morrison, W. R. (1985). The bread baking quality of six wheat starches differing in composition and physical proper- ties. *Journal of the Science of Food and Agriculture*, *36*, 719–727.

Sun, J., Peng, Z., Zhou, W., Fuh, J. Y. H., Hong, G. S., & Chiu, A. (2015). A Review on 3D Printing for Customized Food Fabrication. *Procedia Manufacturing*, *1*, 308–319. https://doi.org/10.1016/j.promfg.2015.09.057

Sun, J., Zhou, W., Huang, D., Fuh, J. Y. H., & Hong, G. S. (2015). An Overview of 3D Printing Technologies for Food Fabrication. *Food and Bioprocess Technology*, *8*(8), 1605–1615. https://doi.org/10.1007/s11947-015-1528-6

Sun, J., Zhou, W., Yan, L., Huang, D., & Lin, L. ya. (2018). Extrusion-based food printing for digitalized food design and nutrition control. *Journal of Food Engineering*, *220*, 1–11. https://doi.org/10.1016/j.jfoodeng.2017.02.028

Sun, Y., Zhang, M., & Chen, H. (2020). LF-NMR intelligent evaluation of rheology and printability for 3D printing of cookie dough pretreated by microwave. *Lwt*, *132*(May), 109752. https://doi.org/10.1016/j.lwt.2020.109752

Szczesniak, A. S. (1963). Classification of textural characteristics. *Journal of Food Science*, *28*, 385–389.

Szczesniak, A. S. (2002). Texture is a sensory property. *Food Quality and Preference*, *13*(4), 215–225. https://doi.org/10.1016/S0950-3293(01)00039-8

Szczesniak, Alina Surmacka. (1986). Review Paper: Correlating Sensory With Instrumental -an Overview of Recent Developments. *Journal of Texture Studies*, *18*(1987), 1–15.

Takahashi, T., Hayakawa, F., Kumagai, M., Akiyama, Y., & Kohyama, K. (2009). Relations among mechanical properties, human bite parameters, and ease of

chewing of solid foods with various textures. *Journal of Food Engineering*, *95*(3), 400–409. https://doi.org/10.1016/j.jfoodeng.2009.05.023

Tan, C., Toh, W. Y., Wong, G., & Li, L. (2018). Extrusion-based 3D food printing - Materials and machines. *International Journal of Bioprinting*, *4*(2), 1–13. https://doi.org/10.18063/IJB.v4i2.143

Thammasena, R., Fu, C. W., Liu, J. H., & Liu, D. C. (2020). Evaluation of nutrient content, physicochemical and functional properties of desalted duck egg white by ultrafiltration as desalination. *Animal Science Journal*, *91*(1), 1–9. https://doi.org/10.1111/asj.13339

Theagarajan, R., Moses, J. A., & Anandharamakrishnan, C. (2020). 3D Extrusion Printability of Rice Starch and Optimization of Process Variables. *Food and Bioprocess Technology*, *13*(6), 1048–1062. https://doi.org/10.1007/s11947-020-02453-6

Tournier, C., Sulmont-rossé, C., & Guichard, E. (2007). Flavour perception: aroma, taste and texture interactions. *Food*, *1*, 246–257.

Trinh, K. T., & Glasgow, S. (2012). *On the texture profile analysis test*.

Vancauwenberghe, V., Delele, M., Vanbiertvliet, J., Aregawi, W., Verboven, P., & Lammertyn, J. (2018). Model-based design and validation of food texture of 3d printed pectin-based food simulants. *Journal of Food Engineering*, *231*, 72–82. https://doi.org/10.1016/j.jfoodeng.2018.03.010

Varghese, C., Wolodko, J., Chen, L., Doschak, M., Srivastav, P. P., & Roopesh, M. S. (2020). Influence of selected product and process parameters on microstructure, rheological, and textural properties of 3D printed cookies. *Foods*, *9*(7). https://doi.org/10.3390/foods9070907

Vesco, A., & Lipson, H. (2009). *Hydrocolloid Printing: A Novel Platform for Customized Food Production*. 807–817.

Wang, L., Zhang, M., Bhandari, B., & Yang, C. (2018). Investigation on fish surimi gel as promising food material for 3D printing. *Journal of Food Engineering*, *220*, 101–108. https://doi.org/10.1016/j.jfoodeng.2017.02.029

Wang, S., Austin, P., & Bell, S. (2011). It's a maze: The pore structure of bread crumbs. *Journal of Cereal Science*, *54*(2), 203–210. https://doi.org/10.1016/j.jcs.2011.05.004

Wang, S., Karrech, A., Regenauer-Lieb, K., & Chakrabati-Bell, S. (2013). Digital bread crumb: Creation and application. *Journal of Food Engineering*, *116*(4), 852–861.

https://doi.org/10.1016/j.jfoodeng.2013.01.037

Weegels, P. L., de Groot, A. M. G., Verhoek, J. A., & Hamer, R. J. (1994). Effects on gluten of heating at different moisture contents. II. Changes in physico-chemical properties and secondary structure. *Journal of Cereal Science*, *19*, 39–47.

Weegels, P. L., Hamer, R. J., & Schofield, J. D. (1996). Critical review. Functional properties of wheat glutenin. *Journal of Cereal Science*, *23*, 1–18.

Wegrzyn, T. F., Golding, M., & Archer, R. H. (2012). Food Layered Manufacture: A new process for constructing solid foods. *Trends in Food Science and Technology*, *27*(2), 66–72. http://dx.doi.org/10.1016/j.tifs.2012.04.006

Wu, M. Y., Chang, Y. H., Shiau, S. Y., & Chen, C. C. (2012). Rheology of fiber-enriched steamed bread: Stress relaxation and texture profile analysis. *Journal of Food and Drug Analysis*, *20*(1), 133–142. https://doi.org/10.38212/2224-6614.2083

Yang, Fan, Zhang, M., & Bhandari, B. (2017). Recent development in 3D food printing. In *Critical Reviews in Food Science and Nutrition* (Vol. 57, Issue 14). https://doi.org/10.1080/10408398.2015.1094732

Yang, Fan, Zhang, M., Fang, Z., & Liu, Y. (2019). Impact of processing parameters and post-treatment on the shape accuracy of 3D-printed baking dough. *International Journal of Food Science and Technology*, *54*(1), 68–74. https://doi.org/10.1111/ijfs.13904

Yang, Fan, Zhang, M., & Liu, Y. (2018). Effect of post-treatment microwave vacuum drying on the quality of 3D-printed mango juice gel. *Drying Technology*, *0*(0), 1–9. https://doi.org/10.1080/07373937.2018.1536884

Yang, Fan, Zhang, M., Prakash, S., & Liu, Y. (2018). Physical properties of 3D printed baking dough as affected by different compositions. *Innovative Food Science & Emerging Technologies*, *49*, 202–210. https://doi.org/10.1016/J.IFSET.2018.01.001

Yang, Fanli, Zhang, M., Bhandari, B., & Liu, Y. (2018). Investigation on lemon juice gel as food material for 3D printing and optimization of printing parameters. *LWT - Food Science and Technology*, *87*, 67–76. https://doi.org/10.1016/j.lwt.2017.08.054

Zghal, M. C., Scanlon, M. G., & Sapirstein, H. D. (1999). Prediction of bread crumb density by digital image analysis. *Cereal Chemistry*, *76*, 734–742.

Zghal, M. C., Scanlon, M. G., & Sapirstein, H. D. (2002). Cellular structure of bread crumb and its influence on mechanical properties. *Journal of Cereal Science*,

36(2), 167–176. https://doi.org/10.1006/jcrs.2001.0445

Zhang, L., Lou, Y., & Schutyser, M. A. I. (2018). 3D printing of cereal-based food structures containing probiotics. *Food Structure*, *18*(August), 14–22. https://doi.org/10.1016/j.foostr.2018.10.002

Zhang, L., Ma, Y., Schutyser, M. A. I., Boom, R. M., & Zhang, L. (2021). Predicting the extrudability of complex food materials during 3D printing based on image analysis and gray-box data-driven modelling. *Innovative Food Science and Emerging Technologies*, *73*(July), 102764. https://doi.org/10.1016/j.ifset.2021.102764

Zhang, M., Liu, Z., Bhandari, B., & Wang, Y. (2017). 3D printing: Printing precision and application in food sector. *Trends in Food Science & Technology*, 564–574. https://doi.org/10.1016/j.tifs.2017.08.018

Zhao, Z., Wang, Q., Yan, B., Gao, W., Jiao, X., Huang, J., Zhao, J., Zhang, H., Chen, W., & Fan, D. (2021). Synergistic effect of microwave 3D print and transglutaminase on the self-gelation of surimi during printing. *Innovative Food Science and Emerging Technologies*, *67*, 102546. https://doi.org/10.1016/j.ifset.2020.102546

5 Appendix

5.1 Co-authored peer-reviewed articles

1. Bruno, B. P., **Fahmy, A. R.**, Sturmer, M., Wallrabe, U., Wapler, M. C. (2019). Properties of piezoceramic materials in high electric field actuator applications. Smart Materials and Structures, 28, 015029. https://doi.org/10.1088/1361-665X/aae8fb
2. Khatri, B., Frey, M., **Fahmy, A. R.**, Scharla, M. V., Hanemann, T. (2020). Development of a multi-material stereolithography 3D printing device. Micromachines, 11, 532. https://doi.org/10.3390/mi11050532

5.2 Non-peer reviewed articles

1. Fahmy, A.R., Jekle, M., Becker, T. (2022). Modulation of cereals and starch-based textures using additive manufacturing. Cereal Technology. Ausgabe 01/2022

5.3 Oral presentations

1. **Fahmy, A. R.**, Jekle, M., Becker, T. (2018). Neues zum 3D-Druck von Lebensmitteln bis hin zum Brot. 7. WIG Frühjahrstagung. Freising, Germany.
2. **Fahmy, A. R.**, Jekle, M., Becker, T. (2018). 3D printing of cereal-based materials: On the relation between rheology and printability. Cereals & Grains AACC annual meeting. London, United Kingdom.
3. **Fahmy, A. R.**, Jekle, M., Becker, T. (2019). Digital food design: 3D printing of customized cereal-based food. 8. WIG Frühjahrstagung. Freising, Germany.
4. **Fahmy, A. R.**, Becker, T., Jekle, M. (2019). Quality analysis of 3D printing cereal-based systems using an imaging morphological approach. 18th European Young Cereal Scientists and Technologists Workshop. San Benedetto del Tronto, Italy.
5. **Fahmy, A. R.**, Becker, T., Jekle, M. (2019). Printing quality and flow behaviour analysis of starch-based systems for 3D printing of cereal matrices. D-A-CH Tagung für angewandte Getreidewissenschaften. Nyon, Switzerland.

6. **Fahmy, A. R.**, Becker, T., Jekle, M. (2019). Flow behaviour analysis for 3D printing of starch-based systems: morphological imaging and multiple stage extrusion characterization through a rheometry imitation approach. 33rd EFFoST International Conference. Rotterdam, Netherlands.
7. **Fahmy, A. R.**, Becker, T., Jekle, M. (2021). Design and modulation of food textures using 3D printing of closed-cell foams in point lattice systems – Hardness targeted design of textures in the elastic regime. DECHEMA - Jahrestreffen Lebensmittelverfahrenstechnik. Online.

5.4 Posters

1. **Fahmy, A. R.**, Becker, T., Jekle, M. (2019). Quality analysis for 3D printing of starch-based systems: morphological imaging and flow behaviour characterization through a rheometry imitation approach. 33rd EFFoST International Conference. Rotterdam, Netherlands.
2. **Fahmy, A. R.**, Becker, T., Jekle, M. (2021). Design and modulation of food textures using 3D printing of closed-cell foams in point lattice systems – Hardness targeted design of textures in the elastic regime. DECHEMA - Jahrestreffen Lebensmittelverfahrenstechnik. Online.